Imperial College London
Department of Physics

Magnetohydrodynamic Simulations of Kelvin-Helmholtz Generated Surface Waves and Vortices at Earth's Magnetopause

Harley Kelly

Thesis submitted for the degree of
Doctor of Philosophy of Imperial College London
and the Diploma of Imperial College London

Abstract

When the magnetised solar wind blows across the magnetopause, a process translates shearing momentum into rotational momentum thus driving vortices and magnetopause surface waves (MSWs) along the magnetopause. This process is called the Kelvin-Helmholtz instability (KHI) and it plays a significant role in the viscous-like mass, momentum, and energy transfer from the solar wind into the magnetosphere.

It is unclear how the plasma properties and magnetic field orientation of the solar wind influence the different evolutionary stages of the KHI. To unbiasedly analyse evolution, a formal definition of a vortex is needed. As one does not exist, a magnetohydrodynamic vortex identification technique, called λ_{MHD}, is derived which is composed of four parts: vortical momentum, density gradients, compressibility, and rotational magnetic tension. Applying this definition to a local simulation shows different drivers are more important in some stages of the KHI than others.

However, the local simulation is a simplification as a realistic magnetopause has a thickness, continuously varying plasma properties, and varying magnetic geometry. Applying λ_{MHD} to a global MHD simulation of the Sun-Earth interaction tests this and finds that the boundary thickness results in inner- and outer-modes which, as they are in different plasma, evolve differently. It is also shown the magnetic geometry limits the latitudinal extent of the vortices.

Finally, there are competing theories surrounding how the KHI influences MSW frequency. These are tested by using dynamic mode decomposition (DMD) - a machine learning technique - on the

global simulation. DMD reveals that the KHI generates, amplifies, and advects MSW frequency across the magnetopause. This results in a complex superposition of frequencies at any one local time. When isolating a single frequency, it is shown that MSW wavelength is Doppler-shifted by the accelerating magnetosheath flow. These results have implications for how MSW frequencies and wavelengths are analysed.

Dedicated to my nan, Juliana Kelly, who always asked me about the stars.

I declare that the work presented in this thesis is my own, except where explicitly indicated otherwise. Information derived from the published and unpublished work of others has been acknowledged in the text and references are given in the list of sources.

The copyright of this thesis rests with the author. Unless otherwise indicated, its contents are licensed under a Creative Commons Attribution-NonCommercial 4.0 International Licence (CC BY-NC).

Under this licence, you may copy and redistribute the material in any medium or format. You may also create and distribute modified versions of the work. This is on the condition that: you credit the author and do not use it, or any derivative works, for a commercial purpose.

When reusing or sharing this work, ensure you make the licence terms clear to others by naming the licence and linking to the licence text. Where a work has been adapted, you should indicate that the work has been changed and describe those changes.

Please seek permission from the copyright holder for uses of this work that are not included in this licence or permitted under UK Copyright Law.

Harley Milo Kelly (2025)

Acknowledgements

Now for the hardest part of the thesis to write, the acknowledgements. I am full of gratitude for so many people who have supported me throughout this journey and I hope to do you all justice here. But first I must thank my examiners, Bob and Tim. Thank you both for reading my thesis, providing helpful corrections, and making my viva an enjoyable discussion.

Firstly I would like to thank my supervisors Martin and Jonathan for their encouragement, guidance, and support. Jonathan I want to thank you for always having the answers to seemingly unanswerable questions, your insight has been invaluable. Martin, without a doubt I would have never have achieved as much as I have if you weren't my supervisor. You have taught me so much and it has been a privilege to be your first PhD student. I am sure you will interview much more thoroughly in the future! Even while starting a family, you have managed to find endless time for me, and for that I am so grateful. Despite all your time and effort, I am sorry that I still do not know the difference between 'effect' and 'affect'.

Next, I would like to thank Harry. I have celebrated finishing my A-levels with you, I endured COVID with you during our undergraduate in Southampton, and now I have finished a PhD with you. When will you leave me alone. Now I know this will be the only part of my thesis you will read, but I want you to know that you are a fantastic friend, and have seen me through the hardest years of my life and I cannot thank you enough. I am sure I speak for us both when I say I look forward to never sharing an office with you again.

This brings me to Adrian and Zoë. I came to Imperial to get a PhD and it appears that instead I drank more tea and coffee than I thought humanly possible. Adrian, I want you to know that you were the most distracting office mate I had. And Zoë, I never thought I would meet someone who overthinks an email more than me. Perhaps my fondness of you both comes from your association with caffeine and the pub. We will never know. I will think of you both every time I boil the kettle.

Now for the rest of the rabble. Thank you to Anna, Arnaud, Cara, Colleen, Domenico, Earn, Heli, Jean, Joseph, Julia, Liam, Lloyd, Kimeel, Luca, Luke, Maddie, Maks, Marie, Matthew, Naïs, Ollie, Pete, Ravi, Rebecca, Rhea, Ronan, Sadie, Sanjee, Stefi, Sophia, Tom, Victor, and Yufei. My time at Imperial would not be the same without you. Special mention to Michaela who wrote her own acknowledgements calling herself my bestest best friend, gym bro, personal trainer, running coach, and #1 fan. You hit the nail on the head. Thank you to my fellow Gorgoon's Joe and Mike, without you I would still be trying to run the code and would have drank far less beer. I would also like to thank my collaborators Katariina and Xuanye for giving me the opportunity to visit the Sunshine state.

I am so blessed to have so many amazing friends. Special mention to Abi, Adam, Adam, Angus, Anthony, Ashley, Charlotte, Ellen, Emma, Gethin, Harry, Jade, Jodie, Josh, Katie, Karriad, Laila, Laura, Meg, Nick, Paige, Rosie, Sam, and Summer for keeping me distracted. I would have gone insane without you. My final thanks are to my parents, step-parents, and brother for their ongoing support. Tyler, I hope you know I only did this so that you have to call me Dr. Whenever the PhD got tough, knowing you all were there made it a little easier.

Contents

1 Introduction **19**

2 A Brief Overview of Relevant Space Plasma Physics **22**

2.1 Space Plasma 22

2.2 Electromagnetism 23

2.3 Single Particle Motion 25

2.4 Kinetic Theory 26

2.5 Magnetohydrodynamics 28

2.5.1 Ideal MHD 29

2.5.2 Magnetic Pressure and Tension 30

2.5.3 The Frozen-in Flux Theorem 32

2.5.4 Magnetic Reconnection 33

2.5.5 MHD Waves 34

2.5.6 Shocks and Discontinuities 38

2.6 The Near-Earth Environment 40

2.6.1 The Solar wind 40

2.6.2 The Magnetosheath 41

2.6.3 The Magnetosphere 42

2.6.4 The Ionosphere . . . 43
2.6.5 The Magnetopause . . . 44

3 The Kelvin-Helmholtz Instability 49

3.1 Linear Theory . . . 51
3.1.1 Incompressible Tangential Discontinuity . . . 51
3.1.2 Compressible Tangential Discontinuity . . . 54
3.1.3 Compressible Finite Boundary . . . 55
3.1.4 Compressible and Bounded Finite Boundary . . . 58
3.1.5 Testing Linear Theory with Observation . . . 60
3.2 Transfer Mechanisms . . . 63
3.2.1 Surface Waves . . . 64
3.2.2 Surface Roll-ups . . . 67
3.3 Waves and Vortices . . . 69
3.3.1 Defining a Vortex . . . 70
3.3.2 Existing Hydrodynamic Vortex Identification Techniques . . . 70
3.3.3 Current Approaches to Vortex Identification at the Magnetopause . . . 72
3.4 Motivation and Questions . . . 74

4 Magnetohydrodynamic Simulations 76

4.1 Local Simulation . . . 78
4.2 Global Simulation . . . 80
4.3 Reconnection in an MHD Simulation . . . 84

5 Helmholtz Decomposition 87

5.1 Fourier Method . . . 90
5.1.1 Example . . . 91
5.2 Hockney-Eastwood Solver . . . 94
5.2.1 Example . . . 96

6 Identifying Kelvin-Helmholtz Generated Vortices in Magnetised Fluids 100

6.1 Introduction . . . 100

6.2 The λ Method for Ideal MHD . . . 101

6.2.1 λ_{MHD} Derivation . . . 103

6.3 Application to Local MHD Simulation . . . 105

6.3.1 Exploring P_{ten} . . . 107

6.3.2 Validating λ_{MHD} . . . 111

6.3.3 Contributions to λ_{MHD} . . . 118

6.3.4 Potential In Situ Applications . . . 124

6.4 Summary . . . 128

7 Effects of a realistic magnetic and plasma environment on KH-generated vortices in a global MHD simulation 132

7.1 Introduction . . . 132

7.2 Simulation Overview . . . 133

7.3 The Effective Pressure . . . 139

7.4 Location of Magnetopause Vortices . . . 143

7.5 Consequences of a realistic plasma environment . . . 153

7.5.1 Equatorial Plane . . . 153

7.5.2 Noon-Midnight Plane . . . 163

7.6 Consequences of a realistic magnetic field geometry . . . 166

7.7 The connection between high-latitude vortices and cusp reconnection . . . 172

7.8 Summary . . . 176

8 How the Frequency and Wavelength of KH-Generated Surface Waves Vary Along the Magnetopause 180

8.1 Introduction . . . 180

8.2 Dynamic Mode Decomposition . . . 182

8.2.1 DMD Algorithm . . . 183

8.2.2 Interpretation and Outputs . . . 186

8.3 DMD of a MHD Fluid . . . 189
8.4 DMD Application . . . 191
8.5 Mode Synopsis . . . 192
8.6 DMD of the Magnetosphere . . . 196
8.7 DMD of the Magnetopause . . . 197
8.7.1 Coordinate frame . . . 197
8.7.2 Frequency Dominance . . . 199
8.7.3 Wavelength Evolution . . . 210
8.8 Summary and Conclusion . . . 219

9 Conclusion **222**

Bibliography **225**

A Permissions **247**

List of Figures

2.1 A two-dimensional cartoon representation of magnetic reconnection. 34

2.2 An illustration of how the phase velocities of the three MHD body waves changes depending on angle to the magnetic field. On the left the Alfvén speed is larger than the sound speed, on the right the opposite. 38

2.3 Illustration of density, temperature, and velocity variations in the magnetosheath. . . 41

2.4 An illustration of Earth's magnetosphere. 42

2.5 A cartoon of the different electrical field-aligned currents connecting the magnetosphere with the ionosphere. 44

2.6 An illustration how the Pederson and Hall currents work in the ionosphere. 45

2.7 An illustration of the Chapman-Ferraro currents. 46

3.1 An illustration of the key stages of the Kelvin-Helmholtz Instability in an idealised geometry. 50

3.2 How the growth rate of the KHI varies depending on M_f and M_A^{-1} 57

3.3 A diagram of the different box and toy models used in KHI theory. 58

3.4 KH-wave occurrence rate as a function of IMF clock angle and cone angle. 62

3.5 Two images of Kelvin-Helmholtz waves in global simulations. 63

3.6 An illustration of the spatial development of the KHI under northward IMF at the magnetopause boundary layer in the equatorial plane. 64
3.7 Illustration of the two different kinds of field line resonances. 65

4.1 An illustrated diagram of the staggered Yee grid used in the Gorgon simulation. . . . 81
4.2 An illustrated diagram of the Gorgon simulation set-up describing the boundary conditions. 85

5.1 A figure demonstrating the effectiveness of a Fourier approach to the Helmholtz Decomposition. 93
5.2 A two-dimensional example of the extended domain used by the Hockney-Eastwood solver. 95
5.3 A computed two-dimensional example showing the extended domain used by the Hockney-Eastwood solver. 97
5.4 A computed two-dimensional example showing the different contributions of the surface, volume, and total integral using the Hockney-Eastwood solver. 98
5.5 A figure demonstrating the effectiveness of a Hockney-Eastwood solver approach to the Helmholtz Decomposition. 99

6.1 A figure showing the equatorial plane of the magnitude of the magnetic field, magnitude of the velocity, and density field in the local simulation. 108
6.2 A figure showing the equatorial plane of the decomposed magnetic tension in the local simulation. 109
6.3 An equatorial ($z = 0$) view of the perturbations from the mean pressure due to magnetic tension, thermal pressure, magnetic pressure, and total pressure. 111
6.4 An equatorial ($z = 0$) view of vortex identification method $-\lambda_{\mathrm{MHD}}$ values on a $\log_{10}$ colour-scale. 113
6.5 An equatorial ($z = 0$) view of vortex identification method $-\lambda_{\mathrm{MHD}}$ values on a $\log_{10}$ colour-scale. 114
6.6 An equatorial ($z = 0$) view of contours for different vortex techniques on a linear colour-scale. These are plotted over the effective pressure variations from the mean. 117

6.7 2D histograms across the entire simulation domain comparing λ_{MHD} with the hydrodynamic vortex criteria. 119

6.8 An equatorial ($z = 0$) view of each contributing term to λ_{MHD}. The values on a symlog$_{10}$ colour-scale where the linear scale is between $\pm 10^{-22}$ Pa m^{-2}. 121

6.9 A 2D histogram across the simulation domain comparing λ_{MHD} with the terms contributing to it. 123

6.10 A spatial slice through the $x = z = 0$ line of the simulation showing $-\lambda_{MHD}$, $-\lambda_{\rho}$, and $-\lambda_{\rho}^{*}$ values. 125

6.11 Vortex criteria values are shown using multi-spacecraft techniques with a mesocentre along the spatial slice through $x = z = 0$ of the simulation with varying radial distances between spacecraft. 127

7.1 Equatorial and noon-midnight cuts of the simulation after 4 hours 17 minutes and 15 seconds of simulation time. 137

7.2 Zoom-ins on the dawn-flank magnetopause in the equatorial plane and the northward magnetopause of the noon-midnight plane of the simulation after 4 hours 17 minutes and 15 seconds of simulation time. 139

7.3 Equatorial and noon-midnight cuts of the simulation after 4 hours 17 minutes and 15 seconds of simulation time. 144

7.4 Equatorial and noon-midnight cuts of the simulation after 4 hours 17 minutes and 15 seconds of simulation time. 148

7.5 Zoom-ins of the Equatorial and noon-midnight cuts of the simulation after 4 hours 17 minutes and 15 seconds of simulation time. 150

7.6 A three-dimensional rendering of the northward dusk flank of the dayside magnetosphere λ_{MHD} plotted with a linear transparency after 4 hours, 17 minutes, and 15 seconds of simulation time. 152

7.7 The mean value of $\overline{\lambda}_{MHD}$ is shown in colour below the threshold value of $\lambda_{MHD} < -1 \times 10^{-25}$, and within 5 R_E of the magnetopause in the equatorial plane 155

7.8 The time-averaged value of $\overline{\lambda}_{M}$, $\overline{\lambda}_{D}$, $\overline{\lambda}_{C}$, $\overline{\lambda}_{T}$ is shown. 157

7.9 Time-averaged values of the density (panel A), magnitude of the velocity (panel B), magnetosonic fast speed (panel C), and the Alfvén speed (panel D) in the equatorial plane. 159

7.10 A cartoon showing how magnetic tension can influence the KHI when it is threading the boundary. The magnetic field lines are shown to be anchored into ionospheres. . 162

7.11 The mean value of λ_{MHD} is shown in colour below the threshold value of $\lambda_{\mathrm{MHD}} < -1 \times 10^{-25}$, and within 5 R_E of the magnetopause in the noon-midnight plane. . . . 164

7.12 The mean value of λ_{M}, λ_{D}, λ_{C}, λ_{T} are shown in colour. 166

7.13 A three-dimensional rendering of the inner- and outer-mode mean value of λ_{MHD} shown using a linear transparency colour below the threshold value of $\lambda_{\mathrm{MHD}} < -1 \times 10^{-25}$, and within 5 R_E of the magnetopause in the noon-midnight plane. 168

7.14 A three-dimensional rendering of field lines of the time-averaged magnetic field at the magnetopause is shown alongside the noon-midnight spatial slice and a cartoon illustrating how the different field lines provide varying latitudinal stability to the magnetopause due to their shape and how parallel they are to the wave vector. . . . 171

7.15 A three-dimensional rendering of λ_{MHD} shown using a linear transparency colour below the threshold value of $\lambda_{\mathrm{MHD}} < -1 \times 10^{-25}$, and within 5 R_E of the magnetopause in the noon-midnight plane. 175

8.1 A cartoon demonstrating how different parameters can be extracted from the complex eigenvalue outputs of DMD. 187

8.2 An illustrative guide to DMD. 189

8.3 A scatter plot of the eigenvalues of the 20 real frequency modes extracted by DMD in colour on an Argand diagram. 193

8.4 A scatter plot of the different mode energies of the 20 real frequency modes extracted by DMD. 194

8.5 A scatter plot of the cumulative fraction of variance from the lowest to highest frequency as a percentage of each of the 20 real frequency modes extracted by DMD. 195

8.6 A scatter plot of the contribution of the magnetic (blue on left), kinetic (red in centre), and internal (green on right) energies to the total mode energies of the 20 real frequency modes extracted by DMD. 195

8.7 Equatorial view of the total pressure fluctuations of mode 2 in colour. The dashed black line shows the redefined inner-boundary which is a sphere of radius 6 R_E. . . . 198

8.8 A figure showing the spatial distribution of the mean total energy fluctuations of the 5 lowest frequency modes integrated within 5 R_E normal of the equilibrium magnetopause. 202

8.9 A plot showing how the mean energy between $Z = -6.5$ to $Z = 6.5$ of a MSW changes along the magnetopause as a function of frequency showing how there is a superposition of wave frequency at all local times. 204

8.10 Figure showing the mean kinetic, magnetic potential, and internal energy fluctuations of mode 2 within 5 R_E normal to the equilibrium magnetopause in the tangential- and Z- directions. 205

8.11 A figure showing the spatial distribution of the time-averaged total energy fluctuations of the 5 lowest frequency modes in the tangential- and normal-directions. 207

8.12 The mean kinetic, magnetic potential, and internal energy fluctuations of mode 2 in the tangential- and normal-directions. Note the different scales on all of the energies. 209

8.13 The spatial distribution of the real part of the total pressure fluctuations of the 5 lowest frequency modes integrated within 5 R_E normal of the equilibrium magnetopause in the tangential and Z directions. 211

8.14 The spatial distribution of the real part of the total pressure fluctuations of the 5 lowest frequency modes in the tangential and normal directions. 213

8.15 The spatial distribution of the real part of the total pressure summed over the 5 lowest frequency modes in the tangential and normal directions. 214

8.16 A figure showing the spatial distribution of the phase of the total pressure fluctuations of the 5 lowest frequency modes integrated within 5 R_E normal of the equilibrium magnetopause in the tangential- and Z- directions. 215

8.17 A figure showing the mean wavelength of the second mode of the total pressure (grey) and the mean of the time-averaged velocity (red) within $\pm 1\,R_E$ of the equilibrium magnetopause boundary as a function of distance along the equilibrium magnetopause from the subsolar point 218

List of Tables

6.1 Table showing the normalisation constants and initial state used in the local simulation. 107

7.1 Table showing the solar wind and IMF conditions of the global simulation. 135

A.1 A table of all the permissions for figures used in this thesis. 247

CHAPTER 1

Introduction

The Sun is a giant ball of hot gas (known as plasma) that resides at the centre of the solar system. Despite how massive it is, the Sun's gravity is not strong enough to hold onto the plasma at its surface resulting in a solar wind which blows out into interstellar space. Earth's magnetosphere, which is the magnetic bubble of space around the terrestrial planet we call home, is a boundary for this solar wind. As the solar wind blows across the magnetosphere's surface, much like wind blowing over the surface of a pond, it generates surface waves through a process known as the Kelvin-Helmholtz instability. These waves allow for energy and momentum to enter Earth's magnetosphere contributing to processes which result in beautiful phenomena such as the Aurora, but also more devastating phenomena such as space weather. The Kelvin-Helmholtz instability contributes a significant amount to the total energy and momentum transfer budget, making it an important piece of the puzzle surrounding how energy and momentum are transferred from the solar wind into the magnetosphere. These surface waves and how they are generated is the focus of this thesis.

The next chapter will contain a brief summary of the space plasma physics used within this work. Following this, Chapter 3 will be where a literature review of the Kelvin-Helmholtz instability will take place, providing vital context for the novel work of this thesis. This review aims to cover the major theoretical breakthroughs concerning the Kelvin-Helmholtz instability at Earth's magnetopause

and summarise them. This chapter will also include a review of relevant observation and simulation based literature, and conclude by summarising what has been discussed and the open questions the novel research chapters aim to answer.

The overall aim of this thesis is simple: to expand understanding about the Kelvin-Helmholtz instability at the surface of the terrestrial magnetosphere. There are many ways to do this. Historically it has been done by developing theory, but since the start of the space age, in-situ measurements of both plasma and electromagnetic fields have been used to verify and challenge the existing theory. Another way to test our current understanding of theory is to use numerical simulations. This is the pathway chosen for this thesis; the reasons as to why will be thoroughly outlined throughout. An overview of the simulations and some numerical methods used to analyse them occurs in Chapters 4, and 5.

This thesis contains three original research chapters which aim to answer three different questions. The first, Chapter 6, attempts to solve a problem about how the properties of the plasma and magnetic field influence the evolution of the Kelvin-Helmholtz instability. To perform this study objectively, an identification technique is derived, validated in a simulation against existing techniques, and is then used to investigate different drivers and stabilisers of the Kelvin-Helmholtz instability. This is important, as a study which considers all the drivers and stabilisers of the Kelvin-Helmholtz instability in a self-consistent and comparable way has not yet been performed.

Building upon this work, which uses a more idealistic plasma and magnetic field environment, the identification technique is applied again but to a more realistic magnetosphere in an attempt to capture the effects the variable magnetospheric environment has on the evolution of the Kelvin-Helmholtz instability. Chapter 7 attempts to bridge the gap between studies which use these simplifying assumptions, and those which do not. To do this, an understanding about the significance and effects of the varying plasma and magnetic environment has on the evolution of the instability is needed. This chapter discerns between the changes caused by the evolution of the instability, and the changes caused by the changing plasma environment and magnetic field geometry.

The final original research chapter, Chapter 8, investigates how the frequencies and wavelengths of the surface waves change spatially. The chapter challenges our understanding about how the instability operates by testing the three dominant competing theories. The work has implications

for commonly used analysis methods both in situ and in simulation. To make this work possible, a data-reduction machine learning technique is used so that a spatio-temporal analysis of an entire global simulation can be conducted.

The thesis closes with a conclusive discussion of the novel results presented in all the original research chapters with suggestions of future work as a result of them.

CHAPTER 2

A Brief Overview of Relevant Space Plasma Physics

2.1 Space Plasma

It is thought that 99% of the observable universe is in the fourth state of matter, plasma. Simply defined, a plasma is a quasi-neutral sufficiently ionised gas which is composed of independently moving charged particles with a higher kinetic energy than electrostatic potential energy. Plasma is a unique state of matter as it is predominantly composed of charged particles meaning that it is coupled to electromagnetic fields through the Lorentz force. This coupling to the electromagnetic fields is what really distinguishes a plasma from a gas as the motion of the plasma particles is not only based on local conditions like it is in a gas, it is also based on the long-range influence of neighbouring plasma and fields – this is known as 'collective behaviour'.

The spatial scale over which a neighbouring particles electrostatic effects persist is known as the Debye length, λ_D, and for an electron-proton plasma this is defined as (Kivelson and Russell 1995),

$$\lambda_D = \sqrt{\frac{\varepsilon_0 k_B T_e}{n_e e^2}}, \tag{2.1}$$

where ε_0 is the is the permittivity of free-space, k_B is the Boltzmann constant, T_e is the electron

temperature, n_e is the electron number density, and e is the electron charge. Over a distance of $L \gg \lambda_D$, it is assumed the electrostatic potential caused by charge imbalances is shielded and screened by the surrounding charged particles. If this effect is perfect, then the plasma as seen from the outside would be overall neutral resulting in the quasi-neutral property of plasma. For this shielding to take place a sphere with a radius of a Debye length, known as a Debye sphere, centred on the shielded charge must contain a sufficient and equal number of positive and negative charges. To know if this is sufficient, the plasma parameter, Λ, must be much greater than unity where

$$\Lambda = n_e \lambda_D^3. \tag{2.2}$$

What makes space plasma particularly special, compared to for example laboratory plasma, is that it has a very low density. This is important as the charged particles are so sparse that 'particle-particle' interactions nearly never occur, restricting how the plasma particles interact with each other to the electromagnetic force fields they perturb resulting in 'wave-particle' and 'wave-wave' interactions only, this is known as being 'collisionless'. This makes understanding the behaviour of the fields fundamental in understanding the behaviour of a plasma.

2.2 Electromagnetism

In the nineteenth century James Clerk Maxwell formulated twenty equations, which fortunately Oliver Heaviside turned into four equations, that completely describe classical electromagnetism (Hunt 2005):

$$\text{Gauss's Law:} \quad \boldsymbol{\nabla} \cdot \mathbf{E} = \frac{\rho_c}{\varepsilon_0}, \tag{2.3a}$$

$$\text{Gauss's Law for Magnetism:} \quad \boldsymbol{\nabla} \cdot \mathbf{B} = 0, \tag{2.3b}$$

$$\text{Ampère's Law:} \quad \boldsymbol{\nabla} \times \mathbf{E} = -\frac{\partial \mathbf{B}}{\partial t}, \tag{2.3c}$$

$$\text{Faraday's Law:} \quad \boldsymbol{\nabla} \times \mathbf{B} = \mu_0 \mathbf{J} + \mu_0 \varepsilon_0 \frac{\partial \mathbf{E}}{\partial t}, \tag{2.3d}$$

where $\mathbf{E}$ is the electric field, ρ_c is the charge density, $\mathbf{B}$ is the magnetic field, $\mathbf{J}$ is the current density, and μ_0 is the permeability of free space. It is often helpful to express the electric and magnetic fields in terms of potential functions. Defining an electric scalar potential as φ and the magnetic vector potential as $\mathbf{A}$, the fields can be written as

$$\mathbf{E} = -\boldsymbol{\nabla}\varphi - \frac{\partial \mathbf{A}}{\partial t}, \tag{2.4a}$$

$$\mathbf{B} = \boldsymbol{\nabla} \times \mathbf{A}. \tag{2.4b}$$

Following Maxwell's formulation of classical electromagnetism, Poynting (1884) derived three fundamental equations describing the energy of electromagnetic waves. The first is known as Poynting vector, $\mathbf{S}$, and describes the directional energy flux of an electromagnetic field, the second is the energy density of the field, U, in some volume:

$$\mathbf{S} = \frac{1}{\mu_0}\mathbf{E} \times \mathbf{B}, \tag{2.5a}$$

$$U = \frac{1}{2}\left(\varepsilon_0|\mathbf{E}|^2 + \frac{1}{\mu_0}|\mathbf{B}|^2\right). \tag{2.5b}$$

The energy density is composed of two parts: the electric energy density, $\varepsilon_0|\mathbf{E}|^2/2$, and the magnetic energy density, $|\mathbf{B}|^2/2\mu_0$. It is worth noting that in the non-relativistic approximation (also known as the low-frequency approximation) the electric energy density is negligible (Walker 2019).

The last equation Poynting derived was a conservation equation known as Poynting's theorem and it describes the conservation of electromagnetic energy,

$$-\frac{\partial U}{\partial t} = \boldsymbol{\nabla} \cdot \mathbf{S} + \mathbf{J} \cdot \mathbf{E}. \tag{2.6}$$

where $\mathbf{J}$ is the current density vector. The three terms of Poynting theorem respectively describe the rate of change of energy density in a volume, the energy flow out of that volume, and the rate at which the fields do work on the charges in that volume.

When dealing with a plasma, many of its properties can evolve and change over time which will in-turn effect the fields and consequently the properties of the plasma such as the charge density,

velocity, and current density. Therefore to try and solve for the dynamic and unique behaviour of space plasmas, many different regimes have been developed all including Maxwell's equations. The simplest with the least assumptions is a single particle motion approach which is a theoretical approach that neglects the collective behaviour of plasma and uses the motion of 'test' particles to explain the plasma's behaviour. Alternatively, a statistical mechanics approach can be used where, instead of treating each particle independently, the particles are assumed to have macroscopic properties derived from the distribution function of the plasma. The final approach is known as magnetohydrodynamics (MHD) where the plasma is considered to be an electrically conducting fluid with average macroscopic physical quantities.

2.3 Single Particle Motion

Single particle motion is the study of how particles behave in a field assuming that the particle does not perturb the field it is moving in. By using this approximation a number of variables can be simply defined. To start, consider a particle with mass, m, charge q, and velocity, $\mathbf{u}$, moving in a constant magnetic field, $\mathbf{B}$, and electric field, $\mathbf{E}$. This particle will experience a Lorentz force, $\mathbf{F}$, defined as,

$$\mathbf{F} = m\frac{d\mathbf{u}}{dt} = q\left(\mathbf{E} + \mathbf{u} \times \mathbf{B}\right). \tag{2.7}$$

If there were only an electric field, the particle would be accelerated by the electric field. If there were only a magnetic field, this force would be orthogonal to $\mathbf{B}$, causing the particle to oscillate and gyrate in a circular motion in the plane threading the magnetic field with a perpendicular velocity of $u_\perp$. It is worth noting that the force from the magnetic field is not along the direction of motion so no work is being done on the particle by the magnetic field i.e. the particle is not gaining kinetic energy from the magnetic field. This means that particles moving obliquely to a magnetic field will gyrate about the field line while also being guided by it. Under these conditions, the radius of the circular path the particle takes is known as the gyroradius, defined as

$$r_g = \frac{mu_\perp}{q|\mathbf{B}|}. \tag{2.8}$$

The angle in radians the particle moves every second is known as the gyrofrequency and is defined as

$$\omega_g = \frac{q|\mathbf{B}|}{m}. \tag{2.9}$$

By inspection it can be seen that lighter particles have a smaller gyroradii and a higher gyrofrequency meaning that they gyrate faster and with smaller rotations than the heavier particles. As well as this, the particle charge will dictate the direction of rotation. These things together do not necessarily impact the plasma behaviour; however if, say, an electric field is also imposed on the plasma, it will. If both an electric and magnetic field is imposed on the charged particle, then the particle would be accelerated in the direction defined by the electric field while also gyrating around the magnetic field causing it to drift in the $\mathbf{E} \times \mathbf{B}$ direction irrespective of charge.

It is clear now that the motion of individual particles is dominated by the fields that are imposed on them, and in certain cases this can result in currents being generated. However, this type of approach is not too helpful when dealing with the large scale collections of particles which are actually present in space plasmas. This leads to the next theoretical approach used in the field called kinetic theory.

2.4 Kinetic Theory

Kinetic theory is a way to model the collective behaviour of a plasma as it statistically parametrises the motion of a particle in the plasma. To understand how of a large number of particles with varying velocities and different charges behave, a more statistical approach is needed which considers the number of particles per species, per unit volume in a six-dimensional parameter space called a phase space. A phase space describes the complete set of possible physical states of the system under a given parametrisation. By doing this, a phase space density distribution function, f, is given for each particle species denoted with a subscript s. This phase space distribution function is six-dimensional and describes the species phase space distributions in position, $\mathbf{r}$, velocity, $\mathbf{u}$, and time, t, yielding: $f_s(\mathbf{r}, \mathbf{u}, t)$.

When the particles in a plasma are in regions where particles of different charges behave differently for example due to the mass variation between a proton and electron, these gyrations can cause

differential flows in protons and electrons – also known as a current. The current density can then be calculated for a plasma with number density n using

$$\mathbf{J} = ne\left(\mathbf{u}_i - \mathbf{u}_e\right), \tag{2.10}$$

where the ions and electron are assumed to have charge e and velocity $\mathbf{u}_i$ and $\mathbf{u}_e$ respectively. Describing the motion of a collection of particles is difficult, but there is a solution.

Fortunately, in 1938 Anatoly Vlasov described how this phase space distribution function evolves when some averaged electric or magnetic field is imposed (Vlasov 1968). A more common formulation given for the collisionless case is (Gurnett and Bhattacharjee 2005),

$$\frac{\partial f_s}{\partial t} + \mathbf{u}_s \cdot \boldsymbol{\nabla}_{\mathbf{r}} f_s + \frac{q_s}{m_s}\left(\mathbf{E} + \mathbf{u}_s \times \mathbf{B}\right) \cdot \boldsymbol{\nabla}_{\mathbf{u}} f_s = 0. \tag{2.11}$$

A more general collisional version, called the Boltzmann equation, predates the Vlasov equation and includes an additional collisional term. However, given that collisional effects are very minor in space plasmas, they are typically neglected making the Vlasov equation sufficient. Despite being a simplification of the collisional Boltzmann equation, the Vlasov equation is still highly non-linear and further simplifications can be made to gain a more macroscopic description of the plasma.

These macroscopic quantities remove the generality of the kinetic theory case, which essentially means that the velocity dependence of the phase space distribution function is removed. These macroscopic quantities are calculated by multiplying the phase space distribution function by the velocity raised to some power and then integrating over the velocity space – this is known as taking the distribution functions moments. Other parameters can also be multiplied with the distribution

function and integrated over to provide useful parameters:

$$n_s = \int_V f_s(\mathbf{u})\, d^3u, \tag{2.12a}$$

$$\rho_s = \int_V f_s(\mathbf{u}) q_s\, d^3u, \tag{2.12b}$$

$$\mathbf{v}_s = \frac{1}{n_s} \int_V \mathbf{u} f_s(\mathbf{u})\, d^3u, \tag{2.12c}$$

$$\mathbf{j} = \sum_s \frac{1}{n_s} \int_V \mathbf{u} f_s(\mathbf{u}) q_s\, d^3u, \tag{2.12d}$$

where d^3u corresponds to the velocity space volume element (e.g. for Cartesian space $du_x du_y du_z$). Taking further moments yields other physical properties, for example the second moment corresponds to the pressure tensor, $\underline{\mathbf{P}}$, with the scalar pressure being found through the trace; the third the heat flux tensor, $\underline{\mathbf{Q}}$. Higher order moments of the equation exist but are less physically tangible.

By ignoring all the micro-quantities and only considering the macro-quantities is an approach known as fluid theory or magnetohydrodynamics.

2.5 Magnetohydrodynamics

Magnetohydrodynamics (MHD) was initially derived by Hannes Alfvén (1942) who combined the Navier-Stokes equations for fluids (Stokes 2009b) with Maxwell's electromagnetic equations (Equations 2.3a-d). MHD is the treatment of a plasma as an electrically conducting fluid with average macroscopic physical quantities. In multi-fluid MHD each fluid typically represents a different species and these differently flowing species allow for parameters to be defined such as current. However, a single fluid description can be found by summing over all the different species.

In a single fluid description, a different equation is needed to describe the current density vector. This equation is known as generalised Ohm's law which is a series of terms that describe the electric fields generated by moving fields and plasmas. However, not all the terms in the equation are relevant to this thesis. The most important version in the context of this work is the resistive Ohm's law,

$$\eta \mathbf{J} = \mathbf{E} + \mathbf{u} \times \mathbf{B} \tag{2.13}$$

where η is the electrical resistance of a unit area of plasma per unit length which is known as resistivity.

Even though MHD is a fluid simplification of the plasma, many different varieties of it exist to best match the needs of the user e.g. multi-fluid MHD which models different species as separate yet interacting fluids. Fortunately, for space plasma physics the simplest is surprisingly effective.

2.5.1 Ideal MHD

The simplest form of MHD is known as ideal MHD and it is a single-fluid approach. For ideal MHD to be valid, it requires a number of assumptions. The motion of the plasma must be non-relativistic ($u^2 << c^2$) and therefore the displacement current ($\partial \mathbf{E}/\partial t$) is zero, simplifying Ampère's law (Equation 2.3c). The time scales at which things change must be larger than the ion gyroperiod and the length scales over which things change must be larger than the gyroradius. The plasma must be quasi-neutral and collisional such that the velocity distribution function is Maxwellian therefore temperature is well-described. In the collisionless case, the assumed thermal equilibrium (which is not at all the case in real space plasmas) is achieved through wave-particle/wave-wave interactions and the resistivity (which is proportional to collision frequency) tends to 0, $\eta \rightarrow 0$, making Ohms law ideal. The electron mass is assumed to be negligible compared to the ion mass. This results in a thermal pressure, P, which is isotropic and therefore scalar meaning that the ideal gas law $P = nk_BT$ is a valid equation of state. The result of all these approximations is a description of large-scale plasma dynamics without the need to consider any complex particle interactions.

In short, ideal MHD can be summarised in the following equations,

$$\text{Continuity Equation:} \quad \frac{\partial \rho}{\partial t} + \boldsymbol{\nabla} \cdot (\rho \mathbf{v}) = 0, \tag{2.14a}$$

$$\text{Cauchy-Momentum Equation:} \quad \frac{\partial}{\partial t}(\rho \mathbf{v}) + \boldsymbol{\nabla} \cdot (\rho \mathbf{v}\mathbf{v}) = -\boldsymbol{\nabla} P + \mathbf{J} \times \mathbf{B}, \tag{2.14b}$$

$$\text{Ideal Ohm's law:} \quad \mathbf{E} + \mathbf{v} \times \mathbf{B} = 0, \tag{2.14c}$$

$$\text{Ideal Induction Equation:} \quad \frac{\partial \mathbf{B}}{\partial t} = \boldsymbol{\nabla} \times (\mathbf{v} \times \mathbf{B}) \tag{2.14d}$$

$$\text{Low-Frequency Ampère's Law:} \quad \boldsymbol{\nabla} \times \mathbf{B} = \mu_0 \mathbf{J} \tag{2.14e}$$

$$\text{Equation of State:} \quad \frac{d}{dt}\left(\frac{P}{\rho^\gamma}\right) = 0, \tag{2.14f}$$

where γ is the heat capacity ratio. The choice of γ will vary case-to-case with $\gamma = 5/3$ in the adiabatic case which treats the plasma as a monatomic gas. The adiabatic equation of state is imposed to close the set of MHD equations otherwise an infinite number of successive moments of the Vlasov equation could be taken without closure being realised.

An important note on the notation is needed here. In Equation 2.14b, the $\mathbf{vv}$ is the outer product of the vectors. This operation is typically notated as $\mathbf{v} \otimes \mathbf{v}$ but can also be written in other ways such as using Einstein summation notations: $v_i v_j$. For unknown reasons this notation is not used in the field hence why the equation has its current form.

2.5.2 Magnetic Pressure and Tension

Through the inspection of the ideal MHD equations, specifically the Cauchy-Momentum equation (Equation 2.14b), two physically meaningful quantities that describe how the magnetic field imposes force on the fluid can be defined. These two effects are known as magnetic pressure and magnetic tension and can be derived by replacing the current density in the Cauchy momentum equation with the curl of magnetic field using Ampère's law to get the following equation,

$$\frac{\partial}{\partial t}(\rho \mathbf{v}) + \boldsymbol{\nabla} \cdot (\rho \mathbf{v}\mathbf{v}) = \frac{(\mathbf{B} \cdot \boldsymbol{\nabla})\,\mathbf{B}}{\mu_0} - \boldsymbol{\nabla} P - \boldsymbol{\nabla} \frac{B^2}{2\mu_0}. \tag{2.15}$$

Here the magnetic tension, $\boldsymbol{\tau} = (\mathbf{B} \cdot \boldsymbol{\nabla})\,\mathbf{B}/\mu_0$, and the magnetic pressure, $P_B = B^2/2\mu_0$, can be identified. To properly communicate the magnetic tension, a magnetic field line needs to be defined.

The idea of the magnetic field being composed of a force carrying 'field line' originated with Maxwell in 1861 (Maxwell 2010). These imaginary field lines sit tangentially to the magnetic field vector and are solely mathematical tools to better understand and visualise a magnetic field. However, in the case of magnetic fields and plasma physics, these field lines do allow for a physical understanding to be extracted. Plasma along the same magnetic field line interact more strongly than those on different field lines due to how the particles gyrate along the field direction due to the field line usually being parallel to the guiding centre. Magnetic field lines themselves also interact with each other. Due to their usefulness, magnetic field lines are often used as if they are physical objects, but it is worth remembering they are just mathematical constructs.

By using the concept of a magnetic field line, the magnetic tension could be thought of as analogous to the mechanical tension of a string. The magnetic tension describes how a bent field line will exert a tension to un-kink/coil/curl the field line and straighten. The magnetic tension can be rewritten in multiple ways such as the divergence of the magnetic stress tensor, $\boldsymbol{\tau} = \boldsymbol{\nabla} \cdot (\mathbf{BB})/\mu_0$, but the clearest way is when the changes in the magnitude of the magnetic field and its direction are separated. Let $\mathbf{B}$ be a magnetic field with spatially uniform field strength such that $\mathbf{B} = B\hat{\mathbf{b}}$ where $B = |\mathbf{B}|$ is the magnitude of the magnetic field and $\hat{\mathbf{b}}$ is the local magnetic field unit vector. When this is done, the magnetic tension can be rewritten as

$$\boldsymbol{\tau} = \frac{(\mathbf{B} \cdot \boldsymbol{\nabla})\,\mathbf{B}}{\mu_0} = \frac{B^2}{\mu_0}\left(\hat{\mathbf{b}} \cdot \boldsymbol{\nabla}\right)\hat{\mathbf{b}} = U\boldsymbol{\kappa}, \tag{2.16}$$

where U is the magnetic energy density and $\boldsymbol{\kappa}$ is the curvature of the field line. The curvature of field lines is inversely proportional to the radius of curvature of the field line under a fixed magnetic field. What this means is that the magnetic tension is directly proportional to how curved/distorted the magnetic field line is. Note that if the magnetic field strength was not uniform, there would be an additional term needed on the right-hand side of Equation 2.16 to capture the magnetic pressure gradient parallel to the field direction. This is why some refer to the magnetic tension force as the curvature force because the mechanical tension analogy does not fully capture the curvature forces

effects.

Alternatively, the magnetic pressure should be thought of as analogous to a thermal pressure – in the same way a gas provides an opposing force to a compression, a magnetic field does the same. This is why the gas and magnetic pressure are typically combined to create a total pressure, $P_{\text{Tot}} = P + P_B$. The ratio of the thermal pressure and the magnetic pressure gives rise to another important variable used in space plasma physics – the plasma beta, β.

The plasma beta is a dimensionless characteristic value which can be used to determine whether the magnetic field or plasma dominates the combined motion of the MHD fluid. It is calculated by finding the ratio of thermal pressure to magnetic pressure,

$$\beta = \frac{\mathrm{P}}{\mathrm{P_B}}. \tag{2.17}$$

Plasmas with a value of plasma beta which is greater than unity are typically thermally dominated. Plasmas with a value of plasma beta which is less than unity are typically magnetically dominated (Baumjohann and Treumann 1996). What this means physically requires a concept which was first introduced by Hannes Alfvén in 1942 (Alfvén 1942) known as the frozen-in flux theorem.

2.5.3 The Frozen-in Flux Theorem

The induction equation can be derived by combining Amperés law (Equation 2.3c) with Faraday's law (Equation 2.3d), and the resistive Ohm's law (Equation 2.13)

$$\frac{\partial \mathbf{B}}{\partial t} = \underbrace{\boldsymbol{\nabla} \times (\mathbf{v} \times \mathbf{B})}_{\text{Convective Term}} + \underbrace{\eta \boldsymbol{\nabla}^2 \mathbf{B}}_{\text{Diffusive Term}}. \tag{2.18}$$

The induction equation specifically states how a magnetic field evolves in time using two terms: the convective term, which describes how the field is changed due to the flow of the plasma, $\boldsymbol{\nabla} \times (\mathbf{v} \times \mathbf{B})$, and the diffusive term which describes how the field diffuses through the plasma, $\eta \boldsymbol{\nabla}^2 \mathbf{B}$.

The ratio of the convective term and the diffusive term yields the magnetic Reynolds number, R_m, which is a measure of the amount of advection a magnetic field undergoes compared to the

amount of diffusion over some length scale. It is defined as

$$R_m = \frac{|\nabla \times (\mathbf{v} \times \mathbf{B})|}{\eta \nabla^2 \mathbf{B}}. \tag{2.19}$$

When R_m is large ($R_m \gg 1$), then the convective term dominates and the convective limit is reached. As space plasmas are typically collisionless, meaning that resistivity tends to 0 ($\eta \to 0$), the convective limit is generally reached and the magnetic field does not diffuse through the plasma. This is known as frozen-in flux.

The frozen-in flux theorem states that under certain conditions magnetic fields embedded in electrically conducting fluids are bound together. What this really means is that the magnetic topology of the fluid cannot change. The consequence of this is that when frozen-in, the plasma either drags the field or the field drags the plasma.

The plasma beta can be used to estimate whether the plasma is dragging and distorting the field ($\beta > 1$) or whether the field is dragging and distorting the plasma ($\beta < 1$). Crucially, if a plasma is frozen-in to a magnetic field it can still drift, flow, and gyrate along the same field line. It is the induction equation which describes how the plasma would distort the field, or how the field distorts the plasma. However there are specific cases when this is not true and the ideal MHD approximations break down violating the frozen-in theorem. The most notable of these occasions is called magnetic reconnection.

2.5.4 Magnetic Reconnection

Magnetic reconnection is a process which occurs in regions with large magnetic shear. From Amperés law (Equation 2.3c) it can be shown that shearing magnetic fields generate a sheet of current. If these fields are forced together, then magnetic pressure causes the current sheet to be squashed and this change of spatial scale alone can allow for the diffusive term to dominate the magnetic Reynolds number. When this occurs, the magnetic field decouples from the plasma, diffuses through it, and threads the current sheet interposing the shear layer. As the field rearranges into a relaxed magnetic topology, it transfers large amounts of stored magnetic energy in the fields into kinetic and thermal energy of the plasma. This process is best explained using a classic two-dimensional visualisation of

reconnection at a current sheet.

Figure 2.1 shows the reconnection process. There are two distinct regions of anti-parallel magnetic field embedded in the plasma. The figure shows the reconnection process whereby there are two opposed inflow regions of plasma with anti-parallel frozen-in magnetic field. The aptly named diffusion region is where the magnetic field diffuses through the mixed plasma, rearranging topology. After the reconnection event, the magnetic field and plasma motion recombine due to the frozen-in theorem. As the magnetic field lines now have a small radius of curvature, they experience a strong magnetic tension force which carries both field and plasma away from the diffusion region generating an outflow jet. These jets have higher kinetic and thermal energy sourced from the field than the original inflowing plasma. The process occurs continuously as long as the inflows are sufficiently thinning the current sheet.

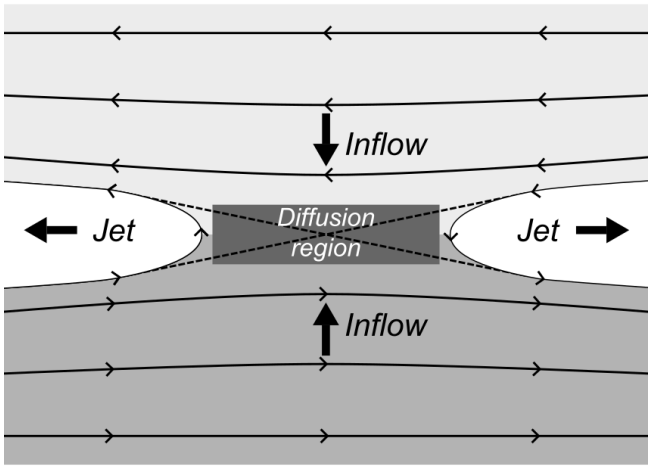


Figure 2.1: A two-dimensional cartoon representation of magnetic reconnection. The black lines with arrows represent the magnetic field. The different shades of grey represent different plasma regions. The grey box in the centre is the diffusion region and the white regions to the left and right of it are the outflow jets. Figure inspired by Eastwood (2008).

Reconnection is an important phenomena in plasma as it allows for energy to be transferred from the fields into the plasma. Another way this can happen is through waves.

2.5.5 MHD Waves

Waves are propagating disturbances which carry both energy and momentum away from their source location allowing 'information' to flow from one location to another. They typically obey a wave

equation of the form

$$\nabla^2\psi = \frac{1}{v^2}\frac{\partial^2\psi}{\partial t^2} \tag{2.20}$$

where $\mathbf{r}$ is a spatial vector, $\psi(\mathbf{r}, t)$ is some parameter of the medium, and v is the wave speed in the direction of propagation. This wave equation is often solved assuming a plane wave (meaning that they can be written as a combination of sine and cosines) solution,

$$\psi(\mathbf{r}, t) = Ae^{i(\omega t - \mathbf{k}\cdot\mathbf{r} + \varphi)} = Ae^{i\phi}\,, \tag{2.21}$$

where $\mathbf{k}$ is the angular wave vector which is related to the wavelength through $|\mathbf{k}| = 2\pi/\lambda$, φ is the phase offset, $\omega = 2\pi\nu$ is the temporal angular frequency, and ν is the wave frequency. Collectively these parameters describe the local phase, ϕ, of the wave.

The phase of the wave is an angle-like quantity which contains information about the fraction of a wavelength covered at point $\mathbf{r}$ at time t. Lines of constant phase in space are known as phase fronts, and the distance between two phase fronts of the same phase along a path of decreasing phase is a wavelength. This means the wave vector can be defined as

$$\mathbf{k} = -\nabla\phi, \tag{2.22}$$

where ϕ is spatially dependent and continuous.

Phase fronts advance through space with a velocity of

$$\mathbf{v}_{ph} = \frac{\omega}{|\mathbf{k}|}\hat{\mathbf{k}}. \tag{2.23}$$

However, this is not the only velocity a wave contains. The wave energy is carried at a group velocity calculated by

$$\mathbf{v}_g = \frac{\partial\omega}{\partial k_x}\hat{\mathbf{x}} + \frac{\partial\omega}{\partial k_y}\hat{\mathbf{y}} + \frac{\partial\omega}{\partial k_z}\hat{\mathbf{z}}. \tag{2.24}$$

Equation 2.23 and Equation 2.24 show that ω depends on $\mathbf{k}$ and are called the wave's dispersion relations. Dispersion relations describe how a waves propagation velocity is dependent on its wavelength, where dispersion refers to a wave packet of mixed wavelengths which spread out due to

varying propagation speeds.

In a uniform ideal gas, wave propagation is isotropic with no preferential direction – this is not the case for a uniform space plasma with an embedded uniform magnetic field. In this case, the frozen-in magnetic field would provide anisotropic conditions in the plasma. These properties of MHD give rise to the three characteristic MHD waves.

One of the fundamental results from the formulation of MHD by Hannes Alfvén (1942), was the discovery that a magnetised plasma can sustain three characteristic wave modes. These additional wave modes can be derived from the ideal MHD equations by perturbing and linearising them about an ideal, stationary equilibrium. After some maths this will give the following velocity perturbation relation (Baumjohann and Treumann 1996),

$$\begin{pmatrix} \omega^2 - v_A^2 k_\parallel^2 - c_{ms}^2 k_\perp^2 & 0 & -c_s^2 k_\parallel k_\perp \\ 0 & \omega^2 - v_A^2 k_\parallel^2 & 0 \\ -c_s^2 k_\parallel k_\perp & 0 & \omega^2 - c_s^2 k_\parallel^2 \end{pmatrix} \delta \mathbf{v} = \mathbf{0}. \tag{2.25}$$

Here we have introduced the Alfvén speed, $v_A = \sqrt{B^2/\mu_0 \rho}$, and sound speed, $c_s = \sqrt{\gamma k_B T/\rho}$. In addition to this, due to the preferential directions caused by the addition of a magnetic field an introduction is needed of $k_\perp$ which defines the x-direction and $k_\parallel$ which defines the z-direction and is parallel to the magnetic field; the y-direction completes the right-handed set.

There are multiple solutions to Equation 2.25, with the simplest being for the Alfvén wave. The above system shows that the velocity fluctuates purely in the y-direction - which is orthogonal to the magnetic field and wave vector - decouple and represent the dispersion relation for an Alfvén wave,

$$\omega_A = \pm v_A k_\parallel. \tag{2.26}$$

Alfvén waves are purely transverse waves that propagate parallel to the magnetic field. They can have a phase velocity transverse to the magnetic field and therefore propagate transverse to the field, but, as their group velocity is along the field, they cannot transmit energy perpendicular to the field. Alfvén waves are caused by perturbed ions oscillating in response to the magnetic tension of magnetic field lines. They can be thought of as analogous to a wave on a string and have a

characteristic speed known as the Alfvén speed, v_A.

By identifying and solving the vanishing determinant of Equation 2.25, the following dispersion relation for the other two wave solutions can be found

$$\omega_{ms}^2 = \frac{k^2}{2}\left(c_{ms}^2 \pm \sqrt{\left(v_A^2 - c_s^2\right)^2 + 4v_A^2 c_s^2 \frac{k_\perp^2}{k_\parallel^2}}\right). \tag{2.27}$$

This relation represents the other wave modes found in MHD known as fast and slow magnetosonic waves. Magnetosonic waves are compressional and are driven by magnetic pressure, magnetic tension, and thermal pressure variations. Typically, they are longitudinal and can be thought of as sound waves modulated through magnetic field lines. The fast-magnetosonic wave takes the positive signed root of the relation and when perpendicular to the field, it propagates at the characteristic speed, $c_{ms_{fast}}^2 = c_s^2 + v_A^2$. It is the only MHD wave which can propagate perpendicular to the background magnetic field and it is the only magnetosonic mode which can have a transverse component. The slow-magnetosonic wave takes the negative root, and when parallel to the field it propagates at the characteristic speed $c_{ms_{slow}}^{-2} = c_s^{-2} + v_A^{-2}$.

Due to the anisotropic conditions in a magnetised plasma, the Alfvén and magnetosonic phase speeds are all dependent on their angle to the magnetic field. This angle is important because it can change the phase speed of an MHD wave as illustrated in Figure 2.2. The figure shows how the phase speed of the three magnetohydrodynamic wave modes change as the angle between the wave vector and the background magnetic field changes. In this diagram the background magnetic field points along the y-direction and the lines display the propagation velocity of the waves depending on their orientation. When the Alfvén speed exceeds the sound speed, shown on the left, the parallel slow magnetosonic mode reduces to a sound wave while the fast magnetosonic wave propagates at the Alfvén speed. Conversely when Alfvén speed is less than the sound speed, shown on the right, the slow mode can propagate up to the Alfvén speed and the fast mode at the sound speed when parallel to the field.

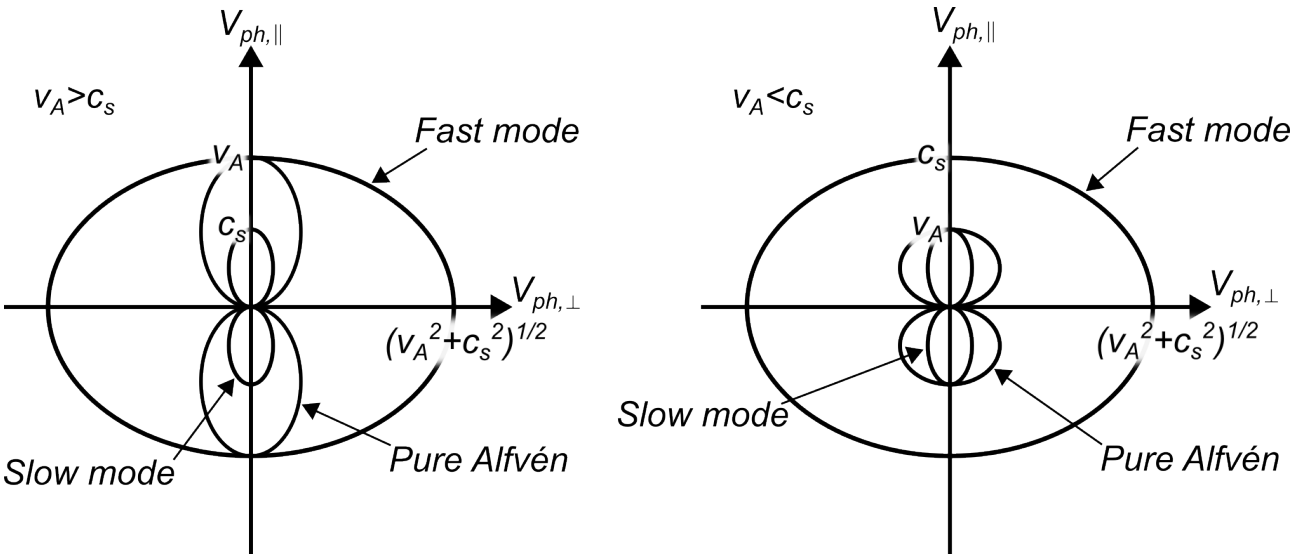


Figure 2.2: An illustration of how the phase velocities of the three MHD body waves changes depending on angle to the magnetic field. On the left the Alfvén speed is larger than the sound speed, on the right the opposite.

2.5.6 Shocks and Discontinuities

As well as allowing for waves, the MHD equations support the existence of boundaries with discontinuous plasma parameters called discontinuities. There are two main types of discontinuities categorised as contact and tangential. A contact discontinuity is when the flow and field is tangential to the boundary meaning that nothing crosses the boundary. The density, and temperature across the boundary can be discontinuous, however, the thermal pressure across the boundary must be conserved. A tangential discontinuity is similar to a contact discontinuity but the thermal pressure can change. This means that the tangential component of the magnetic field must also change across the boundary to allow for the total pressure to be to be conserved at the boundary, as the boundary is in a total pressure equilibrium. If there is flow across the boundary, without change in density or entropy, then it is a rotational discontinuity. But if there is a change in the density or the entropy of the flow as it crosses the discontinuity, then it becomes a shock.

A shock is a discontinuous transition layer in a flow whereby the plasma conditions change such that one side of the boundary is supersonic, and the other side is subsonic. Supersonic refers to being above the characteristic wave speed in that medium, and subsonic being below the characteristic wave speed. In MHD three different types of shocks exist: the slow-mode, intermediate, and fast-mode shock. Intermediate shocks are non-compressive and are similar to rotational discontinuities but the

pressure changes across them. The slow- and fast-mode shocks are compressive and are related to the slow- and fast-magnetosonic characteristic wave speeds. Across the slow-mode, the field decreases however across the fast-mode it increases.

Typically a Mach number is used to determine whether a flow is super- or subsonic. Mach numbers are a ratio of the flow speed and the local wave speed. In MHD the two most important Mach numbers are the fast magnetosonic Mach number, M_f, and the Alfvén Mach number, M_A,

$$M_f = \frac{v}{c_{ms,\,fast}}, \tag{2.28a}$$

$$M_A = \frac{v}{v_A}. \tag{2.28b}$$

Changes in the fast magnetosonic Mach number are commonly used to determine whether or not the flow may develop a shock (Farris and Russell 1994). This means that a shock forms when the flow speed satisfies the equation $M_f > 1$.

Mach numbers can also be used for other purposes than determining a shock. For example, changes in Alfvén Mach number contains information about how the field strength changes across the shock, and the fast magnetosonic Mach number can also be used to determine how compressible a flow is (Miura 1990; Miura and Kan 1992; Palermo et al. 2011), since the proportional change in density due to flow variations scales as $\sim M_f^2$. Values of $M_f < 0.3$ are typically considered incompressible as they result in $\lesssim 10\%$ changes in density. Compressibility here means the relative change in volume, $\partial V/V$, in response to pressure changes.

Due to the simple criterion of $M_f > 1$ for a shock, it can be shown they they can form both when supersonic objects move through subsonic flow, such as the crack of a whip, and when a supersonic flow meets a subsonic object. One example of this is when the supersonic solar wind meets Earth's magnetosphere.

A final remark is about a number used to describe how the density varies across a boundary. The Atwood number, defined as

$$A = \frac{\rho_1 - \rho_2}{\rho_1 + \rho_2}, \tag{2.29}$$

where $\rho_1 > \rho_2$ is a unit-less ratio which describes how much the density varies across a boundary or discontinuity.

2.6 The Near-Earth Environment

The complex interaction between Earth's intrinsic magnetic field and the solar wind results in a cavity in the solar wind forming called the magnetosphere. To properly understand this interaction, some further introductory work is needed about the different components of the Sun-Earth interaction.

2.6.1 The Solar wind

The outermost layer of the Sun's atmosphere - the solar corona - freely expands radially outward at supersonic speeds as a low density plasma known as the solar wind. This plasma is driven outwards despite the strong solar gravity ($\sim 274\,\mathrm{m\,s^{-2}}$) by the huge thermal pressure gradients between the corona and interstellar space. Furthermore, the solar magnetic field is frozen-in to this plasma and dragged outward, forming the interplanetary magnetic field (IMF). Due to the surface of the Sun making a full rotation once every ~ 27 days, this out-flowing plasma and field takes a spiral shape named after its discoverer, Eugene Parker (1958). Recent missions such as Solar Orbiter (Müller et al. 2020) and Parker Solar Probe (Fox et al. 2016), which are currently the closest man-made objects to the Sun, are continuously unveiling new physics as they probe and even intercept the corona.

Despite these forefront missions existing, the most extensive studies on the solar wind have taken place in the near Earth environment which is approximately $1.5 \times 10^8\,\mathrm{km}$ from the Sun. The solar wind plasma here is hot, tenuous, and supersonic consisting predominantly of hydrogen ions and electrons with some heavier ions present (Kivelson and Russell 1995). The IMF in this region is very weak with typical magnetic field strength values on the order of nano Tesla. Near Earth, the solar wind typically has a magnitude of 4 nT magnetic field, a solar wind speed of $350\,\mathrm{km\ s^{-1}}$, an ion temperature of $1 - 10\,\mathrm{eV}$, and a number density between $1 - 10\,\mathrm{cm^{-3}}$ (Ma et al. 2020). When the solar wind reaches Earth, it is slowed and heated by a collisionless shock wave known as the bow shock.

2.6.2 The Magnetosheath

The shocked solar wind beyond the bow shock is known as the magnetosheath and the plasma here is much hotter, denser, slower, and more turbulent than the solar wind plasma. Immediately beyond the bow shock, the magnetosheath values obey shock jump conditions outlined by a set of equations known as the Rankine-Hugoniot jump conditions. The magnetosheath plasma is typically high density ($\sim 10\,\mathrm{cm}^{-3}$) with a cold ion temperature ($\sim 100\,\mathrm{eV}$) (Ma et al. 2020), however it is highly variable as a function of local time. As the plasma moves from the nose to the tail, it accelerates around the magnetosphere (Haaland et al. 2019) due to adiabatic expansion and cooling, rarefying the plasma further in the tail of the magnetosheath. These two effects can be seen in Figure 2.3.

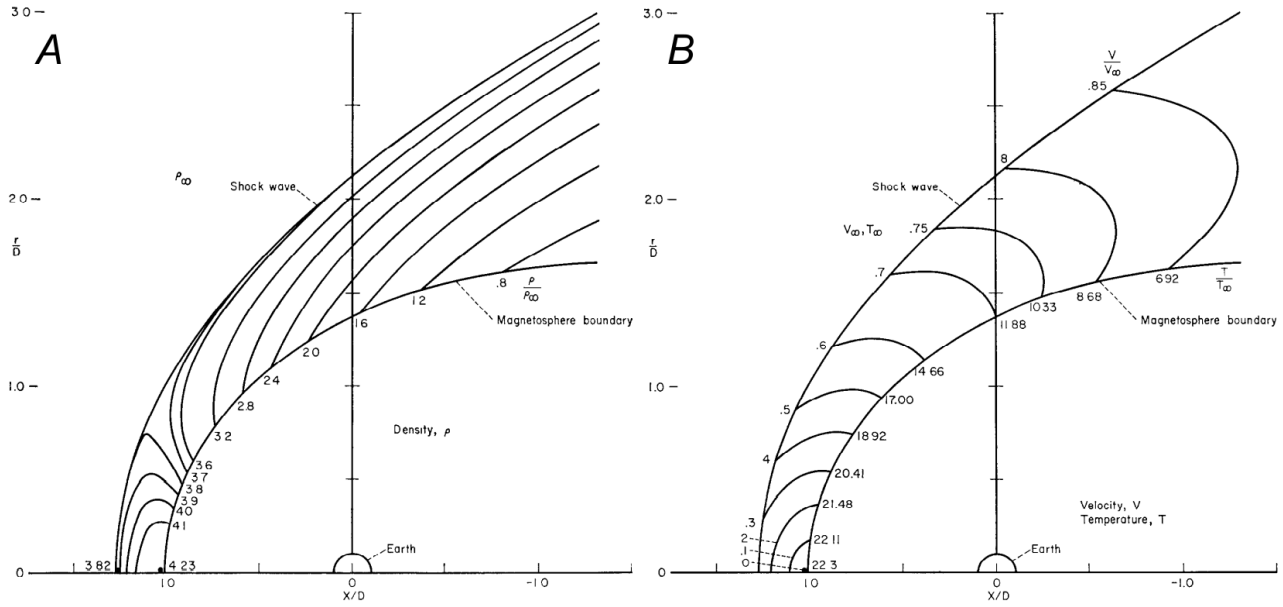


Figure 2.3: An illustration of changes to the density (Panel A) and the temperature and velocity (Panel B) of the plasma in Earth's magnetosheath. In this figure, D is the geocentric distance to the magnetosphere nose. From Spreiter et al. (1966).

As well as being a plasma boundary, Earth's magnetic field causes a magnetic field boundary which means that the IMF 'drapes' over the magnetosphere. Near the subsolar point, if there is magnetic shear reconnection will take place. However, if there is no magnetic shear, then a magnetic pile up region will occur which is a region of increased field within the magnetosheath (Song et al. 1993). The plasma region beyond the magnetosheath is known as the magnetosphere.

2.6.3 The Magnetosphere

Earth emanates a magnetic field which, at the magnetopause, is well described by a dipole with an inclination of $\sim 10^{\circ}$ from the rotational axis. Closer to Earth, this field requires additional multipole contributions to be accurate (e.g. quadrupole contributions). The magnetosphere is the region where this geomagnetic field dominates over the IMF. The plasma within the magnetosphere is quasi-stationary and near-incompressible. Generally speaking, the magnetosphere is cold and tenuous with the majority of the plasma restricted to the inner-regions ($< 2\,R_E$) and the plasma sheet in the tail (Ma et al. 2020). The main regions which make up the Sun-Earth interaction can be seen in Figure 2.4.

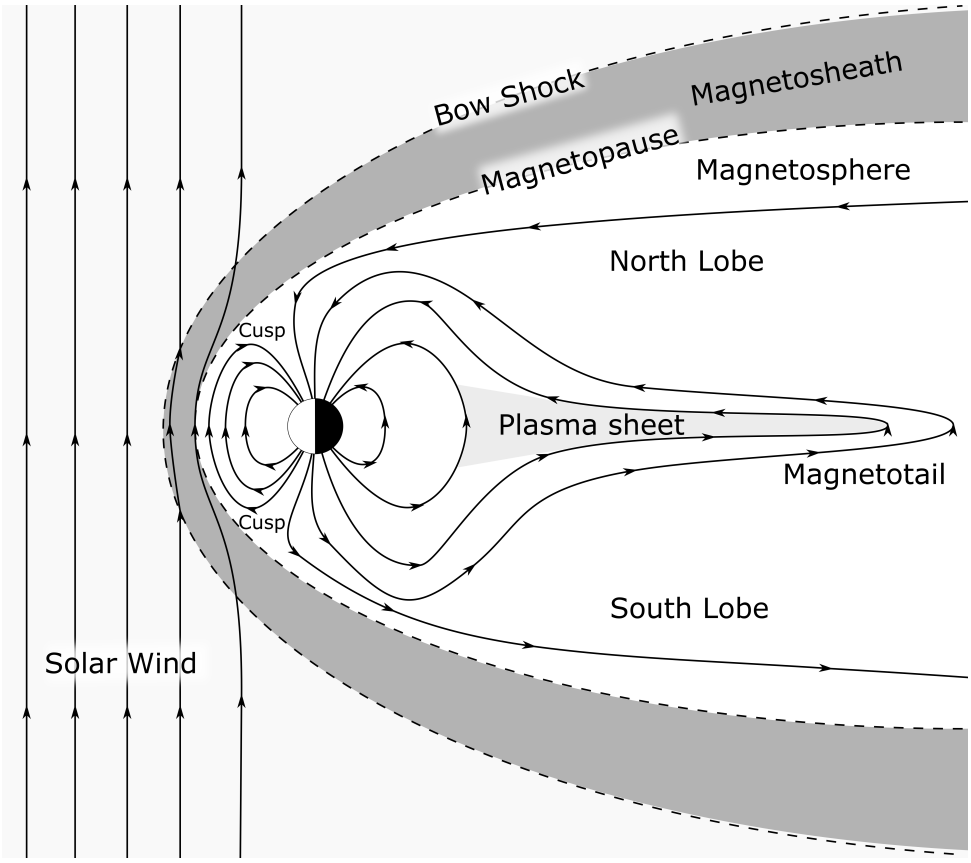


Figure 2.4: An illustration of Earth's magnetosphere including magnetic field lines in black. The different boundaries are shown using a dashed line.

The magnetotail is the part of the magnetosphere which is stretched and drawn-out behind Earth due to it being dragged away from it by the solar wind. The magnetotail is quite dynamic, with two distinctly different regions: the lobes, and the plasma sheet. The lobes make up the majority of the magnetotail volume and are composed of very low density plasma, approximately two orders of

magnitude lower than the magnetosheath. Inside the lobes are near parallel closed magnetic field lines which in the northern lobe point sunward towards the Earth, and in the southern lobe point anti-sunward. The plasma sheet or current sheet is where the majority of the tail plasma is found and is also where tail reconnection takes place. Reconnection which occurs in the tail is the source for the majority of the plasma that drives electromagnetic effects in the ionosphere. The most notable evidence of this is the aurora.

2.6.4 The Ionosphere

The closest point to Earth containing naturally-occurring plasma is the ionosphere which is the conducting layer of Earth's upper atmosphere which contains a collisional plasma of photo-ionised atoms, electrons, and neutrals. As it is conducting, the ionosphere is where Earth's geomagnetic field lines can be thought to be anchored and when both ends of a geomagnetic field line is anchored in the ionosphere, it is said to be closed. Due to how the Earth's (predominantly) dipole field is structured, there are two depression regions in the magnetic field at the cusp locations which allows the magnetosheath plasma to have near direct access to the ionosphere. The plasma flows into the ionosphere via currents as illustrated in Figure 2.5.

Earth's magnetosphere and ionosphere are connected through different currents. Field-aligned currents (FACs) flow along magnetic field lines and are what really connect the magnetosphere to the ionosphere. Across the ionosphere is the Pederson current which is a result of ion-neutral collisions causing charge separation in a region of $\mathbf{E} \times \mathbf{B}$ drift. As ions collide more, the charges separate resulting in an electric field being produced. This causes a current to flow in the electric field direction. The Hall current is a direct result of the ion-neutral collisions occurring more, meaning that the electrons $\mathbf{E} \times \mathbf{B}$ drift faster resulting in a charge separation which causes a current (Equation 2.10). These two currents are illustrated in Figure 2.6.

When energy and momentum enter the magnetosphere, they can drive space weather. Space weather is a phenomena which originates at the Sun and results in electromagnetic effects at Earth. The impacts of space weather are usually mild and benign to society and power grids (Lewis et al. 2022). However, severe space weather is of serious concern to society due to its ability to cause disruption and damage to power, transport, and communication technology (Buzulukova and

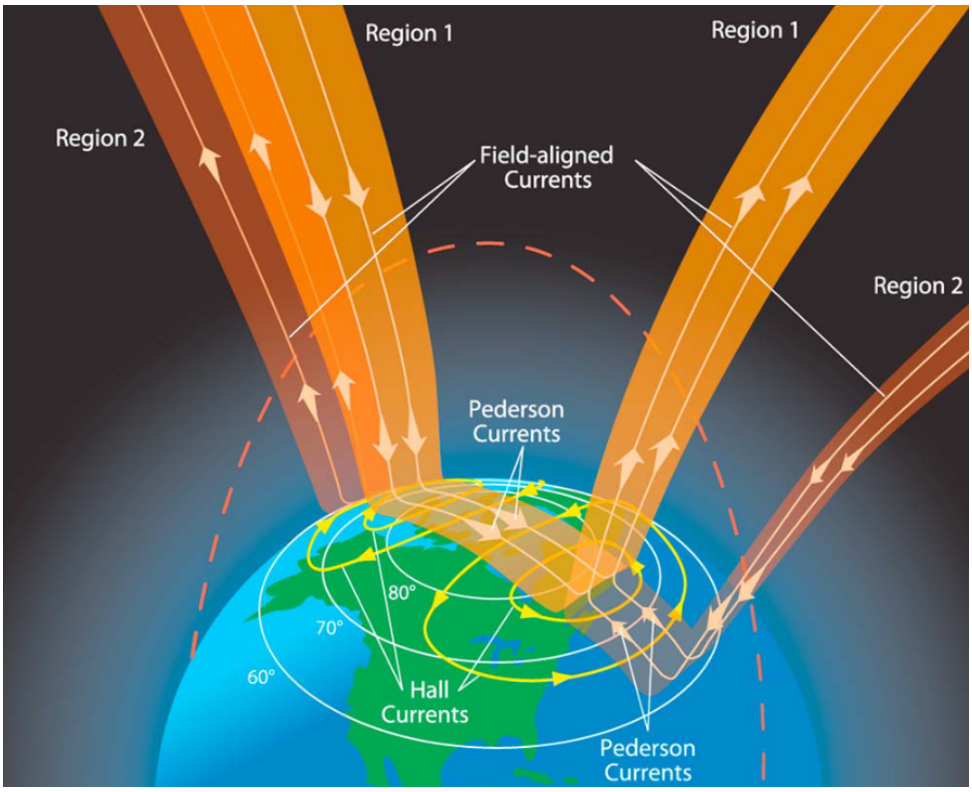


Figure 2.5: A cartoon of the different electrical field-aligned currents connecting the magnetosphere with the ionosphere. Figure from Le et al. (2010).

Tsurutani 2022).

2.6.5 The Magnetopause

Interposed between the magnetosheath and the magnetosphere is a collisionless boundary transition region called the magnetopause. Earth's magnetopause is the surface of the magnetosphere and, due to the frozen-in flux theorem, it is also the plasma boundary between magnetospheric and solar wind plasma. The location of this boundary can be approximated at the subsolar point by finding the pressure balance location between the solar winds dynamic pressure, $P_{\text{dyn}} = \rho v^2$, and the geomagnetic fields magnetic pressure, $4B(r)^2/2\mu_0$ where $B(r)$ is the dipolar field strength, and the factor of 4 is from the dipole field having twice the dipole value at the magnetopause assuming it is planar. As dipole magnetic field strength varies with distance as $1/r^3$, the dipolar magnetic field strength can be rewritten as $B(r) = \mu_0 m/4\pi r^3$, where m is the magnetic moment of the Earth. Equating the two pressures and solving for r provides the estimated magnetopause stand-off distance

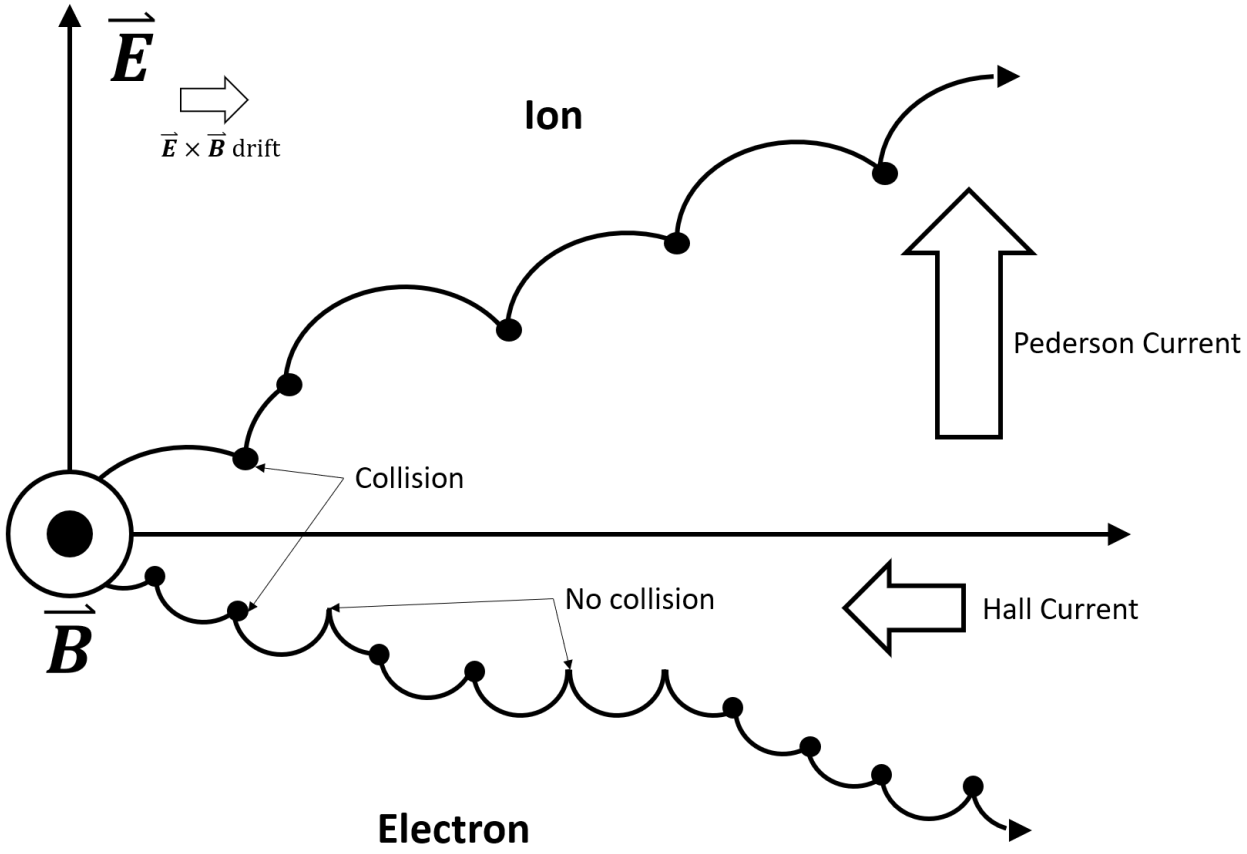


Figure 2.6: An illustration how the Pederson and Hall currents work in the ionosphere. Inspired by Coxon (2015).

of

$$r \approx \sqrt[6]{\frac{\mu_0 m^2}{8\pi^2 \rho v^2}}. \tag{2.30}$$

It is worth remembering this is an approximation as there will be variations in the efficiency of the solar wind driving and the location of the magnetopause is sensitive to transient changes in the solar wind and IMF. More accurate, two- and three-dimensional analytical models of the magnetopause exist which better approximate its location under more extreme solar wind conditions (e.g. Shue et al. 1997; Lin et al. 2010).

The first suggestion of the existence of a magnetopause was by Chapman and Ferraro (1931) who suggested that the Earth was shielded from the Sun by a sheet of current that later became known as the Chapman-Ferraro currents. Later, this current sheet, which closes off across the plasma sheet, became known as the magnetopause. The Chapman-Ferraro currents are generated when charged particles enter the geomagnetic field dominated region which has a stronger field than the

magnetosheath. Due to this, the charged particles undergo a Lorentz force which causes them to undergo a half gyroradius turn and exit the higher-field region. As oppositely charged particles gyrate in opposite directions, a current is generated. This process links the magnetopause thickness and the ion-gyroradii and is illustrated in Figure 2.7. Under the approximation of a weakly-driven boundary and a magnetic field in a vacuum, the magnetopause would be exactly one ion-gyroradius thick, but in reality this is not the case; the real magnetopause is far more complex.

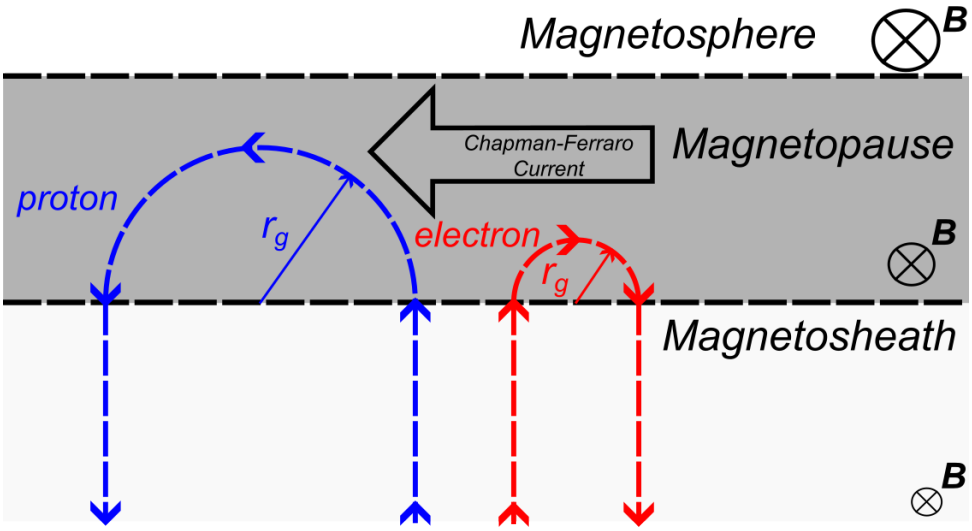


Figure 2.7: An illustration of the Chapman-Ferraro currents. In red is the electron path, and in blue a proton. The current appears due to the charge separation originating from the different sized gyroradii.

Earth's magnetopause is neither idle nor impenetrable. Different mechanisms exist which allow for energy and momentum to near-continuously cross its boundary, with only the most energetic of these events causing space weather. The three main mechanisms by which this penetration occurs are magnetic reconnection (Dungey 1961), a quasi-viscous or viscous-like interaction (Axford and Hines 1961; Axford 1964), and diffusive transfer (Tsurutani and Thorne 1982). The dominant transfer mechanism at Earth is dependent on the local IMF and plasma conditions.

Under southward IMF, the high pressures and large magnetic shear at the nose of Earth's magnetopause can cause the frozen-in theorem to break down enabling magnetic reconnection. This was proposed to be a cyclical transfer of magnetic flux from the solar wind, into the magnetosphere by Dungey (1961). The cycle became known as the 'Dungey cycle' and is as follows: The IMF and geomagnetic field reconnect at the nose of the magnetopause creating a hole in it, allowing solar wind particles to remain frozen-in to the field lines but also penetrate the magnetosphere –

this step is known as dayside reconnection. After this, the magnetic flux, which is anchored into the ionosphere, is transported over the north/south poles of the Earth in the direction of the solar wind flow, and into the magnetotail. When this occurs, flux builds up, creating a magnetic pressure force which squashes the magnetotail current sheet causing it to reconnect, re-closing the open field lines. This is known as night side reconnection. It was originally proposed that day- and night-side reconnection rates were equal, however this is now known to not be the case as the reconnection rates at both sites are sensitive to the local field and plasma conditions which vary on timescales faster than the cycle takes place (~ 1 hour).

Under northward IMF, the magnetic shear at the day-side does not exist, extinguishing the Dungey cycle. However, this does not necessarily mean that reconnection at the magnetopause is no longer taking place. Under northward IMF, the high-latitude magnetopause tailward-of-the-cusp can reconnect (Gosling et al. 1991). However, unlike the Dungey cycle, this reconnection is not coupled to tail reconnection meaning that the plasma transport that takes place under northward IMF leads to the formation of a cold dense plasma sheet (CDPS) (see review by Wing et al. 2014, for further discussion of the CDPS).

Even without magnetic reconnection taking place, momentum and energy can still permeate the magnetopause through a quasi-viscous interaction which also feeds the CDPS. The magnetopause surface is not stationary and the magnetosphere is largely incompressible meaning that boundary motion can facilitate momentum and energy to penetrate the magnetosphere even when the frozen-in theorem prevents particles leaving their respective field lines. The boundary can be driven in numerous ways such as pressure changes in the solar wind causing 'breathing-like' expansions and compressions of the magnetospheric cavity as a whole. It is more common, though, for these boundary motions to be periodic and wave-like in nature. When the boundary moves in this way, it is called a magnetopause surface wave (MSW). MSWs are ubiquitous at the magnetopause due to a process known as the Kelvin-Helmholtz instability (Kavosi and Raeder 2015).

The Kelvin-Helmholtz instability (KHI) is thought to be the dominant way that viscous-like plasma transfer occurs as it allows for magnetosheath plasma to mix with magnetospheric plasma. Given this process predominantly occurs in the low-latitudes, a layer just inside the magnetopause can form known as the low-latitude boundary layer (LLBL) (Nakamura 2021). The LLBL can be

driven by high-latitude reconnection, the KHI, or even Alfvén wave phenomena (Nakamura 2021). The thickness of the LLBL is important as it adds a thickness to the magnetopause which effects how mechanisms such as the KHI operate. The LLBL thickness varies depending on IMF, with it being thicker under northward compared to southward IMF driving (Eastman et al. 1976). There is also a local time dependence on the LLBL where it gets thicker, further from the sub-solar point (Haerendel et al. 1978). Further to this, statistical studies show that the plasma in the LLBL gets denser and more stagnant in the flank-to-tail regions (Hasegawa et al. 2004b). It is thought that plasma from the LLBL diffuses into the plasma sheet and drives the formation of the CDPS (Terasawa et al. 1997). All of these effects are linked to the Kelvin-Helmholtz instability which is the topic of the next chapter.

CHAPTER 3

The Kelvin-Helmholtz Instability

The Kevin-Helmholtz instability, named after Lord Kelvin (formerly known as William Thomson) (Thomson 1871), and Hermann von Helmholtz (Helmholtz 1868), is a fluid instability at interfaces with a velocity shear (Chandrasekhar 1961), which leads to the generation and evolution of surface waves at that interface. A surface wave is an elliptically polarised disturbance at a boundary with opposite polarisation on either side of the boundary, forming flow vortices centred on the interface (Dungey and Southwood 1970). It was Dungey (1955) who first suggested that the magnetopause could be KH-unstable and since then, the KHI has become known to be the dominant driver of the viscous-like interaction between solar wind and magnetospheric plasma's. What this means is that the KHI is the dominant way that energy and momentum enters Earth's magnetosphere when Dungey-like reconnection is not taking place, making it an important driver that needs to be understood.

KH-driven magnetopause surface waves form from small deformations of the boundary about equilibrium known as 'seed' perturbations. Because of the continuous magnetosheath flow adjacent to the magnetopause, plasma parcels closer to the boundary must move faster around these seed perturbations than ones further away. From Bernoulli's principle, this establishes a pressure gradient which acts to further deform the magnetopause surface. These larger deformations subsequently

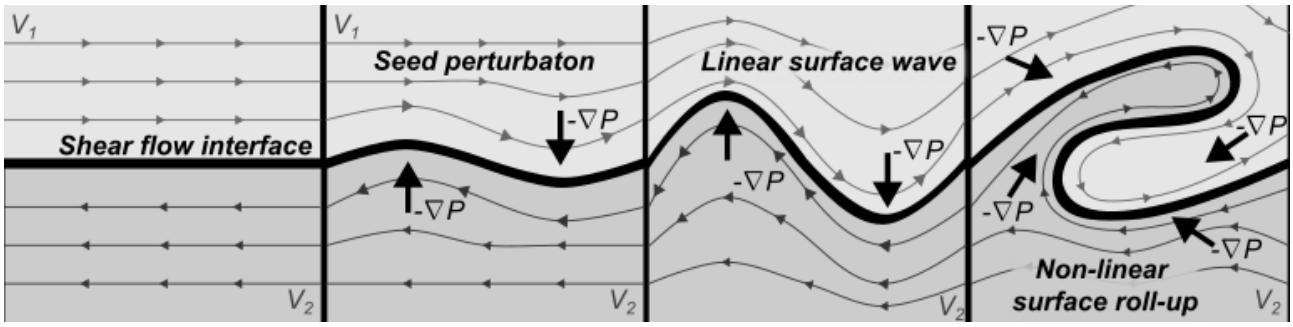


Figure 3.1: An illustration of the key stages of the KHI in an idealised geometry. The thick black line shows the KH-unstable boundary, suggested velocity streamlines are drawn. Thick black arrows are used to illustrate the pressure gradients which drive the instability.

drive greater pressure gradients and so on until the surface folds on itself and rolls up. Thus, in the absence of an additional force to counteract this process and stabilise the boundary, the velocity shear interface is said to be 'KH-unstable'. An illustration of the process can be seen in Figure 3.1.

The KHI occurs not only in space plasma at the terrestrial magnetopause, it has also been observed or predicted at other planetary magnetopauses (Paral and Rankin 2013; Dang et al. 2022; Ruhunusiri et al. 2016; Montgomery et al. 2023; Masters et al. 2012; Donaldson et al. 2024; Masters 2018), the magnetopause of magnetised moon Ganymede (Kaweeyanun et al. 2021), comet tails (Ershkovich 1980), and along the surface of CMEs (Nykyri and Foullon 2013). Observations of surface waves at the magnetopause show that they propagate tailward along the magnetopause due to that being the flow direction of the magnetosheath (Song et al. 1988).

At Earth, the KHI forms along the magnetopause as it is the velocity shear interface between the quasi-stationary magnetospheric plasma and the fast-flowing magnetosheath plasma. The KHI is a non-linear instability meaning that the growth is not constant under constant driving. This makes understanding and trying to predict the disturbances caused by the KHI difficult. The simplest way to overcome this is to only investigate the instability in its linear stages while also making simplifying assumptions about the magnetopause and its environment. This is how the KHI was originally studied, by analytically developing 'linear theory'.

3.1 Linear Theory

Historically, the Kelvin-Helmholtz instability has been studied using mathematical models to try and explain and predict its behaviour. This began by using numerous simplifications to allow for an analytic understanding to be found. Over time, this analytic model has been built upon by stripping the layers of assumptions used, building an understanding of the significance of each simplifying effect. In this section a chronological review of the linear theory literature will be presented, starting with the simplest analytical model, the incompressible tangential discontinuity. This section concludes with some example observations which both support and challenge the discussed theory.

3.1.1 Incompressible Tangential Discontinuity

The simplest model of the magnetopause approximates it as a tangential discontinuity at $z = 0$ between two incompressible homogeneous fluids. The tangential homogeneity means that the plane wave ansatz (Equation 2.21) is valid on each side of the surface. To begin two directions are defined: tangential to the surface, and normal to the surface (the z-direction) such that the wave has a wave vector of $\mathbf{k} = (\mathbf{k}_t, k_z)$.

Let a propagating surface wave exist along the boundary with wave vector $\mathbf{k}$. The sign of the imaginary component of k_z changes across the discontinuity so that the wave amplitude is maximum at the boundary and decays away from it (Kivelson and Chen 1995). Mathematically, this decay comes from the wave equation (Equation 2.21) as a complex value of k_z results in an $i^2 = -1$ in the exponential thus causing the wave to decay exponentially away from the boundary. Physically, this decay is because no free energy is available to support a constant amplitude away from the velocity shear interface. It has been shown that the waves on either side of the boundary satisfy the dispersion relation for magnetosonic waves (Equation 2.27) in their respective plasma rest frames (Southwood 1968). Critically for the KHI, these two plasma velocities differ meaning that the rest frame frequencies on either side are Doppler shifted such that

$$\omega = \omega_i + \mathbf{k}_t \cdot \mathbf{u}_i \tag{3.1}$$

where $\mathbf{k}_t$ is frame independent, and the subscript i denotes the side where 1 is the magnetosphere

and 2 the magnetosheath.

The waves on either side are tied together through boundary conditions: the displacements on either side of the surface must be equal and the total pressure normal to the boundary must balance. By combining the dispersion relation of the two magnetosonic waves (Equation 2.27), and the Doppler shift (Equation 3.1), then the dispersion relation for a surface wave can be derived (**kivelson1995**),

$$\frac{\rho_1 \left[(\omega - \mathbf{k}_t \cdot \mathbf{u}_1)^2 - (\mathbf{k}_t \cdot \mathbf{v}_{A1})^2 \right]}{k_{z1}} = \frac{\rho_2 \left[(\omega - \mathbf{k}_t \cdot \mathbf{u}_2)^2 - (\mathbf{k}_t \cdot \mathbf{v}_{A2})^2 \right]}{k_{z2}}. \tag{3.2}$$

This equation needs to be numerically solved under the compressible assumption. However, an analytic solution can be achieved by: assuming a shear in the velocity is present; assuming incompressibility, such that $c_s \to \infty$ and therefore $k_z^2 = k_t^2$; substituting in Equation 3.1; applying the definition of the Alfvén speed; and finally by using the knowledge that $k_{z1} = -k_{z2}$. After doing this, and with a bit of algebraic gymnastics, Equation 3.2 becomes the following expression for the dispersion relation for a surface wave,

$$\omega = \frac{\mathbf{k}_t \cdot (\rho_1 \mathbf{u}_1 + \rho_2 \mathbf{u}_2)}{\rho_1 + \rho_2} \pm \sqrt{\frac{1}{\mu_0 (\rho_1 + \rho_2)} \left[(\mathbf{k}_t \cdot \mathbf{B}_1)^2 + (\mathbf{k}_t \cdot \mathbf{B}_2)^2 \right] - \frac{\rho_1 \rho_2}{(\rho_1 + \rho_2)^2} \left[\mathbf{k}_t \cdot (\mathbf{u}_1 - \mathbf{u}_2) \right]^2}, \tag{3.3}$$

which has two solutions.

The first solution to Equation 3.3 is an unstable solution where the discriminant of the quadratic is zero, this occurs when the magnetic tension perfectly stabilises the shear flow resulting in a wave with constant frequency. Solving for this analytically yields an equation for the frequency of that stable KHI surface wave (Treumann and Baumjohann 2001),

$$\omega = \frac{\mathbf{k}_t \cdot (\rho_1 \mathbf{u}_1 + \rho_2 \mathbf{u}_2)}{\rho_1 + \rho_2}. \tag{3.4}$$

The second solution to Equation 3.3 is related to when the discriminant is non-zero. If the discriminant is positive, this results in a real angular frequency corresponding to a stable magnetopause surface wave. However, if the discriminant is negative then the angular frequency becomes complex, $\omega = a + ib$. The consequences of this can be seen by substituting this into the plane wave equation

(Equation 2.21)

$$\psi(\mathbf{x}, t) = A\left[e^{i(at-\mathbf{k}\cdot\mathbf{x}+\varphi)}e^{bt}\right]. \tag{3.5}$$

It is clear that when the discriminant is non-zero and real, the plane wave solution holds and the wave does not evolve. However, if the discriminant is non-zero and has an imaginary component, the wave will exponentially evolve in time. This means that when the discriminant is negative, the angular frequency is complex, and the boundary evolves via the multiplication of an exponential making it KH-unstable (Chandrasekhar 1961), this is commonly known as the KHI criterion and is written as

$$\underbrace{\left[\mathbf{k}_t \cdot (\mathbf{v}_1 - \mathbf{v}_2)\right]^2}_{\text{Flow Shear Driver}} > \underbrace{\frac{\rho_1 + \rho_2}{\rho_1 \rho_2}}_{\text{Density Weighting}} \underbrace{\frac{1}{\mu_0}\left[(\mathbf{k}_t \cdot \mathbf{B}_1)^2 + (\mathbf{k}_t \cdot \mathbf{B}_2)^2\right]}_{\text{Magnetic Tension Stabiliser}} \text{ then KHI unstable.} \tag{3.6}$$

If the above criterion is true, then a growth rate, γ, can be defined. The growth rate is the imaginary component of the angular frequency, denoted b above, and can be written as

$$\gamma = \sqrt{\frac{\rho_1 \rho_2}{(\rho_1 + \rho_2)^2}\left[\mathbf{k}_t \cdot (\mathbf{v}_1 - \mathbf{v}_2)\right]^2 - \frac{1}{\mu_0(\rho_1 + \rho_2)}\left[(\mathbf{k}_t \cdot \mathbf{B}_1)^2 + (\mathbf{k}_t \cdot \mathbf{B}_2)^2\right]}. \tag{3.7}$$

Note that the growth rate is only valid if the KH-criterion holds, i.e. if the boundary is KH-unstable.

Equations 3.6 and 3.7 show that wave vectors aligned with the flow shear most efficiently support the flow shear driver term of the KHI and are more likely to be unstable and have a larger growth rate. However, this does not necessarily mean the most unstable $\mathbf{k}_t$ is aligned with the flow shear because of the second term, the stabilising effect of magnetic tension. For the magnetic field tangential to the boundary, and if the densities across the boundary are equal, then the flow shear must be twice that of the root Alfvén speed for the boundary to be unstable else the KHI will be suppressed by the magnetic tension. This is intuitive – as the surface begins to deform, the frozen-in field lines will also be deformed, which magnetic tension will oppose.

In contrast, for magnetic fields orthogonal to $\mathbf{k}_t$, the waves do not cause a curvature of field lines and hence no tension force occurs. Thus the KHI was thought to be uninfluenced by such a magnetic field. If both magnetic fields are perpendicular to the shear flow, the most unstable $\mathbf{k}_t$ is aligned with the flow shear, whereas for magnetic fields not strictly aligned with the flow and under typical magnetopause conditions, $\mathbf{k}_t$ is most unstable perpendicular to the magnetospheric magnetic field. It

has also been shown that the growth rate of the KHI is larger when the magnetic tension stabiliser term is minimised compared to when the shear flow driver is maximised (Southwood 1968). A final remark is that it can also be seen that a large density ratio can reduce the KHI growth rate. This may be important because the magnetosheath is approximately $10\times$ denser than the magnetosphere (Ma et al. 2020).

3.1.2 Compressible Tangential Discontinuity

So far, only the incompressible regime has been considered, but plasma's are malleable and therefore compressibility cannot be ignored. Equations 3.6 and 3.7 show that unstable surface waves can be generated on an incompressible infinitesimally thin tangential discontinuity when the velocity shear exceeds some critical threshold. In the compressible regime these equations are no longer valid. It has been shown that compressibility lowers the unstable threshold relative to the incompressible situation and thus has a destabilising effect; the extent to which Fejer (1964), Sen (1965), and Southwood (1968) disagreed. Further to this, Sen (1965) also suggested that compressibility has both a destabilising effect on the lower critical shear flow velocity, and stabilising effect on the wave growth rate (i.e. a reduction of the growth rate) if the shear flow speed is sufficiently smaller than the magnetosonic speed.

Pu and Kivelson (1983) (for chronology it was first presented at conference in 1980 (Pu and Kivelson 1980)) coupled the results of these works by showing that there are two different KH-modes, quasi-slow and quasi-fast, each with different upper and lower critical shear velocities. These modes are analogous to the magnetosonic waves as the quasi-slow mode is restricted to propagate along the field direction whereas the quasi-fast mode can propagate transverse to the unperturbed magnetic field. The modes are only unstable if the shear velocity is between the upper and lower critical shear velocity values. Pu and Kivelson (1983) show that the lower critical velocity shear of both modes is due to the stabilising effect of magnetic tension, which they show compressibility lowers for both modes compared to the incompressible limit. The upper critical velocity is due to a transition of the unstable surface evanescent wave to a stable body wave when the surface wave's phase speed exceeds this upper limit. The body waves carry energy away from the boundary and into the magnetosphere and magnetosheath, reducing the free energy available for the KHI and consequently stabilising it.

As well as this, Pu and Kivelson (1983) show that compressibility increases the growth rate of one of the modes slightly and significantly reduces the growth rate of the other. They conclude that the impact of compressibility depends on the tangential wave vector, but in general compressibility does not significantly alter the threshold shear velocity in comparison to the incompressible limit.

Crucially, these works insufficiently describe reality by approximating the magnetopause as an infinitely thin tangential discontinuity when in reality it must have a thickness (e.g Le and Russell 1994). This makes all these results only valid for wavelengths much larger than the boundary thickness. For a more realistic analysis, a finite boundary is needed. Ong and Roderick (1972) was the first to do this in the incompressible limit by allowing the boundary to have a finite thickness, by doing this they found that short wavelength perturbations which would have been unstable in the tangential discontinuity case, were stable due to the thickness of the boundary layer. Furthermore, they used the small compressibility limit ($M_f \ll 1$) to show that compressibility further stabilises the boundary layer. Other studies also explored the finite boundary in the incompressible limit. Lee et al. (1981) used a uniform finite boundary layer interposed between two tangential discontinuities with uniform plasma and field either side but limited their study to the incompressible limit. They noted that the smooth variations in the plasma is not applicable to the LLBL but nevertheless, they still found two KH-modes; one on the inner-surface of the magnetopause boundary layer, called the inner-mode, and the other on the outer-surface, named the magnetopause mode. Despite the change in setup, Pu and Kivelson (1983) showed how this can be understood as a combination of solutions obtained for the waves propagating along the two separate surfaces meaning that adding this finite boundary under the incompressible limit did not extend beyond the later studies of Pu and Kivelson (1983). What this shows is that a more realistic and compressible finite boundary is needed to extend the results of Pu and Kivelson (1983).

3.1.3 Compressible Finite Boundary

As discussed above, inconsistencies in growth rates at short wavelengths arise when the magnetopause's finite thickness, denoted throughout as Δ, is ignored (Lerche 1966) as the effects of a finite thickness stabilises the magnetopause to short wavelengths. The issue with the compressible case is that it is not analytically tractable. To try and capture these dynamics, Walker (1981) used smooth variations

of field and plasma across a boundary layer with a tangential discontinuity at the outer surface for the magnetopause. They showed that the KHI is suppressed when wavelengths approach the scale-size of the finite boundary width and suggest that there must be a most unstable mode at the boundary. This unstable mode is shown to be perpendicular to the field, supporting the tangential discontinuity results of Southwood (1968) which suggest the KHI stability is more sensitive to the magnetic tension stabiliser than the shear flow driver.

This work is further extended by Miura and Pritchett (1982) who performed a parametric study on a velocity shear represented as a hyperbolic tangent with uniform background density and field. They noted that the inclusion of varying density and field would shift the wavenumbers and change growth rate slightly and they stated that this did not invalidate the studies application to the LLBL. They used two cases to explore how changing the magnetosonic fast Mach number and Alfvén Mach number influences the KHI growth rate.

The first was the transverse case which considered the case where the magnetic field is orthogonal to the shear flow boundary – in linear incompressible theory (Equation 3.6) this would mean there is no magnetic tension stabiliser. By taking the unstable cases, which they showed analytically were when $M_f < 2$, they found the normalised growth rate as a function of normalised wave number – the dispersion curves – as shown in Figure 3.2A. It can be seen how for large wavelengths (small wavenumbers) the solution tends to the incompressible limit with a tangential discontinuity (the dashed line). As the fast magnetosonic Mach number increases, and hence compressibility becomes more important, the growth rate considerably reduces, highlighting the importance of compressibility on the KHI.

Next, Miura and Pritchett (1982) explored the parallel case where the magnetic tension stabiliser is at a maximum. Figure 3.2B shows that by increasing M_A^{-1}, which corresponds to increasing $|\mathbf{B}|$, the growth rate decreases which is a direct consequence of the magnetic tension stabilising the boundary. They found a critical value of $M_A \sim 2$ below which there is no growing mode. In both cases, only the modes with $k\Delta < 2$ were unstable with the fastest growing mode corresponding to a normalised wave number which satisfies $k\Delta \approx 1$. This means there is a lower bound placed on the wavelength, defined as the ratio of the phase velocity to the wave frequency $\lambda = v_{ph}/\nu$, needed for KH-growth by the thickness of the boundary. It is important to remember that a boundary thickness

limits the frequencies which can exist as well as providing a most unstable frequency; this does not mean that at a single point there cannot still be a complex superposition of frequencies.

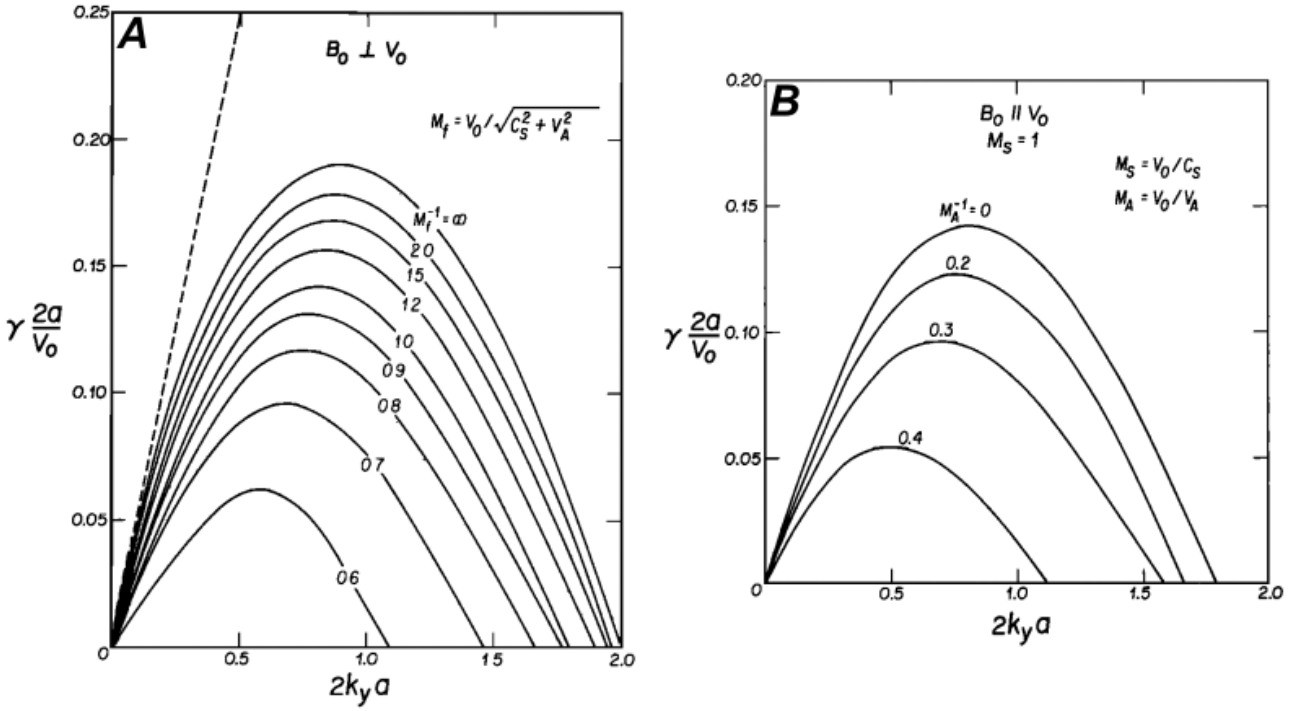


Figure 3.2: Panel A shows how the normalised growth rate varies depending on the normalised wave number for the transverse case. The dashed line is the growth rate for the incompressible case with a discontinuous velocity profile. For $M_f > 2$ there is no growing mode. Panel B shows how the normalised growth rate varies depending on wave number for the parallel case. M_s is the sound Mach number and is set at unity; a is the scale length. Figure from Miura and Pritchett (1982).

As well as the growth rates, the upper and lower critical velocity conditions introduced by Pu and Kivelson (1983) are also affected when instead considering a finite boundary thickness. The lower critical shear velocity is zero when the magnetic field is orthogonal to both the shear flow and the mode's wave vector (Miura and Kan 1992). In addition, the upper critical velocity shear limit is removed when including an inner boundary within the magnetosphere due to the interaction of reflected waves with the magnetopause (Fujita et al. 1996). Further work by Turkakin et al. (2013) showed that the quasi-slow mode should be more important closer (azimuthally) to Earth with the fast mode being more dominant further down flank. In summary, the role of compressibility is dependent on the thickness of the shear interface (Miura and Pritchett 1982) as compressibility plays a significant role in the gradual – but not total – stabilisation of the boundary due to the finite magnetopause thickness (Miura 1992).

Crucially, the current works presented are only true in the unbounded quasi-steady state. In reality, closed magnetospheric magnetic field lines in the vicinity of the magnetopause are necessarily bounded by the ionosphere. This required another approach which extends the compressible finite boundary model that became known as the 'box model'. All the models described thus far are shown in Figure 3.3.

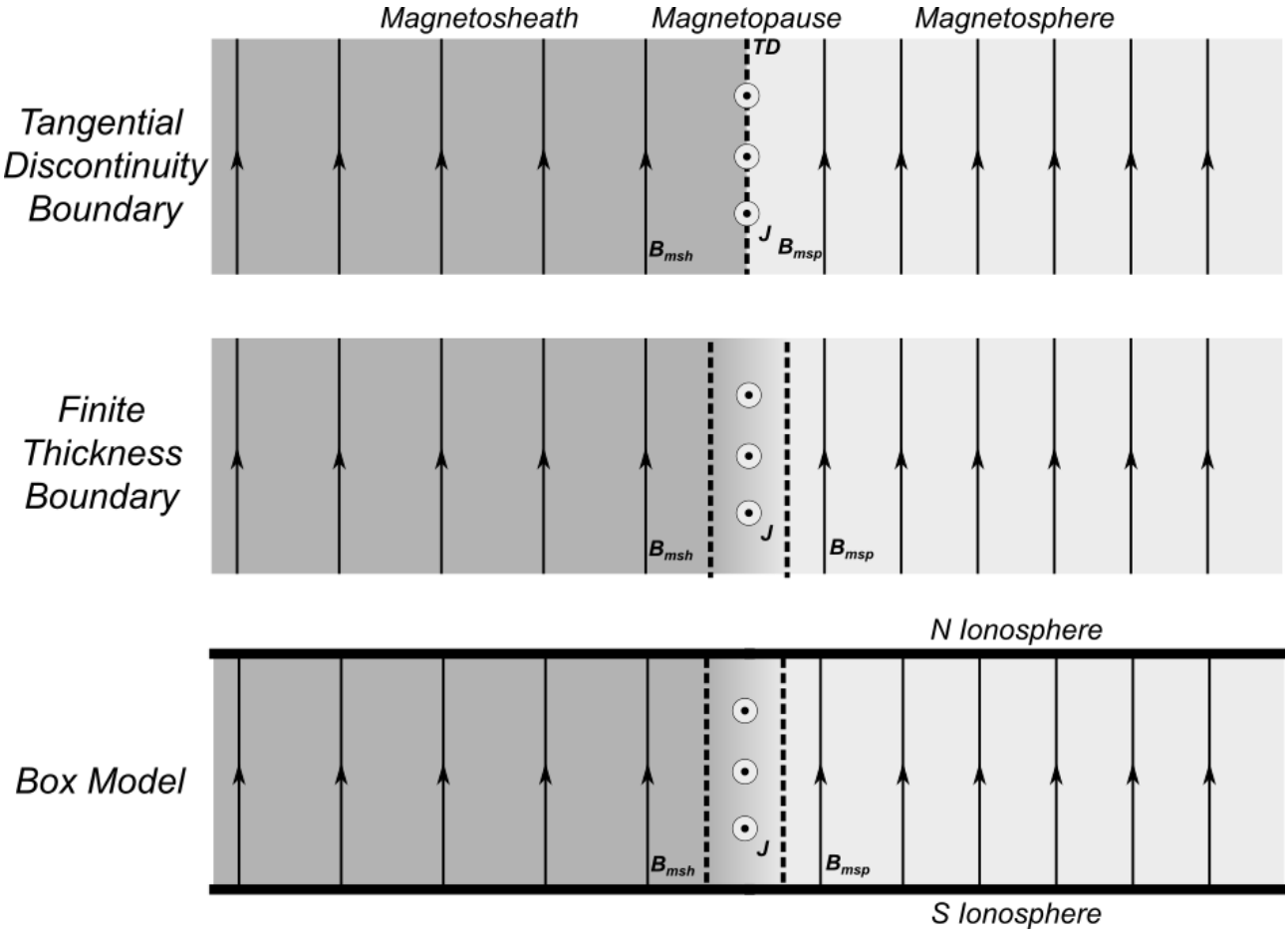


Figure 3.3: A figure visually explaining the different models used. The shades of grey represent different plasma environments and the black lines correspond to the magnetic fields. The dashed line is the boundary where plasma conditions change/begin to change. Figures inspired by Archer et al. (2022).

3.1.4 Compressible and Bounded Finite Boundary

The ionosphere is highly reflecting to magnetosonic modes such as surface waves, almost perfectly reflecting them and thus anchoring closed magnetic field lines in the ionosphere (Kivelson and Southwood 1988). So unlike the unbounded case where a spectrum of field-aligned wavenumbers are possible, the ionospheric boundary conditions quantise the possible field-aligned wavenumbers.

This reflection allows for Alfvén waves to stand along closed field lines (Dungey 1955) meaning that linear surface waves necessarily should have standing structure along the field (Chen and Hasegawa 1974a; Plaschke and Glassmeier 2011; Archer et al. 2019; Archer et al. 2021). If the wave stands between north-south ionospheres it is known as an eigenmode (Chen and Hasegawa 1974a; Plaschke and Glassmeier 2011) but they shall not be discussed further (see Archer et al. 2024, for a review of magnetopause surface eigenmodes). Alfvénic fluctuations within the finite magnetopause on closed field lines can now carry energy away from the boundary into the magnetosphere, dampening the propagating surface wave (De Keyser et al. 1999; Rezeau et al. 1989; Plaschke 2016). Further model set-ups exist to better model the complex magnetopause region, with examples such as adding curved field lines, or only anchoring the field lines in the magnetosphere and not the magnetosheath (Archer et al. 2024).

Unlike in the unbounded state, where the field lines would just move with the plasma, in the bounded state the field will now impose a magnetic tension restoring force even when it is orthogonal to the flow shear. In local simulations, this has shown to stop the vortex development if the z-extent around the equatorial plane is not large enough (Brackbill and Knoll 2001; Hashimoto and Fujimoto 2006; Takagi et al. 2006). In addition to this, it allows for the field topology to evolve. Over time, as the KHI progresses into the nonlinear stage, the bounded magnetic field can become twisted into flux ropes (Otto and Fairfield 2000; Hwang et al. 2020; Hwang et al. 2022) meaning that the magnetic tension will become increasingly important even when the magnetic field is orthogonal to the flow shear. These flux ropes generate current sheets in the mid-latitudes eventually inducing magnetic reconnection (Faganello et al. 2012; Faganello et al. 2014). Furthermore, this twisting requires additional energy which reduces the growth rate of the KHI or stabilises the boundary entirely (Miura 1987). This process is typical of the low-latitude flank magnetopause (e.g. Hwang et al. 2022).

Ultimately, no analytical approach will be representative of the magnetopause as any model requires some type of unrealistic assumption about the magnetopause environment: compressibility, symmetry, homogeneity, or boundary layer thickness; all of which are important factors in a realistic magnetopause. This is the crux of the problem with the KHI, it is not analytically tractable under realistic conditions. However, the theory has highlighted important factors in what affects the KHI: velocity shear, magnetic tension, density variations, and fluid compressibility. It is still unclear which of

these effects are most dominant. To understand these different factors in reality requires observations and simulations. As a result, a number of different studies using both numerical simulation and in situ observation are used to probe linear theory. In the next section a brief review of observations and simulations which both support and challenge the linear KH-driven surface wave theory will be conducted.

3.1.5 Testing Linear Theory with Observation

One of the most important results of linear theory is that the KHI is most unstable when the magnetic field is oriented such that it is perpendicular to the shear flow surface and therefore cannot provide a stabilising force to the boundary. This simple idea, despite being prominent in linear theory, was best shown more recently by Kavosi and Raeder (2015) who performed a statistical study of KH-waves using 7 years of in situ data from the NASA THEMIS (Time History of Events and Macro scale Interactions during Substorms) mission (Angelopoulos 2008). The authors found that KH-waves occur at the magnetopause $\sim 19\%$ of the time regardless of solar wind and IMF conditions, making them a ubiquitous feature of Earth's magnetopause. This result is substantially higher than linear theory would suggest (Kavosi and Raeder 2015), immediately highlighting that linear theory cannot totally capture the physics of the magnetopause. The authors highlight that it is unclear why the data does not reconcile with the theory and attribute it to the theory making simple assumptions about the boundary layer such as it being a tangential discontinuity or having smooth gradients when the authors find that neither of these are true. Without further study it is difficult to test this hypothesis.

Despite showing that the KHI is a prominent phenomena of the magnetopause regardless of IMF orientation, Kavosi and Raeder (2015) do show that the KHI favours more perpendicular IMF orientations inline with linear theory predictions – this is shown in Figure 3.4. Their results show that the KHI is more commonly found under northward IMF conditions compared to southward. This, again, challenges the linear theory which does not distinguish between northward or southward IMF. However, this result was not unexpected as there is a common assumption made that under southward IMF magnetic reconnection dominates, leaving less free-energy for the KHI to develop. What was unexpected was how frequent the KHI appeared to occur under southward IMF – especially

given that so few case studies existed with the first being Hwang et al. (2011).

The IMF cone angle from Kavosi and Raeder (2015)'s statistics (Figure 3.4) showed that the KHI mostly occurred when the IMF was more radial causing, due to the draping pattern of the magnetic field in the magnetosheath, the magnetic field to be weaker in the magnetosheath resulting in a weaker stabilising tension force which is in agreement with linear theory. Furthermore, the authors investigation into the plasma parameters found that KH-occurrence increased with solar wind speed, i.e. velocity shear, which is in agreement with the linear theory. They also found that it increased with Alfvén Mach number which Miura and Pritchett (1982) predicted, however they point out that this dependence is separate to the IMF magnitude meaning that Alfvén speed as a parameter itself is significant, an idea which exists in linear incompressible theory.

Finally, a further investigation which included additional data from MMS (Burch et al. 2016), showed that the KHI is sensitive to the dipole tilt angle of the Earth with notable changes in the KHI occurrence both seasonally and diurnally (Kavosi et al. 2023). Such a strong sensitivity to the magnetic field orientation strongly supports the results of Southwood (1968) and Walker (1981) who suggested the angle between the field and the shear flow dominated KH-stabilisation. Everything discussed so far strongly highlight the importance of a realistic magnetic field geometry over that of the idealised geometries found in linear theory.

Another big challenge which KHI studies present is that, as the KHI is a global phenomenon its features and dynamics cannot be fully captured with single point or even multi-point in situ measurements. As a consequence, the analysis of global KH features under realistic geometry and conditions, such as wavelength, requires a global magnetospheric simulation based approach. Two examples of well captured and visualised KH surface waves are shown in Figure 3.5. Both these simulations are MHD magnetospheric models with panel A being Lyon-Fedder-Mobarry (LFM) (Lyon et al. 2004) and Panel B being a more recent version of LFM called GAMERA (Zhang et al. 2019). These studies have explored significant topics that will be discussed but it is worth highlighting here how Figure 3.5 convincingly shows that the KHI is a global phenomena.

Despite the added complexity of the simulation, both Merkin et al. (2013) and Michael et al. (2021) concluded that the most unstable mode estimated by Miura and Pritchett (1982), $k\Delta \approx 1$, matched those found in the simulation. This is unexpected because the simple model makes incorrect

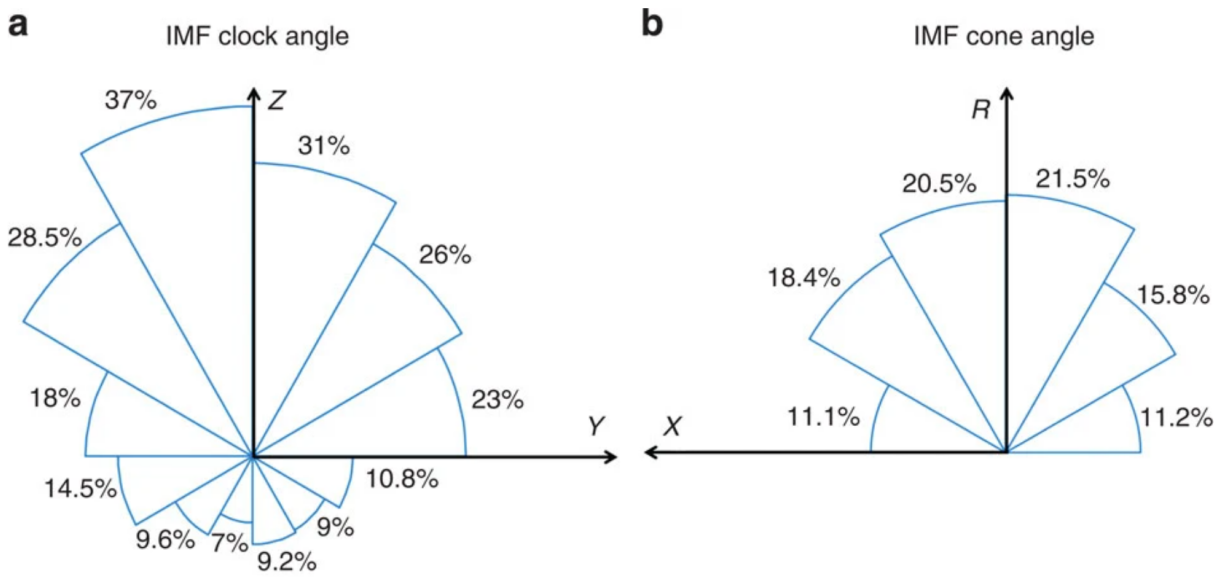


Figure 3.4: KH-wave occurrence rate as a function of IMF clock angle and cone angle. Clock angle (Panel a) is defined as $\arctan(B_y/B_z)$ and cone angle (Panel b) is defined as $\arccos(B_x/|\mathbf{B}|)$ where the Cartesian directions are sunward, dusk-ward, and northward respectively. Figure from Kavosi and Raeder (2015).

assumptions about the wave propagation, the magnetic field, and the plasma environment. Neither Merkin et al. (2013) nor Michael et al. (2021) explore why their results reconcile with linear theory.

A number of MHD simulations of the KHI observe both inner- and outer-modes (e.g Guo et al. 2010; Li et al. 2012; Li et al. 2013; Merkin et al. 2013) as predicted by linear theory (Lee et al. 1981; Pu and Kivelson 1983; Miura and Pritchett 1982). Despite both simulation and theory predicting their existence, these modes have avoided being captured in situ, questioning their existence. This lack of observation may be attributed to the lack of observations in the flank of the tail where the modes are observed in simulation, them being hard to resolve or distinguish due to the nature of in situ observations, or it may be due to them just not existing. More work is needed to better understand the existence of inner- and outer-KH modes.

It is clear now that the linear theory used to explore the KHI is a good approximate model for the KHI but it does not fully capture reality as observations both in situ and with simulation challenge aspects of it. This lack of understanding about how the instability works affects measures of how important the KHI is to the momentum and energy transfer budget from the solar wind into the magnetosphere, which is the focus of the next section.

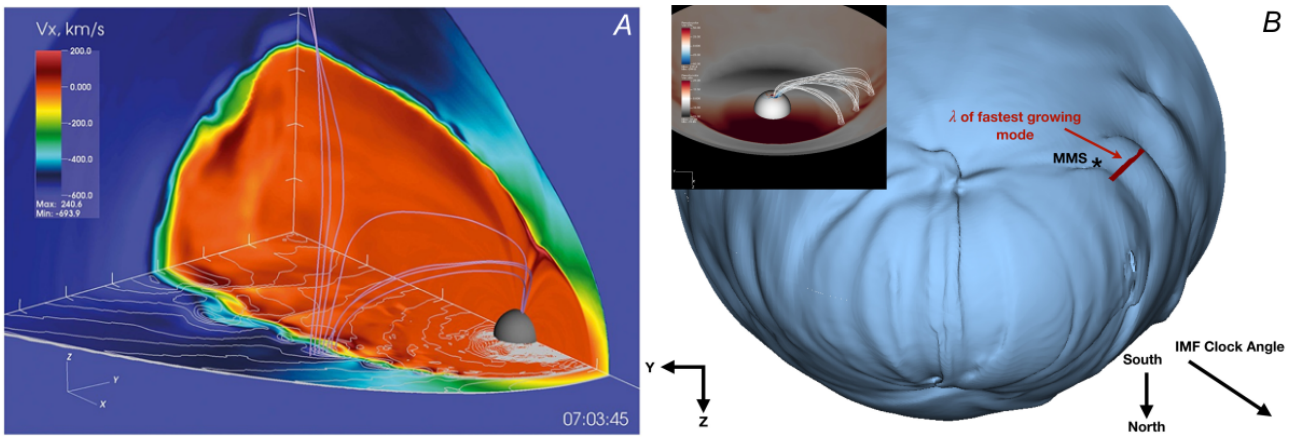


Figure 3.5: Panel A shows the x component of the velocity in the equatorial, noon-midnight meridian, and YZ at $x = -30\,R_E$ planes. The light grey contours is the thermal pressure and the pink lines are magnetic field lines. Panel from Merkin et al. (2013). Panel B shows an iso-surface of the plasma density at $n = 15\,cm^{-3}$ from a GAMERA simulation attempting to recreate an MMS crossing of the magnetopause on the 25th February 2016 at 19:15 UT. The inset shows the residual magnetic field in the equatorial plane, with the dipole field removed. Regions where the field is compressed are in red. Magnetic field lines near the equatorial boundary layer are in white along with the field aligned currents at the spherical inner boundary surface. Panel and inset caption text from Michael et al. (2021).

3.2 Transfer Mechanisms

Being the dominant driver of the viscous-like interaction, the KHI is the second most important transfer mechanism at the magnetopause after large-scale magnetic reconnection. But what does that mean? The following section aims to build upon the linear theory presented by justifying why the frequency and wavelength of KH-waves is a topic of interest. Beyond this, KH-surface waves will be left behind and the non-linear KH-effects will be explored in more depth highlighting why the non-linear stages of the instability are also important. At this point, it is important to discuss and highlight when the linear theory presented above is valid and, maybe more importantly, when it is not.

The KHI introduced above is an idealised version of what is a rather complex, cross-scale, highly-nonlinear instability. At Earth's magnetopause the KHI has been shown to evolve from being seeded to having a tightly rolled-up surface all within 4 hours of magnetic local-time both in simulation (Li et al. 2012) and observations (Nakamura et al. 2013). The evolution of the magnetopause boundary due to the KHI is shown in Figure 3.6. The figure shows how the KHI is seeded close to the subsolar point and grows quite quickly into a linear growth phase – this is where the linear theory is most

applicable. After the linear growth phase comes a non-linear growth phase where the waves evolve non-linearly until the boundary becomes so deformed it begins to roll-up. These surface roll-ups are what is most commonly associated with the KHI at the magnetopause. It is necessary to distinguish between the surface roll-up stage and the surface wave stage because they transfer momentum and energy across the magnetopause in very different ways.

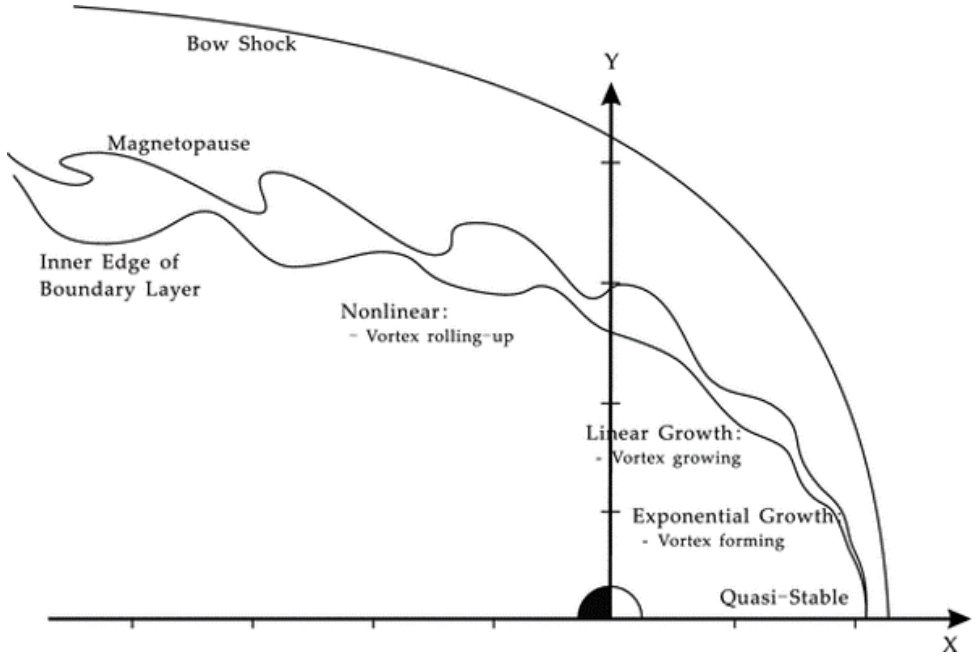


Figure 3.6: An illustration of the spatial development of the KHI under northward IMF at the magnetopause boundary layer in the equatorial plane. Figure from Li et al. (2012)

3.2.1 Surface Waves

Ultra Low Frequency (ULF) waves are waves with a frequency in the range of 1 mHz - 5 Hz (Jacobs et al. 1964) and have long been observed using ground-based magnetometer data. ULF wave signatures were first suggested to be related to the KHI by Samson et al. (1971). However, problematically there was no mechanism known to exist which could allow for a connection to be made between the magnetopause and the Earth's surface. This led to Chen and Hasegawa (1974a) and Southwood (1974) to theoretically develop a mechanism to connect the two. They each suggested that standing Alfvén waves driven by MSWs may be responsible for transferring energy from the magnetopause down to Earth's surface through a process known as field line resonances. Field line resonances (FLRs) are when global wave modes, e.g. surface waves, propagate compressional energy into the

magnetosphere at some frequency which resonates with a local field line and generates an Alfvén wave that, as it is reflected at the ionosphere, locally stands along the closed field line (Elsden et al. 2022). See Figure 3.7 for an illustration of the two different types of FLR. These Alfvén waves carry/couple to field-aligned currents (FACs) which then feed energy and particles into the ionosphere, eventually driving space weather effects. This process has been observed (e.g Agapitov et al. 2009).

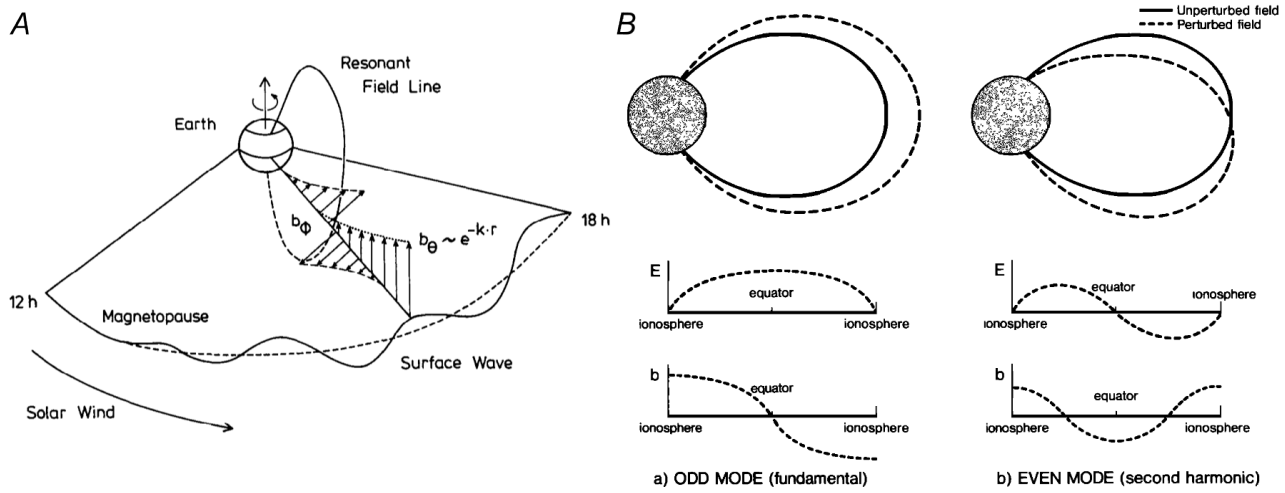


Figure 3.7: Panel A is an illustration of a toroidal field line resonance from Glassmeier (1995). Panel B is an illustration of a poloidal field line resonance from Southwood and Kivelson (1981)

Another way that MSWs can couple to the Alfvén mode and generate FACs is through waveguide modes (Plaschke 2016). MSW's can generate waveguide modes when they either drive some inner-surface which couples to a waveguide mode, or they transition into body modes (Pu and Kivelson 1983) which then couple to a waveguide mode. Waveguide modes are fast magnetosonic waves which are reflected between turning points: one inside the magnetosphere, and the other typically at the magnetopause (Plaschke 2016). These broadband compressional waveguide modes from MSWs can excite field lines, essentially 'plucking them' and sending Alfvén waves along the field (Hasegawa and Chen 1974). These lone Alfvén waves can also generate FAC's at the ionosphere like the FLRs. It has also been shown that these waveguide modes can also couple to FLRs (e.g Mann et al. 2002). Finally, despite being evanescent from the boundary, surface waves do persist into the magnetosphere driving ULF waves. It has been shown using a collection of spacecraft that during periods of time where ULF waves are observed but neither waveguide modes or FLRs are observed, that ULF waves exist (Wang et al. 2017b). These ULF waves were attributed to both inner and outer modes of the KH-waves and their associated flow vortices.

However, ULF waves inside the magnetosphere can also be driven by transient structures in the magnetosheath impacting the magnetopause and being processed as they propagate Earthward (Takahashi 1998) (for further discussion see review by Zhang et al. 2022). Furthermore, surface waves can be driven by a number of other phenomena such as solar wind pressure variations (e.g. Archer et al. 2022) and magnetosheath transients (e.g. Archer et al. 2019). This raises questions surrounding the origin of the frequencies inside the magnetopause and whether they are a symptom of the frequencies characteristic to the upstream conditions at Earth, or whether the KHI has processed and filtered the solar wind such that only the frequencies determined by the KHI exist. This is why KH-frequency and wavelength is so important because it allows for an understanding of the origin of magnetospheric ULF waves, and currently the majority of studies heavily rely on linear theory which has repeatedly been shown, and admits, to rely on invalid assumptions at the magnetopause.

Linear theory has shown that the most unstable KH-wavelength is dependent on the shear layer thickness (Miura and Pritchett 1982). Furthermore, studies have shown that the KHI can amplify pre-existing disturbances over a wide range of frequencies/wavelengths (e.g. Belmont et al. 1995; Miura 1999a; Miura 1999b; Nykyri et al. 2017) with simulation based studies suggesting that an inverse cascade occurs from shorter wavelength near the dayside towards longer wavelengths further down tail (Winant and Browand 1974; Belmont and Chanteur 1989). It has also been suggested that the KHI advects unstable frequencies in the upstream, and smears them into the downstream, creating a superposition of frequency at a given local time (Mills et al. 2000). As a result, the most unstable mode at a given local time may not be the most dominant as suggested by linear theory. What this means is that the KHI has been suggested to generate, amplify, and advect frequency along the magnetopause. However it is unclear in studies which of these effects is dominant.

Observational studies exist which show that the wavelength of the KHI has an inverse dependence on the IMF clock angle (Farrugia et al. 2003; Foullon et al. 2008). These wavelengths are much larger than linear theory predicts, with the stretching not being captured at all. This study is contrasted by Lin et al. (2014) who show the opposite and suggested that the thickening of the LLBL is responsible for the changes. Li et al. (2012) found varying the total solar wind speed did not affect the way the wavelength extended in the tail. Instead they found that the phase speed increased with increasing longitude and that the wave characteristics were self-consistent with $v_{ph} = \nu\lambda$. This is supported by

Lin et al. (2014) who showed that the wavelength also increased with distance from the subsolar point. However, it is still unclear in these studies whether the frequency is changing as well as the wavelength, or whether the varying phase speed due to the magnetosheath acceleration (Haaland et al. 2019) is modulating the changes.

In summary, KH-waves are responsible for a portion of energy transfer into the magnetosphere, predominantly through Alfvén mode coupling to FACs. This is one of the primary ways that the KHI transfers energy from the solar wind into the magnetosphere (see Plaschke (2016) for further discussions surrounding this subject). However, this is not the only way that the KHI transfers energy. The other ways occur in the non-linear stages which, in the last few years, studies have revealed that a multitude of different secondary and kinetic-scale processes can occur.

3.2.2 Surface Roll-ups

So far, only the quasi-linear stages of a KH-generated surface wave has been explored, but interesting energy-transfer processes do take place in the non-linear regime which cannot take place in the quasi-linear stages of the KHI making it an important stage to discuss. At some point, when the wave amplitude has grown sufficiently large, a linear surface wave will transition into the non-linear growth phase – this is contingent on the stabilising forces being deficient. The non-linear growth causes the previously sinusoidal waves to become skewed and asymmetric as the shear interface deforms and undergoes wave steepening (e.g. Chen and Kivelson 1993; Plaschke et al. 2016). This wave steepening at the magnetopause can occur on both the leading (anti-sunward) and trailing (sunward) edge of the wave, but KH-only events typically exhibit steepening on the leading edge of the wave (Plaschke et al. 2016).

After the non-linear wave growth, the wave fronts collide, merge, and evolve into larger scale waves and vortices as an inverse cascade (Winant and Browand 1974; Belmont and Chanteur 1989) causing the surface to roll-up (Li et al. 2012). Simulations have shown this non-linear development results in a near-linear relationship between the dominant wavelength as suggested by Miura and Pritchett (1982) and time since the initial perturbation occurred (Miura 1999a; Miura 1999b). Due to its nature, analytic studies on the non-linear stages of a surface wave do not exist (Alì and Hunter 2003). This has not deterred people from developing theory using incompressible assumptions and a

tangential discontinuity (Hollweg 1987; Alì and Hunter 2003), however, as it has limited application, it will not be discussed here.

Due to the non-linear development of the plasma and fields, the KHI can drive diffusive transport of plasma across a boundary through the priming and triggering of secondary instabilities such as the Rayleigh-Taylor instability (e.g. Nakamura et al. 2022) and secondary KHI (e.g. Matsumoto and Hoshino 2004; Faganello et al. 2008). These secondary instabilities impede the large-scale inverse cascade evolution of the KHI by reducing the available free energy, syphoning it into turbulent diffusive particle transport (Stawarz et al. 2016); a process not fully captured by MHD. A more complete discussion about the multi-scale processes of the KHI can be found in Rice et al. (2024).

Despite this, local MHD simulations can be useful in investigating the deviations from linear theory that occur in the non-linear stages such as Ma et al. (2024) who used 2-dimensional MHD simulations to explore the role of density asymmetry on the KHI. They show that the KHI growth rate is uneffected by this density gradient. However, it is worth noting the lack of realistic conditions which may contribute to this divergence from linear theory; in particular this simulation set-up will effect the role of the Alfvén Mach number which has been shown to be an important variable (Miura and Pritchett 1982). There are other reasons linear theory can differ from observations, such as when the shear layer thickness approaches the ion-inertial length enabling diffusive transfer (Cowee et al. 2010) or other kinetic effects to diverge observations from theory (Faganello and Califano 2017) – these effects in particular are not captured in MHD meaning that numerical MHD simulations may not reflect reality.

The kinetic effects which can occur during the non-linear stages of the KHI are responsible for the cross-scale energy transfer attributed to the KHI. Cross-scale here means the transfer of energy from the macro-scale (MHD/fluid scale) to the micro-scale (particles). One of these micro-physical processes which MHD simulations do capture is known as vortex-induced reconnection (VIR). VIR is when magnetic reconnection is triggered in a current sheet which has been thinned by a KH-vortex. Nakamura et al. (2008) distinguished between the two different types which existed in the literature: Type I or mid-latitude VIR which is when there is also a magnetic shear across the velocity shear layer (e.g. Pu et al. 1990; Nakamura et al. 2017); and Type II or in-plane VIR which is when the velocity shear interface is tightly rolled-up and the wrapped field lines, which were initially parallel, become

antiparallel and reconnect (Nykyri and Otto 2001). Type I reconnection occurs under southward IMF but Type II can occur under both. There are observations of the magnetic field undergoing "double mid-latitude reconnection" which is when the field twists and reconnects in a candy wrapper-like way (Faganello et al. 2012). VIR may explain the findings of Kavosi and Raeder (2015) who found that the KHI does exist during southward IMF however it exists for much shorter timescales. This idea was explored by Nakamura et al. (2020) who performed 3D kinetic simulations to show that under southward IMF, KH-vortices decayed quickly due to the disruption of the field and flow pattern by the VIR outflow jets. They go on to suggest this may explain the lack of observations under southward IMF.

In summary, the KHI has a range of different transfer mechanisms associated with it dependent on which regime it is in. This makes studying the KHI quite difficult because there are few features which are present at every stage. One of the processes which is present at every stage is a vortex. A vortex occurs in the flow adjacent to a wave in the linear stages and in the surface roll-up of the highly non-linear stage. As a vortex is unlikely to exist at the magnetopause due to other phenomena, it is a useful feature of the KHI to look for in data if trying to isolate KH features.

3.3 Waves and Vortices

Typically, MSWs due to the KHI at the magnetopause are identified in situ by using hodograms to show quasi-periodic fluctuations of the magnetopause surface passing over spacecraft (Hasegawa et al. 2004a). This method is deficient if only single spacecraft measurements are used as it can be difficult to characterise structure size (Hasegawa et al. 2004a). As well as this, the method cannot identify magnetopause vortex structures (Cai et al. 2018). Vortical patterns will be present in the data from both surface roll-up and the boundary adjacent vortices the waves generate in the boundary-adjacent flow. It is important to be able to distinguish between them as surface roll-ups only occur in the nonlinear stages of the KHI but boundary-adjacent vortical flow can occur at any stage (Chandrasekhar 1961; Hwang et al. 2022).

3.3.1 Defining a Vortex

Although a vortex is a pervasive and familiar concept which is qualitatively understood as a region of swirling fluid about some arbitrary axis line, perhaps remarkably a universally accepted mathematical vortex definition still does not exist (Jeong and Hussain 1995; Yao and Hussain 2018; Cai et al. 2018). To aid the discussion, it is important to understand the origins of a vortex in general. Vortices are formed when shearing momentum is redirected in some way, translating it into rotational momentum. Without an adequate restoring centripetal force, the centrifugal motion of the fluid in a vortex will tear itself apart, diffusing it. In hydrodynamics, the centripetal force that prevents this usually comes from gradients in pressure which originate from velocity gradients, following Bernoulli's principle. This is known as cyclostrophic balance and is only true in a steady inviscid planar flow (Jeong and Hussain 1995).

The MHD case complicates this by introducing magnetic pressure and magnetic tension forces. In MHD the restoring force will also include magnetic field contributions which are caused when the field is perturbed by the moving plasma (Collado-Vega et al. 2018). As the stress in an MHD fluid is anisotropic, due to magnetic tension introducing bias along the field direction, the consequential pressure contribution from the field will be a complex superposition of the magnetic pressure and some part of the magnetic tension. This added complexity means that MHD requires some formal vortex definition beyond that of hydrodynamics.

3.3.2 Existing Hydrodynamic Vortex Identification Techniques

Identifying and/or quantifying a vortex is a problem which still exists and is widely researched in the hydrodynamic community (see review by Zhang et al. 2018b, and references therein). Most of these methods typically stem from the velocity gradient tensor, $\boldsymbol{\nabla}\mathbf{v}$ where

$$\mathbf{G} = \boldsymbol{\nabla}\mathbf{v} = \begin{bmatrix} \partial_1 v_1 & \partial_1 v_2 & \partial_1 v_3 \\ \partial_2 v_1 & \partial_2 v_2 & \partial_2 v_3 \\ \partial_3 v_1 & \partial_3 v_2 & \partial_3 v_3 \end{bmatrix}. \tag{3.8}$$

One example of a popular vortex core line identification technique derived from the velocity gradient tensor is the Q definition (Hunt et al. 1988). This defines a vortex as a connected fluid region with a positive second invariant of $\boldsymbol{\nabla}\mathbf{v}$. Finding the characteristic equation of $\mathbf{G}$ gives

$$\det\left(\mathbf{G} - \lambda\mathbf{I}\right) = \lambda^3 - P\lambda^2 + Q\lambda - R = 0 \tag{3.9}$$

where the first, second, and third invariants of $\mathbf{G}$ are defined respectively as

$$P = \mathrm{Tr}\left(\mathbf{G}\right) \quad ; \quad Q = \frac{1}{2}\left[\mathrm{Tr}\left(\mathbf{G}\right)^2 - \mathrm{Tr}\left(\mathbf{G}^2\right)\right] \quad ; \quad R = \det\left(\mathbf{G}\right). \tag{3.10}$$

For an incompressible fluid ($\nabla \cdot \mathbf{v} = \mathrm{Tr}\left(\mathbf{G}\right) = 0$), the Q criterion is equivalent to a region where the magnitude of the rotation rate tensor, $\boldsymbol{\Omega} = \frac{1}{2}\left(\mathbf{G}^T - \mathbf{G}\right)$, is larger than the magnitude of the strain-rate tensor, $\mathbf{S} = \frac{1}{2}\left(\mathbf{G}^T + \mathbf{G}\right)$. This is expressed as $(||\boldsymbol{\Omega}||_F^2 - ||\mathbf{S}||_F^2)$ where $||\cdot||_F$ is the Frobenius norm given by $||\underline{\mathbf{X}}||_F = \sqrt{\sum_{i=1}^{n}\sum_{j=1}^{m} X_{ij}^2}$. Due to its simplicity, this strictly incompressible definition of Q is usually applied, even when dealing with compressible fluids.

Another popular vortex core line identification technique derived from the velocity gradient tensor, and based on locating local pressure minima, is the λ_2 definition (Jeong and Hussain 1995). The technique starts with the Navier-Stokes momentum equation and derives the pressure Hessian, containing local pressure extrema information. After discarding unsteady irrotational straining and viscous effects, which are unrelated to vortical motion, this becomes

$$\partial_i\partial_j P_{\mathrm{adp}} = S_{ik}S_{kj} + \Omega_{ik}\Omega_{kj}, \tag{3.11}$$

where P_{adp} is the adapted pressure (pressure with the unsteady irrotational straining and viscous effects removed). An adapted pressure minimum in some plane requires, through a second partial derivative test on P_{adp}, two negative eigenvalues of $\mathbf{S}^2 + \boldsymbol{\Omega}^2$. Hence a vortex core in this method is defined as a connected region which satisfies this condition. This can be simplified by sorting the eigenvalues in descending order: $\lambda_1 > \lambda_2 > \lambda_3$ and stating a vortex occurs where $\lambda_2 < 0$ (a step-by-step derivation can be found in the appendix of Cucitore et al. 1999). λ_2 can be interpreted as identifying a local pressure minima in some arbitrary intersecting plane. Due to how the value is

constructed, the magnitude of the parameters does not have any physical significance except for comparison to other values of itself. Cucitore et al. (1999) show that the λ_2 method is a requirement of some measure of the rotation rate prevailing over some measure of the strain rate, implying that λ_2 and Q are comparable.

Both of these criteria are only valid for homogeneous and incompressible hydrodynamic fluids. In addition, as they both only use the velocity vector field, they are ignorant to the momentum they represent. Extensions to these techniques do exist which provide weighting dependent on momentum. The simplest is weighted-λ_2 (Yao and Hussain 2018) (denoted as $\overline{\lambda_2}$ herein) which is identical to λ_2 but weights Equation 3.11 by density. This results in a shifting of power from high velocity vortices to high momentum vortices. A further extension is known as λ_ρ (Yao and Hussain 2018) which extends λ_2 to be valid for compressible, inhomogeneous hydrodynamic fluids. This is achieved by using the symmetric part to the tensor product of the momentum gradient tensor, $\boldsymbol{\nabla}(\rho\mathbf{v})$, and the velocity gradient tensor, $\boldsymbol{\nabla}\mathbf{v}$, along with the symmetric part of the momentum compressibility gradient tensor, $\boldsymbol{\nabla}\left[(\boldsymbol{\nabla}\cdot\mathbf{v})\,\rho\mathbf{v}\right]$. λ_ρ can be broken into three parts which represent the vortical momentum, the fluid compressibility, and the density gradients. If the definition is applied to an incompressible and homogeneous fluid then it reduces to $\overline{\lambda_2}$. A useful feature of the Q and λ-family of techniques is that they are Galilean invariant (Jeong and Hussain 1995), meaning the methods are consistent across all inertial frames of reference.

3.3.3 Current Approaches to Vortex Identification at the Magnetopause

Numerous vortex identification techniques applicable to the magnetopause have been developed but all have deficiencies (see review by Hasegawa 2012). For example, a sensible starting place for vortex identification would be using the vorticity vector. However, at shear boundary regions vorticity is high even in the absence of any rotating flows, meaning that it is not suitable for KH vortex identification. Takagi et al. (2006) suggested using low-density plasma moving faster than the magnetosheath plasma to detect surface roll-ups. However, Plaschke et al. (2014) showed that this signature is not unique to surface roll-ups due to the plasma depletion layer and vortices from MSWs

providing false-positives. Alternatively, based on a hybrid Vlasov simulation of the KHI, Settino et al. (2021) suggest kinetic signatures such as ion non-Maxwellianity, total current density, temperature anisotropy, agyrotropy, and magnetic field gradients might serve as proxies for KH-vortices.

Another popular method used for both simulation and in situ analysis investigates local total pressure minima, where the total pressure is the sum of thermal and magnetic pressures (Nykyri et al. 2017; Rice et al. 2022). Pressure minima are coupled to vortices due to Bernoulli's principle as discussed above. This approach, and using the vorticity vector, typically fails when fluctuations are large or if other physical processes which can interfere with the dynamics of the KHI (e.g. reconnection) are taking place (Settino et al. 2021). Other drawbacks of local pressure minima arise due to the vortex not containing a three-dimensional pressure minima and also pressure minima not always being associated with vortices as other physical process can create them.

The simpler hydrodynamic vortex identification techniques (Q and λ_2) have also been used to study the KHI at Earth's magnetopause, though this is only possible for multi-point analysis due to the necessity of calculating gradients (Settino et al. 2021). Cai et al. (2018) used data from the Cluster Mission (Escoubet et al. 2001) to identify vortical structures at Earth's magnetopause. They applied the method to magnetic field data rather than the velocity data, assuming these vary similarly via the frozen-in flux theorem. They conclude that Q is easy to implement but imprecise and that λ_2 is more precise but does not provide geometric information about the vortex core. These results agree with a different study performed by Collado-Vega et al. (2018) who investigated the effectiveness of Q and λ_2 in identifying vortices in a 3-dimensional BATS-R-US global MHD magnetosphere simulation (Tóth et al. 2005). They state that neither method is immune to false identifications and conclude by stating that incorporating the effects of the magnetic field will likely increase the scientific yield. Since both techniques derive from hydrodynamics, this can only be done by deriving the equivalent to the λ-family of methods from the MHD equations.

Palermo et al. (2011) investigated the influence of plasma homogeneity and compressibility on the formation of KH vortices and found that compressibility, inhomogeneity, and magnetopause thickness all play a role in vortex formation and propagation and state that compressibility effects stabilise the magnetopause. They showed that the vortices produced by the KHI act as obstacles to the driving flow, which can lead to compressions and even shocks within the plasma. Other studies

have shown that plasma inhomogeneity decreases growth rates as the gradients increase (Amerstorfer et al. 2010). Ma et al. (2024) suggest that the KHI growth rate is insensitive to the density gradient across the shear flow boundary in the compressible regime and go on to show that these variations affect the secondary processes which the KHI trigger.

Overall, whilst this shows that the role of compressibility and magnetic tension on the KHI is a stabilising one, the significance of magnetic tension, compressibility, and density variations on vortex formation at the magnetopause is still an open question. One reason for this is because identifying MSWs and their coupled vortices using in situ measurements or simulation is not trivial (Plaschke 2016). Given the major role that the Kelvin-Helmholtz instability is thought to play in the viscous-like interaction between the solar wind and magnetosphere, the ability to clearly identify the vortices produced by this process is important.

3.4 Motivation and Questions

The literature presented above highlights a number of unanswered avenues to pursue research. Linear theory has shown that plasma momentum, inhomogeneity, compressibility, and magnetic tension all play a role in determining how unstable a boundary is to the KHI. But beyond linear theory there is a lack of understanding about how these physical effects influence and affect the evolution of KH-flow vortices. To perform this study objectively, a vortex identification technique valid for MHD will need to be derived, validated in a local simulation, and investigated with an aim to provide information about the different drivers and stabilisers of the KHI. This will be the subject of the first work chapter of this thesis.

Following on from this work, the importance of realistic conditions has been highlighted throughout literature due to the complexity of a global magnetosphere and the different processes it encompasses. These inhomogeneities simply cannot be captured by local simulations. Building upon the findings of the local simulation which investigates how the different physical effects influence the evolution of KH-vortices, the next work chapter will aim to investigate how realistic magnetospheric plasma and magnetic field geometry changes how the KHI evolves and how the different drivers/stabilisers effect its evolution. This study aims to discern between the vortex evolution which is caused by the

progression of the KHI, and the changes which can be attributed to the changing plasma environment and magnetic field geometry found in a realistic magnetosphere.

The final work chapter of this thesis aims to question how applicable linear theory really is in a realistic magnetosphere by investigating the frequency spectrum present at the magnetopause. By doing this, an understanding about how dominant the 'most unstable frequency' predicted by linear theory actually is will be gained. It is currently unclear whether an observed MSWs frequency is dominated by a locally-generated mode controlled by the local plasma and field conditions, or if it is a smeared superposition of advected modes from upstream. This study aims to understand which frequency mechanism is most dominant in the KHI at the magnetopause: generation, amplification, or advection.

The remaining portion of the thesis will be structured in the following way: Chapter 4 will provide an overview of the simulations used. Chapter 5 will briefly introduce the Helmholtz Decomposition as it is widely used throughout the thesis. Chapters 6, 7, and 8 will contain the original research chapters covering the topics described above. The thesis will be concluded in Chapter 9 with a discussion about the wider implications of the results of the research chapters and future research directions as a consequence of them.

CHAPTER 4

Magnetohydrodynamic Simulations

Simulations are valuable tools in science as they can provide a way to test physics without it needing to take place. In the context of space plasmas, simulations range from kinetic simulations of electron heating in turbulence-driven magnetic reconnection (Franci et al. 2022), to using MHD to simulate the heliosphere (Heerikhuisen et al. 2024). Despite capturing very different physics and being used for a different purpose, all simulations essentially work in the same way: they use numerical methods to solve a predefined set of equations to capture the relevant physics within the limits of available resources. This outlines the four vital components to a simulation: the numerical methods that it uses, the equations being solved, why the simulation is an appropriate tool for the question being asked, and for an appropriate amount of resource. The final point here is probably the one that constrains simulations the most.

Computational resource is the limiting factor of physics-based simulations. Take the two examples from above, of course it would be invaluable to kinetically simulate the entire heliosphere however computationally this is just not feasible; the required resource does not currently exist for that scale of calculation to take place on a useful timescale. Instead, appropriate approximations about the problem can be made which make the calculations more computationally feasible. It would not be appropriate to simulate electron heating using an MHD assumption even if multiple fluids were used

as fluid equations do not capture the nuanced behaviour of the electron. However, a fluid-scale approximation is valid when investigating dynamics on the scale of the heliosphere because the 'local' fine-scale kinetics not captured by MHD are not expected to influence the 'global' dynamics of the system. This outlines the two different types of simulation: local and global.

A local simulation is typically used when trying to understand a single process such as magnetic reconnection, a Kelvin-Helmholtz vortex, or the turbulent cascade. A local simulation, is a typically small scale simulation allowing for high-resolution. Local simulations often have simplifications such as homogeneous conditions. Despite this, the conditions in a local simulation can be totally customizable allowing for near-complete control of the parameter space. They are better equipped for understanding the physics of a process and usually include more finer-scale physics such as kinetics. Alternatively, a global simulation is typically used when trying to understand a system or set of systems such as the heliosphere or Earth's magnetosphere. These simulations are less controllable and usually have lower-resolution than local simulations. As they evolve self-consistently, controlled only through preconditioning, boundary inflows/conditions and governing equations/numerics, global simulations typically generate a more representative environment compared to local simulations. This comes at the cost of making it harder to investigate individual physical processes in a global simulation (e.g. KH-vortex evolution along the magnetopause) because, due to the simulation's complexity, the effects of individual processes are harder to isolate. This makes global and local simulations appropriate for different types of investigations.

In fluid simulations there are two main types: Eulerian and Lagrangian. Eulerian simulations work by defining a grid and then advecting the fluid through those positions, analogous to measuring a fluid in multiple fixed locations using a mesh of sensors. Lagrangian simulations are mesh-free and work by tracking a single fluid parcel through the domain, this should be thought of as allowing the sensors to free-flow with the fluid. Both the local and global MHD simulation used in this thesis are Eulerian. An overview of the simulation numerics will be given here, starting with the local simulation. The specific simulation set-up will be described at the beginning of each study.

4.1 Local Simulation

The local simulation results used in this thesis are obtained from a three-dimensional MHD code which has been used in a number of previous studies (Otto 1990; Otto and Fairfield 2000; Nykyri and Otto 2001; Ma et al. 2014b; Ma et al. 2017; Ma et al. 2019; Ma et al. 2024). The code works by solving the following set of resistive MHD equations:

$$\frac{\partial \tilde{n}}{\partial t} = \boldsymbol{\nabla} \cdot (\tilde{n}\tilde{\mathbf{v}}), \tag{4.1a}$$

$$\frac{\partial (\tilde{n}\tilde{\mathbf{v}})}{\partial t} = -\boldsymbol{\nabla} \cdot \left(\tilde{n}\tilde{\mathbf{v}}\tilde{\mathbf{v}} + \frac{1}{2}\left(\tilde{p} + \tilde{\mathbf{B}}^2\right)\mathbf{I} - \tilde{\mathbf{B}}\tilde{\mathbf{B}} \right), \tag{4.1b}$$

$$\frac{\partial \tilde{\mathbf{b}}}{\partial t} = \boldsymbol{\nabla} \times \left(\tilde{\mathbf{v}} \times \tilde{\mathbf{B}} - \eta\tilde{\mathbf{j}} \right), \tag{4.1c}$$

$$\frac{\partial h}{\partial t} = -\boldsymbol{\nabla} \cdot (h\tilde{\mathbf{v}}) + \frac{\gamma - 1}{\gamma} h^{1-\gamma} \eta \tilde{\mathbf{j}}^2, \tag{4.1d}$$

$$\tilde{\mathbf{j}} = \boldsymbol{\nabla} \times \tilde{\mathbf{B}}, \tag{4.1e}$$

where $h = (\tilde{p}/2)^{1/\gamma}$, $\gamma = 5/3$, and all the quantities are dimensionless denoted using a tilde. The parameters are made dimensionless by normalising length scales to the half width $L_0/2$ of the initial shear-layer thickness which is user defined. The number density and magnetic field are normalised by user defined parameters, the average number density, n_0, and the average magnetic field, $\mathbf{B_0}$. After this, the other normalisation parameters are determined through physical quantities: the pressure parameter is defined from the magnetic pressure, $p_0 = B_0^2/2\mu_0$, the velocity parameter is defined from the Alfvén speed, $v_0 = B_0/\sqrt{\mu_0 n_0}$ and timescales are normalised by the Alfvén time, $t_0 = L/v_0$.

The simulation is initialised with a one-dimensional transition layer with a flow shear at $x = 0$ which separates the two different plasma regions and is supposed to represent the magnetopause. This is imposed by initially setting the $x-$profile of the following parameters:

$$\mathbf{B}_0(x) = \frac{1}{2}(B_{z\,sh} + B_{z\,sp}) + \frac{1}{2}(B_{z\,sh} - B_{z\,sp}) \tanh\left(\frac{x}{L_0}\right)\hat{\mathbf{z}}, \tag{4.2a}$$

$$n_0(x) = \frac{1}{2}(n_{sh} + n_{sp}) + \frac{1}{2}(n_{sh} - n_{sp}) \tanh\left(\frac{x}{L_0}\right), \tag{4.2b}$$

$$\mathbf{v}_0(x) = \frac{1}{2}\tanh(x/L_0)\hat{\mathbf{y}}, \tag{4.2c}$$

$$P_0(x) = P_{sh} + \left(B_{z\,sh}^2 - B_z^2(x)\right)/2\mu_0. \tag{4.2d}$$

This transition layer is only initially imposed with characteristic thickness of L_0 and maintains the total force balance across the sheared flow layer (i.e., the sum of the thermal pressure and magnetic pressure is constant). The KHI is triggered by a velocity perturbation localised in the vicinity of the equatorial plane (i.e., $z = 0$), which is given by $\mathbf{v} = \nabla\Phi(x, y) \times \mathbf{e}_z f(z)$. Here, the stream function is $\Phi(x, y) = \delta v \cos(k_y y) \cosh^{-2} \sec(x/l_x)$, the normal scale of the perturbation is $l_x = 2L_0$, the KH wave number is $k_y = \pi/L_y$, the amplitude of the velocity perturbation is $\delta v = V_{A0}/20$, and the localisation function $f(z)$ is given by $f(z) = 0.5\{\tanh[(z + z_d)/L_0 D_z] - \tanh[(z - z_d)/L_0 D_z]\}$, where $z_d = 20L_0$, and $D_z = 3$. The boundary conditions along the y-direction are periodic. Along the x-direction, the boundaries are closed, in which $v_x = 0$ and $\partial_x = 0$ for the rest of the quantities. To maintain the top boundary from the perturbation, an artificial friction term $-\nu(z)(\mathbf{v} - \mathbf{v_0})$ is applied to the right-hand side of the momentum equation in the simulation (Ma et al. 2017). Here, $\mathbf{v_0}$ is the unperturbed bulk velocity, which also represents the solar wind or ionosphere speed. The friction term tends to force the plasma to move at its initial velocity, or equivalently it absorbs perturbations, maintaining the initial boundary layer away from the equatorial plane. The friction coefficient is given by $\nu(z) = 0.5\{2 - \tanh[(z + z_\nu)/L_0 D_\nu] + \tanh[(z - z_\nu)/L_0 D_\nu]\}$, $z_\nu = 30L_0$, and $D_\nu = 3$, which has been switched on only near the top and bottom boundaries (Ma et al. 2017; Ma et al. 2021).

Once initialised, the KHI is then let to numerically evolve by time-stepping explicitly through Equations 4.1a-e solving them using a leap-frog scheme in a Cartesian coordinate system. This means the numerical algorithm used to solve these equations is based off of a discrete approximation. Leap-frog integration works similar to that of Euler method, but instead of being derived from the forward difference differentiation method, leap-frog integration uses the central difference method. The term leap-frog comes from how the solver uses the derivative to 'jump' over the point being evaluated.

The size of the time-step is limited by the Courant-Freidrichs-Lewy (CFL) condition (Courant et al. 1928) which is necessary for convergence. The CFL condition essentially imposes that the time-step must be sufficiently small such that the fastest moving fluid/wave does not move further than one grid cell in one time-step. This means that the time-step is limited by both the grid cell size and the maximum flow speed plus the characteristic speed of the fastest wave, which in MHD is

the flow speed plus the fast magnetosonic wave.

4.2 Global Simulation

Gorgon is a three-dimensional Eulerian resistive MHD code originally developed to simulate dense, collisional laboratory plasmas (e.g. Chittenden et al. 2004; Ciardi et al. 2007). Since then, Mejnertsen (2018) adapted the existing MHD and hydrodynamic solvers to simulate planetary magnetospheres, studying both Neptune (Mejnertsen et al. 2016) and Earth (Mejnertsen et al. 2018). Eggington (2021) then extended the code by coupling the inner-boundary to a thin-shell ionosphere model to allow for studies into dipole tilt effects (Eggington et al. 2020), and large-scale magnetic reconnection at Earth (Eggington et al. 2022a; Eggington et al. 2022b). The version of the code used in this thesis is identical to that described in Eggington (2021) meaning that the following description is largely derived from there and further details can be found there.

The Gorgon MHD code employs a fully explicit, Eulerian formulation of the semi-conservative MHD equations, solved on a staggered Yee grid (Yee 1966) using finite volume methods. The different parameters calculation location on the staggered Yee grid can be seen in Figure 4.1. Using a staggered Yee grid means that not every parameter is calculated at the same location. The magnetic vector potential, electric field, and the current density are all calculated on the cell edge centres; the density, pressure, and energies at the cell centre, and the magnetic field at the centre of the cell faces. The equations are solved in the following conservative form (Ciardi et al. 2007):

$$\frac{\partial \rho}{\partial t} + \boldsymbol{\nabla} \cdot (\rho \mathbf{v}) = 0, \tag{4.3a}$$

$$\frac{\partial}{\partial t}(\rho \mathbf{v}) + \boldsymbol{\nabla} \cdot (\rho \mathbf{v}\mathbf{v}) = -\boldsymbol{\nabla}(p_i + p_e) + \mathbf{J} \times \mathbf{B}, \tag{4.3b}$$

$$\frac{\partial \epsilon_p}{\partial t} + \boldsymbol{\nabla} \cdot (\epsilon_p \mathbf{v}) = -p_p \boldsymbol{\nabla} \cdot \mathbf{v} - \Delta_{pe}, \tag{4.3c}$$

$$\frac{\partial \epsilon_e}{\partial t} + \boldsymbol{\nabla} \cdot (\epsilon_e \mathbf{v}) = -p_e \boldsymbol{\nabla} \cdot \mathbf{v} + \eta \mid \mathbf{J} \mid^2 + \Delta_{pe}, \tag{4.3d}$$

$$\text{where} \quad \eta \mathbf{J} = -\frac{\partial \mathbf{A}}{\partial t} + \mathbf{v} \times \mathbf{B}. \tag{4.3e}$$

Gorgon is distinguished from other widely used global magnetospheric MHD codes (e.g. Gordeev et al. 2013; Tóth et al. 2005) as it provides the extended ideal MHD capabilities of electron-ion

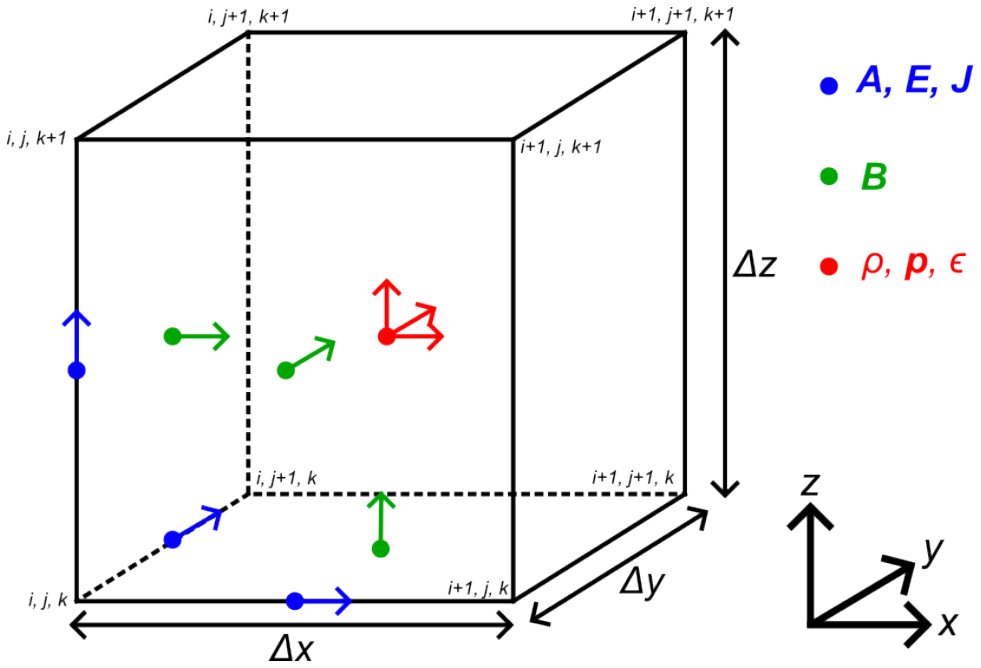


Figure 4.1: An illustrated diagram of the staggered Yee grid used in the Gorgon simulation. Figure inspired by (Eggington 2021).

energy exchange, Δ_{pe}. This is set to negligibly small when applying the code to space plasmas giving an ideal MHD description.

As well as this, Gorgon uses separate energy equations for ion energy, ϵ_i, and electron energy, ϵ_e, while treating the plasma as a single fluid thus allowing for the calculation of independent ion and electron temperatures for the study of particle acceleration. Moreover, the energy equations allow for complex equations of state including the effects of kinetic energy exchanges in collisions as well as Ohmic heating. However, the reason the code is only semi-conservative is that only the internal energy is explicitly conserved meaning that changes in magnetic and kinetic energies are not. However the total energy is typically conserved within 10% (Ciardi et al. 2007). Finally, a divergence-free magnetic field is realised by using the vector potential, $\mathbf{A}$. As $\mathbf{B} = \boldsymbol{\nabla} \times \mathbf{A}$ and since $\boldsymbol{\nabla} \cdot (\boldsymbol{\nabla} \times \mathbf{A}) \equiv 0$, Gorgon simulations cannot mathematically contain a diverging magnetic field. This is further enforced, as will be shown later, through the use of a Yee grid.

The size of δt in Gorgon is limited by the CFL condition (Courant et al. 1928) while also requiring the time-step to be smaller than 1. Each time-step is broken into three processes: a magnetic solver, a hydrodynamic solver, and the inner ionosphere. The magnetic solver primarily depends on the magnetic vector potential $\mathbf{A}$. Gorgon uses a split dipole approximation such that $\mathbf{B} = \mathbf{B}_{\text{Dipole}} + \mathbf{B}_1$,

where the magnetic vector potential defines $\mathbf{B}_1 = \boldsymbol{\nabla} \times \mathbf{A}$. By doing this, the divergence of the magnetic field, $\boldsymbol{\nabla} \cdot \mathbf{B}$, remains null to machine precision as the large gradients near the inner-boundary from $\mathbf{B}_{\text{Dipole}}$ are removed as $|\mathbf{B}_{\text{Dipole}}| \sim 1/r^3$. This also means that the current density vector can be calculated using $\mu_0 \mathbf{J} = \boldsymbol{\nabla} \times \mathbf{B}_1$ as a dipole field is current-free removing numerical error.

The gauge used in Gorgon is the Weyl gauge which defines the magnetic potential such that

$$-\frac{\partial \mathbf{A}}{\partial t} = \mathbf{E} = \underbrace{\mathbf{E}_{\text{res}}}_{\eta \mathbf{J}} + \underbrace{\mathbf{E}_{\text{adv}}}_{-\mathbf{v} \times \mathbf{B}} . \tag{4.4}$$

E_{adv} is therefore the flux of the cell-averaged magnetic field across the cell faces. Once this is calculated, $\mathbf{A}$ is updated by an Euler method which is a first-order numerical method. Once the the fields are updated, they can then be advected by using an Euler scheme to solve the diffusive part of the induction equation (Equation 2.14d). After this, the resistive diffusion of the fields takes place. The resistive diffusion of the fields is switched off in this version, for details on it please see Mejnertsen et al. (2016) and Jennings (2006). Now that the electromagnetic fields are all advected, the plasma needs to be advected.

The hydrodynamic solver works by evolving the plasma based on how it is accelerated, expanded, and heated from pressure and electromagnetic forces. This is done by utilising a Lagrangian-remap scheme which first evolves the fluid quantities based on the pressure and magnetic forces, a Lagrangian approach, and then advects this evolved fluid by 'remapping' it onto the Eulerian grid (Eggington 2021). The Lagrangian step involves solving Equations 4.3b-4.3d in the absence of $(\mathbf{v} \cdot \boldsymbol{\nabla}) \rho \mathbf{v}$, and $\nabla \cdot (\epsilon_{p,e} \mathbf{v})$, by using a second order Runge-Kutta predictor-corrector scheme (Benson 1992). This scheme works by calculating the field and plasma properties at a half time-step. Then, by using the forces and adiabatic heating at the half time-step, the plasma properties at the full time-step can be integrated for from the initial time-step. This makes the simulation calculate the fields using a first-order in time method, and the plasma using a second-order in time method. The remapping occurs when the plasma is advected by a third-order in space flux conservation Monotonic Upstream-centered Scheme for Conservation Laws (MUSCL) Van Leer advection scheme (Van Leer 1977).

During the Lagrangian-remapping, the fluxes at the cell boundaries are conserved. But as

mentioned previously, the kinetic energy is not explicitly conserved meaning that any issues with anomalous kinetic energy changes are exacerbated in regions where a shock is present. This is because the advection schemes change to lower orders near shocks to reduce numerical effects. Like other MHD codes, Gorgon uses an artificial viscosity in shocks to decelerate and heat the plasma while also reducing numerical overshoots and anomalous downstream oscillations (Arber et al. 2001). The artificial viscosity used in Gorgon is a modified von Neumann which works by adding an additional viscous 'pressure', P_v, during the Lagrangian step and is applied anywhere a sufficient velocity jump between cells is present (Benson 1992). The modifications are that the pressure is instead defined by using a Wilkins viscosity (Wilkins 1980) such that

$$P_v = c_1 \rho c_{ms} |\Delta \mathbf{v}| + c_2 \rho c_{ms} |\Delta \mathbf{v}|^2, \tag{4.5}$$

where c_1 and c_2 are dimensionless coefficients with a determined value. Further modifications were made by using a Christensen flux-limited viscosity (Benson 1992) to calculate the $\Delta \mathbf{v}$ to higher order while also effectively 'switching off' the viscosity in regions with smooth solutions. Effectively what these viscosities do is spread the shock over multiple grid cells, allowing the shock to be resolved.

The final component to the Gorgon solver is the inner-boundary ionosphere model. This model uses an electrostatic thin conducting shell approximation with height-integrated conductivities to take magnetospheric field-aligned currents at the inner-boundary as an input, scale them according to the dipole due to converging flux tubes, map them onto the ionosphere, solve for an ionospheric electric potential, and then map and scale the ionospheric potential's response back onto the inner-boundary's surface. The inner-boundary that maps to the ionosphere can be placed at any height, in this thesis the height was set at $4\,R_E$. The model does this using current continuity by solving for the electric potential, ψ, on the ionosphere given a field-aligned current distribution, $j_{\parallel}$, mapped-down from the ionosphere defined by

$$j_{\parallel} = \boldsymbol{\nabla} \cdot (\boldsymbol{\Sigma} \cdot \boldsymbol{\nabla} \psi), \tag{4.6}$$

where $\mathbf{\Sigma}$ is the conductance tensor defined by

$$\mathbf{\Sigma} = \begin{pmatrix} \Sigma_P/\cos(\delta) & \Sigma_H \\ -\Sigma_H & \Sigma_P \cos(\delta) \end{pmatrix}, \tag{4.7}$$

where Σ_P and Σ_H are the height-integrated conductivities of the Pederson and Hall currents, and δ is the angle between the radial direction and the unit dipole magnetic field. By then expanding Equation 4.6 using Equation 4.7 a set of partial differential equations can be obtained which is then solved using a central finite differencing method (King et al. 2003) on a regular two-dimension spherical grid using a successive over-relaxation method.

Finally, the simulation initialisation and boundary conditions can be discussed. Figure 4.2 illustrates the Gorgon set up. All the simulation outer-boundaries are free-flow meaning that the plasma leaves the simulation domain except for the sunward inflow boundary. The solar wind inflow boundary allows for the inflowing solar wind density, velocity, temperature, and magnetic field to be defined; it is the primary source of all the plasma within the simulation.

Inside the inner-boundary, close to the planet, there is a defined plasma density, temperature, and velocity. Due to this, the MHD equations are not solved in this region but the cells just outside the boundary are updated based on the inner-boundary's plasma and field meaning that a colder, more dense plasma forms close to the planet resembling a plasmasphere. Any plasma that flows into the inner-boundary region is overwritten by the defined values meaning it is essentially removed.

Previous iterations of the Gorgon code were shown to perform just as well as other global magnetospheric codes when benchmarked using a method described in Gordeev et al. 2015 (Mejnertsen 2018). The ionosphere has been benchmarked by comparing the Gorgon predicted field aligned currents and potential patterns in the ionosphere to another Global MHD code driven by identical solar wind conditions (Merkin and Lyon 2010; Eggington 2021).

4.3 Reconnection in an MHD Simulation

A final remark is needed in this section regarding the presence of collisionless magnetic reconnection in MHD simulations. Magnetic reconnection is a process which occurs when the frozen-in flux

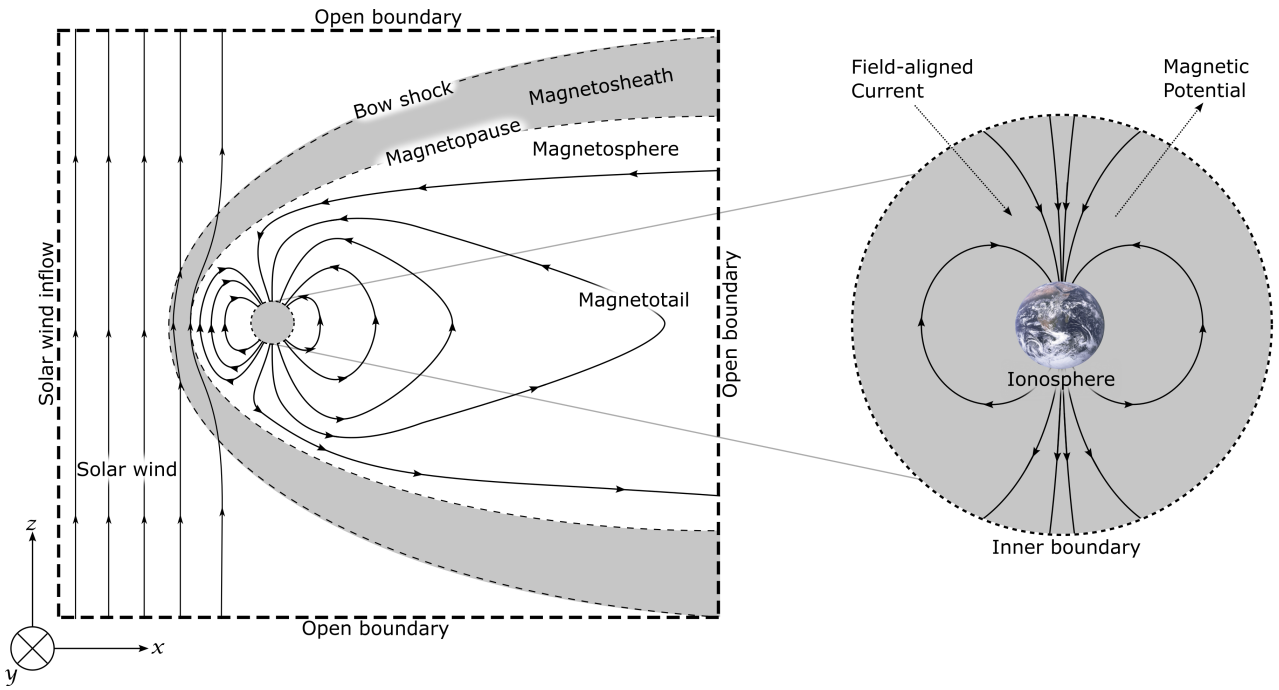


Figure 4.2: An illustrated diagram of the Gorgon simulation set-up describing the boundary conditions. Figure inspired by (Eggington 2021).

assumption breaks down meaning that the magnetic field topology of the plasma can change. In MHD simulations, the accommodation of magnetic field diffusion is not captured by the equations being solved, as it is a kinetic scale processes (Pontin and Priest 2022). Instead, MHD simulations approximate the magnetic field diffusion in two ways: numerical diffusion (e.g. Laitinen et al. 2006) and artificial resistive diffusion (e.g. Pérez-Coll Jiménez et al. 2022).

Resistivity describes how much the fields are allowed to diffuse through the plasma meaning that an increased resistivity allows for more field diffusion. Some global MHD simulations used include local artificial resistivity in regions where reconnection is desired to encourage the likelihood of reconnection taking place in these regions (e.g. Arnold et al. 2023).

Numerical diffusion is a process where features in a numerical simulation 'spread out' more than they would in reality and is caused by continuous differential equations being solved on a discrete grid using finite-differencing methods. An example of this could be trying to advect a fluid parcel diagonally on a Cartesian grid: as this cannot happen, the fluid parcel would be stepped in vertical and horizontal directions instead of the desired diagonal direction, thus causing it to spread more than it would have done in a continuous system. This is ironic as these supposedly simplifying approximations actually cause the MHD system to be more diffusive and complicated than the physics

would otherwise dictate. When numerical diffusion occurs on the field it is often referred to as numerical resistivity, and when it occurs on the momentum it is known as numerical viscosity. It is this numerical resistivity which allows for the field to diffuse through the plasma and for reconnection to take place in an MHD simulation. Numerical diffusion can be improved by using higher-order schemes and higher-resolution grids, but it can never be completely eliminated from the numerics.

CHAPTER 5

Helmholtz Decomposition

Throughout this thesis, the Helmholtz decomposition is used meaning that is important to introduce and explain the methods used to calculate it. The Helmholtz decomposition in three-dimensions was first described by George Stokes in 1849 for the purpose of diffraction theory (Stokes 2009a). Nearly ten years later Hermann von Helmholtz (1858) published works on hydrodynamics which included a version of the theory. The decomposition theorem is an important tool used throughout vector calculus resulting in the theorem also being coined the 'fundamental theorem of vector calculus'. The theorem states that any sufficiently smooth vector field which exists in the domain V and is twice continuously differentiable inside V, can be decomposed into the sum of a curl-free vector field, and divergence-free vector field.

This can be proved in three dimensions at any point $\mathbf{r} \in V$ by using a scalar potential field, $P(\mathbf{r})$, and a vector potential field, $\mathbf{U}(\mathbf{r})$. Let $\boldsymbol{\tau}$ be a vector field which is sufficiently smooth, exists in the domain V, and is twice continuously differentiable inside V. The theorem can be then be derived by stipulating that the curl and divergence of the vector function $\boldsymbol{\tau}(\mathbf{r})$ exists and is known both inside the domain and on its surface. From this, any point in the field can be found using a Dirac delta

function meaning that $\boldsymbol{\tau}$ can be expanded into the integral

$$\boldsymbol{\tau}(\mathbf{r}) = \int_V \boldsymbol{\tau}(\mathbf{r}')\,\delta^3(\mathbf{r}-\mathbf{r}')\mathrm{d}V'. \tag{5.1}$$

Using the definition of the Dirac delta in three-dimensional space:

$$\delta^3(\mathbf{r}-\mathbf{r}') = -\frac{1}{4\pi}\boldsymbol{\nabla}^2\frac{1}{|\mathbf{r}-\mathbf{r}'|}\,, \tag{5.2}$$

where $\boldsymbol{\nabla}^2 := \boldsymbol{\nabla}\cdot\boldsymbol{\nabla}$ is the Laplace operator, it can be shown that

$$\boldsymbol{\tau}(\mathbf{r}) = -\frac{1}{4\pi}\boldsymbol{\nabla}^2\int_V \frac{\boldsymbol{\tau}(\mathbf{r}')}{|\mathbf{r}-\mathbf{r}'|}\mathrm{d}V'. \tag{5.3}$$

Applying the definition of the vector Laplacian: $\boldsymbol{\nabla}^2\mathbf{F} = \boldsymbol{\nabla}(\boldsymbol{\nabla}\cdot\mathbf{F}) - \boldsymbol{\nabla}\times(\boldsymbol{\nabla}\times\mathbf{F})$, gives

$$\boldsymbol{\tau}(\mathbf{r}) = -\frac{1}{4\pi}\left[\boldsymbol{\nabla}\left(\boldsymbol{\nabla}\cdot\int_V\frac{\boldsymbol{\tau}(\mathbf{r}')}{|\mathbf{r}-\mathbf{r}'|}\mathrm{d}V'\right) - \boldsymbol{\nabla}\times\left(\boldsymbol{\nabla}\times\int_V\frac{\boldsymbol{\tau}(\mathbf{r}')}{|\mathbf{r}-\mathbf{r}'|}\mathrm{d}V'\right)\right] \tag{5.4a}$$

$$= -\frac{1}{4\pi}\left[\boldsymbol{\nabla}\left(\int_V\boldsymbol{\tau}(\mathbf{r}')\cdot\boldsymbol{\nabla}\frac{1}{|\mathbf{r}-\mathbf{r}'|}\mathrm{d}V'\right) + \boldsymbol{\nabla}\times\left(\int_V\boldsymbol{\tau}(\mathbf{r}')\times\boldsymbol{\nabla}\frac{1}{|\mathbf{r}-\mathbf{r}'|}\mathrm{d}V'\right)\right]. \tag{5.4b}$$

Applying the linearity of function argument, $f(cx) = cf(x)$:

$$\boldsymbol{\nabla}\frac{1}{|\mathbf{r}-\mathbf{r}'|} = -\boldsymbol{\nabla}'\frac{1}{|\mathbf{r}-\mathbf{r}'|}, \tag{5.5}$$

gives

$$\boldsymbol{\tau}(\mathbf{r}) = -\frac{1}{4\pi}\left[-\boldsymbol{\nabla}\left(\int_V\boldsymbol{\tau}(\mathbf{r}')\cdot\boldsymbol{\nabla}'\frac{1}{|\mathbf{r}-\mathbf{r}'|}\mathrm{d}V'\right) - \boldsymbol{\nabla}\times\left(\int_V\boldsymbol{\tau}(\mathbf{r}')\times\boldsymbol{\nabla}'\frac{1}{|\mathbf{r}-\mathbf{r}'|}\mathrm{d}V'\right)\right]. \tag{5.6}$$

From here, the following vector identities are applied:

$$\mathbf{F}\cdot\boldsymbol{\nabla}\psi = -\psi(\boldsymbol{\nabla}\cdot\mathbf{F}) + \boldsymbol{\nabla}\cdot(\psi\mathbf{F}) \tag{5.7a}$$

$$\mathbf{F}\times\boldsymbol{\nabla}\psi = \psi(\boldsymbol{\nabla}\times\mathbf{F}) - \boldsymbol{\nabla}\times(\psi\mathbf{F}) \tag{5.7b}$$

which gives

$$\begin{aligned}\boldsymbol{\tau}(\mathbf{r}) = -\frac{1}{4\pi}\Bigg[&- \boldsymbol{\nabla}\left(-\int_V \frac{\boldsymbol{\nabla}'\cdot\boldsymbol{\tau}(\mathbf{r}')}{|\mathbf{r}-\mathbf{r}'|}\mathrm{d}V' + \int_V \boldsymbol{\nabla}'\cdot\frac{\boldsymbol{\tau}(\mathbf{r}')}{|\mathbf{r}-\mathbf{r}'|}\mathrm{d}V'\right) \\ &- \boldsymbol{\nabla}\times\left(\int_V \frac{\boldsymbol{\nabla}'\times\boldsymbol{\tau}(\mathbf{r}')}{|\mathbf{r}-\mathbf{r}'|}\mathrm{d}V' - \int_V \boldsymbol{\nabla}'\times\frac{\boldsymbol{\tau}(\mathbf{r}')}{|\mathbf{r}-\mathbf{r}'|}\mathrm{d}V'\right)\Bigg].\end{aligned} \tag{5.8}$$

By virtue of Gauss's (or Ostrogradsky's depending on preference) divergence theorem:

$$\int_V (\boldsymbol{\nabla}\cdot\mathbf{F})\,dV = \oint (\mathbf{F}\cdot\hat{\mathbf{n}})\,dS, \tag{5.9}$$

where $\hat{\mathbf{n}}$ is the outward pointing surface normal, the above can finally be rewritten as

$$\begin{aligned}\boldsymbol{\tau}(\mathbf{r}) = &- \boldsymbol{\nabla}\underbrace{\left(\frac{1}{4\pi}\int_V \frac{\boldsymbol{\nabla}'\cdot\boldsymbol{\tau}(\mathbf{r}')}{|\mathbf{r}-\mathbf{r}'|}\mathrm{d}V' - \frac{1}{4\pi}\oint_S \hat{\mathbf{n}}'\cdot\frac{\boldsymbol{\tau}(\mathbf{r}')}{|\mathbf{r}-\mathbf{r}'|}\mathrm{d}S'\right)}_{P(\mathbf{r})} \\ &+ \boldsymbol{\nabla}\times\underbrace{\left(\frac{1}{4\pi}\int_V \frac{\boldsymbol{\nabla}'\times\boldsymbol{\tau}(\mathbf{r}')}{|\mathbf{r}-\mathbf{r}'|}\mathrm{d}V' - \frac{1}{4\pi}\oint_S \hat{\mathbf{n}}'\times\frac{\boldsymbol{\tau}(\mathbf{r}')}{|\mathbf{r}-\mathbf{r}'|}\mathrm{d}S'\right)}_{\mathbf{U}(\mathbf{r})}\end{aligned} \tag{5.10a}$$

$$= -\boldsymbol{\nabla}P + \boldsymbol{\nabla}\times\mathbf{U}, \tag{5.10b}$$

where S is the enclosing surface of V.

Axiomatically, P and $\mathbf{U}$ are not unique. Any arbitrary constant scalar can be added to the scalar field P to provide the same distinct irrotational solution. Similarly, any arbitrary gradient field can be added to the vector field $\mathbf{U}$ to yield the same rotational field.

This approach is computationally demanding as it requires a sum over all paris of points meaning a different approach is needed if the Helmholtz decomposition can be computed on large data sets e.g. a parameter in a global MHD simulation. The following sections will explore two different methods used to compute the Helmholtz decomposition in this Thesis.

5.1 Fourier Method

Computationally, it is more efficient to perform the Helmholtz decomposition in Fourier space

$$\boldsymbol{\tau} = \int_V \hat{\boldsymbol{\tau}}(\mathbf{k}) e^{i\mathbf{k}\cdot\mathbf{r}} dV_k, \tag{5.11}$$

where $\hat{\boldsymbol{\tau}}$ denotes the Fourier Transform of the vector function $\boldsymbol{\tau}(\mathbf{r})$. In an unbounded domain this requires that the vector function decays faster than $1/r$. By splitting the vector function's Fourier transform $\hat{\boldsymbol{\tau}}(\mathbf{k})$ into its components parallel and perpendicular to $\mathbf{k}$,

$$\hat{\boldsymbol{\tau}}_{\parallel}(\mathbf{k}) = \frac{\mathbf{k}\cdot\hat{\boldsymbol{\tau}}(\mathbf{k})}{|\mathbf{k}|^2}\mathbf{k}, \tag{5.12}$$

$$\hat{\boldsymbol{\tau}}_{\perp}(\mathbf{k}) = -\mathbf{k}\times\frac{\mathbf{k}\times\hat{\boldsymbol{\tau}}(\mathbf{k})}{|\mathbf{k}|^2}, \tag{5.13}$$

it can be seen that

$$\hat{\boldsymbol{\tau}}(\mathbf{k}) = \hat{\boldsymbol{\tau}}_{\parallel}(\mathbf{k}) + \hat{\boldsymbol{\tau}}_{\perp}(\mathbf{k}) \tag{5.14a}$$

$$= -i\mathbf{k}\frac{i\mathbf{k}\cdot\hat{\boldsymbol{\tau}}(\mathbf{k})}{|\mathbf{k}|^2} + i\mathbf{k}\times\frac{i\mathbf{k}\times\hat{\boldsymbol{\tau}}(\mathbf{k})}{|\mathbf{k}|^2} \tag{5.14b}$$

$$= -i\mathbf{k}\hat{P}(\mathbf{k}) + i\mathbf{k}\times\hat{\mathbf{U}}(\mathbf{k}) \tag{5.14c}$$

where the Fourier Transforms of the scalar field P and the vector field $\mathbf{U}$ are defined as

$$\hat{P}(\mathbf{k}) = i\frac{\mathbf{k}\cdot\hat{\boldsymbol{\tau}}(\mathbf{k})}{|\mathbf{k}|^2}, \tag{5.15}$$

$$\hat{\mathbf{U}}(\mathbf{k}) = i\frac{\mathbf{k}\times\hat{\boldsymbol{\tau}}(\mathbf{k})}{|\mathbf{k}|^2}. \tag{5.16}$$

Substituting into Equation 5.11 demonstrates this provides the Helmholtz decomposition

$$\boldsymbol{\tau} = \underbrace{\int_V -i\mathbf{k}\hat{P}(\mathbf{k})e^{i\mathbf{k}\cdot\mathbf{r}}dV_k}_{-\boldsymbol{\nabla}P} + \underbrace{\int_V i\mathbf{k}\times\hat{\mathbf{U}}(\mathbf{k})e^{i\mathbf{k}\cdot\mathbf{r}}dV_k}_{\boldsymbol{\nabla}\times\mathbf{U}}, \tag{5.17}$$

since in Fourier space $\nabla \rightarrow i\mathbf{k}$. This approach assumes an infinite volume hence it neglects the surface terms.

Computationally implementing this method requires a discrete Fourier transform which requires periodic boundary assumptions for its application to be valid. If this is the case, then the Fourier method to calculate the Helmholtz decomposition should be exact. This can be seen in the example below.

5.1.1 Example

Consider the Gaussian potential field

$$\phi = \frac{a}{(2\pi)^{\frac{3}{2}}\sigma^3} \exp\left(-\frac{x^2+y^2+z^2}{2\sigma^2}\right) \tag{5.18}$$

where $\sigma = 0.05$, $a = 3.1 \times 10^{12}$ has the exact solution of (Zou et al. 2021)

$$\psi = \frac{a}{4\pi} \frac{1}{\sqrt{x^2+y^2+z^2}} \text{erf}\left(\frac{\sqrt{x^2+y^2+z^2}}{\sqrt{2}\sigma}\right) \tag{5.19}$$

where erf is the error function.

Figure 5.1A-C shows slices at $z = 0$ of the analytically solved irrotational field, $\boldsymbol{\nabla}\phi$, the analytically solved rotational field, $\boldsymbol{\nabla} \times (0, 0, \phi)^T$, and how these fields can be combined to produce a total field, $\boldsymbol{\nabla}\phi + \boldsymbol{\nabla} \times (0, 0, \phi)^T$. Panel A shows a simple irrotational field which is diverging. Irrotational fields tend to look like sink (converging) or source (diverging) regions and tend to not have any flow which appears to be circulating. Panel B shows a simple rotational field which is seen to be circulating. Rotational fields tend to have circulating regions and lack any type of diverging/converging flow. Panel C shows how the combination of both rotational and irrotational fields can make a simple diverging and circulating flow.

Figure 5.1D-F shows slices at $z = 0$ of the irrotational, rotational,and total field calculated using the Fourier method outlined above by taking the total analytic field as an input. It is clear in these panels that there is no visible difference from the Fourier solution (D-F) and the analytic solutions (A-C).

Figure 5.1G-I shows slices at $z = 0$ of the error in the Fourier calculated irrotational, rotational, and total field calculated by subtracting the analytic solutions from the Fourier solutions. The error in the method is constrained to the edges of the box. The error arises because the method assumes that field drops to null at the boundary which is not true, as well as this it assumes that boundary has periodic conditions. Here we are testing the boundary assumptions and the maximum percentage error is on the order of 1% for both the irrotational and rotational solutions. The slight striping in the Cartesian directions is known as Gibbs phenomena and is a result of their being a discontinuity at the boundary which cannot be captured by a Fourier transform. Fortunately, when combined these edge effect errors cancel each other out, resulting in the method having an accuracy of the error in a distributive Fourier transform.

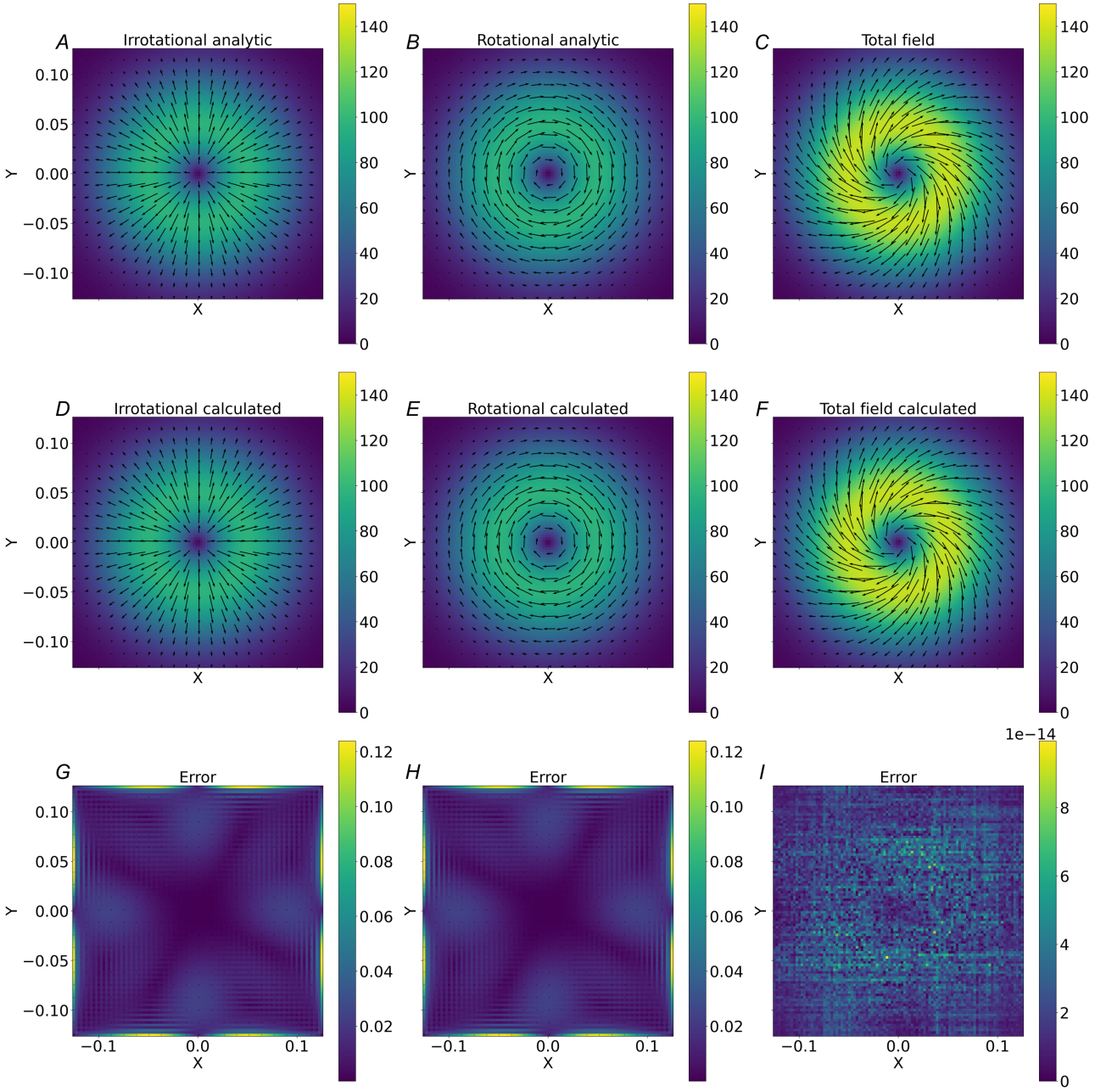


Figure 5.1: A $z = 0$ view of the analytic rotational field (Panel A), analytic irrotational field (Panel B), and analytic total field (Panel C) defined using Equation 5.19 as described in the text are shown in the first row. A $z = 0$ view of the calculated rotational field (Panel D), calculated irrotational field (Panel E), and calculated total field (Panel F) by decomposing the analytic total field using the Fourier method is shown in the second row. A $z = 0$ view of the error (Fourier − Analytic) of the calculated rotational field (Panel G), calculated irrotational field (Panel H), and calculated total field (Panel I) is shown in the final row. The magnitude of the fields is shown in colour with overlaid xy-plane only quivers n black; the arrow length also varies due to magnitude. Note their are no quivers plotted on the error.

The Fourier method is a reliable way to decompose the fields accurately as it provides an approximate free-space solution but it relies on assumptions which may not always be valid. Because

of this, another method is also needed which is valid on any and all boundary conditions.

5.2 Hockney-Eastwood Solver

A more widely applicable way to solve the Helmholtz decomposition is by using a Hockney-Eastwood solver (Hockney and Eastwood 2021) to solve for P and $\mathbf{U}$ in Equation 6.3b. A simple example to explain how the technique works is shown below.

Consider Poisson's equation for the electrostatic potential, ϕ, due to charge density, ρ,

$$\boldsymbol{\nabla}^2\phi = -\rho \tag{5.20}$$

with free-space boundary conditions meaning that the electric field solution $\mathbf{E} = -\nabla\phi$ vanishes at infinity. Begin by defining a three-dimensional uniform mesh grid (u, v, w) where there are n number of points in each direction and h is the spacing. Now define the Green's function as

$$\mathcal{G}_{u,v,w} = \frac{1}{4\pi h\sqrt{u^2+v^2+w^2}}\,, \tag{5.21a}$$

$$\tag{5.21b}$$

$$\mathcal{G}_{0,0,0} = 1\,. \tag{5.21c}$$

Assume free-space boundary conditions such that the potential at point (u, v, w) can always be written as the sum of contributions from all other point sources (u', v', w') which gives

$$\phi_{u,v,w} = \sum \rho_{u',v',w'}\,\mathcal{G}_{u-u',v-v',w-w'}\,. \tag{5.22}$$

Equation 5.22 writes the potential as the convolution of the Green's function with the charge density. As the convolution theorem states that the Fourier transform of a convolution is the product of the Fourier transforms of the quantities involved (Hockney and Eastwood 2021), Equation 5.22 can be rewritten as

$$\hat{\phi}_{k,l,m} = \hat{\mathcal{G}}_{k,l,m}\,\hat{\rho}_{k,l,m}, \tag{5.23}$$

where the circumflex denotes the Fourier transform and k, l, m are harmonic wave numbers.

Before the calculation can be performed, an extended zero-padded domain is needed to eliminate unphysical edge effects which arise from using a discrete Fourier based convolution, not a linear convolution. The extended domain has an extent of $2n-1$ and is null when $u > n$, $v > n$, or $w > n$. Figure 5.2 is a two-dimensional illustration of the extended domain which is only needed in the calculation and is discarded afterwards.

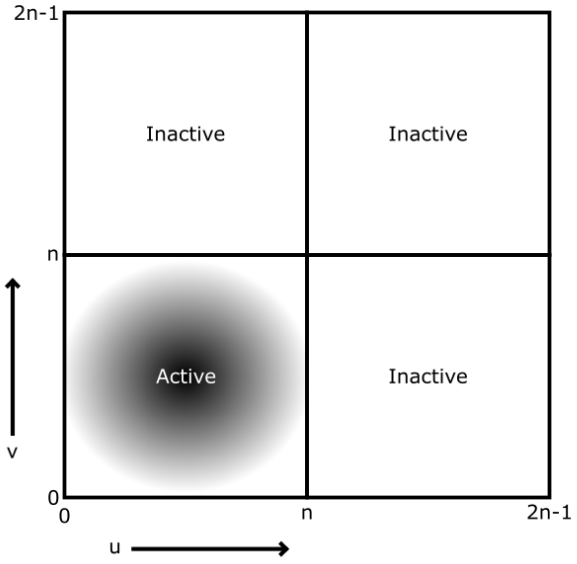


Figure 5.2: A two-dimensional example of the extended domain used by the Hockney-Eastwood solver. (Redrawn from Hockney and Eastwood 2021).

Now extending the problem to three-dimensions, the potential can be computed using the following equation (Zou et al. 2021):

$$\tilde{\phi} = h_x h_y h_z \, FFT^{-1} \left\{ FFT \left\{ \tilde{\rho} \right\} FFT \left\{ \tilde{\mathcal{G}} \right\} \right\} \tag{5.24}$$

where the tilde represents the quantity in the extended domain and FFT is the Fast Fourier Transform. ϕ is realised by truncating $\tilde{\phi}$ from the extended into the original domain.

It is possible to use this method to solve for the Helmholtz decomposition by generalising the Green's function solution to the Helmholtz decomposition of the vector function $\boldsymbol{\tau}(\mathbf{r})$, written in

Equation 6.3. By doing this it can be shown that

$$\phi(\mathbf{r}) = \int_V \left[\boldsymbol{\nabla}' \cdot \boldsymbol{\tau}\left(\mathbf{r}'\right)\right] \mathcal{G}\left(\mathbf{r}-\mathbf{r}'\right) \mathrm{d}V' - \oint_S \left[\hat{\mathbf{n}}' \cdot \boldsymbol{\tau}\left(\mathbf{r}'\right)\right] \mathcal{G}\left(\mathbf{r}-\mathbf{r}'\right) \mathrm{d}S', \tag{5.25a}$$

$$U_i(\mathbf{r}) = \int_V \left[\boldsymbol{\nabla}' \times \boldsymbol{\tau}\left(\mathbf{r}'\right)\right]_i \mathcal{G}\left(\mathbf{r}-\mathbf{r}'\right) \mathrm{d}V' - \oint_S \left[\hat{\mathbf{n}}' \times \boldsymbol{\tau}\left(\mathbf{r}'\right)\right]_i \mathcal{G}\left(\mathbf{r}-\mathbf{r}'\right) \mathrm{d}S', \tag{5.25b}$$

where, ϕ is the scalar field, U_i for $i = x, y, z$ is the vector potential, $\mathcal{G}$ is the Green's function, and $\boldsymbol{\tau}$ is the field being decomposed. It is now apparent that both the volume and surface integral of $\phi(\mathbf{r})$ and each component of $U_i(\mathbf{r})$ can be solved in the identical way as the charge distribution has been above.

5.2.1 Example

The Gaussian charge density:

$$\rho = \frac{Q}{(2\pi)^{\frac{3}{2}}\sigma^3\varepsilon_0} \exp\left(-\frac{x^2+y^2+z^2}{2\sigma^2}\right) \tag{5.26}$$

where $\sigma = 0.05$, $Q = 27.24$ nC, and $\varepsilon_0 = 8.85 \times 10^{-12}\,\mathrm{F\,m^{-1}}$ has the exact solution of (Zou et al. 2021)

$$\phi = \frac{Q}{4\pi\varepsilon_0} \frac{1}{\sqrt{x^2+y^2+z^2}} \mathrm{erf}\left(\frac{\sqrt{x^2+y^2+z^2}}{\sqrt{2}\sigma}\right) \tag{5.27}$$

where erf is the error function. By using this exact solution and comparing it with the Hockney-Eastwood solution, the solver error can be quantified.

Figure 5.3 shows the volume integral of the scalar potential (first term on the right-hand side of Equation 5.25a) calculated in the extended domain. By inspection is is clear why the extended domain is needed as without it the unwanted edge effects seen in the inactive domains would be present in the active domain. The patterns seen in the extended domain are due to an incorrect assumption of periodic boundary conditions which are implicit when using a Fourier transform. By discarding the extended domain, a comparison of the calculated and exact solutions can be made.

Figure 5.4 shows a comparison of the volume, surface, and complete (sum of the volume and surface) scalar potential against the error, $\phi_{\mathrm{Calculated}} - \phi_{\mathrm{Exact}}$, in the calculation. Comparing Figure 5.4 A, B, C shows that the volume integral term contributes the most to the total solution as well as

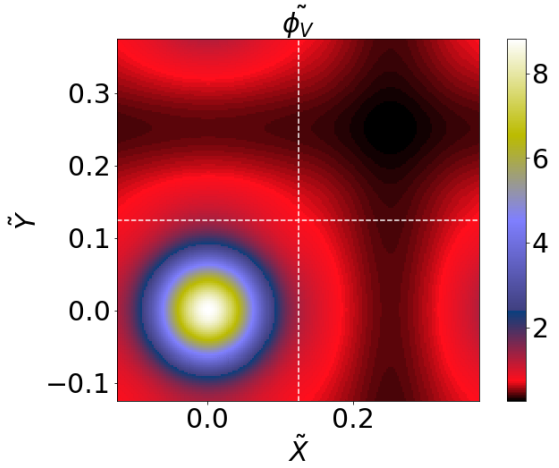


Figure 5.3: A two-dimensional $\tilde{X}\tilde{Y}$-slice at $\tilde{Z} = 0$ of the volume integral of the scalar potential defined in Equation 5.25a calculated in the extended domain using the Hockney-Eastwood solver.

showing that it approximates it well. Comparing Figure 5.4 B, D, F shows that the surface term makes up the majority of the error in the volume term and by including it in the complete calculation, the maximum error reduces from $\sim 11\%$ to $\sim 2\%$. Figure 5.4A,E indicates that the volume integral takes a more rectangular shape than a circular one which is likely an indication that the high power potential near the edges is being affected in the volume integral. As Figure 5.4C is more circular this suggests that including the surface integral helps this issue.

Figure 5.5A-C shows slices at $z = 0$ of the analytically solved irrotational field, $\boldsymbol{\nabla}\phi$, in panel A. The analytically solved rotational field, $\boldsymbol{\nabla} \times (0, 0, \phi)^T$, is shown in Panel B. The combined total field, $\boldsymbol{\nabla}\phi + \boldsymbol{\nabla} \times (0, 0, \phi)^T$, is shown in Panel C.

Figure 5.5D-F shows slices at $z = 0$ of the irrotational, rotational,and total field calculated using the Hockney-Eastwood method outlined above by taking the total analytic field as an input. A difference can be seen between the analytic and calculated panels at the centre of the edges where the calculated value drops to zero whereas the analytic solution does not. Furthermore by comparing the calculated total field to the analytic total field it can be seen that the calculated field is more square than the analytic field which is a result of the boundary shape.

Figure 5.5G-I shows slices at $z = 0$ of the error in the Hockney-Eastwood calculated irrotational, rotational, and total field calculated by subtracting the analytic solutions from the Hockney-Eastwood solutions. The error in the method is constrained to the edges of the box. The maximum percentage error is approximately 3% for the irrotational solution. The rotational solution is 3 times larger as

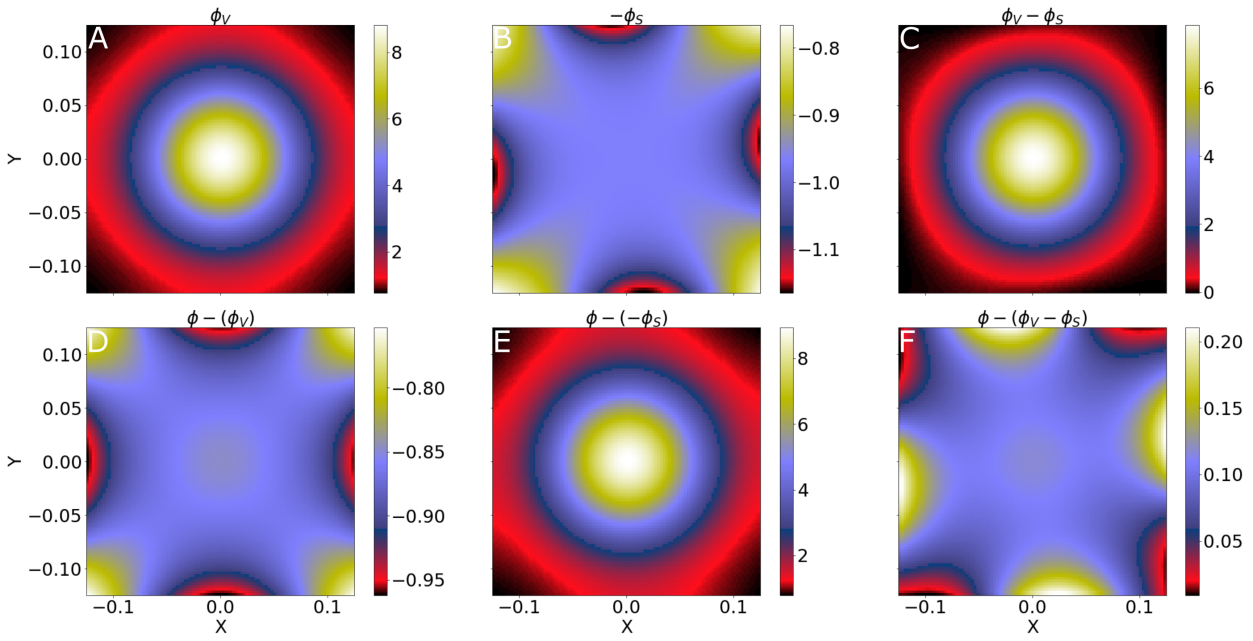


Figure 5.4: A two-dimensional xy-slice at $z = 0$ of the volume, surface, and complete (sum of the volume and surface) scalar potential as defined in Equation 5.25a calculated in the extended domain using the Hockney-Eastwood solver. The error, $\phi_{\text{Calculated}} - \phi_{\text{Exact}}$, in the calculation is shown beneath.

it uses the method a total of three times: one for each spatial direction. This causes a total error on the reconstructed field to be $\sim 12\%$ near the edges. However away from the edges the error is much smaller and also if a different field is used which does not have large values near the edges, the techniques error is much smaller.

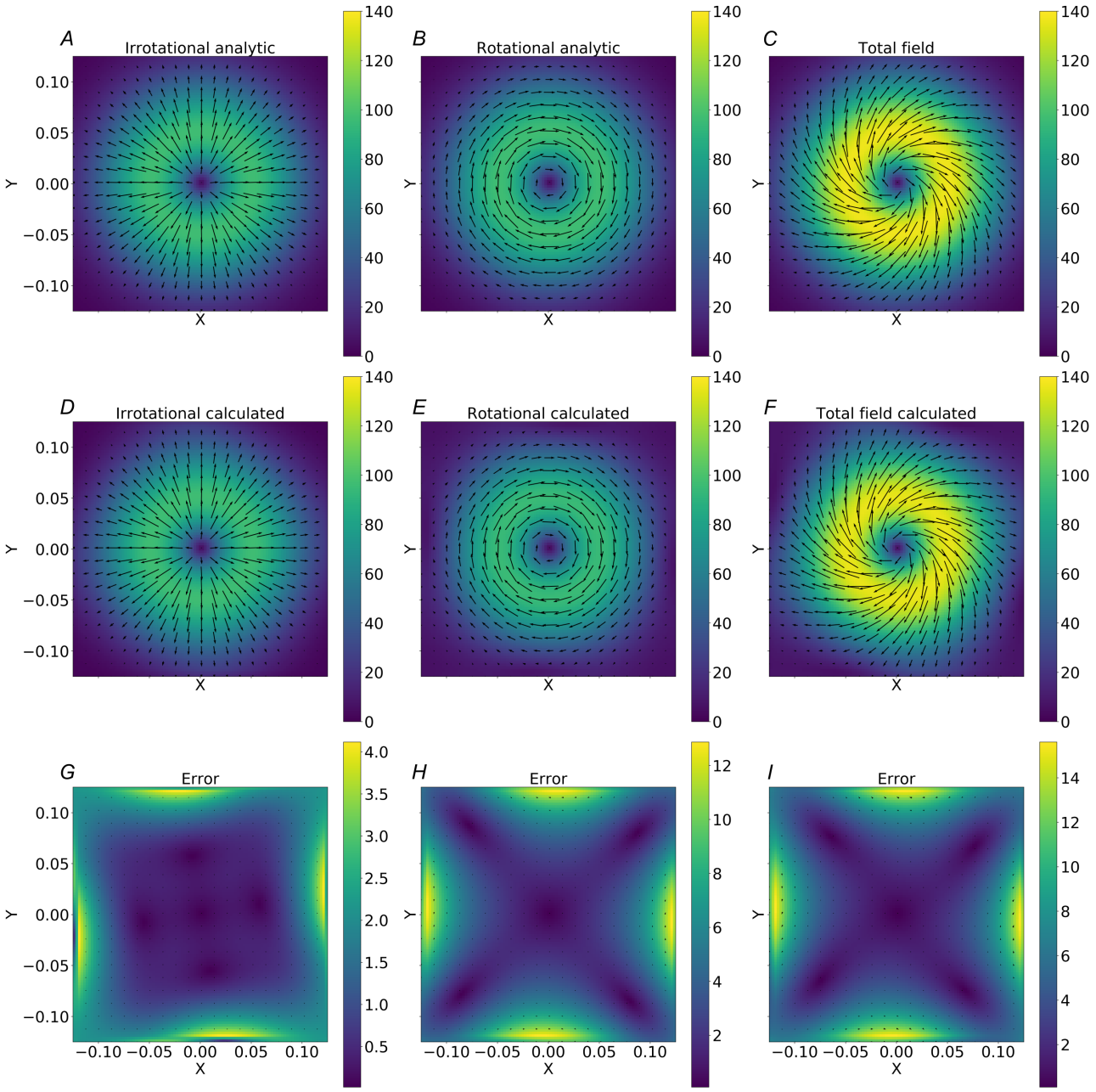


Figure 5.5: A $z = 0$ view of the analytic rotational field (Panel A), analytic irrotational field (Panel B), and analytic total field (Panel C) defined using Equation 5.19 as described in the text are shown in the first row. A $z = 0$ view of the calculated rotational field (Panel D), calculated irrotational field (Panel E), and calculated total field (Panel F) by decomposing the analytic total field using the Hockney-Eastwood method is shown in the second row. A $z = 0$ view of the error (Hockney-Eastwood − Analytic) of the calculated rotational field (Panel G), calculated irrotational field (Panel H), and calculated total field (Panel I) is shown in the final row. The magnitude of the fields is shown in colour with overlaid xy-plane only quivers n black; the arrow length also varies due to magnitude.

CHAPTER 6

Identifying Kelvin-Helmholtz Generated Vortices in Magnetised Fluids

Most of the work presented in the following chapter has been published in:
Kelly HM, Archer MO, Ma X, Nykyri K, Eastwood JP and Southwood DJ (2024) Identification of Kelvin-Helmholtz generated vortices in magnetised fluids. *Front. Astron. Space Sci.* 11:1431238. doi: 10.3389/fspas.2024.1431238

6.1 Introduction

The Kelvin-Helmholtz instability, as reviewed in Chapter 3, is an actively researched phenomenon which, through observations, has been shown to play a significant role in the viscous-like transfer of mass, momentum, and energy from the shocked solar wind into the magnetosphere. The KHI does this via the growth of MSW's and their coupled vortices. KH vortices are catalysts for secondary transfer processes making their identification both important and necessary. Despite being a pervasive phenomena, suitable MHD-valid detection methods for KH vortices are currently lacking. To overcome this, a novel MHD-valid vortex identification technique has been developed based on the well-established λ-family of hydrodynamic criteria summarised in Chapter 3.3.2. These techniques work by defining a vortex as a local minimum in some adapted pressure field. The following chapter

derives, explores, and validates a novel λ method for ideal MHD by defining a new MHD effective pressure field.

6.2 The λ Method for Ideal MHD

The λ-family of definitions all work by performing a second partial derivative test on some adapted pressure Hessian to find local pressure minima. By local pressure minima, one refers to a minima in a plane of the pressure field, not a three dimensional minima in the field. This is because some vortices only have a pressure minima in a plane perpendicular to the vortex axis rather than a three dimensional minima (e.g. Burgers vortex). In the case of hydrodynamics without any external forces, the only inviscid force acting on the fluid arises from thermal pressure gradients. Thus, for hydrodynamics, the thermal pressure is the field used and adapted by discarding any contributions which cause pressure minima without being associated with vortical flow, e.g. sink flow (Jeong and Hussain 1995). However, in MHD the plasma is also subject to magnetic pressure and magnetic tension forces. The total pressure generally used in ideal MHD is the sum of magnetic pressure, $P_{\text{mag}} = |\mathbf{B}|^2/(2\mu_0)$, and thermal pressure, $P_{\text{therm}} = nk_BT$. However this does not necessarily describe all the pressure-like forces on the plasma – those which can be expressed as an irrotational field $-(\boldsymbol{\nabla} P)$. The magnetic tension $\mathbf{B} \cdot \boldsymbol{\nabla}\mathbf{B}/\mu_0$ may also have a pressure-like part to it. One example of this is the magnetic dipole, which is a current- and force-free magnetic field. Since this exhibits magnetic pressure gradients, these must be completely cancelled by magnetic tension forces; thus tension can, in part, contribute to the total of pressure-like forces in ideal MHD. In an alternative case where current is induced, such as in a field aligned current, the magnetic tension will be a highly rotational field as stress is transmitted along the field. This highlights that in a dynamic environment such as KH vortices, the magnetic tension will be composed of both rotational and irrotational components, making the pressure-like tension force pertinent.

A Helmholtz decomposition can be used to find this pressure-like component of the magnetic tension. Applying the Helmholtz decomposition to the magnetic tension gives

$$\boldsymbol{\tau} = -\boldsymbol{\nabla} P_{\text{ten}} + \boldsymbol{\nabla} \times \mathbf{U} = \boldsymbol{\tau}_{\text{irr}} + \boldsymbol{\tau}_{\text{rot}}, \tag{6.1}$$

where P_{ten} is the pressure field associated with the irrotational part of the tension force and $\mathbf{U}$ is the vector potential field describing the rotational part to the tension. The Helmholtz decomposition allows for an effective total pressure field in MHD to be defined as the sum of thermal pressure, magnetic pressure, and the pressure-like part of the tension:

$$P_{\text{eff}} = nk_B T + \frac{B^2}{2\mu_0} + P_{\text{ten}} = P_{\text{therm}} + P_{\text{mag}} + P_{\text{ten}}. \tag{6.2}$$

A general solution to Equation 6.1 can be derived so that P_{ten} can be investigated. This is derived in Chapter 5 and provides the solution,

$$\begin{aligned} \boldsymbol{\tau}(\mathbf{r}) = &- \boldsymbol{\nabla} \underbrace{\left(\frac{1}{4\pi} \int_V \frac{\boldsymbol{\nabla}' \cdot \boldsymbol{\tau}(\mathbf{r}')}{|\mathbf{r} - \mathbf{r}'|} \mathrm{d}V' - \frac{1}{4\pi} \oint_S \hat{\mathbf{n}}' \cdot \frac{\boldsymbol{\tau}(\mathbf{r}')}{|\mathbf{r} - \mathbf{r}'|} \mathrm{d}S' \right)}_{P_{\text{ten}}(\mathbf{r})} \\ &+ \boldsymbol{\nabla} \times \underbrace{\left(\frac{1}{4\pi} \int_V \frac{\boldsymbol{\nabla}' \times \boldsymbol{\tau}(\mathbf{r}')}{|\mathbf{r} - \mathbf{r}'|} \mathrm{d}V' - \frac{1}{4\pi} \oint_S \hat{\mathbf{n}}' \times \frac{\boldsymbol{\tau}(\mathbf{r}')}{|\mathbf{r} - \mathbf{r}'|} \mathrm{d}S' \right)}_{\mathbf{U}(\mathbf{r})} \end{aligned} \tag{6.3a}$$

$$= -\boldsymbol{\nabla} P_{\text{ten}} + \boldsymbol{\nabla} \times \mathbf{U}, \tag{6.3b}$$

where S is the enclosing surface of V and $\hat{\mathbf{n}}'$ is the outward pointing surface normal. Recall that the decomposition is not unique. As the effective pressure itself is not directly required in λ-family methods, only its unique Hessian, this gauge freedom is unimportant here.

The Fourier method has been used to perform the decomposition seen in the following section. The simulation described in Chapter 4.1 has boundary conditions which are valid for the Fourier approach to the Helmholtz decomposition of the magnetic tension. The y-boundary is periodic, which a Fast Fourier Transform assumes. The x-dimension is suitably large that perturbations decay before reaching the simulation edges (the x-extent of the simulation is twice that shown in Figure 6.1). The large dimension along the z-direction, along with the frictional term at the boundary, means that the Alfvén wave is fully damped before it reaches the top/bottom simulation edges. No evidence of Gibbs effects were found to be present from the application of the Fourier approach to the Helmholtz decomposition and no filtering process was used to reduce Gibbs effects.

6.2.1 $\lambda_{\mathbf{MHD}}$ Derivation

Here, a λ-family vortex definition applicable to ideal MHD is derived called λ_{MHD}. The derivation closely follows that of λ_ρ found in Yao and Hussain (2018). The aim is to find the Hessian of the MHD effective pressure defined in Equation 6.2 so that a second partial derivative test can be performed on it to identify local pressure minima. Gravitational effects are assumed to be negligible. Viscous effects are neglected in the below derivation due to space plasmas typically being collisionless. However, this definition is valid for a viscous ideal MHD fluid as a viscosity term in the pressure Hessian is neglected (see Yao and Hussain 2018) as viscosity can provide centripetal forces (e.g. Kármán's viscous pump) and remove the pressure minima in the fluid. Neglecting this term allows for the method to be able to successfully identify a vortex even when pressure-minima are not providing the centripetal restoring force (see Jeong and Hussain 1995; Yao and Hussain 2018, for further description of the viscous case in hydrodynamics).

The λ_{MHD} derivation starts with the ideal MHD Cauchy-Momentum equation, where the Helmholtz decomposition of the magnetic tension has been performed

$$\frac{\partial}{\partial t}(\rho\mathbf{v}) + \boldsymbol{\nabla}\cdot(\rho\mathbf{v}\mathbf{v}) = -\boldsymbol{\nabla}P_{\mathrm{eff}} + \boldsymbol{\tau}_{\mathrm{rot}}. \tag{6.4}$$

Rewriting this in tensor notation (using the Einstein summation convention) for component i and taking the gradient in coordinate j,

$$\partial_t\partial_j(\rho v_i) + \partial_j\partial_k(\rho v_i v_k) = -\partial_j\partial_i P_{\mathrm{eff}} + \partial_j\tau_{i\ \mathrm{rot}}. \tag{6.5}$$

Apply the chain rule twice

$$\begin{aligned}&\partial_t\partial_j(\rho v_i) + \partial_j v_k\partial_k(\rho v_i) + v_k\partial_k\partial_j(\rho v_i)\\ &\quad+\partial_j(\rho v_i)\,\partial_k v_k + (\rho v_i)\,\partial_k\partial_j v_k = -\partial_j\partial_i P_{\mathrm{eff}} + \partial_j\tau_{i\ \mathrm{rot}}.\end{aligned} \tag{6.6}$$

Using the definition of the material derivative $\frac{D}{Dt} = \partial_t + v_k\partial_k$ this can be simplified to

$$\frac{D}{Dt}(\partial_j(\rho v_i)) + \partial_j v_k\partial_k(\rho v_i) + \partial_j((\rho v_i)\,\partial_k v_k) = -\partial_j\partial_i P_{\mathrm{eff}} + \partial_j\tau_{i\ \mathrm{rot}}. \tag{6.7}$$

Taking the irrotational part of Equation 6.7 by applying to each $\partial_i A_j$ field the symmetric operator $1/2\left(\partial_j A_i + \partial_i A_j\right)$

$$\begin{aligned}&\frac{D}{Dt}\left(\frac{1}{2}\left(\partial_j\left(\rho v_i\right) + \partial_i\left(\rho v_j\right)\right)\right) + \frac{1}{2}\left(\partial_j v_k \partial_k\left(\rho v_i\right) + \partial_i v_k \partial_k\left(\rho v_j\right)\right)\\ &+ \frac{1}{2}\left(\partial_j\left(\left(\rho v_i\right)\partial_k v_k\right) + \partial_i\left(\left(\rho v_j\right)\partial_k v_k\right)\right) = -\partial_j\partial_i P_{\text{eff}} + \frac{1}{2}\left(\partial_j \tau_{i\ \text{rot}} + \partial_i \tau_{j\ \text{rot}}\right).\end{aligned} \tag{6.8}$$

Substitute in the symmetric, $S_{ij} = 1/2\left(\partial_j v_i + \partial_i v_j\right)$, and anti-symmetric, $\Omega_{ij} = 1/2\left(\partial_j v_i - \partial_i v_j\right)$, parts of the velocity gradient tensor

$$\begin{aligned}&\frac{D}{Dt}\left(\frac{1}{2}\left(\partial_j\left(\rho v_i\right) + \partial_i\left(\rho v_j\right)\right)\right) + \rho\left(S_{ik}S_{kj} + \Omega_{ik}\Omega_{kj}\right) + \frac{\partial_k \rho}{2}\left(v_i \partial_j v_k + v_j \partial_i v_k\right)\\ &+ \frac{1}{2}\left(\partial_j\left(\left(\rho v_i\right)\partial_k v_k\right) + \partial_i\left(\left(\rho v_j\right)\partial_k v_k\right)\right) = -\partial_j\partial_i P_{\text{eff}} + \frac{1}{2}\left(\partial_j \tau_{i\ \text{rot}} + \partial_i \tau_{j\ \text{rot}}\right).\end{aligned} \tag{6.9}$$

The effective pressure Hessian (denoted **H**) can now be written as,

$$-H_{ij} = -\partial_j\partial_i P_{\text{eff}} = E_{ij} + M_{ij} + D_{ij} + C_{ij} + T_{ij}. \tag{6.10a}$$

Where each term represents a different physical property:

$$\text{Unsteady Strain: } E_{ij} = \frac{D}{Dt}\left(\frac{1}{2}\left(\partial_j\left(\rho v_i\right) + \partial_i\left(\rho v_j\right)\right)\right), \tag{6.10b}$$

$$\text{Vortical Momentum: } M_{ij} = \rho\left(S_{ik}S_{kj} + \Omega_{ik}\Omega_{kj}\right), \tag{6.10c}$$

$$\text{Density Gradients: } D_{ij} = \frac{\partial_k \rho}{2}\left(v_i \partial_j v_k + v_j \partial_i v_k\right), \tag{6.10d}$$

$$\text{Compressibility: } C_{ij} = \frac{1}{2}\left(\partial_j\left(\left(\rho v_i\right)\partial_k v_k\right) + \partial_i\left(\left(\rho v_j\right)\partial_k v_k\right)\right), \tag{6.10e}$$

$$\text{Rotational Magnetic Tension: } T_{ij} = -\frac{1}{2}\left(\partial_j \tau_{i\ \text{rot}} + \partial_i \tau_{j\ \text{rot}}\right). \tag{6.10f}$$

As discussed by Jeong and Hussain (1995) and Yao and Hussain (2018), there is an inconsistency between the existence of a pressure minimum and a vortex core in Equation 6.10a. Simply finding a local pressure minimum is not sufficient in identifying a vortex core as unsteady irrotational motion can cause pressure minima in a fluid without vortical flow as a consequence of unsteady strain in

the fluid. In the example of a surface wave in an incompressible isothermal hydrodynamic fluid, a vortex would not be identifiable in pressure alone as there would not be a pressure minimum despite vortical flow being present. However, removing the unsteady strain provides the minimum needed in the adapted pressure Hessian to allow for vortex identification in this case. Choosing to neglect the unsteady strain effect in Equation 6.10a completes the derivation,

$$-\mathbf{H} = \mathbf{M} + \mathbf{D} + \mathbf{C} + \mathbf{T}. \tag{6.11}$$

Equation 6.11 outlines that only contributions from $\mathbf{M}+\mathbf{D}+\mathbf{C}+\mathbf{T}$ are required to identify a pressure minimum in a plane, which requires two positive eigenvalues of the pressure Hessian tensor (Jeong and Hussain 1995; Yao and Hussain 2018). Consequently, λ_{MHD} defines a vortex as a connected region with two negative eigenvalues of $\mathbf{M} + \mathbf{D} + \mathbf{C} + \mathbf{T}$. Since this tensor is real and symmetric, it has real eigenvalues only. Thus if its eigenvalues $\lambda_1 > \lambda_2 > \lambda_3$, then λ_{MHD} is equivalent to the requirement that $\lambda_2 < 0$ within the vortex core.

In summary, λ_{MHD} adds a correction term to λ_ρ which extends its usage to a magnetised ideal MHD fluid. λ_{MHD} is constructed of four terms which each represent different physical effects believed to affect the formation of the vortices such as in the KHI: vortical momentum ($\mathbf{M}$), density gradients ($\mathbf{D}$), fluid compressibility ($\mathbf{C}$), and rotational magnetic tension ($\mathbf{T}$).

6.3 Application to Local MHD Simulation

A local MHD simulation representative of near-flank magnetopause conditions (Ma et al. 2020) under northward interplanetary magnetic field (IMF) is used for this study. This region was chosen as it is the location where KHI is predicted to be most unstable along the magnetopause due to the large velocity shear (Southwood 1968). Northward IMF is chosen as it is also most unstable orientation predicted by linear theory (Chandrasekhar 1961) and confirmed by observations (Kavosi and Raeder 2015). As well as this, northward IMF prevents large-scale reconnection being induced by magnetic shear (Vernisse et al. 2016; Fadanelli et al. 2018; Sisti et al. 2019). The plasma beta has a value of $\beta = 0.5$ in region 1 (the magnetosheath), meaning magnetic field dynamics dominate over plasma dynamics; and $\beta = 5.0$ in region 2 (magnetosphere), meaning that plasma dynamics

dominate over the magnetic field here. The fast magnetosonic Mach number in the simulation frame has values of $M_f \sim 0.4$, corresponding to the weakly compressional regime where compressibility should be non-negligible. The Alfvén Mach number has moderate values of $M_A \sim 0.89$ in region 1 and $M_A \sim 0.55$ in region 2, meaning that magnetic tension cannot be neglected. These Mach numbers have been calculated in the simulation frame as the vortex is approximately stationary in the centre of the simulation throughout (cf. Palermo et al. 2011).

The MHD KHI is numerically simulated by solving a full set of normalised resistive MHD equations using a leap-frog scheme in a Cartesian coordinate system (Otto 1990; Nykyri and Otto 2001; Ma et al. 2014b; Ma et al. 2014a; Ma et al. 2017). The x direction points along the normal to the unperturbed sheared flow layer, the y direction is along the sheared flow direction, and the z direction is determined by the right-hand rule. All physical quantities are normalised by characteristic values and their initial states are outlined in Table 6.1. The length scale, L_0, magnetic field scaling factor, B_0, and number density scaling factor, n_0 may be chosen freely, whereas all other scaling quantities are derived from these. To provide physical context, values have been assigned to the dimensionless simulation units which best represent the near-flank magnetopause (Ma et al. 2020). These values were chosen by Xuanye Ma of Embry-Riddle as he provided the simulation for analysis. However, these values are arbitrary and do not affect the physics of the simulation or any of the results presented.

The whole simulation domain is given by $[-L_x, L_x] \times [-L_y, L_y] \times [-L_z, L_z]$ along the x-, y-, and z-directions, where $L_x = 25L_0$, $L_y = 10L_0$, and $L_z = 120L_0$. The grid has 203 cells in each direction with a resolution of $0.1L_0$ in the y-direction, $0.6L_0$ in the z-direction and is stretched along the x-direction with a minimum resolution of $0.1L_0$. The dimension along x is large enough to ignore the influence from the boundaries such as MHD wave reflections. To overcome issues with Fourier analysis and noise from differentiation, all the data is trilinear interpolated on to a regular grid of resolution $0.1L_0$ in all directions for our investigations.

The initial steady state is a one-dimensional transition layer with a flow shear, the conditions of which are outlined in Table 6.1. This transition layer is initially imposed by a hyperbolic tangent function with characteristic thickness of L_0 and maintains the total force balance across the sheared flow layer (i.e., the sum of the thermal pressure and magnetic pressure is constant). The KHI is triggered by a velocity perturbation localised in the vicinity of the equatorial plane

Quantity	Value	Initial State		
		Region 1 ($x > 0$)	Region 2 ($x < 0$)	x-profile
Length Scale, L_0	600km			
Magnetic Field, B_0	60nT	$(0, 0, 0.5B_0)^T$	$(0, 0, B_0)^T$	$1/2(B_{z1} + B_{z2}) + 1/2(B_{z1} - B_{z2})\tanh(x/L_0)\mathbf{e}_z$
Number Density, n_0	11cm^{-3}	$0.8n_0$	$1.2n_0$	$1/2(n_1 + n_2) + 1/2(n_1 - n_2)\tanh(x/L_0)$
Velocity, V_{A0}	$B_0/\sqrt{\mu_0\rho_0} = 394$ km/s	$-0.5V_{A0}$	$0.5V_{A0}$	$0.5\tanh(x/L_0)\mathbf{e}_y$
Pressure, P_0	$B_0^2/2\mu_0 = 1.4$nPa	$1.25P_0$	$0.5P_0$	$P_1 + (B_{z1}^2 - B_z^2(x))/2\mu_0$
Plasma Beta, β	P_{therm}/P_{mag}	5	0.5	
Alfvén Mach Number, M_A	$\lvert V\rvert/V_A$	0.89	0.55	
Fast Mach Number, M_f	$\lvert V\rvert/c_f$	0.39	0.46	
Time, t_0	$L_0/V_{A0} \sim 1.5$ s			
Atwood Number, A	$(\rho_2 - \rho_1)/(\rho_1 + \rho_2) = 0.2$			

Table 6.1: Table showing the normalisation constants and initial state used in the simulation.

(i.e., $z = 0$), which is given by $\mathbf{v} = \nabla\Phi(x, y) \times \mathbf{e}_z f(z)$. Here, the stream function is $\Phi(x, y) = \delta v \cos(k_y y)\cosh^{-2}\sec(x/l_x)$, normal scale of the perturbation $l_x = 2L_0$, KH wavenumber $k_y = \pi/L_y$, amplitude of the velocity perturbation $\delta v = V_{A0}/20$, and the localisation function $f(z)$ is given by $f(z) = 0.5\{\tanh[(z + z_d)/L_0 D_z] - \tanh[(z - z_d)/L_0 D_z]\}$, where $z_d = 20L_0$, and $D_z = 3$.

Figure 6.1 shows 3 snapshots of the simulation in the equatorial plane. $t = 30t_0$ is approximately during the quasi-linear surface wave stage, $t = 80t_0$ is during the nonlinear surface roll-up stage of the KHI, and $t = 130t_0$ is during the turbulent stage beyond the surface roll-up. These three stages are used throughout this chapter. At time $t = 80t_0$, and $t = 130t_0$ there are secondary KHI forming as highlighted in panels 6.1b and 6.1c. The dashed black line is plotted along the $\rho = \rho_0$ line as a visual aid to the reader for identifying the proxy-boundary. As $M_f \sim 0.4$ this proxy-boundary should be little affected by compressible effects. Note also that different methods of magnetopause identification (e.g. last closed field line, density/velocity gradients etc.) in simulations are known not to always be co-located (Gordeev et al. 2013; García and Hughes 2007). It does not feature in the turbulent stage as there is no clear single boundary between the two sides.

6.3.1 Exploring P_{ten}

A key step in the derivation of λ_{MHD} is the realisation that a part of the magnetic tension contributes to the pressure-like forces on the plasma, which is achieved through a Fourier-based Helmholtz decomposition of the magnetic tension into rotational and irrotational vector fields. Figure 6.2 shows this decomposition. In the quasi-linear stage ($t = 30t_0$), tension is shown to be acting as a stabilising force opposing the deformation of the boundary as expected. The tension is entirely rotational in this initial stage, as expected for a linear incompressible surface wave (Plaschke 2016). This implies the

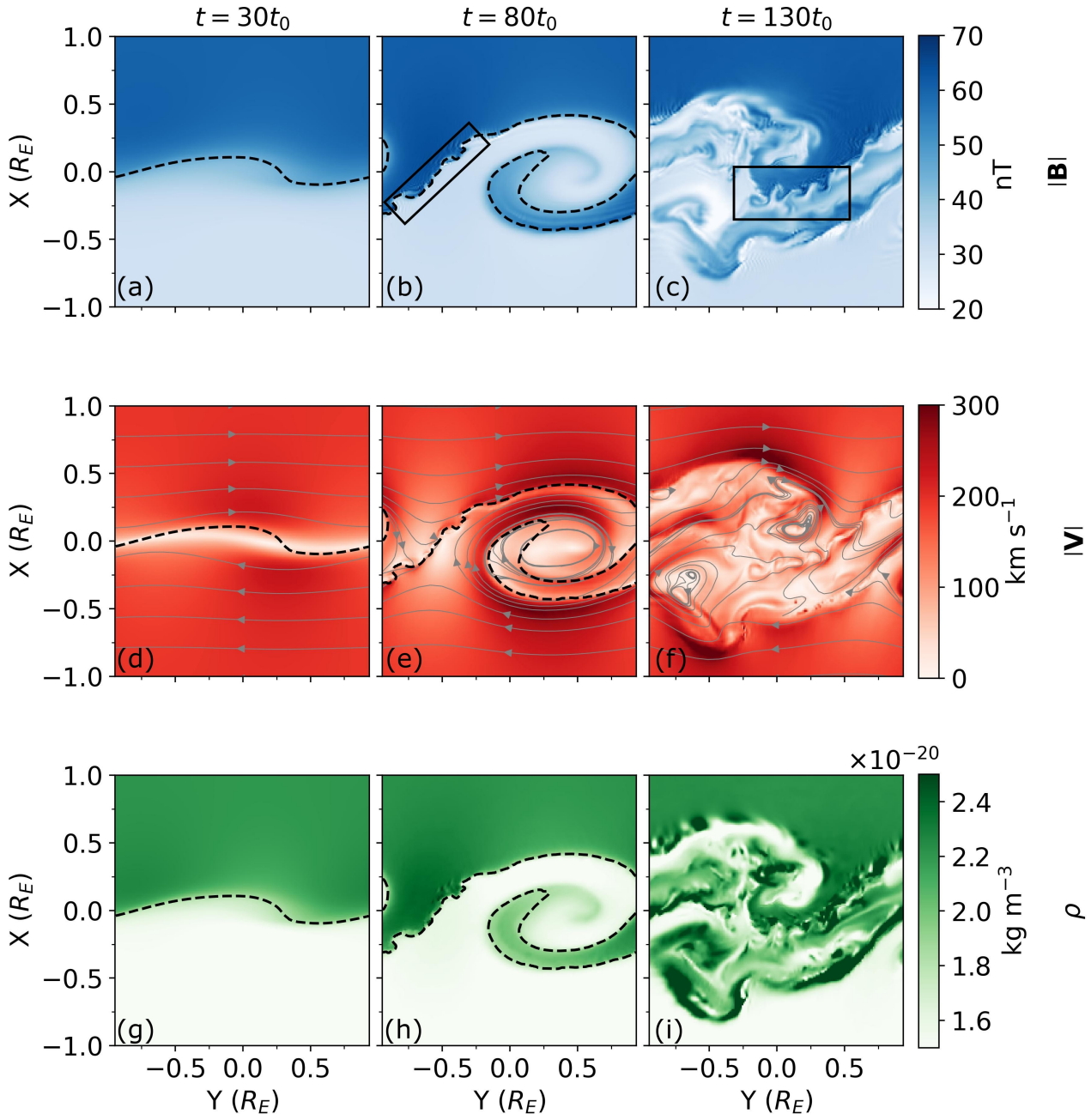


Figure 6.1: An equatorial ($z = 0$) view of the magnitude of the magnetic field, magnitude of the velocity, and density at the quasi-linear ($t = 30t_0$), nonlinear surface roll-up ($t = 80t_0$) and turbulent ($t = 130t_0$) stages of the simulation. The black boxes in panels b and c highlight secondary KHI. The dashed black line is plotted along $\rho = \rho_0$ contour as a proxy for the boundary between the two sides. There are streamlines present in grey on the velocity plots to demonstrate the velocity shear.

tension field is not yet perturbed enough to provide a (nonlinear) pressure-like contribution. In the nonlinear surface roll-up stage ($t = 80t_0$), the tension field has become sufficiently twisted for the tension to start exhibiting a pressure-like part, but the tension overall is still predominantly rotational. The force is again pointing in directions to try and restore the boundary to its original shape – with

the pressure-like part now also contributing to this. In the turbulent stage ($t = 130t_0$) it becomes unclear on the behaviour of the tension as the KHI-generated structures have evolved turbulently – it is however clear that the forces are still predominantly rotational. The tension generally has a larger magnitude in regions where secondary KHI are present.

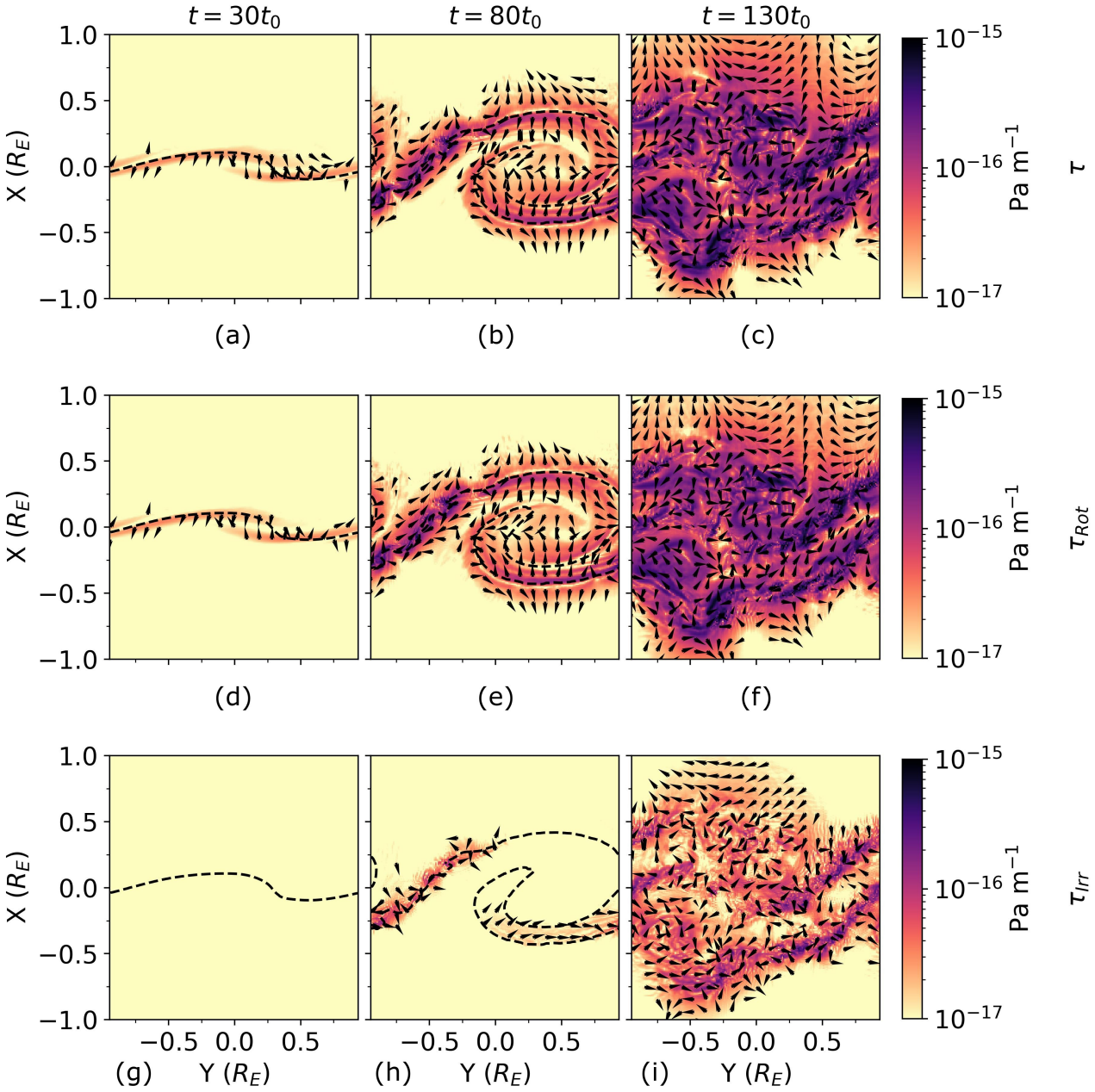


Figure 6.2: An equatorial ($z = 0$) view of the total τ, rotational part, τ_{Rot}, and irrotational part, τ_{Irr}, of the magnetic tension as found through a Helmholtz decomposition. In colour is the magnitude with overlaying unit vectors to indicate the acting direction in the xy-plane. The quasi-linear ($t = 30t_0$), nonlinear surface roll-up ($t = 80t_0$) and turbulent ($t = 130t_0$) stages are shown. The dashed black line is plotted along $\rho = \rho_0$ contour as a proxy for the boundary between the two sides.

Since λ_{MHD} relies upon finding an effective pressure minimum, the various forms of pressure

in Figure 6.3 can be shown. Here the variation of the pressure fields about their respective mean is shown – this eliminates any bias from P_{ten} lacking uniqueness. In the quasi-linear stage, the effective pressure has a single minimum near the centre of the simulation between the points where the boundary is most deformed. In the nonlinear stage, the effective pressure has a minimum near the centre of the surface roll up. There is now also an obvious maximum adjacent to it. Along the boundary in the region of secondary KHI (as highlighted in Figure 6.1b) several small-scale effective pressure minima are also present. There are also other minima in regions where it is clear turbulence/inhomogeneity is present by looking at the other pressures. It is evident that δP_{Ten} does not play a major role in how the total effective pressure is defined as it is generally an order of magnitude smaller than the other pressure variations. δP_{Ten} becomes larger in regions where the magnetic field lines are contorting, but overall it is smaller than $\delta P_{\text{therm}} + \delta P_{\text{mag}}$. This can also be seen in the Figure 6.3c where the δP_{Ten} minima appear to sit along the upper and lower boundaries of the mixed/turbulent plasma and the homogeneous plasma.

Like the tension force itself, $|\delta P_{\text{Ten}}|$ appears to be largest in regions where secondary smaller-scale KHI structures are present. This is likely down to the following two reasons. Firstly, recall that the curvature of field lines, $\boldsymbol{\kappa}$, is expressed as

$$\boldsymbol{\kappa} = (\mathbf{b} \cdot \boldsymbol{\nabla})\, \mathbf{b} \tag{6.12}$$

where $\mathbf{b}$ is the magnetic field unit vector. The curvature of field lines is inversely proportional to the radius of curvature under fixed magnetic field. It is related to the magnetic tension by the following equation,

$$\boldsymbol{\tau} = \frac{(\mathbf{B} \cdot \boldsymbol{\nabla})\, \mathbf{B}}{\mu_0} = \frac{|\mathbf{B}|^2}{\mu_0} \boldsymbol{\kappa}. \tag{6.13}$$

This means that rolled-up, smaller scale structures will have a greater magnetic tension force. Additionally, the growth rate of smaller scale structures is greater than larger scale ones (Nagano 1979; Rice et al. 2022; Sundberg et al. 2010) meaning they will roll-up and evolve faster, i.e. increasing the field line curvature.

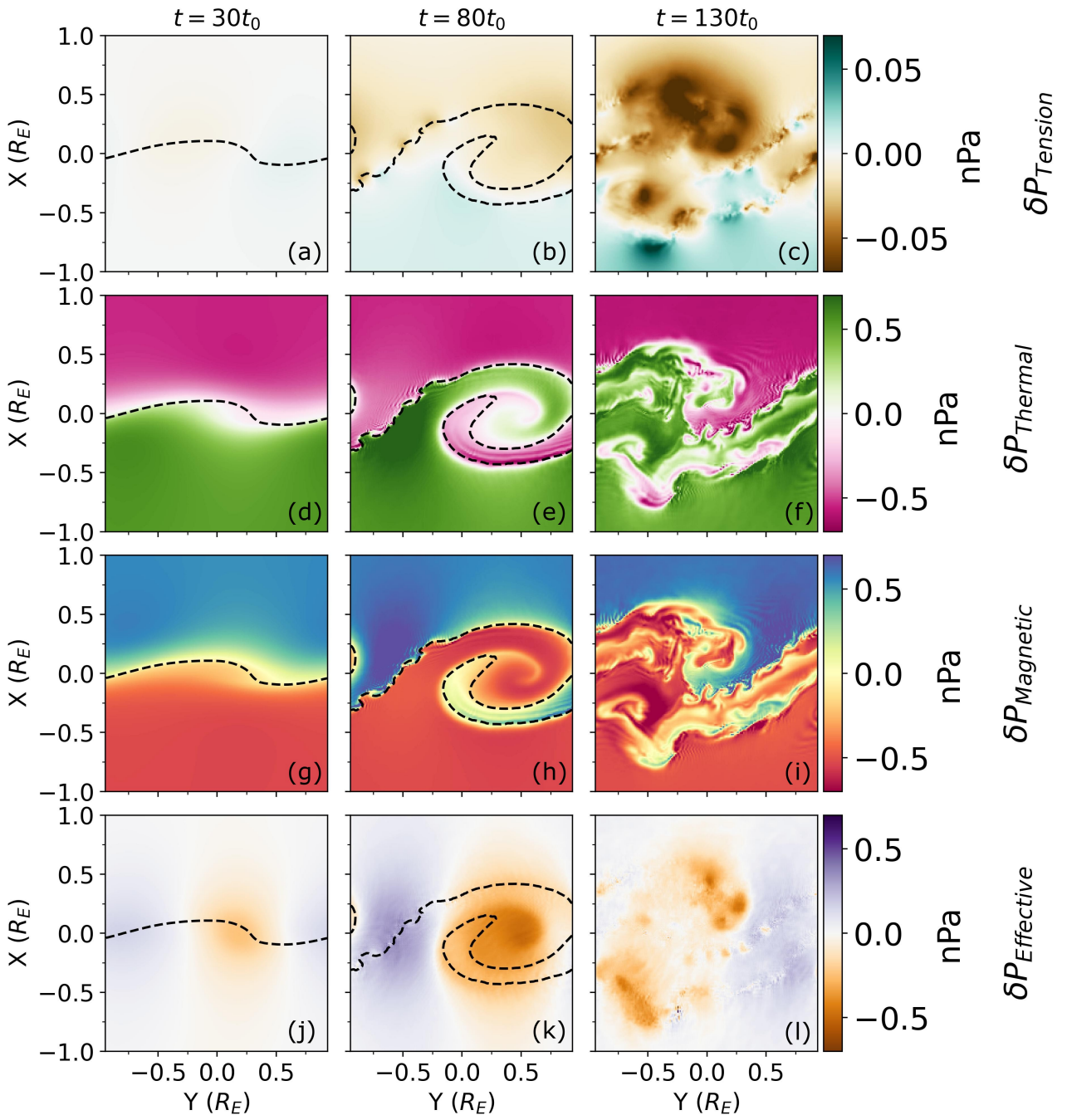


Figure 6.3: An equatorial ($z = 0$) view of the perturbations from the mean pressure due to magnetic tension, thermal pressure, magnetic pressure, and total pressure. The quasi-linear ($t = 30t_0$), nonlinear surface roll-up ($t = 80t_0$) and turbulent ($t = 130t_0$) stages are shown. The dashed black line is plotted along $\rho = \rho_0$ contour as a proxy for the boundary between the two sides.

6.3.2 Validating $\lambda_{\mathbf{MHD}}$

Section 6.3.1 demonstrates that the contributions to the effective pressure from the pressure-like part of the magnetic tension are small for this simulation. Consequently, hydrodynamic techniques might be sufficient in identifying vortices for the simplified magnetopause in this simulation. Therefore a

comparison between λ_{MHD} and the other hydrodynamic vortex criteria mentioned in section 3.3 can be made.

The different vortex methods are applied to every cell in the simulation, where spatial derivatives are undertaken through second order accurate central differences in the interior points and first order accurate differences at the boundaries. To remove machine noise in the gradients a multidimensional Gaussian filter with a standard deviation of 0.5 grid cells is applied. The smoothed data is then passed through a $3 \times 3 \times 3$-cell multidimensional median filter to ensure that the regions are 'connected' – meaning that more than one adjacent cell in a plane must be identified as vortical for a positive identification. Typically with these types of techniques a threshold is chosen to define a vortex (Dong and Tian 2020), however to allow for a more complete comparison of the techniques and what they physically represent, a threshold has not been used.

Figure 6.4 shows the λ_{MHD} vortex definition compared to the 2-dimensional velocity streamlines (v_z is negligible throughout this plane) to qualitatively assess whether the technique is correctly identifying vortices. In the quasi-linear stage of the KHI ($t = 30t_0$), there is a single vortex core identified (region 1) which is centred around the steep edge of the deformed shear flow boundary. After some evolution to the nonlinear roll-up stage ($t = 80t_0$), the previous vortex has now evolved and been stretched and torn into four large structures (regions 2, 4, 5, 6). The strongest signature in the simulation is region 2, a structure at the edge of the simulation that is the leading edge of the rolled up surface (recalling the boundary conditions in y are periodic). The other three structures are in the centre of the simulation, again where the surface roll-up is present. Interestingly, the secondary small-scale KHI vortices (region 3) have a stronger signature than the three vortex structures within the roll-up (regions 4, 5, 6). It appears the vortices are all situated where the principal curvature of the boundary is greatest, with the strength being proportional in some way to the curvature of the boundary i.e. stronger vortices deform the boundary more.

The original large-scale vortex becomes unidentifiable in the turbulent stage, it is possible that region 4 becomes region 7 and region 5 becomes region 9, but this is ambiguous. Instead strong λ_{MHD} signatures are present in much of the simulation domain due to lots of small-scale vortical structures being present throughout. There are two large vortices present (regions 7 and 9). Some of the strongest signatures are found where secondary KHI is present (region 8). Generally, speaking

λ_{MHD} grows with time as the strongest signatures are seen in the turbulent stage and the weakest in the quasi-linear stage.

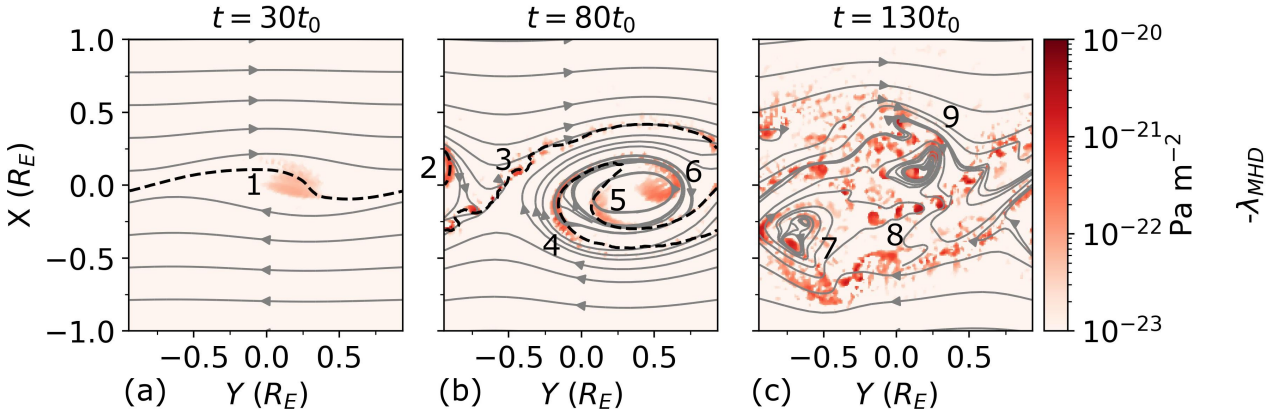


Figure 6.4: An equatorial ($z = 0$) view of vortex identification method $-\lambda_{MHD}$ values on a $\log_{10}$ colour-scale. The quasi-linear ($t = 30t_0$), nonlinear surface roll-up ($t = 80t_0$) and turbulent ($t = 130t_0$) stages are shown. In grey are 2D velocity field streamlines. The numbers in the plot indicate regions of interest discussed in the text. The dashed black line is plotted along $\rho = \rho_0$ contour as a proxy for the boundary between the two sides.

Figure 6.5a shows a zoom in of vortex region 4 from the nonlinear roll-up stage. In the simulation frame the vortex is not immediately apparent in the flow, despite λ_{MHD} identifying a distinct vortex in this region. However, recalling and exploiting the Galilean invariance of the method, the velocity field is transformed into a different frame in panel b. This clearly demonstrates an isolated vortex is present, hence the distinct regions identified by λ_{MHD} within the KHI roll-up are real vortical features in the flow. This again highlights the need for vortex identification techniques, since they can pinpoint vortices which are not clear from visual analysis. It is emphasised that the vortices these techniques identify are not simply the large-scale roll-up structure of the boundary overall, but flow vortices present as substructure within this roll-up which are ultimately responsible for the boundary deformations.

Figure 6.6 shows the MHD effective pressure with overlaying contours of the different vortex identification methods (λ_{MHD} and those mentioned in section 3.3.2), which should identify pressure minima. Contour levels have been arbitrarily chosen to display behaviour at extremes of large and small values that constitute a vortex (Dong and Tian 2020). Visually comparing the hydrodynamic criteria and λ_{MHD}, it appears that all the definitions of a vortex identify similarly compact regions. This further qualitatively validates λ_{MHD} and also suggests the simpler hydrodynamic criteria may be

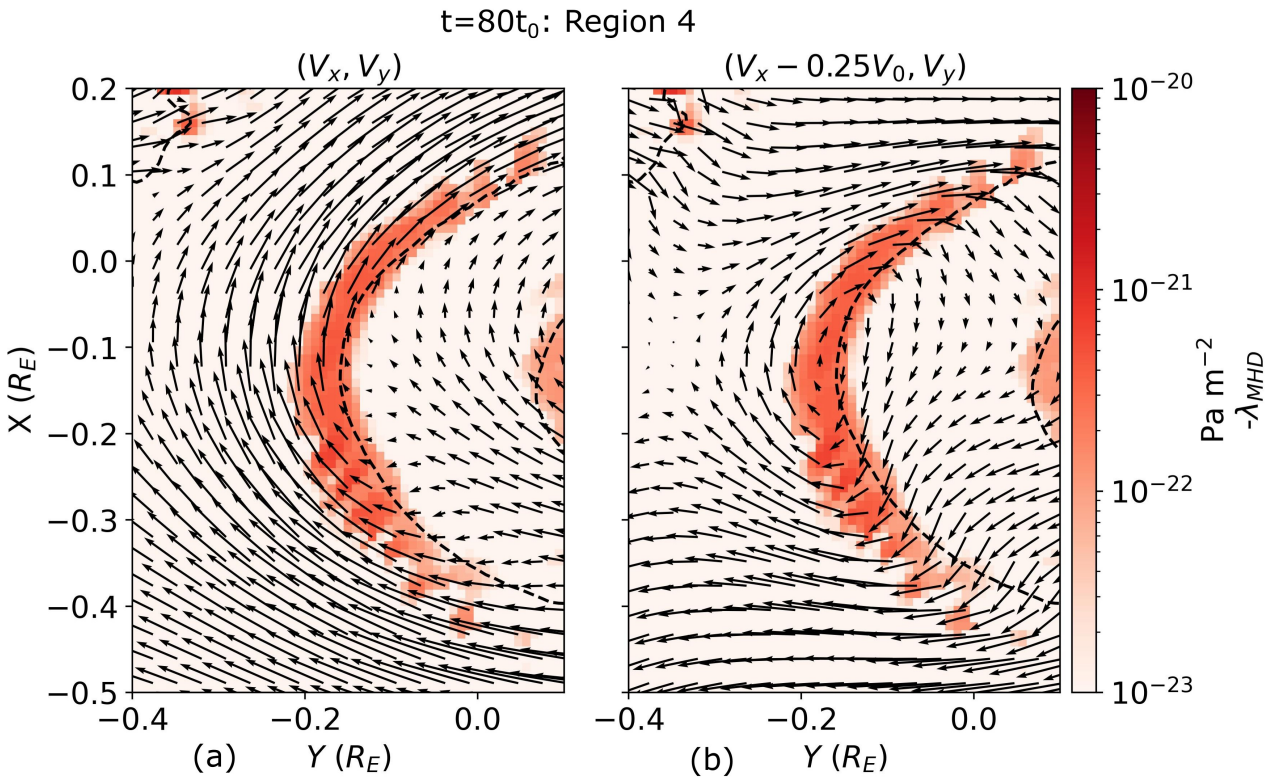


Figure 6.5: An equatorial ($z = 0$) view of vortex identification method $-\lambda_{\mathrm{MHD}}$ values on a $\log_{10}$ colour-scale. Region 4 (see Figure 6.4b) of the nonlinear surface roll-up ($t = 80t_0$) stage is shown. Panel a and b show the same λ_{MHD} colour map calculated in the simulation frame. In black are 2D velocity field quivers, panel (a) shows the original velocity field quivers, panel (b) shows a Galilean transformed field where the $V_x' = V_x - 0.25V_{A0}$. The dashed black line is plotted along $\rho = \rho_0$ contour as a proxy for the boundary between the two sides.

used as proxies for λ_{MHD}. Since each method makes different levels of assumptions about the fluid, comparing the different definitions explores how introducing these different physical effects affects the regions identified as a vortex core, hence their importance in vortex formation and evolution.

Q and λ_2 perform almost identically across the three time steps shown in Figure 6.6 and identify similar regions to those discussed in Figure 6.4. The criteria identify regions where the local boundary is most deformed and by comparing to effective pressure in Figure 6.3, it is clear that they are locating local pressure minima in the quasi-linear stage. In the nonlinear and turbulent stages, this is less clear. The minima located by them differ to the local minima in the effective pressure plots. The effective pressure appears to highlight the general region however the criteria clearly outlines the vortex core regions. This is because the neglected parts of the adapted effective pressure Hessian are non-negligible in these stages and neglecting them allows for a clearer identification. This suggests that making these adaptations to the pressure Hessian are vital to the success of the λ-family of

techniques. Furthermore, it demonstrates that while local total pressure minima may be reliable in the quasi-linear stage as an approximate identification tool, beyond this the method is not precise enough and advanced vortex identification techniques are necessary.

Comparing Q and λ_2 to $\overline{\lambda_2}$ probes the importance of momentum flow over velocity flow in the identification of a vortex. Crucially, the relative magnitudes of those regions shift to locations where there is larger vortical momentum instead of just vortical velocity. Since $\overline{\lambda_2}$ simply weights λ_2 by local density, the sign remains unchanged and thus it identifies identical regions to λ_2. Unlike Q and λ_2, the units of $\overline{\lambda_2}$ are comparable to those of λ_{MHD} allowing for direct comparisons to be made between the two criteria. In this simulation, the λ_2 and $\overline{\lambda_2}$ results do not appear to differ much – this is likely due to the uniform initial density along the streaming direction and the small relative density change and Atwood number.

Comparing the results of λ_ρ to that of $\overline{\lambda_2}$ allows for an insight into how fluid compressibility and density gradients influence where a vortex core is identified. It is apparent that these two factors do influence vortex identification as there is an obvious reduction in the volume that λ_ρ identifies as vortical compared to the less advanced methods. In particular, the vortex appears less strongly in λ_ρ at the $t = 30t_0$ stage compared to the earlier considered methods. In the later stages of the KHI, there are more detached vortical regions seen in λ_ρ compared to the less advanced methods. This suggest that λ_ρ is capable of distinguishing between multiple vortices in close proximity. The less advanced methods appear to smear these multiple vortices into one large vortex core structure making them less useful if studying vortex shedding, complex regions, or turbulent stages. Due to this, λ_ρ is better suited for revealing finer details of the complex physics taking place.

λ_{MHD} includes the influence of the magnetic field to the definition of a vortex core. λ_{MHD} appears to identify almost the same structures as λ_ρ, indicating that magnetic tension may not play a dominant role in the large-scale vortices in this simulation. This is somewhat expected since under northward IMF the magnetic tension is least effective at suppressing the KHI, and the scale of variations along the anchored field lines are much larger than those perpendicular to the field (equation 3.6). Nonetheless, λ_{MHD} does identify additional finer-scale archipelago-like structures less dominant in the hydrodynamic approaches. These occur at the small-scale secondary KH vortices, likely because the tension term becomes more important in these regions as previously discussed in

Section 6.3.1. As many of these values are relatively close to zero, this may suggest that in practical applications a higher threshold value than the lowest contour displayed of 0.01×10^{-22} Pa m^{-2} may be needed for the λ_{MHD} (and maybe λ_ρ) technique(s). This would reduce the number of small scale structures being identified, enabling focus on stronger vortices and their large-scale structure. How best to set such vortex thresholds is an area of ongoing research even in hydrodynamics (Chakraborty et al. 2005; Pierce et al. 2013; Liu et al. 2019; Dong and Tian 2020).

Figure 6.7 shows 2-dimensional histograms over the entire simulation domain quantitatively comparing each hydrodynamic vortex criterion (vertical axes) with λ_{MHD} (horizontal axes). In all the histograms there is a main data population confined to a $y \propto x$ line (except for Q where the criteria for a vortex is positive not negative making it $y \propto -x$ instead) meaning all the techniques have a good correlation with λ_{MHD} – especially λ_ρ during the linear and nonlinear stages. This is reflected in the strong Pearson's correlation coefficients, R. There are two secondary populations in the histograms. The first is along the $y = 0$ region – largely with negative λ_{MHD} values. These correspond to regions where λ_{MHD} has identified a vortex where the hydrodynamic definition has not. Assuming λ_{MHD} is successfully identifying vortices and given the only difference between it and the λ_ρ definition is the introduction of the rotational tension term, this feature must be due to magnetic field effects that λ_{MHD} is able to extract which the hydrodynamic definitions cannot. The second is around the $x = 0$ region, this is due to the hydrodynamic definitions identifying larger regions as vortical compared to λ_{MHD}. This supports the previous finding that the simpler hydrodynamic definitions have a poorer precision than λ_ρ or λ_{MHD}. As the simulation becomes turbulent, there is a larger variance about the linear relationship between the hydrodynamic and MHD methods, though the correlation is still reasonable. The increased variance is expected as, e.g. the magnetic tension term becomes more important in the small-scale structures which form. An analysis of each technique's performance against λ_{MHD} can provide a better understanding of how different regimes can affect vortex formation and identification.

The Q, λ_2, and $\overline{\lambda_2}$ comparisons all demonstrate good correlations with the λ_{MHD} technique which strongly suggests that compressibility and plasma inhomogeneity do not play a significant role in the identification of the vortex, as these techniques are ignorant of these effects. The secondary populations break this pattern and are not as present in λ_ρ which reinforces that the regions identified

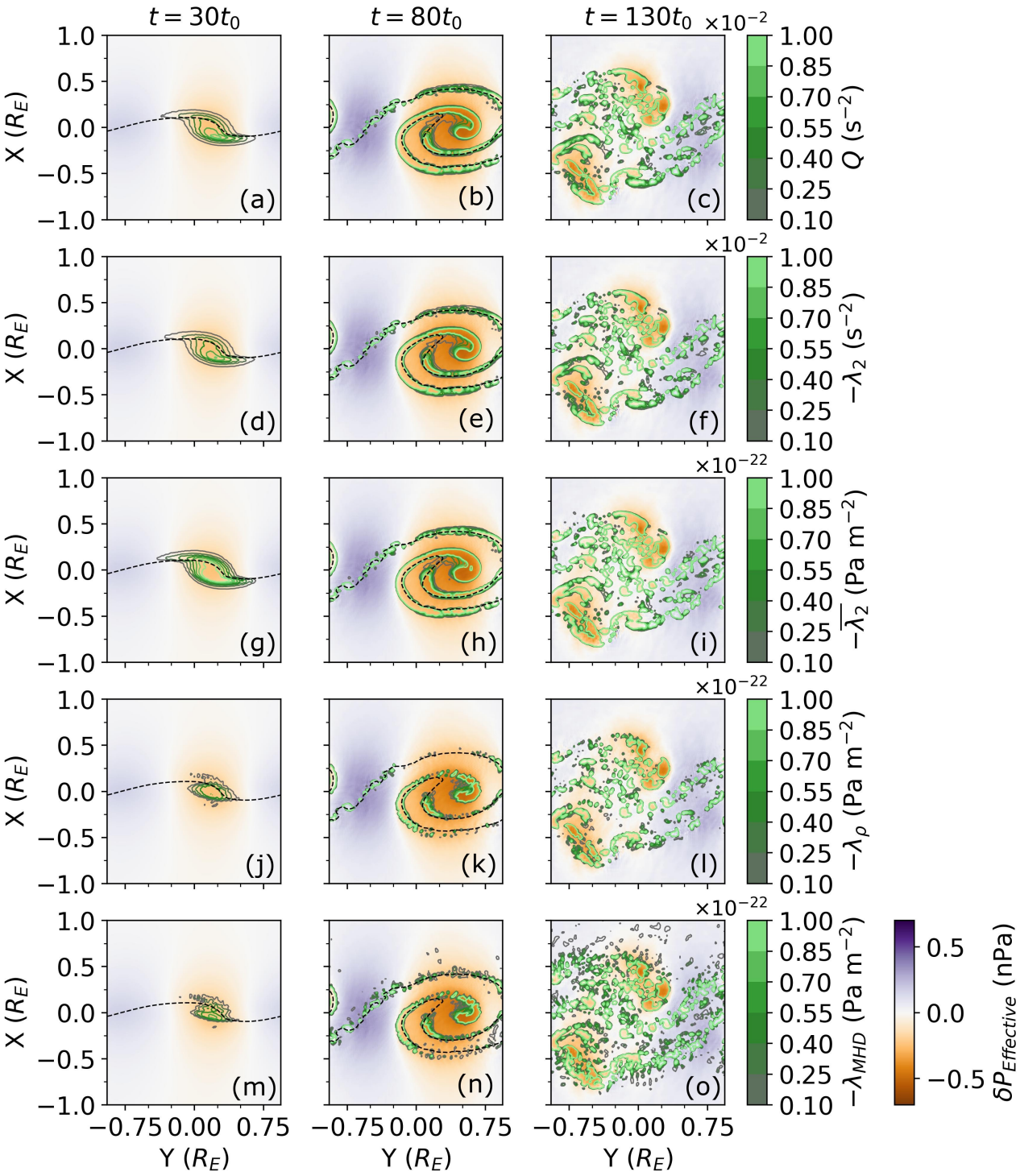


Figure 6.6: An equatorial ($z = 0$) view of contours for different vortex techniques on a linear colour-scale. These are plotted over the effective pressure variations from the mean. The quasi-linear ($t = 30t_0$), nonlinear surface roll-up ($t = 80t_0$) and turbulent ($t = 130t_0$) stages are shown. The dashed black line is plotted along $\rho = \rho_0$ contour as a proxy for the boundary between the two sides.

by the simplest hydrodynamic criteria are not as precise as the more advanced methods. Previous research has found that the simpler hydrodynamic techniques struggle to distinguish between two

vortices situated close together in space and tend to blur the volumes into one large structure (Cai et al. 2018; Collado-Vega et al. 2018) – our results agree with these findings.

The square of Pearson's correlation coefficient between λ_ρ and λ_{MHD} indicates the amount of variance in λ_{MHD} explainable by hydrodynamic effects alone. λ_ρ has a very good Pearson's correlation coefficient with λ_{MHD} of 0.97 in the quasi-linear stage, hence vortex identification is virtually entirely described by hydrodynamics and magnetic effects are negligible during this early stage of the KHI within this simulation (again likely due to the northward IMF conditions used along with long field lines). As it evolves into the nonlinear surface roll-up stage, hydrodynamics only explains 71% of the variations present. Magnetic tension term therefore plays a non-negligible role, likely due to magnetic tension's effects becoming more important as secondary KHI begin to form. In the turbulent stage of the KHI, less than half (47%) of the variations in λ_{MHD} are due to hydrodynamic effects alone, meaning that magnetic tension becomes an essential component likely due to the increased number of smaller-scale magnetic structures present.

The analysis has shown that (for this simulation at least) Q, λ_2, and $\overline{\lambda_2}$ are good approximations of a vortex in the MHD regime. However, they are prone to false-identifications as they struggle to distinguish between multiple vortices in close proximity. Including density gradient and compressibility effects allows λ_ρ to more successfully distinguish between these close proximity vortices, allowing it to provide more precise vortex identifications. Effects from magnetic tension, only incorporated into λ_{MHD}, become more important over time due to structural evolution and field line twisting, wrapping, and distortion. While the different vortex criteria include and/or exclude different physical effects related to vortex formation, quantitatively comparing these eigenvalues does not self-consistently enable a thorough investigation of the interplay these physical effects since each criterion has a different eigenvector. A different quantitative method needs to be used to fully explore how each different term, and therefore effect, influences vortex identification.

6.3.3 Contributions to λ_{MHD}

As derived in section 6.2.1, there are four physical effects which contribute to λ_{MHD}: vortical momentum (**M**), fluid compressibility (**C**), density gradients (**D**), and the rotational tension (**T**). Here, the extent of each each terms contribution to λ_{MHD} within the simulation is investigated.

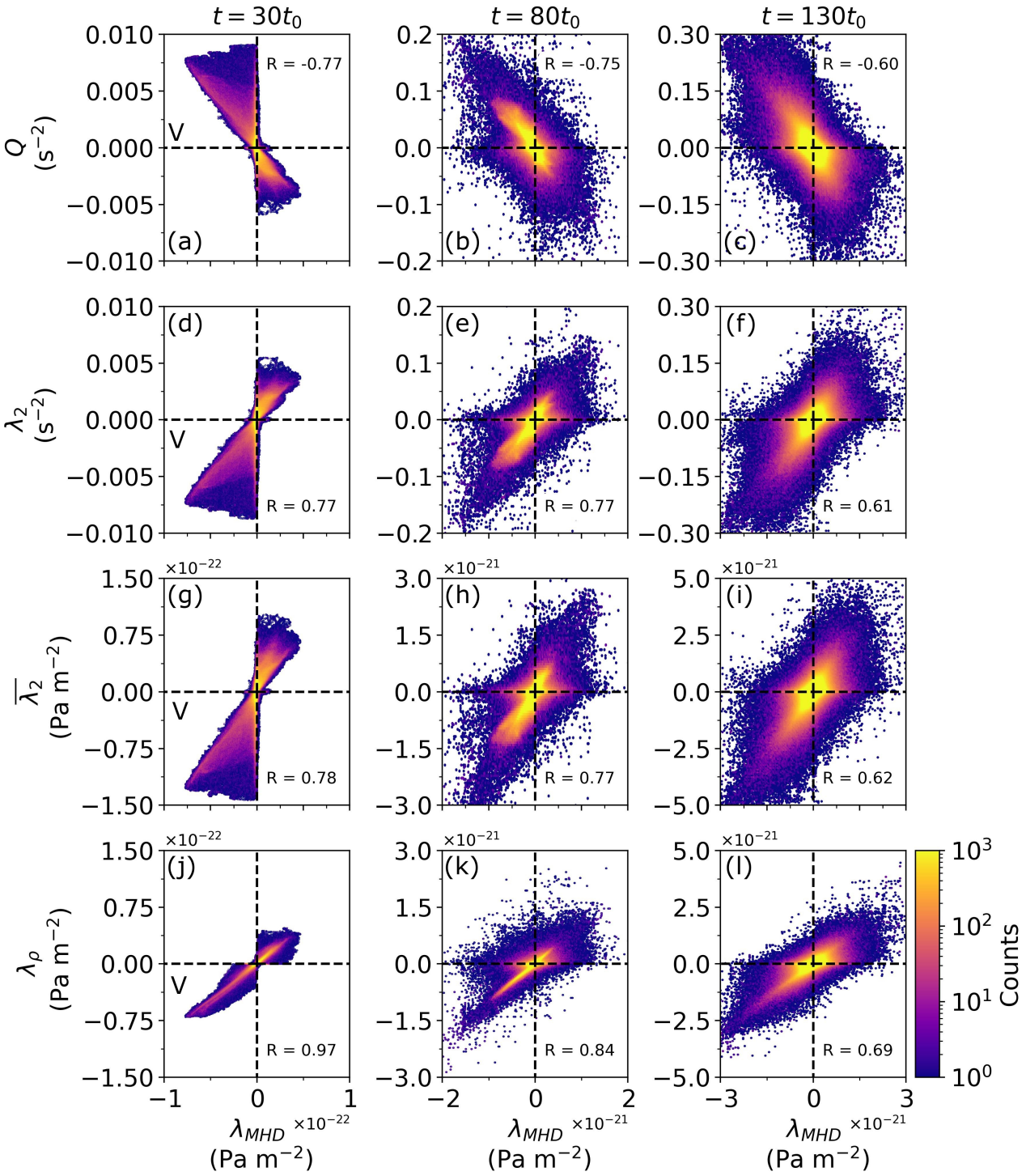


Figure 6.7: 2D histograms across the entire simulation domain comparing λ_{MHD} with the hydrodynamic vortex criteria. Counts are plotted using a $\log_{10}$ colour scale. The quadrant which represents a vortex in both λ_{MHD} and the comparison definition is labelled with 'V'. The R value denotes Pearson's correlation coefficient.

The effective pressure Hessian tensor, **H**, is real and symmetric (hence also Hermitian). It therefore has real eigenvalues whose eigenvectors can be chosen to be real and orthonormal. From

the spectral theorem the Hessian's eigenvalue can be rewritten as a linear combination of eigenvector projections, known as a spectral eigendecomposition. Let $\hat{\mathbf{V}}_{H,2}$ be the normalised eigenvector of $\mathbf{H}$ corresponding to the second eigenvalue, λ_{MHD}. Right multiply Equation 6.11 by $\hat{\mathbf{V}}_{H,2}$ and left multiply by the transpose to get,

$$\lambda_{\mathrm{MHD}} = -\hat{\mathbf{V}}_{H,2}^{T}\mathbf{H}\hat{\mathbf{V}}_{H,2} \tag{6.14a}$$

$$= \hat{\mathbf{V}}_{H,2}^{T}\mathbf{M}\hat{\mathbf{V}}_{H,2} + \hat{\mathbf{V}}_{H,2}^{T}\mathbf{D}\hat{\mathbf{V}}_{H,2} + \hat{\mathbf{V}}_{H,2}^{T}\mathbf{C}\hat{\mathbf{V}}_{H,2} + \hat{\mathbf{V}}_{H,2}^{T}\mathbf{T}\hat{\mathbf{V}}_{H,2} \tag{6.14b}$$

$$= \lambda_M + \lambda_D + \lambda_C + \lambda_T. \tag{6.14c}$$

For clarity $\lambda_{M,D,C,T}$ are not eigenvalues of their respective matrices, but are the contributions to the λ_{MHD} eigenvalue of $\mathbf{H}$. This demonstrates how each term directly contributes to λ_{MHD} which allows for quantitative analysis and comparison of the different contributions each physical effect has on λ_{MHD}.

Figure 6.8 shows a spatial map of the contribution each term has to λ_{MHD} at each of the three stages considered. The values shown are processed like before. In overview, it is clear that the vortical momentum term (panels a–c) generally dominates the λ_{MHD} definition, supporting the conclusion that Q, λ_2, and $\overline{\lambda_2}$ are reasonable approximations of λ_{MHD}. The other terms appear to act as corrections to the vortical momentum term. Density gradients (panels d–f) generally oppose the vortical momentum. The fluid compressibility term (panels g–i) is generally small at all three stages shown. Over the course of the three stages, the rotational component of the magnetic tension (panels j–l) tends to grow in regions where smaller-scale vortices form, reinforcing its importance over these scales. However, all the terms appear to have a complex relationship with λ_{MHD} overall, supporting in some locations but opposing in others.

In the quasi-linear stage, vortical momentum is the dominant term. There are two different populations in this term, the first (region 2) is in support of a vortex and lies between where the interface is most deformed. The other population (regions 1 and 3) oppose a vortex. Density gradients (panel d) oppose the formation of a vortex at the centre of simulation (region 5). Interestingly, this opposition is strongest at the edges along the normal of the vortical momentum region (2) rather than at the centre. This serves to reduce the volume being identified as vortical and is the reason the

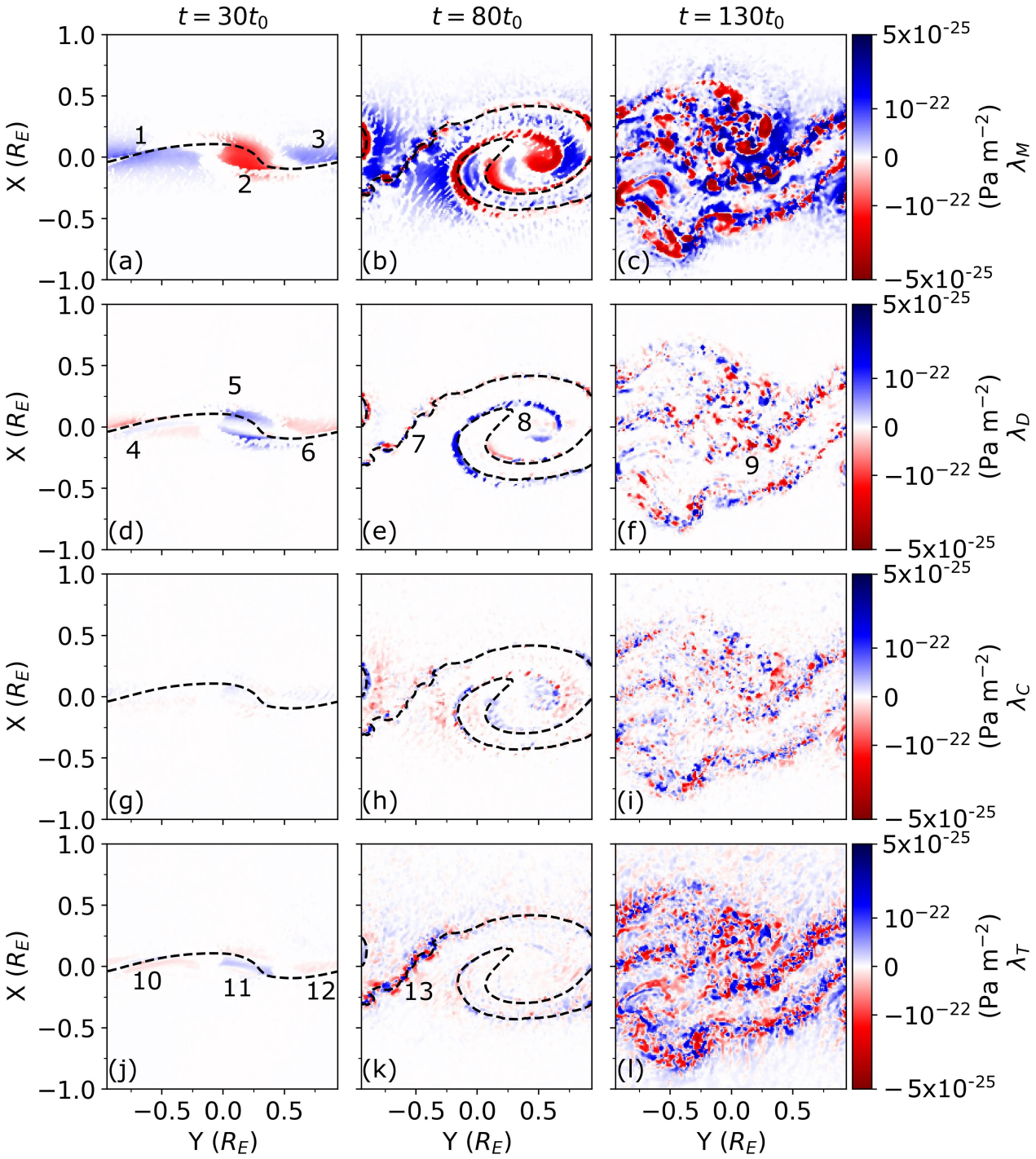


Figure 6.8: An equatorial ($z = 0$) view of each contributing term to λ_{MHD}. The values on a symlog$_{10}$ colour-scale where the linear scale is between $\pm 10^{-22}$ Pa m^{-2}. Negative regions (red) support λ_{MHD}, positive values (blue) are regions in opposition with λ_{MHD}. The quasi-linear ($t = 30t_0$), nonlinear surface roll-up ($t = 80t_0$) and turbulent ($t = 130t_0$) stages are shown. The dashed black line is plotted along $\rho = \rho_0$ contour as a proxy for the boundary between the two sides.

λ_{MHD} method is more precise, allowing for better vortex core identification. This suggests that the density gradient term is crucial for the reliable identification of multiple vortices in close proximity.

Furthermore, the density gradient term contributes to the existence of vortices at the outer edges of the simulation near the boundary (regions 4 and 6) where vortical momentum is not present (regions 1 and 3) – this may alternatively be a reduction in the non-vortex signature provided by the momentum term. Compressibility appears negligible at this stage. The rotational tension term is complex in regions 10, 11, 12 – there is weak opposition along the boundary (the dashed line) in regions 10, 11, and 12 implying tension is acting to stabilise the boundary as expected. However, the term appears to weakly support off the boundary in these regions too.

In the nonlinear surface roll-up stage, the density gradient term strongly opposes the larger scale vortex (region 8) but has little power on the small-scale secondary KHI (region 7) implying the term may have a scale- or KHI-stage- bias. The density gradient term appears to have the same relationship with the small-scale secondary KH vortices (region 7) as it has with the single vortex in the quasi-linear stage – it opposes the formation of a vortex at the centre of simulation on edges of the region of vortical momentum, but not at the centre where it supports it. The compressibility term does not appear to show any obvious trend and is generally small at this stage. The rotational magnetic tension term has become large in region 13 where the small-scale secondary KH vortices are present, opposing their formation. It appears to have little impact on the large scale vortex.

In the turbulent stage, the density gradient term appears to have the same relationship with the small-scale secondary KH vortices (region 9) as it has with the single vortex in the quasi-linear stage. This was also seen in region 7 meaning that the relationships between the physical effects for the secondary KHI at these stages can be considered as analogous to those for the large-scale vortex during its quasi-linear stage. The compressibility term again remains small with no clear relationship to the vortices. Rotational magnetic tension has further grown, now opposing the secondary KH vortices.

These trends have only been qualitatively explored in the equatorial plane. Further quantitative analysis can be made to better understand the general contributions over the entire simulation domain.

Figure 6.9 shows 2-dimensional histograms of the entire simulation domain comparing each term in equation 6.14c with λ_{MHD}. Across all three time steps the fluid compressibility term is small and poorly correlated to λ_{MHD} implying that fluid compressibility is not a dominant component in the

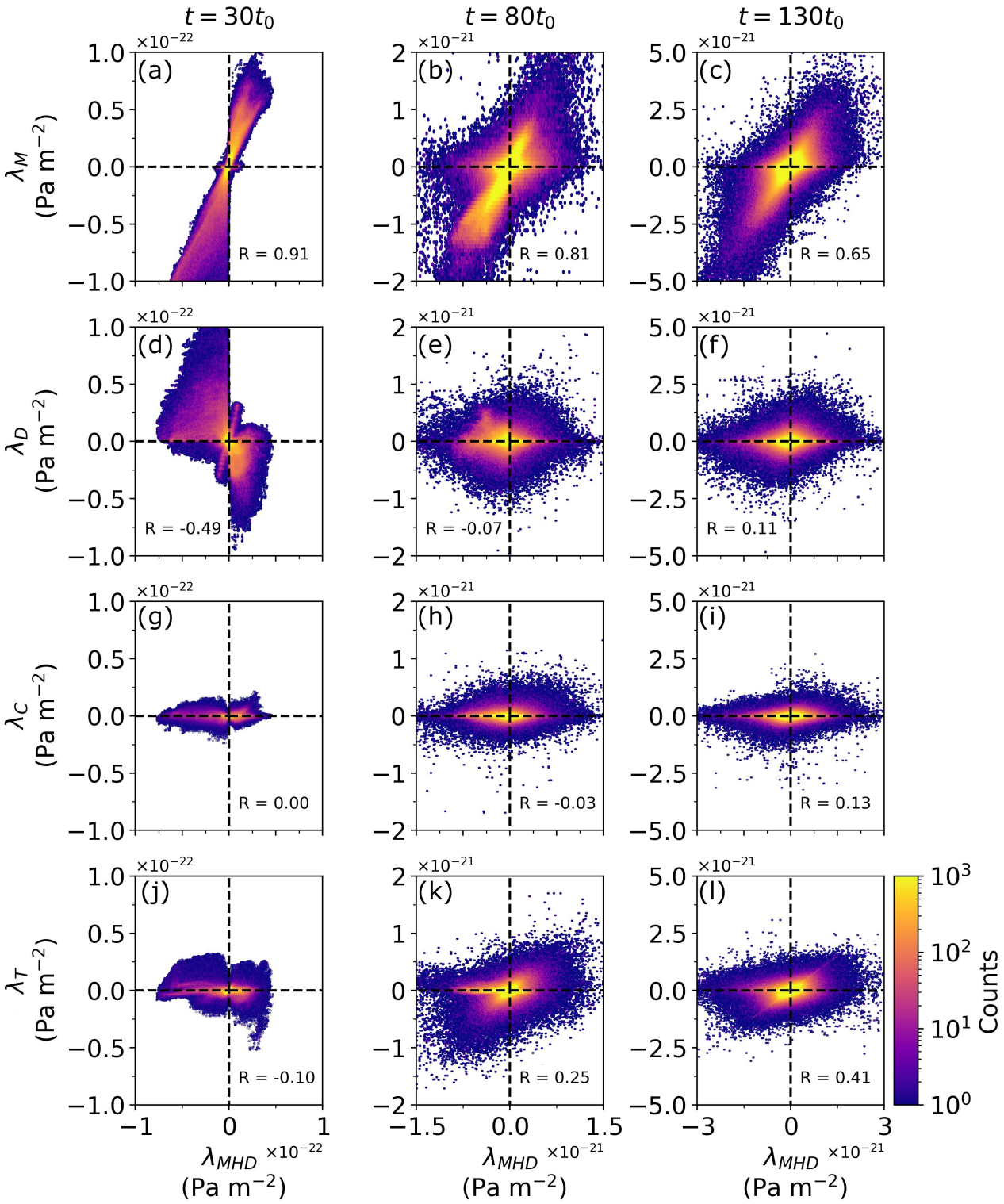


Figure 6.9: A 2D histogram across the simulation domain comparing λ_{MHD} with the terms contributing to it. Counts are plotted using a $\log_{10}$ colour scale. The R value shown is the Pearson's correlation coefficient.

existence of a KH vortex in this simulation. This might be attributed to the low fast magnetosonic Mach number used in this simulation, meaning the plasma is weakly compressible (representative of

the near-flank magnetopause environment; Ma et al. (2020)).

Figure 6.9d shows that the density gradient term strongly opposes the formation of a vortex in the quasi-linear stage of its growth but becomes less significant in the later stages. This suggests that the density difference across the shearing fluid is important in the initial stages of KH wave formation. Physically this makes sense, as the flow with a lower density will have insufficient momentum to change the direction of the high momentum flow with heavier mass making the initial wave harder to generate. Beyond the quasi-linear stage, the flow is sufficiently deformed that this density variation becomes less significant in comparison to the driving shear flow. There is a smaller secondary population in this term which supports the vortex and can also be seen in Figure 6.9d.

Figure 6.9j–l also indicates that the rotational component of the magnetic tension term becomes larger as the KHI advances. The plot suggests that during the turbulent stage, where vortices are expected to have a small spatial volume and thus larger tension effects, this term becomes a significant contributor to λ_{MHD}. This is also reflected in the Pearson's correlation value. Finally, the rotational component of the magnetic tension term has multiple populations within itself. In the nonlinear stage, there is a population which sits along a $y \propto x$ line which will be the population where the term supports the identification of a vortex – this likely corresponds to the small scale secondary KH vortices. The second population sits along the $y = 0$ line where the tension term does not contribute to λ_{MHD} – this likely corresponds to the single large scale vortex. This pattern is also present in the turbulent stage. There is a strong population along a $y \propto x$ line indicating that this term is important in the turbulent stage. However, there is a larger spread in the $y = 0$ population which may be because the histograms include the entire simulation domain and so will contain variations out-of-plane which are not seen in Figure 6.9.

6.3.4 Potential In Situ Applications

So far λ_{MHD} has been applied to gridded simulation data. However, it would be helpful to also explore its potential application to multi-point in situ measurements, though somewhat challenging. While the momentum and density gradient terms involve only first-order spatial derivatives, thus can be calculated with four suitably instrumented spacecraft in a tetrahedron, e.g. Magnetospheric Multiscale (MMS) (Burch et al. 2016), the compressibility term involves second-order derivatives

which require 10 spacecraft that do not lie on any quadric surface (Zhou and Shen 2024). Finally, the rotational tension term is challenging since it involves a Helmholtz decomposition, which is inherently non-local requiring information throughout space. It may be possible through equation 6.3b and suitable interpolation methods to estimate the decomposition for a multi-spacecraft mission such as HelioSwarm (Klein et al. 2023). Determining how to do this, however, is beyond the scope of this study.

Given these limitations, a tetrahedral spacecraft configuration is considered meaning only the momentum and density gradient terms can be used to construct the adapted pressure Hessian – this essentially gives in an incompressible version of λ_ρ denoted as λ_ρ^* herein. Section 6.3.2 demonstrated λ_ρ accurately approximates λ_{MHD} in this simulation during the linear and nonlinear roll-up stages, with Section 6.3.3 showing compressibility and magnetic tensions make negligible contributions. An example application is shown in Figure 6.10, which uses a spatial slice of the simulation data along the y-axis to emulate a spacecraft encounter with the magnetopause. The figure compares λ_{MHD} with λ_ρ and λ_ρ^*, demonstrating that λ_ρ and λ_ρ^* are near identical techniques which both approximate λ_{MHD} well in the linear, and nonlinear stages here. Unsurprisingly, the techniques appear to be less useful in the turbulent stage, however, they do still replicate the λ_{MHD} results overall. Thus λ_ρ^* may be a sensible proxy which could be realised by tetrahedral in-situ data. The qualitative visual differences between the three stages suggests they may also be used to distinguish between different evolutionary phases; a prospect chosen to be left for quantitative exploration in future work.

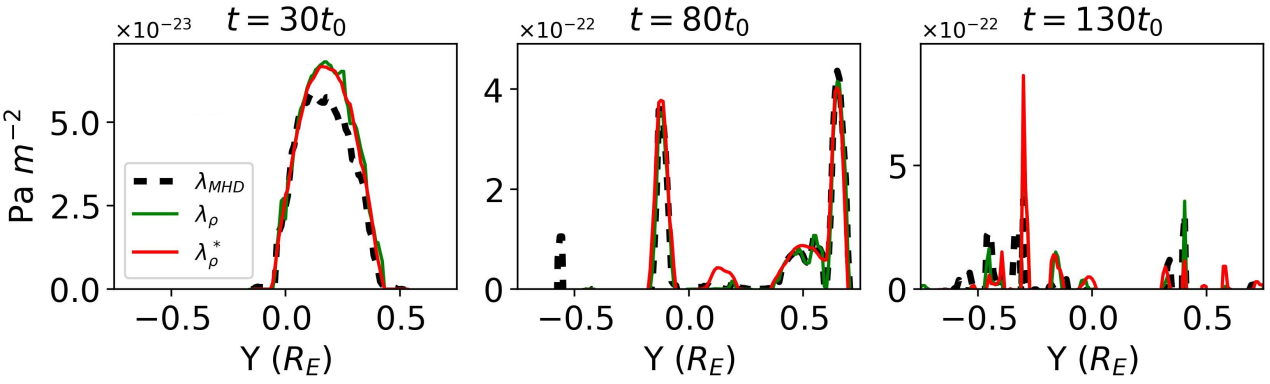


Figure 6.10: A spatial slice through the $x = z = 0$ line of the simulation showing $-\lambda_{\text{MHD}}$, $-\lambda_\rho$, and $-\lambda_\rho^*$ values. Only the vortex identifying values are shown.

Regular tetrahedra of spacecraft are considered, with mesocentres along the x-axis. Simulation

data are trilinearly interpolated to spacecraft locations. Since spacecraft separation affects the quality and scales over which gradients can be estimated (De Keyser 2008), the tetrahedra's radial distances r vary as 60km, 100km, and 200km (the simulation grid-spacing is 60km). These cover the range of MMS separations over the course of the mission, excluding its smallest tetrahedron sizes. Gradients are calculated using techniques outlined in Paschmann and Daly (1998) and are used to calculate Q, λ_2, $\overline{\lambda_2}$, and λ_ρ^*. Figure 6.11 shows how each technique performs with different tetrahedra sizes, compared also with the true values from the simulation grid.

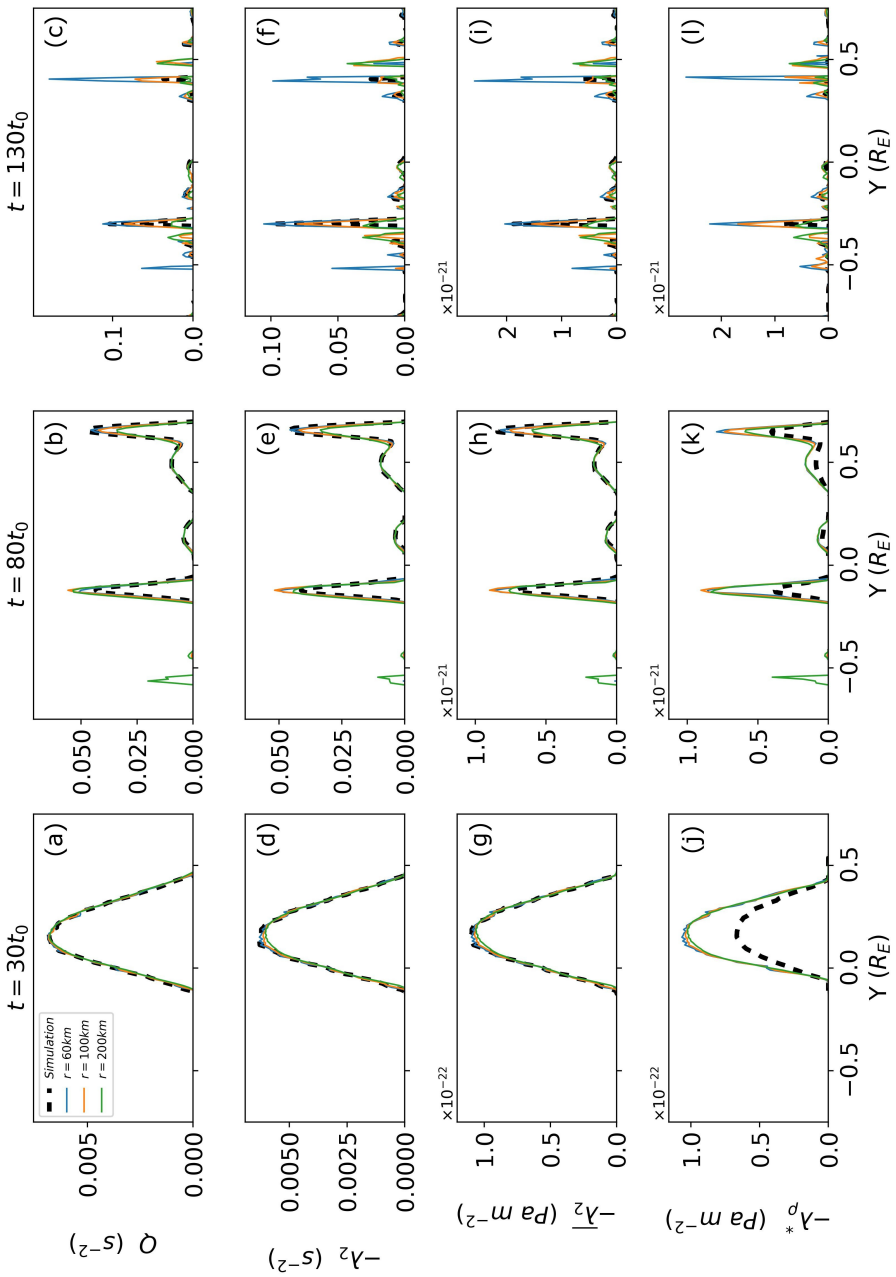


Figure 6.11: Vortex criteria values are shown using multi-spacecraft techniques with a mesocentre along the spatial slice through $x = z = 0$ of the simulation with varying radial distances between spacecraft. Only the vortex identifying values are shown.

Figure 6.11 shows that all the techniques considered might be applied to virtual spacecraft observations with varying success. Generally speaking, the smaller the tetrahedron, the closer the virtual spacecraft value is to the simulation value. All the techniques reliably approximate the simulation values during the linear and nonlinear stages of the KHI regardless of virtual spacecraft separation. Interestingly, the smaller tetrahedron separation more precisely mimics the simulation results of all the techniques but contains larger amounts of noise, likely due to the interpolation – this is best seen in the quasi-linear stage. Notably, the widths of the peaks in the λ_ρ^* technique are narrower than those in the less advanced techniques implying that a more specific region is being located by this technique – the core of the vortex. This is easiest seen when comparing Figure 6.11a and 6.11j.

6.4 Summary

The Kelvin-Helmholtz instability is a dominant driver of the viscous-like transfer of mass, momentum, and energy across the magnetopause through surface waves and their coupled vortices. A vortex detection method suitable for MHD, called λ_{MHD}, has been derived by self-consistently incorporating the $\mathbf{J} \times \mathbf{B}$ Lorentz force into the λ-family of hydrodynamic vortex identification techniques. These methods define a vortex as a local minimum within some 2D plane of an adapted pressure field. Within ideal MHD, the effective pressure field is defined as the sum of the thermal pressure, magnetic pressure, and the pressure-like part of the magnetic tension which is extracted using a Helmholtz decomposition. This is then adapted by removing the effects of unsteady straining, which can result in pressure minima unrelated to vortices, which is key to the λ-family methods' success. λ_{MHD} has been validated against the velocity field and other hydrodynamic techniques using a local three-dimensional MHD simulation representative of near-flank magnetopause conditions under northward interplanetary magnetic field (IMF). The technique has shown that commonly used vortex identification techniques such as total pressure minima (Nykyri et al. 2017; Rice et al. 2022) are not sufficient in identifying a vortex beyond the linear stages.

λ_{MHD} is composed of four components: vortical momentum, density gradients, fluid compressibility, and the rotational part of the magnetic tension. These effects have separately been shown to

influence KHI formation (e.g. Chandrasekhar 1961; Pu and Kivelson 1983; Miura and Pritchett 1982; Amerstorfer et al. 2010). In this work it was found that the vortical momentum dominates λ_{MHD} in the simulation at all times, meaning that hydrodynamic techniques which capture this effect only, may be good proxies for λ_{MHD}. During the linear growth phase, density gradients generally act to oppose vortex formation but become less important in the later stages of vortex evolution. This is in agreement with previous work where plasma inhomogeneity was found to not affect growth rate (Ma et al. 2024). The rotational part of the magnetic tension has been shown to become important in small-scale structures suggesting that the hydrodynamic definitions would be insufficient at identifying these. Fluid compressibility was found to be insignificant at all stages.

Some of these results will be due to the choice of plasma parameters used, which are representative of the near-flank magnetopause. Dimensionless scaling arguments might infer the implications of this work under different plasma regimes though. The simulation is only weakly compressible ($M_f \sim 0.4$), but compressibility effects are expected to vary as $\sim M_f^2$ (Palermo et al. 2011). This scaling is assumed for the compressibility term, λ_C. It is also assumed that the vortical momentum term, λ_M, might be unaffected by the fast magnetosonic Mach number. Over the three stages of the simulation presented, the ratio of these terms' standard deviations, $\sigma(\lambda_C)/\sigma(\lambda_M)$, constitute 6%, 14%, and 21% respectively. For the compressibility term to be as significant as the momentum term during the quasi-linear regime, scaling arguments suggest a supermagnetosonic Mach number ($M_f \gtrsim 1.6$) would be needed. In contrast, for the non-linear and turbulent stage, trans-magnetosonic Mach numbers ($0.8 \lesssim M_f \lesssim 1.2$) might suffice. These Mach numbers are likely underestimates as the poor correlation of compressibility with λ_{MHD} has not been taken into account. These estimates are in agreement with previous works which suggest compressibility affects the later stages of the KHI (growth rate) more than the initial stages (lower critical velocity). Similar arguments can be made for the magnetic tension term, λ_T, by considering the Alfvén Mach number which is $M_A \sim 0.9$ and $M_A \sim 0.6$ in regions 1 and 2 respectively. The relative importance of magnetic tension should scale as $\sim M_A^{-2}$ (equation 3.6). Performing similar analysis to compressibility, the ratio of the standard deviations, $\sigma(\lambda_T)/\sigma(\lambda_M)$, is found to be 10%, 27%, and 47% respectively. For the tension to be of similar importance to the momentum suggests weaker Alfvén Mach numbers $0.3 \lesssim M_A \lesssim 0.6$ may be required on both sides (likely overestimates due to weak correlation). It is expected from linear

theory that the field being modelled perfectly transverse to the shear flow will result in the magnetic tension playing a sub-dominant role especially during the linear growth (Chandrasekhar 1961). Note this scaling argument does not take into account how tension's importance in λ_{MHD} may vary by introducing magnetic shear. This is known to not only increase the tension's stabilising effect on the KHI, but also breaks the north-south symmetry, complicating the KHI's evolution with secondary processes such as vortex-induced reconnection being triggered earlier in the instabilities lifetime than otherwise expected (Vernisse et al. 2016; Fadanelli et al. 2018; Sisti et al. 2019). Our discussion overall highlights how the different physical effects known to affect the KHI depend on both plasma conditions and evolutionary stage.

Due to the higher-order gradients and non-local Helmholtz decomposition required for the calculation of λ_{MHD}, it cannot simply be applied to current tetrahedral spacecraft missions (e.g. MMS) – however this might change with future missions with more spacecraft such as HelioSwarm (Klein et al. 2023; Zhou and Shen 2024). For tetrahedral missions, an incompressible version of the hydrodynamic definition λ_ρ is the most advanced definition which can be applied. Virtual satellite data from the simulation suggest that this is a good approximation to λ_{MHD}, better than other simpler techniques. Despite this, there are drawbacks of using these for spacecraft data which are not explored here, such as cold magnetospheric ions making it difficult to measure densities and velocities (Archer et al. 2019). It would be advantageous to make use of only measurements unaffected by such instrumental effects, such as the magnetic field. Cai et al. (2018) did this assuming that magnetic field perturbations were correlated to those in velocity. However, this is not necessarily the case as the frozen-in flux theorem applies to magnetic field lines rather than vectors. In linear MHD wave theory the vector perturbations in magnetic field depend on plasma displacement variations along field-lines (Singer et al. 1981). Recent investigations have also shown that in realistic magnetic geometries, magnetic perturbations can even be oppositely polarised to those of the velocity (Archer et al. 2022). Therefore, care is needed in using other quantities as proxies in these vortex identification methods and ideally a full derivation is required for each.

On the whole, all the different techniques explored are useful for identifying vortices in magnetised fluids, and which technique to use is dependent on the desired purpose. Section 6.3.2 shows that hydrodynamic techniques are valid to use in MHD fluids with varying success. The Q, λ_2, and $\overline{\lambda_2}$

techniques were found to reliably locate broad vortical regions, which provide general information of the shape and location of the large-scale vortex. Alternatively, the λ_ρ, and λ_{MHD} techniques, through incorporating further physical effects, allow them to better hone in on the vortex core specifically instead of the wider vortical region. This result is also echoed when exploring tetrahedral spacecraft applications. There are, however, disadvantages to these techniques. The most obvious is that the rotational axis and orientation of the vortex is not captured by any of the scalar criteria considered, meaning complimentary analysis is needed for this (Liu et al. 2019). Another issue is the sensitivity of the different methods, particularly λ_ρ, and λ_{MHD}, to any vortex threshold chosen – a subject of ongoing studies within hydrodynamics also (e.g. Chakraborty et al. 2005; Pierce et al. 2013; Liu et al. 2019). It is important to note that there is no single proper vortex threshold — especially if strong and weak vortices co-exist. Higher thresholds neglect weaker and smaller-scale vortices, while potentially splitting up larger-scale vortices due to their substructure. On the other hand, lower thresholds smear out weaker vortices by over saturating the stronger ones and may introduce fine-scale structure, which could be related to turbulence or merely instrument/numerical noise. Consequently, it is suggested that any practical applications of a vortex identification method uses some data-driven threshold, bearing in mind the focus of the study at hand and how the threshold level will affect this.

Extensions to the work presented will further our understanding of the factors important for the formation and detection of KH vortices at the magnetopause. Applications of λ_{MHD} to real multi-point spacecraft data is required. Further investigation into how the drivers of vortex identification – in particular compressibility – change in a more realistic magnetospheric environment needs to be performed. The most obvious approach would be applications to several local MHD runs with different plasma conditions (e.g. Otto 1990; Nykyri and Otto 2001; Ma et al. 2014a; Ma et al. 2014b; Ma et al. 2017) to help determine how the relationships presented vary with plasma parameters. This would be the simplest and quickest to implement, however the limitations of the current study concerning the global magnetic field geometry and varying plasma conditions as the KHI evolve will still be present. This leads to the next chapter of this thesis where an application to a global magnetosphere model is presented in the hope to capture more realistic magnetic geometries and evolving plasma conditions.

CHAPTER 7

Effects of a realistic magnetic and plasma environment on KH-generated vortices in a global MHD simulation

7.1 Introduction

When studying the KHI, it is common to make simplifying assumptions about the plasma environment the KHI evolves in such as compressibility, homogeneity, and idealised geometry. Studies also typically make simplifying assumptions about the magnetic geometry e.g. by using box models (Archer et al. 2024; Ma et al. 2024). Unfortunately, these assumptions are not wholly valid; in reality the plasma environment at the magnetopause is highly inhomogeneous and compressible (e.g. Spreiter et al. 1966), and the magnetic field lines are strongly curved (e.g. Hwang et al. 2022). As a result, the studies that use these simplifying assumptions fail to capture the effects this continuously evolving environment has on the KHI and its evolution, divorcing studies which can capture these conditions (global simulations and in-situ measurements) from those which cannot (local simulations). To bridge the gap between these studies, an understanding about the significance of the varying plasma and magnetic environment on the evolution of the KHI is needed to discern between the changes to the KHI which is caused by KHI evolution alone, and those caused by the changing plasma environment

and magnetic field geometry.

To achieve this, the following work uses a global three-dimensional MHD simulation which exhibits strong KH-behaviour to capture the effect the variable magnetopause conditions has on the KHI. The λ_{MHD} vortex identification technique is then applied to this simulation to isolate the vortices at the flanks, this is necessary as the vortices are the only feature present throughout the entire KH-evolution allowing for all stages to be captured unbiased by differing techniques. λ_{MHD} is then decomposed to allow for an analysis of how different plasma conditions effect the KH-vortices as they evolve and advect around the magnetopause. Three-dimensional visualisation and analysis tools are then used to reveal the complex interaction between KH-vortices and Earth's magnetic field lines. The results presented in this chapter reveal the three-dimensional structure of a KH-vortex which has never been visualised. Furthermore, the study finds that the inner- and outer-modes of the KHI evolve through different plasma and geomagnetic field environments and as a result, they are effected differently by the magnetic field and plasma environment.

This chapter is structured by first introducing the simulation (section 7.2). This is followed by how λ_{MHD} is calculated in a global MHD simulation (Section 7.3). Next, the location of KH-vortices is explored (Section 7.4). The role of a realistic plasma environment (Section 7.5) and the impact of a realistic magnetic field (Section 7.6) is then analysed in this simulation. Finally, a brief investigation is conducted into how cusp reconnection is a source driver for global MSWs and how flux ropes can cause magnetopause perturbations (Section 7.7). This chapter closes with a summary of results and conclusion.

7.2 Simulation Overview

The global MHD simulation outlined in Section 4.2 is used to simulate Earth's magnetosphere for this study. The driving solar wind and IMF conditions are outlined in Table 7.1. Simple IMF driving conditions were chosen as in both incompressible (Chandrasekhar 1961) and compressible (Pu and Kivelson 1983; Miura and Pritchett 1982) linear theory it has been shown that magnetic field stabilisation is the most important factor in KH-formation (Southwood 1968; Walker 1981). This has been confirmed by observation statistics (Kavosi and Raeder 2015) which show that perfectly

northward IMF provides the best conditions for the KHI to occur on the magnetopause. As well as this, northward conditions reduce complications from introducing magnetic shear in the vortices which results in VIR (e.g. Nakamura et al. 2017).

The values of the solar wind are nominal with perhaps a slightly faster wind than the average of a 12 year statistical study which found an average speed of $\sim 350\,\mathrm{km\,s^{-1}}$ (Ma et al. 2020). This was chosen as faster wind has been shown to increase the likelihood of of the KHI forming (Kavosi and Raeder 2015). The magnetosphere was initialised under southward IMF conditions, $(0, 0, -5)^T$ nT, for two hours of simulation time to strongly drive the Dungey cycle (Dungey 1955) and empty plasma from the initialised magnetosphere. Following this, the IMF direction was flipped to perfectly northward, $(0, 0, 5)^T$ nT, with the solar wind plasma remaining unchanged. Under these conditions, the magnetosphere was driven for a further two hours to allow for all the southward IMF to leave the simulation domain and the magnetosphere to reach a quasi-stationary state. Once this occurred, the input was unchanged and data was taken every 15 seconds for 27 minutes and 30 seconds of simulation time.

The simulation is set up such that the origin is at the centre of the Earth, X points anti-sunward along the Sun-Earth line, Z intersects the magnetic poles pointing northward, and the Y direction completes the right-handed set. The simulation is solved on a uniform Cartesian grid with square grid cells of side length $0.25\,\mathrm{R_E}$. The X dimension contains 480 cells spanning from $-30\,\mathrm{R_E}$ to $90\,\mathrm{R_E}$, the Y and Z dimensions contains 320 cells spanning from $-40\,\mathrm{R_E}$ to $40\,\mathrm{R_E}$. The boundary at $X = -30$ is an inflow boundary where the solar wind is injected, the other simulation surfaces are open boundaries allowing the plasma and field to freely leave the simulation domain. The simulation also contains a coupled thin-shell ionosphere model as described in Section 4.2 at the inner-boundary which is a radial distance of $4\,\mathrm{R_E}$ from the simulation centre. The Pederson conductivity is set at $10\,\mathrm{Sm^{-1}}$ as this is representative of the dayside ionosphere, the Hall conductivity is set to null. The dipole tilt is ignored as it has been shown that this can effect where the KHI forms (Foullon et al. 2008; Kavosi et al. 2023). Co-rotation of the inner-boundary is also switched off as this has been suggested to create asymmetric driving (Zhang et al. 2018a).

The symmetric driving conditions and Earth setup of the simulation should theoretically result in a perfectly symmetric simulation with both flanks being mirrored across the Sun-Earth line. However,

Quantity	Value
Simulation Cell Size	$0.25\,\mathrm{R_E}^3$
Simulation Domain Shape	$L_x : \{-30, 90\}\,R_E\ ;\ L_{y,z} : \{-40, 40\}\,R_E$
Simulation Domain Size	$L_x = 480\ ;\ L_{y,z} = 320$
Interplanetary Magnetic Field	$(0, 0, 0.5)^T$ nT
Solarwind Number Density	$5\,\mathrm{cm}^{-3}$
Solarwind Velocity	$(400, 0, 0)^T$ $\mathrm{km\,s}^{-1}$

Table 7.1: Table showing the solar wind and IMF conditions of the simulation.

this is not the case. Recall that Gorgon utilises the Yee (1966) staggered grid as discussed in Section 4.2. Despite the symmetric driving conditions, it is thought that the intersection of the staggered grid with the inner-boundary can introduce asymmetries in the simulation numerics.

Figure 7.1 shows equatorial (A, C, E) and noon-midnight plane (B, D, F) snapshots of the simulation after 4 hours 17 minutes and 15 seconds of simulation time. The colour corresponds to the magnitude of the magnetic field (panels A, B), magnitude of the velocity field (panels C, D), and the density (panels E, F). The dashed black line shows the simulation inner-boundary which is a sphere of radius $4\,\mathrm{R_E}$. In panels B, C, D there are grey stream lines which in panel B represent the magnetic field lines in this plane, and in C, D represent the two-dimensional flow in the plane shown.

As different magnetopause identification methods in simulations are known to not always be co-located (García and Hughes 2007; Gordeev et al. 2013) a proxy has been used which is shown as the dotted line. This proxy is the open-closed magnetic field line boundary of the time-averaged magnetic field coined as the equilibrium magnetopause. The equilibrium magnetopause location is found by using a 4th order Runge-Kutta field line tracer described in Mejnertsen et al. (2021) to identify the open-closed magnetic field boundary of the time-averaged magnetic field. This boundary is then smoothed over using a 15x15x15-cell ($3.75\,\mathrm{R_E} \times 3.75\,\mathrm{R_E} \times 3.75\,\mathrm{R_E}$) median filter to reduce any anomalous identifications. The equilibrium boundary is used over the instantaneous boundary as it shows the location of where the magnetopause should be if it were at equilibrium meaning that the wave amplitudes can be seen. Broadly speaking, the equilibrium magnetopause boundary appears to fit the data well, especially sunward of the dawn-dusk line where the magnetopause is expected to not exhibit strong KH-waves. This is best seen in panels C and D which show the magnitude of the

velocity to sharply drop at the boundary. The equilibrium boundary is especially useful beyond the dawn-dusk line, where the KHI is expected to be growing more non-linearly and therefore have larger amplitude waves (e.g. Li et al. 2012) meaning that it is hard to assume where the boundary would be if it were at rest because the waves are no longer approximately sinusoidal in nature.

Figure 7.1B shows how the northward IMF conditions result in magnetic field line draping around the magnetopause (Song et al. 1988). The deformed dipole shape ('squashed' on the dayside and 'expanded' on the nightside) can also be seen, as can the extension of the field lines in the plasma sheet. The bow shock is visible in all the quantities, as is the plasma sheet. The cusp indentation region can be seen in panels B and F.

The black box in panels A, C, E highlights a transient region of fast return flow with low density and magnetic field in the simulation which lasts for a few minutes. It is suggested to be anomalous return flow in the simulation, and is mentioned here as it may cause a larger velocity shear at the dawn flank magnetopause compared to the dusk. This may explain why the KH-waves have larger amplitude on the dawn flank compared to the dusk flank in this otherwise symmetrically-driven simulation. Other consequences of this anomalous return flow may be a thicker LLBL on the dawn side of the magnetosphere altering the plasma conditions and effecting the inner- and outer-modes differently (Lee et al. 1981; Pu and Kivelson 1983; Miura and Pritchett 1982). However, the existence of this feature is not necessarily unphysical as return flow is a physical phenomena which can be triggered, for example, by tail-reconnection (Angelopoulos et al. 1992). It is unclear what is causing this return flow and, as it is not of immediate relevance to this study, it is left unexplored. There are no immediate signs suggesting it is causing unphysical results as the dawn flank is not behaving in an extreme way e.g. the wave amplitude is comparable on both flanks. A closer inspection of the magnetopause is needed to better reveal the KH-waves present at the flanks.

Figure 7.2 is a subregion of Figure 7.1 showing the waves along the dawn-flank and northward midnight meridian tailward of the cusp magnetopause. The arrows point to deformations in the magnetopause boundary. The tailward of the cusp deformations appear to be less characteristic of the KHI given they are inhomogeneous and appear to be more like a wave-packet than a continuous instability. The existence of tailward of the cusp waves is thought to contradict the typically assumed to be true linear KH theory (Chandrasekhar 1961) due to the magnetic tension stabilisation force

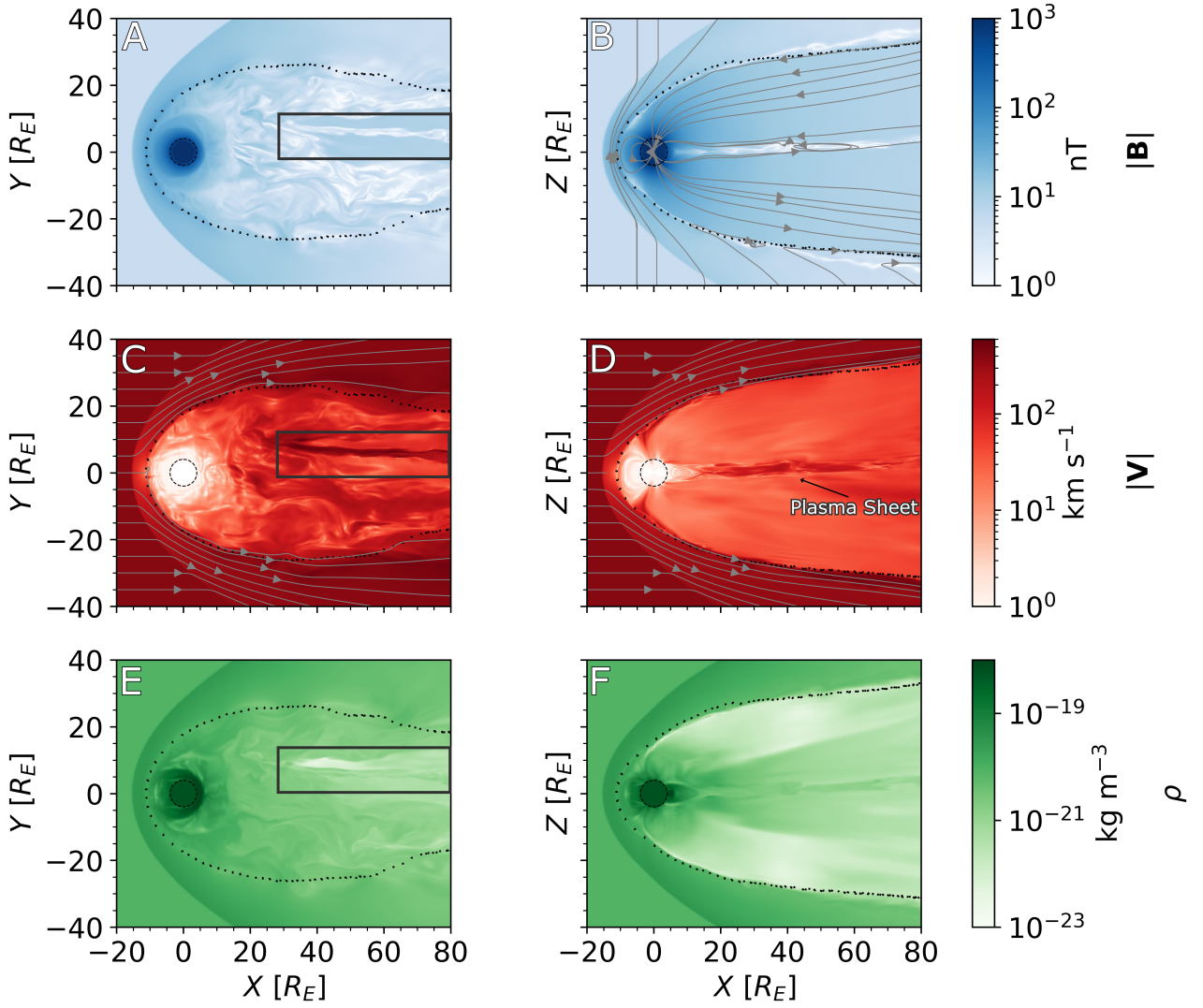


Figure 7.1: Equatorial (A, C, E) and noon-midnight (B, D, F) cuts of the simulation after 4 hours 17 minutes and 15 seconds of simulation time. The colour corresponds to the magnitude of the magnetic field (panels A, B), magnitude of the velocity field (panels C, D), and the density (panels E, F). The dashed black line shows the simulation inner-boundary which is a sphere of radius 4.5 R_E. The dotted line is the equilibrium magnetopause. The black box highlights the return flow discussed in the text.

originating from the magnetic field orientation seen in Figure 7.2. The formation of KH-waves in this region would contradict the findings of Southwood (1968) and Walker (1981) who show that the magnetic field orientation is the most important factor in KH-stability.

At this point, the common approach in the literature would be to apply incompressible linear theory in the form of the KH-criterion. It is important to stress that this equation is simply not valid in this simulation which includes a finite thickness magnetopause and compressibility. However, it is useful as a lower-bound for whether a surface is KH-unstable as compressible effects are thought to

make a boundary more unstable but not significantly alter the limit (Pu and Kivelson 1983).

Recall Equation 3.6 (Chandrasekhar 1961),

$$\underbrace{\left(\hat{\mathbf{k}}\cdot(\mathbf{v}_1-\mathbf{v}_2)\right)^2}_{\text{Flow Shear Driver}} - \underbrace{\frac{\rho_1+\rho_2}{\rho_1\rho_2}}_{\text{Density Weighting}} \underbrace{\frac{1}{\mu_0}\left[\left(\mathbf{B}_1\cdot\hat{\mathbf{k}}\right)^2+\left(\mathbf{B}_2\cdot\hat{\mathbf{k}}\right)^2\right]}_{\text{Magnetic Tension Stabiliser}} > 0 \text{ then KHI unstable.}$$

From this equation it is shown that the magnetic tension stabiliser should be at a maximum when the field is aligned with the wave vector. By assuming the wave vector is pointing in the $\hat{X}$ direction, which in this location is relatively appropriate given that surface waves can only propagate tangential to the magnetopause which in these locations is essentially in the X-direction, it can be seen from Panels A and B that the low-latitude magnetopause is likely to be KH-unstable and the high-latitude is likely to be KH-stable. By taking example plasma and field values from either side of the boundary at the crossed coordinates in panel A at $(7.5, 21 \pm 2, 0)^{\mathsf{T}}\ R_E$, the test can be performed and the value is $\sim 5.5 \times 10^{10}\,\mathrm{m^2 s^{-2}}$. This is more than 0 suggesting that the low-latitudes are KH-unstable according to incompressible linear theory. Extending this idea to the compressible regime, Pu and Kivelson (1983) have shown compressibility destabilises the boundary meaning that this result would not change if compressible theory were used. Taking the values in panel B at $(35, 0, 28.5 \pm 2)^{\mathsf{T}}\ R_E$ and performing the test on the tailward of the cusp magnetopause gives a value of $\sim -135 \times 10^{10}\,\mathrm{m^2 s^{-2}}$. This is significantly less than 0 suggesting that the tailward of the cusp magnetopause is KH-stable according to incompressible linear theory. As compressibility is not thought to significantly alter this limit (Pu and Kivelson 1983), it is clear that the tailward of the cusp boundary must be KH-stable according to theory.

However, these crude estimations are not totally sufficient in ruling out the KHI as the theory is just not valid in this region for many reasons e.g. compressibility, not linear stages. Another convincing reason why the tailward of the cusp waves are not thought to be KH-driven is that the deformations do not look periodic in anyway, and if the wave were to originate from the KHI, there would have to be some periodicity. If the wave started in the non-linear stages, this may not be the case but given there are no structures in the solar wind which could drive the surface perturbations (e.g. pressure pulses Sibeck 1990), the tailward of the cusp deformations are unlikely to be KH-waves and therefore must be driven by some other internal mechanism.

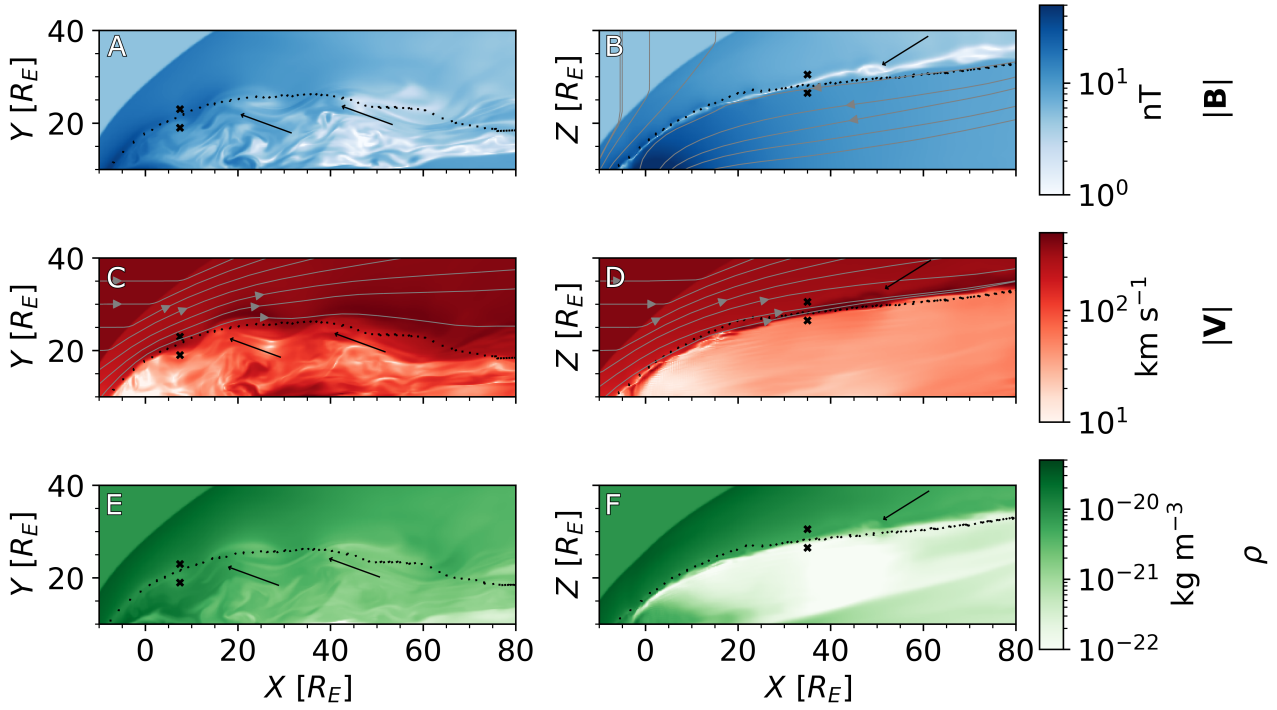


Figure 7.2: Zoom-ins on the dawn-flank magnetopause in the equatorial plane (A, C, E) and the northward magnetopause of the noon-midnight plane (B, D, F) of the simulation after 4 hours 17 minutes and 15 seconds of simulation time. The colour corresponds to the magnitude of the magnetic field (panels A, B), magnitude of the velocity field (panels C, D), and the density (panels E, F). The dotted line is the equilibrium magnetopause boundary. The arrows point to visible magnetopause deformations and the crosses are locations used to calculate how unstable the boundaries are to the KHI. The Y- and Z- axis have the same range.

Ruling out the tailward of the cusp perturbations from the study, the λ_{MHD} vortex identification technique can now be applied. This technique is used as it can identify KH-vortices in all the stages of the KHI without bias meaning it can allow for this study into the effects of a realistic magnetic and plasma environment on KH-generated vortices.

7.3 The Effective Pressure

Recall that the λ_{MHD} technique works by defining a vortex as a minima in an effective pressure field. This field is found through a Helmholtz decomposition of the magnetic tension. As a result, applying λ_{MHD} in a global simulation requires a different approach to the Fourier Helmholtz decomposition method used in the previous chapter as the inflow boundary, inner boundary, and the open boundary conditions in the Gorgon simulation invalidates the periodic assumptions needed for the application

of the Fourier method. To overcome this challenge, the Hockney-Eastwood solver (Hockney and Eastwood 2021) discussed in Chapter 5 is used to solve the Green's function solution to the Helmholtz decomposition.

As well as the issue with boundary conditions, the numerical finite-difference methods used to calculate the gradients in $\mathbf{B}$ to construct the magnetic tension, $\boldsymbol{\tau} = (\mathbf{B} \cdot \boldsymbol{\nabla})\,\mathbf{B}/\mu_0$, becomes noisy and unreliable in regions with strong gradients e.g. close to the inner boundary. Recall that this is overcome in the simulation numerics by computing the field as a split curl-free dipole, $\mathbf{B}_{\text{Dipole}}$, and a non-dipolar component, $\mathbf{B_1} = \boldsymbol{\nabla} \times \mathbf{A}$, where only the latter is used to calculate the currents (Tanaka 1994; Mejnertsen 2018; Eggington 2021). As the entire simulation is integrated over in the computation of the Helmholtz decomposition, global errors arise due to the sharp gradients in the near-Earth region if the decomposition is applied to the magnetic tension. To reduce numerical noise due to this, the Helmholtz decomposition is performed on the $\mathbf{J} \times \mathbf{B}$ Lorentz force instead as the magnetic pressure gradients, completely cancel magnetic tension forces in a dipole field. Using the Lorentz force is mathematically synonymous to the previous chapter as the pressure-like irrotational part of the Lorentz force is equal to the sum of the traditional magnetic pressure, $P_{\text{mag}} = |\mathbf{B}|^2/2\mu_0$, and pressure due to tension, i.e.

$$P_{\text{Lorentz}} = P_{\text{mag}} + P_{\text{ten}}, \tag{7.1}$$

meaning that the rotational component of $\mathbf{J} \times \mathbf{B}$ should be equal to the rotational component of the magnetic tension, $\boldsymbol{\tau}_{\text{Rot}}$. This allows for the effective pressure to be written as

$$P_{\text{eff}} = P_{\text{therm}} + P_{\text{mag}} + P_{\text{ten}} = P_{\text{therm}} + P_{\text{Lorentz}}. \tag{7.2}$$

By substituting the Lorentz force into the Green's function solution to the Helmholtz decomposition

of the magnetic tension (see Chapter 5), the Lorentz pressure is defined as

$$P_{\text{Lorentz}}(\mathbf{r}) = \int_V \left[\boldsymbol{\nabla}' \cdot (\mathbf{J}(\mathbf{r}') \times \mathbf{B}(\mathbf{r}'))\right] \mathcal{G}(\mathbf{r} - \mathbf{r}')\, \mathrm{d}V' - \oint_S \left[\hat{\mathbf{n}}' \cdot (\mathbf{J}(\mathbf{r}') \times \mathbf{B}(\mathbf{r}'))\right] \mathcal{G}(\mathbf{r} - \mathbf{r}')\, \mathrm{d}S' \tag{7.3a}$$

$$U_i(\mathbf{r}) = \int_V \left[\boldsymbol{\nabla}' \times (\mathbf{J}(\mathbf{r}') \times \mathbf{B}(\mathbf{r}'))\right]_i \mathcal{G}(\mathbf{r} - \mathbf{r}')\, \mathrm{d}V' - \oint_S \left[\hat{\mathbf{n}}' \times (\mathbf{J}(\mathbf{r}') \times \mathbf{B}(\mathbf{r}'))\right]_i \mathcal{G}(\mathbf{r} - \mathbf{r}')\, \mathrm{d}S' \tag{7.3b}$$

where S is the enclosing surface of V.

It is now apparent that both the volume and surface integral of $P_{\text{Lorentz}}(\mathbf{r})$ and each component of $U_i(\mathbf{r})$ for $i = x, y, z$ can be solved using the Hockey-Eastwood solver. It is important to note that Gorgon has both an inner and outer boundary meaning that there are two surfaces which are integrated over. The integration over the inner boundary is set as a sphere with a radius of $6\,R_E$, which is larger than the simulation inner boundary of $4\,R_E$ to reduce any issues with spurious values close to the inner-boundary. For the inner boundary the normal vectors are computed individually at each cell.

Figure 7.3 shows the variation of the tension pressure, thermal pressure, magnetic pressure, Lorentz pressure, and the effective pressure fields about their respective mean – this eliminates any bias from P_{Tension} and P_{Lorentz} lacking uniqueness. A threshold of 0.1 nPa is placed on the mean to prevent it being biased by the large number of small pressure values in the solar wind. The figure shows snapshots of the equatorial plane (A, C, E, G, I) and noon-midnight plane (B, D, F, H, J) of the simulation after 4 hours, 17 minutes, and 15 seconds of simulation time. In each panel there is a dashed line at the inner-boundary at $6\,\mathrm{R_E}$ and a dotted line at the equilibrium magnetopause boundary as described above. Panels A, B show the thermal pressure, $P_{\text{Therm}} = nk_B(T_i + T_e)$, perturbations, panels C, D show the magnetic pressure, $P_{\text{mag}} = |\mathbf{B}|^2/2\mu_0$, variations, panels E, F show the Lorentz pressure variations which has been calculated using the Hockney-Eastwood method to solve Equation 7.3a. Panels G, H show the tension pressure variations which has been calculated by taking the perturbations of Equation 7.3a and rearranging such that

$$\delta P_{\text{Tension}} = \delta P_{\text{Lorentz}} - \delta P_{\text{Magnetic}}. \tag{7.4}$$

Finally panels I, J show the effective pressure fluctuations.

The magnetic and thermal pressures are the dominant pressures in Earth's magnetosphere. The magnetic pressure perturbations in Panels A, B show how the nose of the magnetopause has a spike in pressure due to the solar wind and IMF compressing the geomagnetic dipolar field. The magnetic pressure perturbations are large around the inner boundary with the colour scale saturating due to the strong magnetic field close to Earth. Generally speaking the plasma sheet is mostly homogeneous in the magnetic pressure. At the magnetopause, there are no obvious signs of magnetic pressure minima which could be a consequence of KHI waves in either plane. The thermal pressure perturbations in panels C, D show how in general the magnetosphere and magnetosheath has a higher pressure towards the nose of the magnetopause and is lower in the tail with the mean value sitting at around the $X = 0$ line region. This is a consequence of the dayside magnetosheath being hotter and more dense than the night side, due to approximate adiabatic expansion of the magnetosheath plasma (Spreiter et al. 1966). Again, the thermal pressure does not contain any clear pressure minima which could be signatures of KHI waves in either plane.

The Lorentz pressure perturbations are shown in panels E, F. By comparing the Lorentz pressure to the magnetic pressure, some understanding about the importance of the pressure due to magnetic tension can be gained. The large spikes close to Earth in the magnetic pressure are eliminated by the inclusion of the pressure due to tension. This is because a dipolar field is a force-free field implying that the magnetic pressure and the pressure due to tension should cancel close to Earth when the field is approximately dipolar. The night side has a decaying value which can be simply explained as the field is decaying approximately as $\sim 1/|\mathbf{r}|^3$. Along the magnetopause behind the cusps, there are small local low pressure spikes which are in the Lorentz pressure. However, these are more visible in the tension pressure perturbations.

Generally speaking, the tension pressure perturbations are of the same order of magnitude as the thermal and magnetic pressure perturbations. This differs from the results of the local simulation in the previous chapter indicating that a more realistic plasma environment and magnetic geometry does affect the significance of the pressure due to tension. The tension pressure perturbations have strong values close to the Earth to achieve the force-free dipolar field. The bow shock is present in the field which is likely due to the tension trying to oppose the bending of the IMF as it crosses the

curved shock and drapes over the magnetopause as shown in Figure 7.1B.

Other than around the inner boundary, the tension pressure perturbations do not take any strong values at the equatorial magnetopause. However, in the noon-midnight plane, the tension pressure perturbations do fluctuate at the magnetopause as highlighted by the arrows in panel H. These pressure peaks and troughs have some periodicity along the high-latitude magnetopause and are not north-south symmetric. This pattern is not obviously present in the magnetic pressure perturbation field, however it is visible in the Lorentz pressure perturbations but gets smeared out in the effective pressure perturbation field. The pattern is not visible Sunward of the cusp region suggesting that whatever is causing the pressure fluctuations is potentially originating at the cusp and being advected down tail by the magnetosheath flow.

Summing all the effects described results in the effective pressure perturbation field which is the sum of the thermal and Lorentz pressure perturbations. The effective pressure perturbation field shows that the dayside of the magnetopause is more compressed than the night side. There are no large pressure gradients anywhere in the magnetosphere which is expected when the system is in a quasi-steady state. In the equatorial plane there are obvious pressure minima along the low-latitude magnetopause in the approximate locations of where the KH-waves are seen in Figures 7.1 and 7.2. The pressure minima previously identified along the high-latitude magnetopause in the Lorentz and the tension pressure perturbation field are no longer visible in the effective pressure field. Applying λ_{MHD} will determine whether the local pressure minima are due to vortices and are therefore related to the KHI, or whether they are just features of the magnetic field.

7.4 Location of Magnetopause Vortices

Like in Section 6.3.2, λ_{MHD} is applied to every cell in the simulation, where spatial derivatives are undertaken through second order accurate central differences in the interior points and first order accurate differences at the boundaries. The data is then passed through a $3 \times 3 \times 3$-cell multidimensional median filter to ensure that the regions are 'connected' – meaning that more than half (14) cells in the 27 cell large filter box must be identified as vortical for a positive identification. As discussed in the previous chapter and the literature (e.g. Dong and Tian 2020),

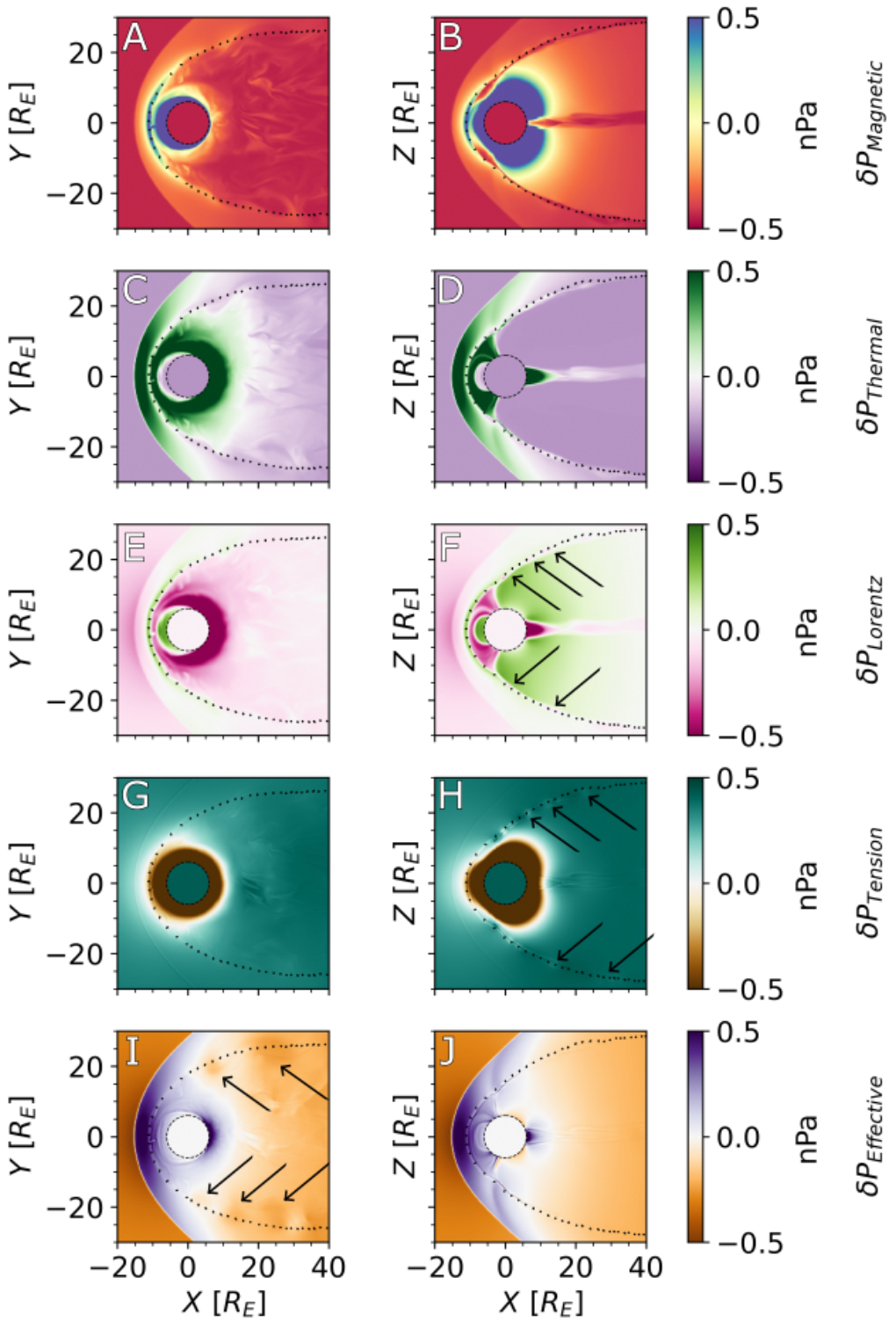


Figure 7.3: Equatorial (A, C, E, G, I) and noon-midnight (B, D, F, H, J) cuts of the simulation after 4 hours 17 minutes and 15 seconds of simulation time. The colour corresponds to the fluctuations from the mean of the magnetic pressure (panels A, B), thermal pressure (panels C, D), Lorentz pressure (panels E, F), tension pressure (panels G, H), and the effective pressure (panels I, J). The dashed black line shows the simulation inner-boundary which is a sphere of radius 4.5 R_E. The dotted line is the equilibrium magnetopause. The black arrows highlight regions discussed in the text.

typically these types of techniques require a threshold to be chosen to define a vortex. The definition used throughout this chapter is chosen to be that a vortex is identified if the region has a value of $\lambda_{\mathrm{MHD}} < -1 \times 10^{-25}$ Pa m^{-2}. This has been chosen as it includes approximately 30% of the most negative (therefore 'most vortical') λ_{MHD} values within 5 R_E of the open-closed magnetic field line magnetopause boundary.

Figure 7.4 shows a snapshot of $-\lambda_{\mathrm{MHD}}$ masked to within 5 R_E of the open-closed boundary. The dotted line is the equilibrium magnetopause boundary, the black dashed line is the inner-boundary location of 6 R_E, and the blue dashed line is a region which is 10 R_E from the centre of the simulation. The reason this is plotted is because the analytic work shown in Chapter 5 indicated that the numerical potential solver produces errors near boundaries. This implies that the λ_{MHD} values are unreliable near the boundaries. By inspecting the velocity field, the values identified by λ_{MHD} within this region are actually not vortical and should be ignored as they are misidentifications. Panel A of the figure shows the equatorial plane of the simulation which contains the low-latitude vortices, panel B the high-latitude vortices.

The numbers in panel A indicate different stages of a vortex's evolution along the magnetopause: 1 is an initial/seed stage, 2 and 3 are different quasi-linear stages, 4 is the non-linear stages, and 5 is the turbulent stage. The stages appear to be approximately evenly distributed along the magnetopause boundary which supports that the KH waves are quasi-periodic. Looking now only at the dusk flank which is expected to be relatively unaffected by the return flow event in the tail discussed in Section 7.2, the value of λ_{MHD} is more negative in stage 2 than stage 1. As well as this, the cross-sectional area of the vortex has increased which would correspond to a growth in the size of the vortex in the plane shown. Together these results strongly suggest that the vortex is getting both larger in spatial scale and also stronger, meaning that vortex transfer mechanisms are more significant in stage 2 than stage 1. As well as this, the vortex is associated with a wave meaning that a growth in the vortex corresponds to the wave's amplitude growing meaning that MSW wave energy transfer would also be more important at stage 2. This growth is important as it suggests that the majority of energy coming from the flank viscous-like interaction comes from the dawn/dusk sides of the Earth, not the day/night sides like it does with large-scale magnetic reconnection.

Vortices appear to spatially diffuse from stage 2 to 3 as the stage 3 vortices take a different

shape from that at stage 2; this new shape is similar to that from the quasi-linear stage seen in the previous chapter. Due to the short distance travelled, it is unlikely this change is due to the varying field or plasma conditions in the magnetosheath (Spreiter et al. 1966) and is instead likely due to the vortex evolution i.e. the vortex in the quasi-linear stage in the local simulation from the previous chapter is on the brink of being in the non-linear stage. The vortices in stage 4 can be seen to be propagating along the inner- and outer- edges of the LLBL which indicates the magnetopause has a non-negligible thickness here as the vortices are found on the inside and outside of the equilibrium magnetopause. The formation of the vortices on the inner- and outer- edge occurs by the vortex in stage 3 tearing apart, resulting with one half propagating along the inner-edge and the other along the outer-edge of the LLBL; this is in progress for the vortex shown at stage 3 on the dusk flank. This idea of the vortex being torn in two is supported by the two vortices in stage 4 having approximately half the λ_{MHD} value of the vortices seen in stage 3.

The vortex bifurcation into two different modes can be explained by the thickening of the magnetopause as it allows for a bifurcation of the KHI into inner and outer modes as discussed in Section 3.2.1. Recall that the inner- and outer-modes were first suggested to exist in linear theory which showed that the magnetopause boundary layer can sustain two surface waves: one at the outer edge, and one at the inner edge of the magnetopause boundary layer (Lee et al. 1981; Pu and Kivelson 1983; Miura and Pritchett 1982). As the vortex bifurcation takes place approximately at the $X = 0$ line in this simulation, it suggests that beyond the $X = 0$ line is approximately where the magnetopause is expected to have a sufficient thickness such that it can sustain inner- and outer-modes. This also implies that perhaps before the mode bifurcation location, linear theory which assumes a tangential discontinuity (Chandrasekhar 1961; Pu and Kivelson 1983) may be valid and sufficient at describing the wave behaviour. This bifurcation has also been observed in other global simulations (e.g. Guo et al. 2010; Li et al. 2012; Li et al. 2013; Merkin et al. 2013) however they generally find that this process occurs closer to the dayside. This difference is likely due to the finer grid resolutions used in these studies allowing for the bifurcation to be resolved on smaller spatial scales meaning it would be expected to occur nearer the dayside due to the local-time dependence on the LLBL thickness (Haerendel et al. 1978).

Finally, the turbulent stage is seen far down flank of the magnetopause. At this stage the vortices

are much smaller, sporadically located, and are weaker as represented by their smaller values of λ_{MHD}. This is not a direct result of the vortex evolution as the smaller vortices in the local simulation of the previous chapter are stronger. This means that the weaker values are due to the changing plasma conditions in the global simulation i.e. the changing magnetosheath and LLBL conditions (Spreiter et al. 1966; Haerendel et al. 1978). It is suggested that the vortices are also weaker because they have dissipated energy into the magnetosphere through MHD body wave coupling (Pu and Kivelson 1983; Wang et al. 2017b) but also diffusive transport across the boundary.

In summary, from the nose to the $X = 0$ line the vortices are observed to approximately be in the linear regime, beyond the $X = 0$ line they enter the non-linear regime. As the LLBL develops, the vortices begin to bifurcate as the MSWs are forced onto either the inner- or outer-surface of the LLBL. After this, the vortices continue to non-linearly evolve until the surface folds onto itself, rolling up and causing the turbulent stage. These findings are in agreement with the results of Li et al. (2012) who showed similar results using a different global MHD simulation (see Chapter 3).

Despite the high-latitude magnetopause being stable to the KHI, λ_{MHD} identifies vortices present along the high-latitude magnetopause which are shown in Panel B. These vortices occur tailward of the cusps and are highlighted by the ellipse. The high-latitude perturbation is visible in Figure 7.2 but interestingly the vortices are not present in the location where the magnetopause is visibly the most perturbed suggesting that vortices, and therefore waves, are not responsible for this surface deformation. At this stage it is unclear what is causing the tailward of the cusp waves.

Another notable high-latitude phenomenon shown in Figure 7.4B is that the outer cusp regions are associated with strong vortical values of λ_{MHD}. The cause of these vortices has been explained previously using observations by Tkachenko et al. (2008) who used two-point measurements and a statistical study to show that under northward IMF conditions, a sunward flowing reconnection jet from cusp reconnection can interact with the tail-ward edge of the magnetopause cusp indentation and generate vortical flow. The scale of the structure is approximately $4\,R_E$ which is larger than the one suggested by Tkachenko et al. (2008) who measured a diameter of $\sim 1800\,km$ or $0.25\,R_E$. It is suggested that this might be due to the IMF not being the same as this is known to change the cusp size (Pitout and Bogdanova 2021), or may be due to the resolution of the simulation not allowing for a physical scale size being captured, making it larger in simulation than reality like it does for MP

thickness. A further investigation into this discrepancy is needed however as it is not KHI related, it is beyond the scope of this work. By plotting the velocity field, an understanding of the plane the vortices circulate in can be gained to know whether the high-latitude vortices are physical or a misidentification.

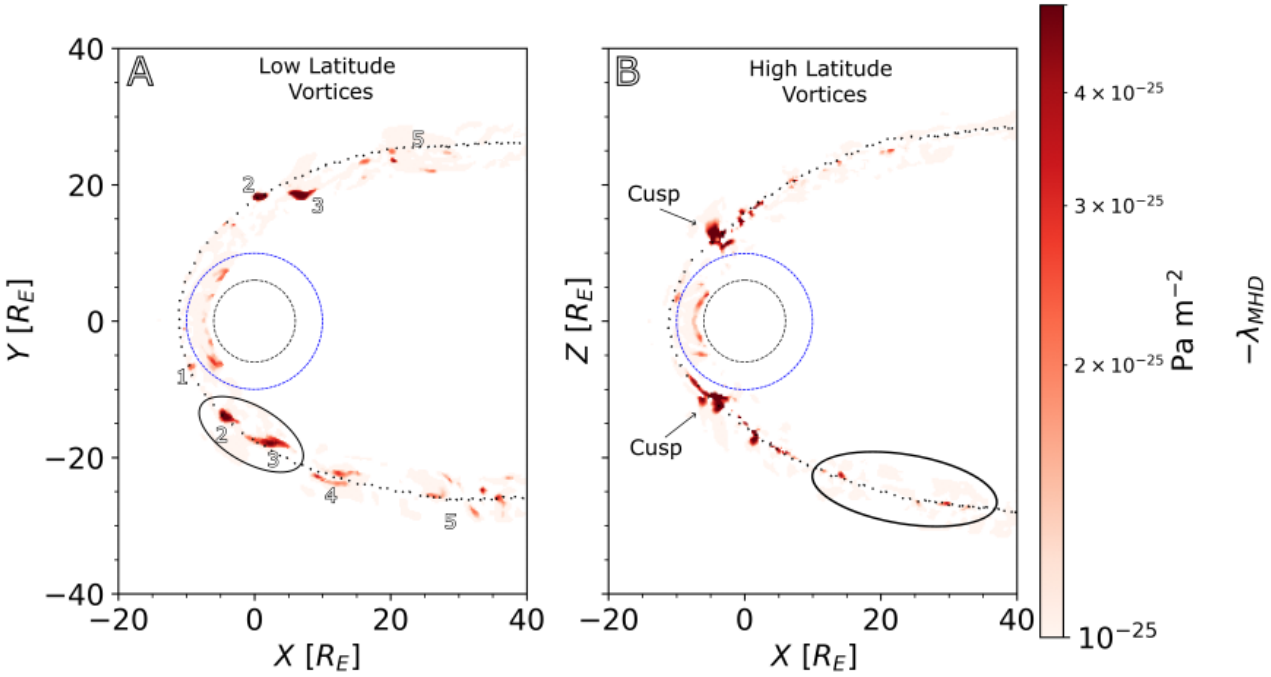


Figure 7.4: Equatorial (A) and noon-midnight (B) cuts of the simulation after 4 hours 17 minutes and 15 seconds of simulation time. The logarithmic colour scale represents $-\lambda_{\mathrm{MHD}}$ with the numbers highlighting approximate evolutionary stages of the KH-vortex identified by eye. The dashed black circle shows the simulation inner-boundary which is a sphere of radius 4.5 R_E. The blue dashed circle has a 10 R_E radius encloses the region thought to be too close to the inner boundary to be true. The dotted line is the open-closed magnetic field line boundary of the time-averaged magnetic field. The black ellipse shows the high-latitude vortices.

Figure 7.5 shows the low-latitude (Panel A) and high-latitude (Panel B) magnetopause with overlaid quivers showing the instantaneous velocity field minus the time-averaged velocity field dubbed here as the velocity perturbation field. The blue circles indicate vortical regions which are identified by λ_{MHD}. The vortices shown are approximately 2 $\mathrm{R_E}$ in diameter and the λ_{MHD} signature is approximately directly where the flow vortex is. It is necessary here to discuss the vortical patterns in the velocity perturbation field which are not being identified by λ_{MHD}. Recall from Chapter 6 and Jeong and Hussain (1995), the λ-family of vortex identification techniques, including λ_{MHD}, are Galilean invariant. This means that the vortices can be identified in any Galilean frame. The frame shown here is an accelerating frame as the subtracted velocity field is not uniform due to the

accelerating magnetosheath flow (Haaland et al. 2019). Therefore the vortical patterns being seen which are not identified, are actually a result of the mean subtraction not the presence of a vortex and therefore they should be ignored. If the time-averaged flow at that local point is subtracted everywhere to give Galilean frame, the vortex is found to not be present – this has been explicitly checked. This result reiterates the need for this vortex identification technique to prevent this type of misidentification taking place.

Figure 7.5B shows a cross-sectional cut of the high-latitude vortices present within the simulation. These are much less obvious and have a weaker λ_{MHD} value. It is clear that λ_{MHD} is correctly identifying vortices in both panels. The low-latitude vortices are normal to the equatorial plane which is expected for the low-latitude KHI. The high-latitude vortices can be seen to be threading the noon-midnight plane. Given that the vortices are decaying rather than growing it is unlikely that they are KH-driven and are instead being sourced by some transient event in the cusp and then decaying. This process will be explored later in Section 7.7.

Currently, all the analysis has been restricted to the equatorial plane and as shown by the high-latitudes being KH-stable and the low-latitudes being KH-unstable, the plasma and magnetic conditions change in latitude. Therefore three-dimensional analysis of these vortices is needed to allow for a proper understanding of the process taking place. This is not readily possible with other vortex identification techniques which are commonly used in the field. Fortunately, λ_{MHD} allows for a three-dimensional volume rendering visualisations of the vortices to be able to better understand their shape, size, and structure.

Figure 7.6 shows a three-dimensional rendering of the northward dusk flank of the dayside magnetosphere seen in Figure 7.4. λ_{MHD} is plotted in red and white with a linear transparency after 4 hours, 17 minutes, and 15 seconds of simulation time. Spatial cuts of the magnetic field at this time is also shown for spatial context of λ_{MHD}.

Generally speaking, the low-latitude vortices all differ from each other in shape and structure. Interestingly, the vortices are not isolated to the low-latitudes. In the cusps there appears to be a mixture of small vortical structures which were not apparent in the equatorial plane. This may suggest that the cusp vortices in this simulation are more similar in scale to those detected by Tkachenko et al. (2008). There are additional vortices in the high-latitudes and behind the cusps, however these

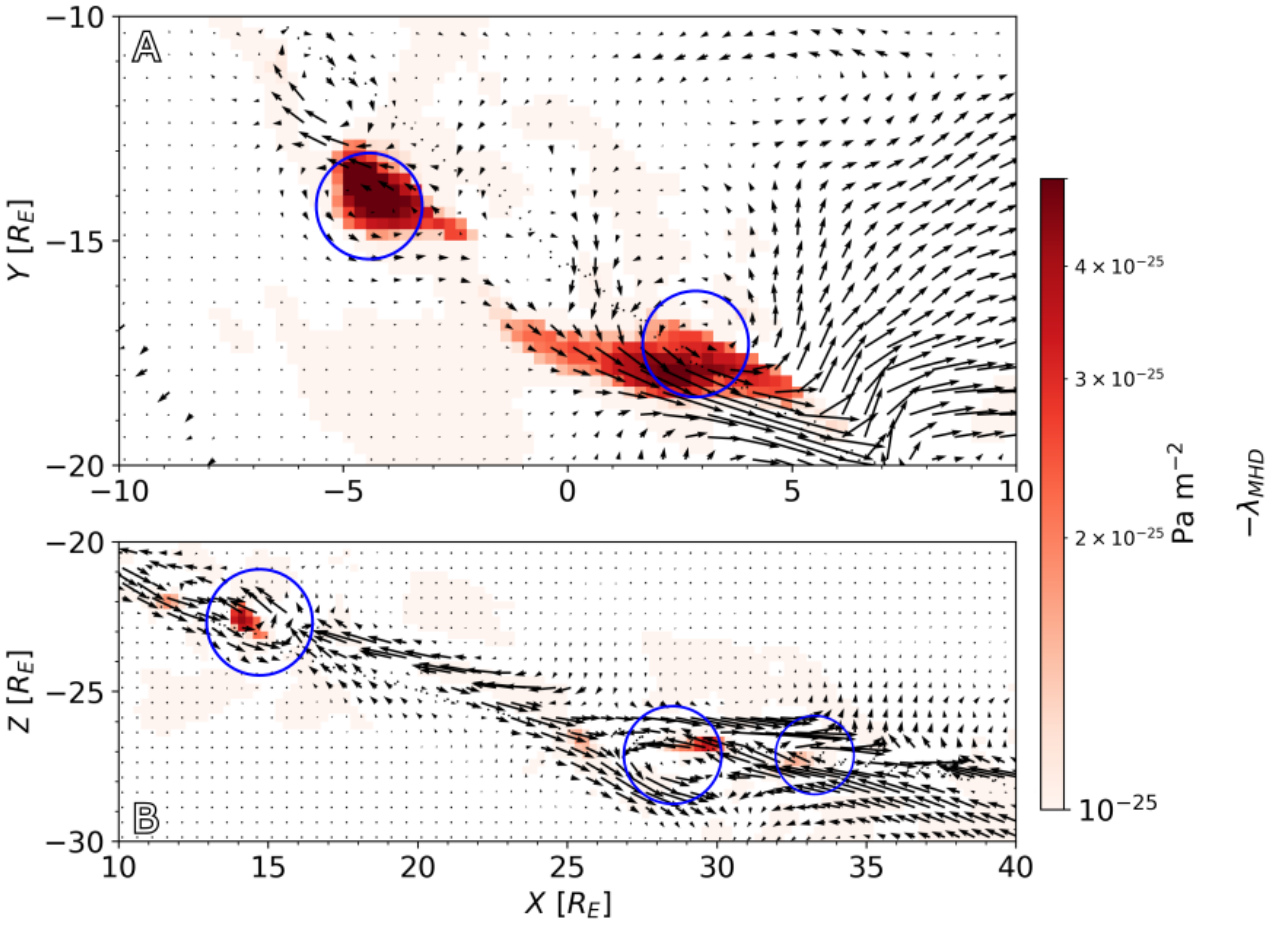


Figure 7.5: Zoom-ins of the Equatorial (A) and noon-midnight (B) cuts of the simulation after 4 hours 17 minutes and 15 seconds of simulation time. The logarithmic colour scale represents $-\lambda_{\mathrm{MHD}}$. Overlaid are quivers of the two-dimensional velocity field showing both direction and magnitude. The length of the quivers are scaled where $1\mathrm{R_E} = 1250\,\mathrm{km\,s^{-1}}$in the equatorial plane and $1\mathrm{R_E} = 2500\,\mathrm{km\,s^{-1}}$ the noon-midnight plane. The dotted line is the open-closed magnetic field line boundary of the time-averaged magnetic field.

are small structures and do not appear to perturb the magnetopause. There does not appear to be a single vortex near the large high-latitude perturbation at approximately $X = 50\,\mathrm{R_E}$ identified in Figure 7.2 further suggesting a vortex is not driving this perturbation supporting the conclusion that this is not a surface wave.

The large-scale high-power vortices all seem to be restricted to the low-latitude region and appear to inexplicably reduce in latitudinal extent as they evolve around the magnetopause. Alternatively, the surface waves which they are associated with visibly grow with local time in Figure 7.2 meaning that the KHI must be being restricted further into the lower latitudes with increasing local time. This is revisited and explained later in Section 7.6.

Vortex 1 is found to be extending out of the cusp region and reaching down into the low-latitudes. Recall that this stage 1 vortex was previously identified as being in the initial seeding region for the KHI. What is shown is thought to be related to the outflow of a reconnection jet deforming the dayside magnetopause and perturbing the low-latitude magnetopause, acting as a seed perturbation for the KHI to grow into the larger vortex structures seen at stage 2.

Vortex 2, which is in the quasi-linear stages of the KHI, has a height of $\sim 10\,R_E$ and is asymmetric about the equatorial plane. It extends $\sim 3\,R_E$ further northward than southward, this bias is explained by it also having been seeded by the North cusp. What this suggests is that during the quasi-linear stages of the KHI, asymmetry about the equatorial plane can exist due to the conditions which seed the initial vortex. However, this asymmetry about the equatorial plane is not present in the vortex at stage 3. This is either due to the KH-vortices being restricted into the equatorial plane or it may be a result of this vortex not originally being associated with the cusp. The vortex shown at stage 3 has a reduced height of $\sim 5\,R_E$ but appears to be more stretched out across the local magnetopause surface than the vortex at stage 2.

The beginning of the bifurcation of the vortex can be seen at stage 3 where there is a clear structure separating from the top of the vortex. By the time a vortex has split at stage 4, it is clear that a vortex would further shrink in height and almost be totally reduced into the equatorial plane. The vortices here are small and quite diffuse which is expected in this non-linear stages where the vortex is dissipating energy. The vortices identified at stage 5 are small in size both latitudinally and longitudinally. Their signatures are weak and diffuse with them not appearing to exist at all beyond $X \approx 40\,R_E$.

So far, a contextual understanding of where the vortices are located has been shown. It has been found that the vortex power decays with local time. This phenomena is not found for the local simulation which investigates the vortex evolution only, meaning that the changing plasma conditions and magnetic field geometry must be responsible. Furthermore, the vortices latitudinal extent has also been shown to decay with increasing local time. An explanation for both these patterns is presented by investigating the realistic plasma conditions and the realistic magnetic field geometry in the next two sections.

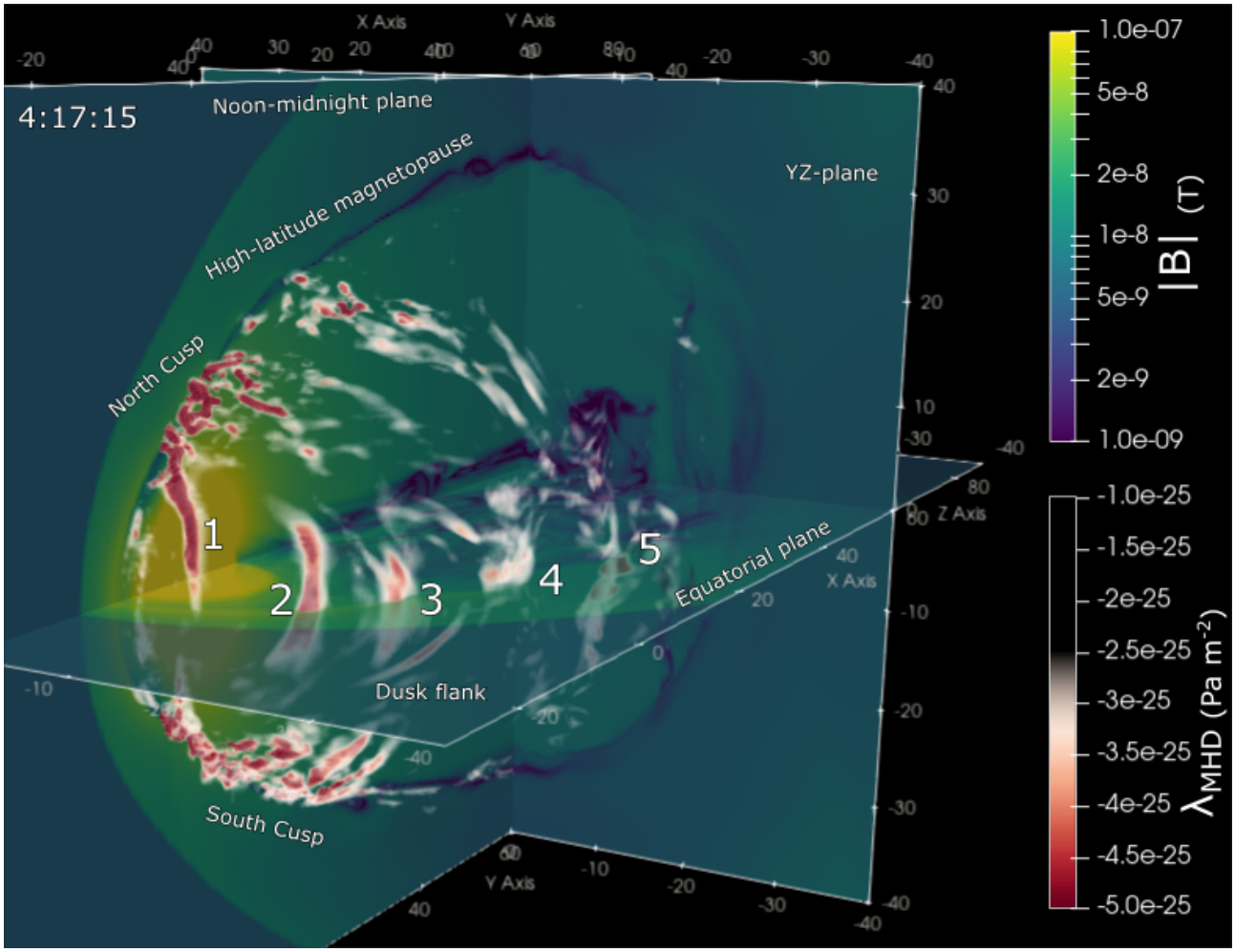


Figure 7.6: A three-dimensional rendering of the northward dusk flank of the dayside magnetosphere λ_{MHD} plotted with a linear transparency after 4 hours, 17 minutes, and 15 seconds of simulation time. The $y = 0$ slice, $x = 60$ slice, the $z = 0$ slice of the magnitude of the magnetic field is also shown; the $z = 0$ slice has a fixed transparency of 0.7. The numerical labels correspond to vortices mentioned in the associated text and correspond to those in Figure 7.4.

7.5 Consequences of a realistic plasma environment

The low-latitude KH vortices have been shown to change shape, size, and power as they evolve and advect around the magnetopause flanks. In the previous study it has been shown that the evolution alone is not responsible for this meaning that either the changing plasma environment or the varying magnetic field geometry must be responsible. This section shall explore the influences of the changing plasma environment on the KH-vortex evolution. This is difficult as a single time slice is insufficient for trying to explain the full evolution of the vortices within this simulation. One way to investigate whether the local-time variations in plasma conditions is responsible for these changes is by decomposing λ_{MHD} into its physical drivers and investigating whether this can explain the changes seen. Furthermore, it allows for an investigation into how the effects of compressibility, inhomogeneity, and magnetic tension change throughout the evolution of a KH-vortex along the magnetopause. To overcome the challenge of time, a statistical approach is taken by averaging over the temporal dimension.

7.5.1 Equatorial Plane

Figure 7.7 shows the time-averaged λ_{MHD} below the threshold value of $\lambda_{\mathrm{MHD}} < -1 \times 10^{-25}\,\mathrm{Pa\,m^{-2}}$, and within $5\,R_E$ of the magnetopause. This average is taken over 100 time steps corresponding to 25 minutes of simulation time. As KH-vortices are advected along the magnetopause as they evolve, looking along the magnetopause in local time allows for an understanding of how λ_{MHD} varies throughout the different stages of a vortex's evolution.

Figure 7.7 shows λ_{MHD} in the equatorial plane and demonstrates that low-latitude vortices are seeded near the nose of the magnetopause, approximately $1\,R_E$ or $\sim 6^\circ$ from the Sun-Earth line. This coincides with the cusp seeding discussed above and differs from the longitude of 15° triggered by the KHI. Comparatively, this is closer to the subsolar point than the results of Guo et al. (2010), who found a KH-seed angle of 28°. The consequences of this are that magnetopause oscillations near the nose of the magnetopause, which are typically attributed as solar wind pressure-variation seeded, may also be a result of pressure variations originating from cusp reconnection. This opens questions regarding the importance of this process for momentum and energy transfer into the magnetosphere

as well as how, or if, it couples to magnetopause surface eigenmodes.

During the seed and linear stages of the KHI, a vortex is typically strongly tied to the boundary location and occurs within $\sim 1.5\,R_E$ of the time-averaged magnetopause boundary. However, once a vortex enters its non-linear evolutionary stage, where the surface roll-up occurs, the vortices can exist up to $\sim 5\,R_E$ from the time-averaged magnetopause boundary – this region is mostly within the equilibrium magnetopause boundary suggesting the inner-mode varies spatially more than the outer-mode. It was discussed above that approximately at the $X = 0$ line the vortices appear to bifurcate. In Figure 7.7 this can clearly be seen to be the point where the vortices split onto the inner- and outer-surface of the LLBL. This is clear as the power of λ_{MHD} bifurcates on both flanks at this approximate region with there being peaks on the two edges of the LLBL. The bifurcation appears to take place at $X \approx -5\,R_E$ on the dawn flank, and is slightly further tailward on the dusk flank at $X \approx 0\,R_E$. This discrepancy may be due to the anomalous return flow present in the tail causing a thicker and more sunward LLBL than on the dusk flank.

The inner mode appears to have a more negative λ_{MHD} value in both flanks and survives much further into the tail than the outer mode. This supports the findings of Lee et al. (1981) who suggested that the inner boundary was more KH-unstable than the outer boundary. The two modes appear to be approximately split by the equilibrium magnetopause boundary. This is comparative to the results of Guo et al. (2010) who show that the instantaneous magnetopause boundary separates the inner- and outer-modes. This is illustrated in the figure. The trends seen here may be clearer if more data were available to improve the statistics which is important to note for future studies. It is suggested that twice the simulation run time would be needed to ensure multiple KH-wave periods are captured in the statistics, but unfortunately, due to data storage limitations, this was not possible for this study.

The outer mode's λ_{MHD} value drops beyond $X = 35\,R_E$ on the dawn and $X = 45\,R_E$ on the dusk flank. The inner mode's λ_{MHD} value drops beyond $X = 50\,R_E$ on the dawn and $60\,R_E$ on the dusk flank. At these points, the vortices have dissipated enough to no longer surpass the set threshold meaning that energy dissipation and evolution is still taking place at these distances down tail. Additionally, this may be related to how efficiently the instability can extract energy from the solar wind. If the magnetopause thickness is sufficiently large, the velocity shear will be reduced due

to viscous-like effects causing a thickness in the velocity shear boundary (i.e. the magnetopause / LLBL) instead of the shear being a discontinuity. This makes the KHI less effective on the outer-edge of the boundary versus the inner-edge which will have a much stronger shear. The strongest average vortex power is at $X \approx 5\,R_E$. Given the strong power in this region, it is likely where the most unstable KHI mode exists.

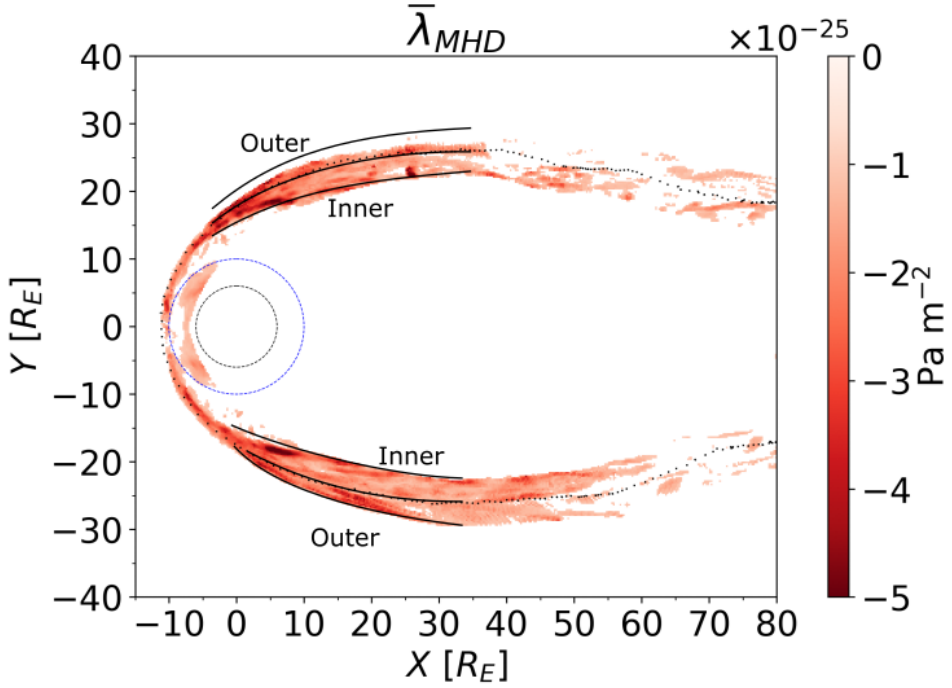


Figure 7.7: The mean value of $\overline{\lambda}_{\mathrm{MHD}}$ is shown in colour below the threshold value of $\lambda_{\mathrm{MHD}} < -1 \times 10^{-25}$, and within $5\,R_E$ of the magnetopause in the equatorial plane. The dashed black circle shows the simulation inner-boundary which is a sphere of radius $4.5\,R_E$. The blue dashed circle with a $10\,R_E$ radius encloses the region thought to be too close to the inner boundary to be true. The dotted line is the open-closed magnetic field line boundary of the time-averaged magnetic field.

Now that an understanding of the averaged vortex location has been explored, an investigation into the different contributory terms can be performed to understand the influence of the different plasma properties on vortex identification. The purpose here is to try and discern between whether a realistic plasma environment is responsible for the observed decay in vortex power with increasing local time. In addition, it also allows for an investigation into how significant each effect is in each stage of the KHI in more realistic conditions. Recall that the contributor terms of λ_{MHD} are vortical momentum, λ_M, density gradients, λ_D, fluid compressibility, λ_C, and rotational magnetic tension, λ_T (see Section 6.3.3 for the derivation). As all the vortices are advected along the magnetopause as they evolve, then like before, looking along the magnetopause in local time allows for an understanding

of how λ_{MHD}'s contributory terms vary throughout the different stages of a vortex's evolution in a realistic plasma and magnetic environment.

Figure 7.8 shows the terms which contribute to λ_{MHD} shown in Figure 7.7. Generally speaking, the momentum term dominates like in the previous chapter. As well as this, the density term opposes the vortices which was a similar conclusion as before. The compressibility term can be seen to be on a comparable order of magnitude in this simulation unlike in the local simulation. The magnetic tension term appears to have a more complex relationship with the vortices which is not scale-dependent which was what was previously concluded.

Figure 7.8A shows the vortical momentum term in the equatorial plane. This term appears to be in near total agreement with λ_{MHD} agreeing with the findings of the previous chapter. However, the simplified geometry and plasma conditions does affect the influence of the momentum term on KH-vortex formation as the vortical momentum term has decaying power from the nose to the tail. In the local simulation, the power of the momentum term did not significantly change with the evolutionary stages of the KHI (perhaps a slight increase from quasi-linear to non-linear and slight decrease from non-linear to turbulent), but that is the relationship being shown here. This can be explained physically by understanding that the vortices have less momentum with increased local time meaning that momentum must be being lost throughout progressive evolutionary stages of the KHI. The majority of this momentum loss occurs in the highly-nonlinear and turbulent stages of the vortices. This is a similar local-time to where Merkin et al. (2013) found magnetopause surface wave power to decay. The reduction in momentum must be due to dissipative processes such as the wave phase speed being accelerated by the increasing magnetosheath velocity (Haaland et al. 2019), and therefore transitioning from a surface wave into a stable body wave (Pu and Kivelson 1983) transferring energy away from the boundary and into the magnetosphere. As well as this, it is likely linked to the rarefication of the magnetosheath with increasing local time (Spreiter et al. 1966) meaning that the vortices contain less mass and therefore less momentum.

The bifurcation of the KH-modes is clearly visible in this term at $\sim X = 0\,R_E$ on the dusk flank and slightly further sunward on the dawn flank. The strong λ_M signatures of the inner mode are quickly lost within $\sim 5 - 10\,R_E$ of the mode bifurcation despite the power of the inner mode surviving much further into the tail. The outer-mode, however, retains strong negative λ_M signatures further

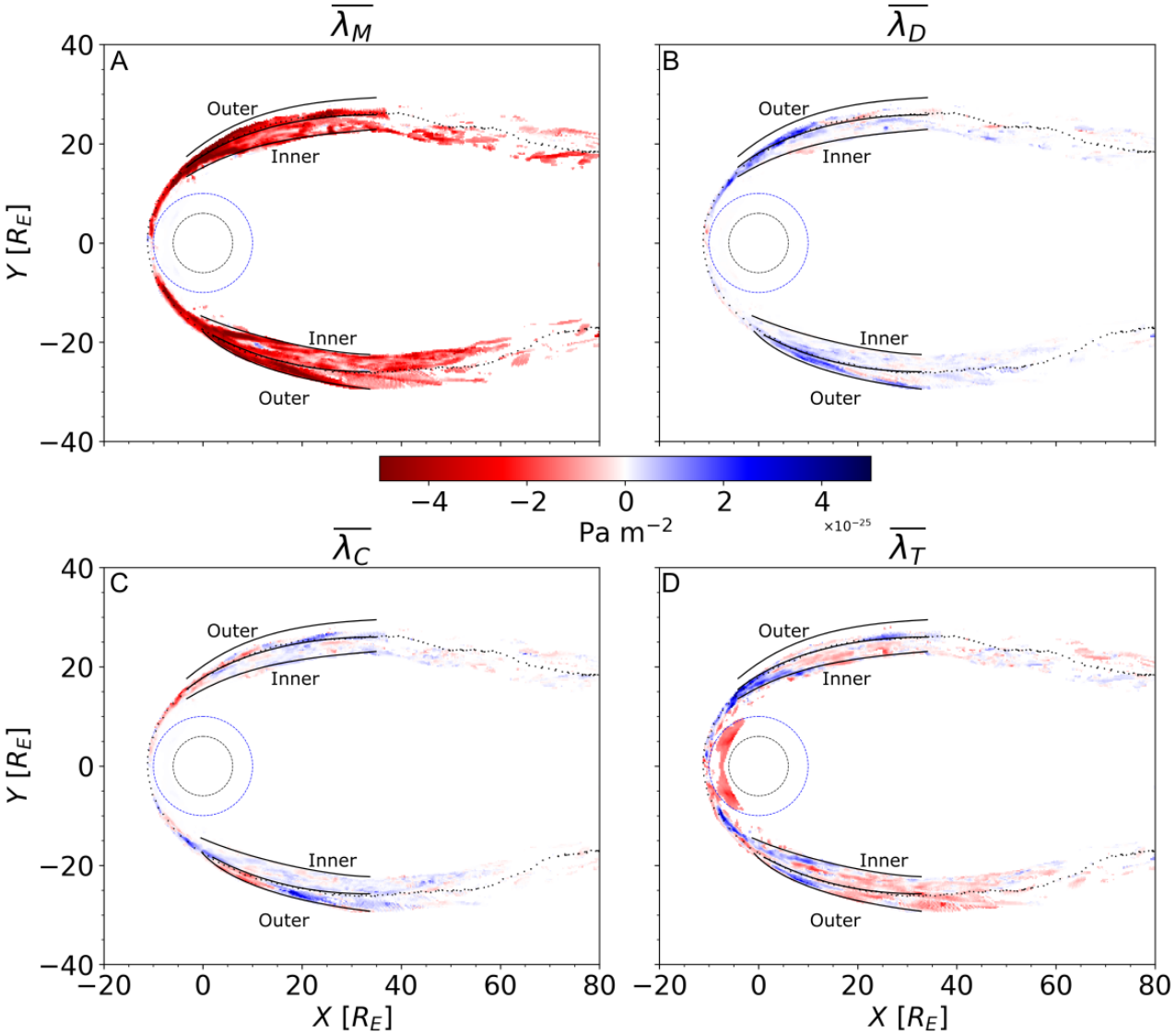


Figure 7.8: The time-averaged value of $\overline{\lambda}_M$, $\overline{\lambda}_D$, $\overline{\lambda}_C$, $\overline{\lambda}_T$ is shown. The values are selected by being contributing to values below the threshold value of $\lambda_{MHD} < -1 \times 10^{-25}$, and within $5\,R_E$ of the magnetopause in the equatorial plane. The dashed black circle shows the simulation inner-boundary which is a sphere of radius $4.5\,R_E$. The blue dashed circle with a $10\,R_E$ radius encloses the region thought to be too close to the inner boundary to be true. The dotted line is the open-closed magnetic field line boundary of the time-averaged magnetic field.

down tail to $\sim X = 30\,R_E$. By labelling this higher-power region as the non-linear growth region would suggest that the two modes must be evolving differently i.e. the inner mode transitions to the turbulent stages closer to the subsolar point. This can be explained as the outer-mode vortices move 2.5× faster than those on the inner mode as shown by Merkin et al. (2013). This added velocity would allow the outer-mode vortices to reach larger local times before they reach their turbulent stages which breaks apart these compact strong momentum structures.

To summarise, the momentum of the vortices are effected by the local time changes in the realistic plasma environment. Momentum is lost by the vortices due to the phase speed of the wave being accelerated by the increasing magnetosheath flow causing the surface wave to transition into body waves and transfer momentum away from the surface. As well as this, the inner- and outer-modes are accelerated differently. The thickness of the LLBL means that the outer-mode KH-vortices move $\sim 2.5\times$ faster than the inner-mode and therefore the inner-mode evolves into turbulent stages closer to the subsolar point faster than the outer-mode. This results in the inner-mode causing more diffusive transfer closer to the Earth than the outer-mode.

Figure 7.8B shows how density gradients contribute to λ_{MHD} shown in Figure 7.7. Figure 7.9A shows the time-averaged density, ρ_0, for comparison. The equatorial plane vortices shown in Figure 7.8B clearly show that density gradients oppose the formation of a vortex in their linear to non-linear stages which is in agreement with the local simulation results presented in the previous chapter. The term clearly only has a significant effect on the outer-mode of the KHI. Considering the term is largest in the region where the KHI is suggested to be most unstable, these results are in agreement with those of Amerstorfer et al. (2010) and Ma et al. (2024) who showed that increasing the density on the outer-boundary only, decreased the growth rate of the KHI in a non-linear way. Physically, this is intuitive because the pressure gradients in the lighter flow will generate an insufficient impulse to perturb the heavier flow and therefore the instability cannot grow; this idea is present in the linear theory (e.g. Chandrasekhar 1961; Pu and Kivelson 1983; Miura and Pritchett 1982). The idea that the KH-growth rate is reduced by density gradients across the boundary supports the findings that the outer-mode of the KHI exists further down tail than the inner-mode.

The discrepancy between the flanks of the term significance can be explained by the difference of where the single mode bifurcates into the inner- and outer-modes. This is reflected in Figure 7.9A which shows the LLBL on the dawn-side is denser and thicker than that of the dusk side. Again, this should be attributed to the anomalous return flow on the dawn flank of the tail. With the context of ρ_0, it is now obvious why the inner mode has a negligible contribution by the density gradient terms as the density where the inner-mode exists is smooth. Furthermore, as the magnetosheath flow increases, the density in the sheath drops reducing the density asymmetry across the boundary and therefore reducing the significance of the density gradient term as a function of local time.

In summary, the evolution of the KHI is shown to be weakly effected by density gradients, with only the outer-mode of the KHI being significantly affected. The term appears to only have strong values approximately within the non-linear evolution stage which is in agreement with the previous chapters findings. The role of density gradients appears to solely be due to evolutionary stage which makes physical sense as the density shear is only important when the deformed flow on one side of the boundary must carry the other – this stage is inhibited if the momentum of one side cannot carry the other. When the two sides have comparable mass e.g. the inner-mode, this effect, and therefore term, becomes negligible.

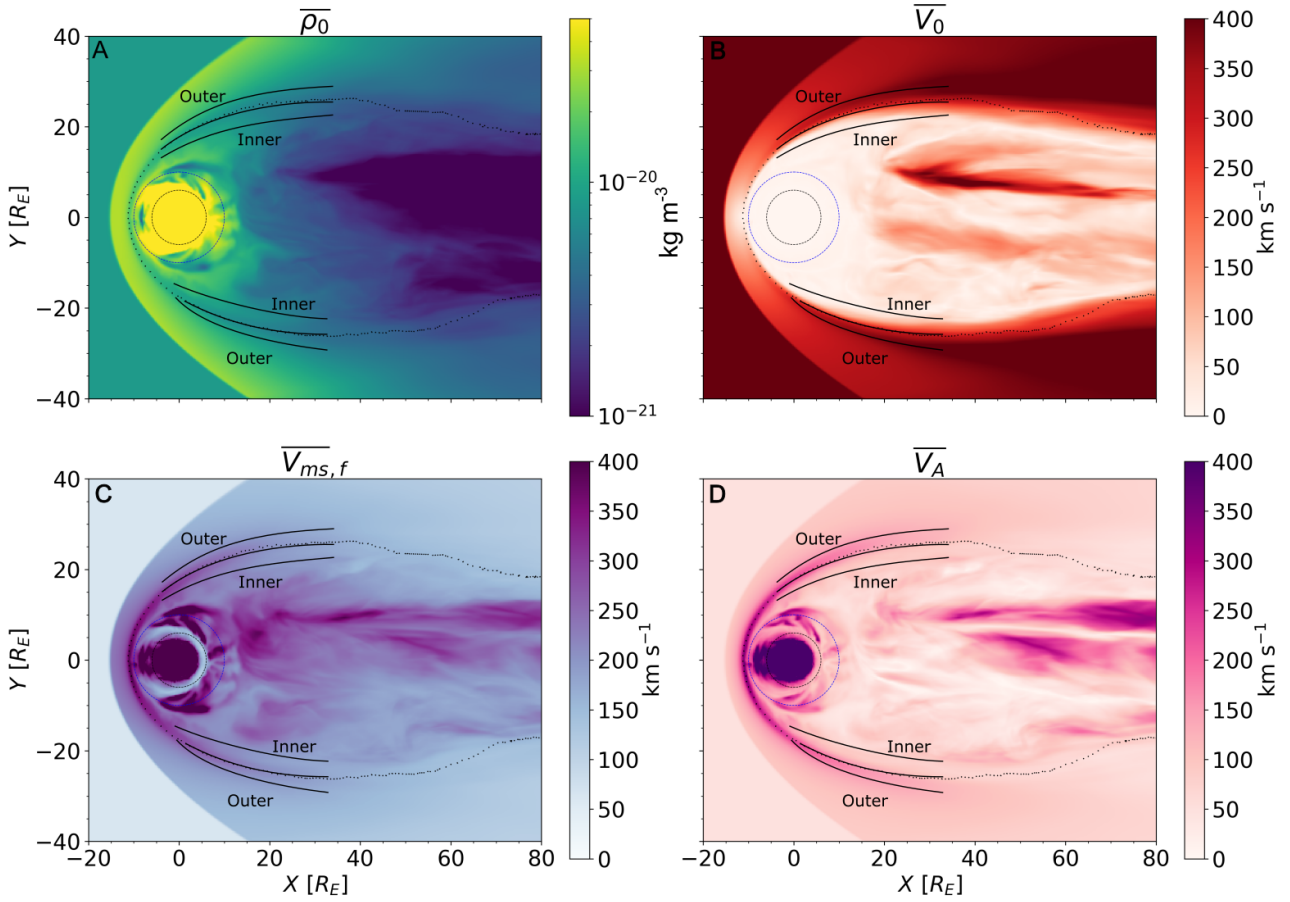


Figure 7.9: Time-averaged values of the density (panel A), magnitude of the velocity (panel B), magnetosonic fast speed (panel C), and the Alfvén speed (panel D) in the equatorial plane. The magnetosonic fast speed and Alfvén speed are calculated using time-averaged values. The dashed black circle shows the simulation inner-boundary which is a sphere of radius 4.5 R_E. The blue dashed circle with a 10 R_E radius encloses the region thought to be too close to the inner boundary to be true. The dotted line is the open-closed magnetic field line boundary of the time-averaged magnetic field.

Figure 7.8C shows how fluid compressibility contributes to λ_{MHD} shown in Figure 7.7. Immediately,

it is clear that the compressibility term is of a comparable order of magnitude and therefore these results are different to those of the local simulation which found compressibility to be negligible at all stages. The trends of the compressibility term seen in the equatorial plane differs on each flank and only appears to contribute to the outer-mode of the KHI.

To understand how compressibility influences a vortex at different points, the fast magnetosonic Mach number in the vortex frame is needed, where the speed of the vortex is calculated by $V_{\text{vortex}} = (V_1 + V_2)/2$ where $V_{1,2}$ is the speed directly adjacent to the vortex, e.g. for the outer mode it would be the magnetosheath flow at that point and the LLBL speed. The fast magnetosonic Mach number is then calculated in each region through $M_f = (V_{1,2} - V_{\text{vortex}})/c_{ms,f}$. As this is hard to do for a varying vortex velocity in local time, a comparison of $\overline{\lambda_C}$ using Figure 7.9B, the magnitude of the time-averaged velocity, V_0, and Figure 7.9C, the fast magnetosonic speed calculated using time-averaged parameters, $\overline{V}_{ms,f}$, is used to try and explain these trends and perform some approximate calculations to aid the discussion.

Near the subsolar point, the velocity on both sides of the equilibrium magnetopause boundary is on the order of 10's of $\mathrm{km\,s^{-1}}$ meaning the vortex is moving slowly and the plasma would be very weakly compressional explaining why the compressibility term is small in this region. The vortices beyond this region bifurcate into the inner- and outer-modes. Merkin et al. (2013) found that vortices on the outer-mode propagated 2.5× faster than those on the inner-mode meaning that there are expected differences on the role of compressibility on the inner- and outer-modes due to this vortex velocity difference. Beyond the bifurcation point, approximately $5\,\mathrm{R_E}$ down tail, the vortex speed is increased to approximately $(300\,\mathrm{km\,s^{-1}} + 100\,\mathrm{km\,s^{-1}})/2 =\sim 200\,\mathrm{km\,s^{-1}}$ on the outer mode and $(100\,\mathrm{km\,s^{-1}} + 0\,\mathrm{km\,s^{-1}})/2 =\sim 50\,\mathrm{km\,s^{-1}}$ on the inner mode. In the frame of the vortex, given a magnetosonic fast speed of $250\,\mathrm{km\,s^{-1}}$, this corresponds to a lower bound fast magnetosonic Mach number of ~ 0.4 meaning the plasma in this region is weakly compressional and, due to the increasing flow speed and reducing magnetosonic speed, compressibility is becoming more important further from the subsolar which would make compressibility more important which is what is seen. For the inner-mode, the fast magnetosonic Mach number would be ~ 0.2 which is essentially incompressible explaining why the compressible term is negligible for the inner-mode. To explain the varying positive and negative contributions, results from the previous chapter and other previous studies are needed.

Recall that previous studies have suggested that compressibility lowers the KH critical onset threshold relative to the incompressible situation and thus has a destabilising effect of the boundary to the KHI (Fejer 1964; Sen 1965; Southwood 1968). Further to this, it was also suggested that compressibility has both a destabilising effect on the lower critical shear flow velocity, and stabilising effect on the wave growth rate (i.e. a reduction of the growth rate) if the shear flow speed is sufficiently smaller than the magnetoacoustic speed (Sen 1965). What these other studies show is that just off the nose of the magnetosphere, the compressibility term contributes to λ_{MHD} because it is lowering the critical shear flow velocity and therefore destabilising the boundary to the KHI and allowing for the growth of quasi-linear vortices. Transitioning into the non-linear stages where the single mode appears to bifurcate, the compressibility term contributes to the vortex on the outer-mode, but negates from it for the inner-mode. This is because the inner-mode exists in a subsonic regime and therefore compressibility reduces the growth rate (Sen 1965). The outer-mode, however, is in a super-magnetosonic regime meaning that compressibility destabilises the boundary, increasing the growth rate (Fejer 1964; Sen 1965; Southwood 1968; Pu and Kivelson 1983).

In the highly-nonlinear stage the KHI is stabilised by compressibility. From scaling arguments, knowing that the magnetosheath is accelerating and the fast magnetosonic speed is reducing, the non-linear regime occurs in the highly compressible region. The vortex speed $\sim 20\,R_E$ down tail is $\sim 350\,km\,s^{-1}$ which exceeds the magnetosonic fast speed. The stabilisation can then be explained by recalling that if the wave phase speed exceeds the MHD fast speed in the plasma, then the KH-driven evanescent surface wave has grown suitably such that it transitions into a leaky oscillatory wave or "body wave" (Pu and Kivelson 1983). This body wave then carries energy away from the boundary and into the magnetosphere and magnetosheath, consequently stabilising the KHI. Finally, the role of compressibility is also dependent on the thickness of the shear interface (Miura and Pritchett 1982) as compressibility plays a significant role in the gradual – but not total – stabilisation of the boundary due to the finite magnetopause thickness (Miura 1992). This explains the slight differences between the two flanks – the magnetopause boundary thickness differs on both sides due to the anomalous return flow and this results in a slightly different KH-behaviour on each flank as varying frequencies and wavelengths compete for dominance. This will be explored further in the next chapter.

Figure 7.8D shows how rotational magnetic tension term contributes to λ_{MHD} shown in Figure

7.7. Like before, because it is hard to calculate the vortex frame Alfvén Mach number, a comparison of $\overline{\lambda_T}$ using Figure 7.9B, the magnitude of the time-averaged velocity, V_0, and Figure 7.9D, the Alfvén speed calculated using time-averaged parameters, $\overline{V}_{ms,f}$, is used to try and explain these trends and perform some approximate calculations to aid the discussion.

The stand-out from this figure is that it clearly demonstrates that the magnetic tension plays a role in identification of low-latitude vortices regardless of their evolutionary stage. This differs from the results of the local simulation which found the tension to only matter in the later stages of the KHI when small-scale structures were formed. The rotational component of the magnetic tension term has sizeable contributions in all stages meaning that a global magnetic geometry and realistic plasma conditions do impact the role of this term. The way it does this is illustrated using a box-model set up (see Figure 3.3) in Figure 7.10. The idea is that the evolution of plasma into a vortical shape twists frozen-in magnetic field lines which would then impose a rotational force which will oppose the vortex wrapping up.

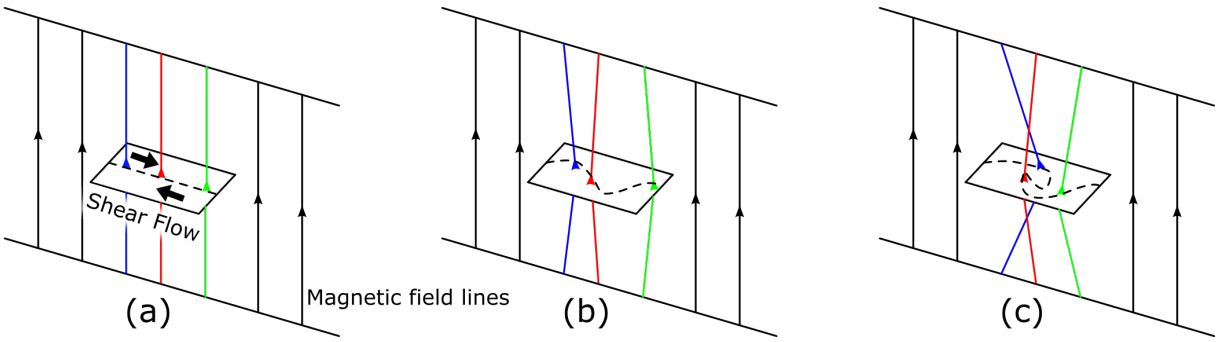


Figure 7.10: A cartoon showing how magnetic tension can influence the KHI when it is threading the boundary. The magnetic field lines are shown to be anchored into ionospheres. From panel A to C it can be seen how the field lines, which are frozen-in to the plasma, get wrapped up and twisted such that they would impose a rotational force on the plasma as they unravel.

The rotational magnetic tension appears to be most important for the inner mode of the KHI compared to the outer mode. This is likely to be due to the inner mode existing in a region with greater field strength meaning that the vortex-threading field lines can provide a larger rotational tension force compared to those of the outer mode. Moreover, the inner mode will be tied to closed field lines which are anchored in the ionosphere and can therefore provide a larger rotational tension force compared to those threading the outer mode. This results in the term opposing the vortex on the dayside, where the field lines are tightly tied into the ionosphere meaning that they resist

the vortices twist, opposing it. Around $X \approx 15\,R_E$, the term begins supporting the existence of a vortex. These different patterns can be explained by using results from the previous chapter and other studies.

The relative importance of magnetic tension should scale as $\sim M_A^{-2}$ (equation 3.6) and it was found in the previous chapter that for the tension term to be of similar importance to the momentum term, Alfvén Mach numbers of $0.3 \lesssim M_A \lesssim 0.6$ may be required on both sides. Like the other terms, λ_T also has a local-time dependence like that seen in the other previous terms. This can be explained by calculating some approximate Alfvén Mach numbers. Beyond the bifurcation point, approximately $5\,\mathrm{R_E}$ down tail, the vortex speed was approximated as $\sim 200\,\mathrm{km\,s^{-1}}$ on the outer mode and $\sim 50\,\mathrm{km\,s^{-1}}$ on the inner mode. In the frame of the vortex, given an Alfvén speed of $200\,\mathrm{km\,s^{-1}}$, this corresponds to an Alfvén Mach number of ~ 0.5 on the outer-mode and ~ 0.25 on the inner-mode. This explains that the inner-mode would have stronger values of λ_T. Beyond this, far down tail within the turbulent stage region, the Alfvén Mach number is quite high implying that the magnetic tension effects in this region are less significant explaining why the term contribution is weak far down tail.

To briefly summarise, it is clear that the evolving plasma environment that a vortex evolves in significantly influences the identification and therefore formation of KH-vortices. This is reflected in the momentum, density gradient, and fluid compressibility terms which all show varying properties based both on evolutionary stage but also the local plasma conditions. Furthermore, it was shown that a realistic magnetic geometry significantly alters the role which the rotational component of the magnetic tension on the formation of a vortex. What these terms explain is why the local time dependence exists in the power of the vortices, but as this study was reduced to the equatorial plane it does not explain the latitudinal dependences of the vortices. Now that the lower-latitude vortices have been investigated, the same analysis can be performed on the high-latitude vortices in the hope to explain their origins.

7.5.2 Noon-Midnight Plane

Figure 7.11 shows the mean value of λ_{MHD} below the threshold value of $\lambda_{\mathrm{MHD}} < -1 \times 10^{-25}\,\mathrm{Pa\,m^{-2}}$, and within $5\,R_E$ of the magnetopause. The vortices in the Noon-Midnight plane are shown to be

tightly restricted around the magnetopause boundary existing no further than $\sim 1.5\,R_E$ from the magnetopause boundary. Importantly, in Figure 7.2B the high-latitude disturbance amplitude clearly grows as it moves down tail. As well as this, it is located outside the equilibrium magnetopause. The highest vortical power is found in the cusps and tailward of the cusps. A vortex's power drops beyond $40\,R_E$ on both the north and south flanks meaning flow dissipation is taking place which may allow energy to cross the magnetopause into the magnetosphere. This decay occurs much sooner along the tailward of the cusp magnetopause than it occurs in the equatorial plane. It is suggested that, as this boundary is not expected to be KH-unstable, the disturbances cannot reach as far down tail as they are not KH-driven. Further investigation is needed into the efficiency of this potential transfer process and the pathways the associated energy and momentum may take.

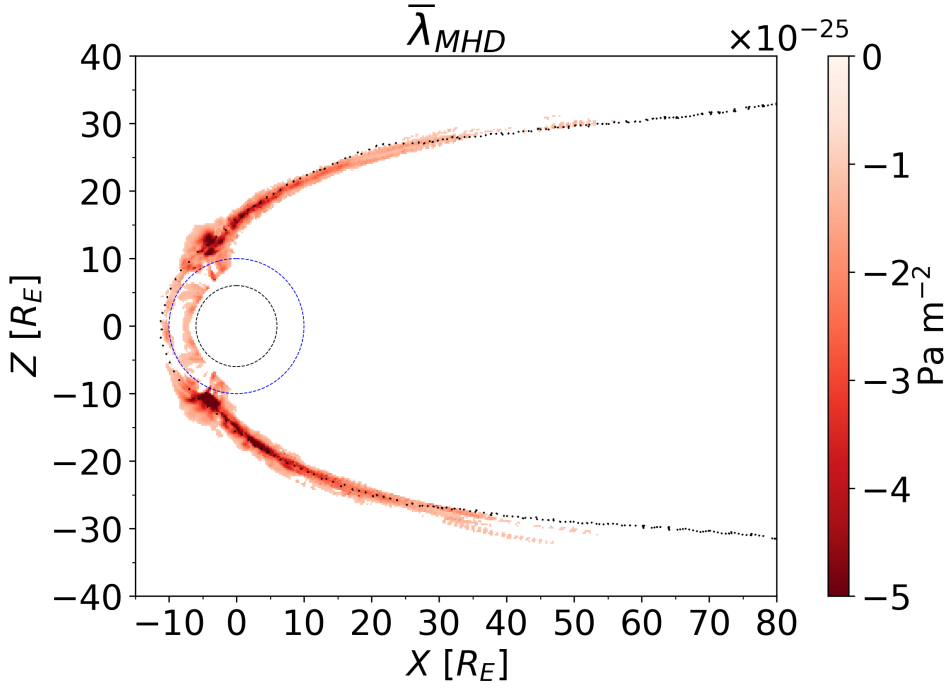


Figure 7.11: The mean value of λ_{MHD} is shown in colour below the threshold value of $\lambda_{\mathrm{MHD}} < -1 \times 10^{-25}$, and within $5\,R_E$ of the magnetopause in the noon-midnight plane. The dashed black circle shows the simulation inner-boundary which is a sphere of radius $4.5\,R_E$. The blue dashed circle with a $10\,R_E$ radius encloses the region thought to be too close to the inner boundary to be true. The dotted line is the open-closed magnetic field line boundary of the time-averaged magnetic field.

Figure 7.12 shows the different contributory terms to λ_{MHD} shown in Figure 7.11. By inspection it is clear that the rotational component of the magnetic tension dominates the identification of these vortices, followed by a small but non-negligible contribution from the vortical momentum term. The fluid compressibility and density gradients are seen to play an insignificant role in vortex identification

here. This is simply explained by the vortices existing only on the inside of the magnetopause where the plasma has been shown to be near incompressible and the density to be smooth without strong variations. Importantly, the vortical momentum term has a strong signature confirming that these identifications are associated with physical vortices and are not just a magnetic effect.

The cusp vortices are seen to have a momentum component which is less strong than that of the rotational magnetic tension effects which dominate the cusp region; compressibility is insignificant throughout. It is important to note that there are positive values of the momentum term within the cusp region suggesting that the vortices here are not solely magnetic. A similar correlation is found with respect to the high latitude vortices behind the cusps. The signatures here are dominated by the rotational magnetic tension term which has a vortex value in a band $\sim 2.5\,R_E$ thick along the equilibrium magnetopause. These signatures extend up to $\sim 40\,R_E$ down tail. The vortical momentum term, however, is restricted to a thin band $\sim 1.5\,R_E$ thick which is within the proxy magnetopause but it does also extend to $\sim 40\,R_E$ down tail. This suggests that the vortices in the high-latitudes behind the cusps are flow vortices however it is clear they are not KH-driven, that is momentum-driven; instead they appear to be magnetically-driven.

Currently, the results suggest magnetic effects may be driving the high-latitude perturbations as they are all dominated by rotational magnetic tension. Furthermore, the presence of the cusp vortex suggests cusp reconnection may be taking place. This is because Tkachenko et al. (2008) suggest that the cusp vortices are a result of tailward of the cusp reconnection outflow jets causing a velocity shear in the cusp region which results in a vortex forming. An investigation into the cusp reconnection is performed in Section 7.7.

Recall that Figure 7.6 clearly demonstrated a three-dimensional latitudinal dependence on the vortices. So far, only the equatorial longitudinal dependence on the vortex strength has been explained using the evolving plasma environment meaning a further investigation is needed into the three-dimensional structure of these vortices and how they couple to a realistic magnetic field geometry in a hope to explain the latitudinal decay.

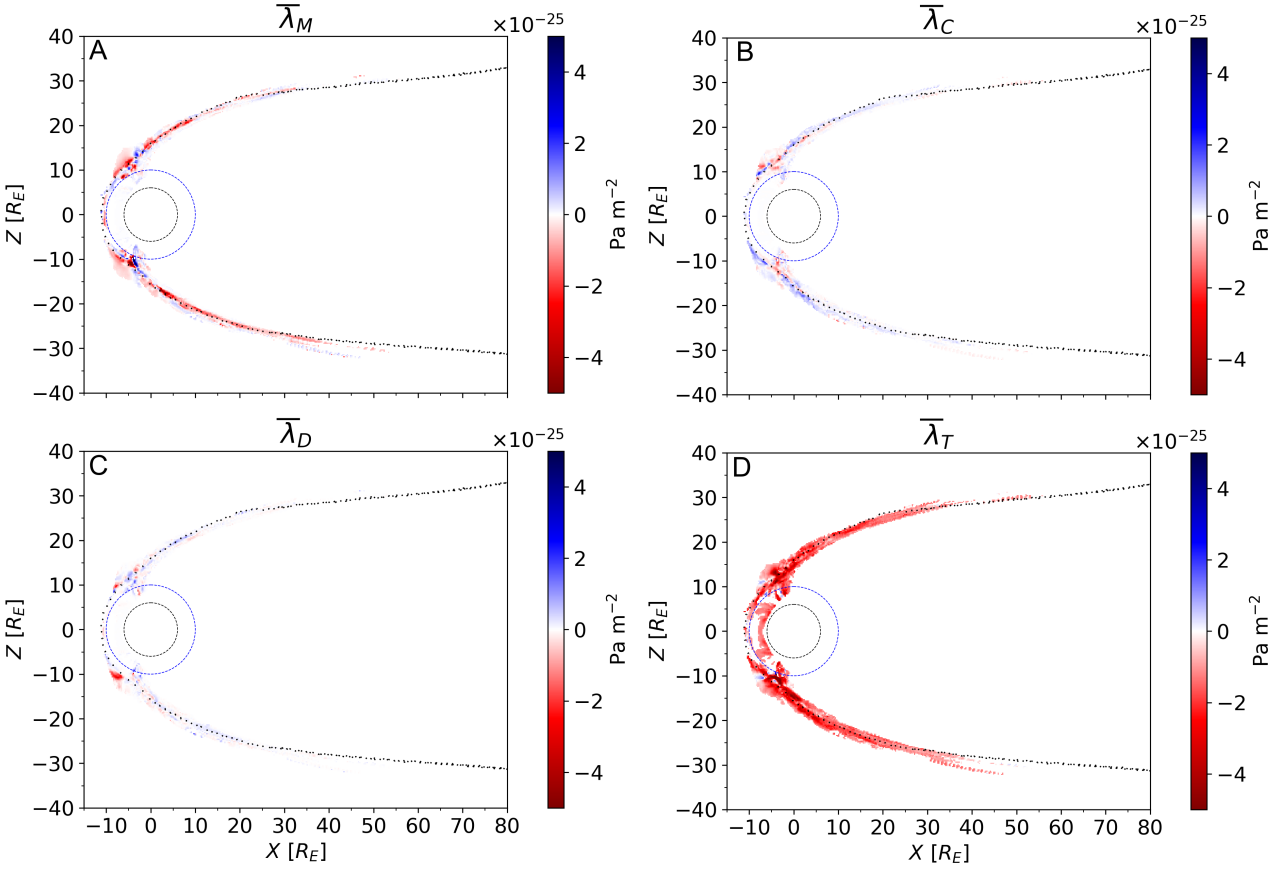


Figure 7.12: The mean value of λ_M, λ_D, λ_C, λ_T are shown in colour. They are selected by being contributing to values below the threshold value of $\lambda_{MHD} < -1 \times 10^{-25}$, and within 5 R_E of the magnetopause in the noon-midnight plane. The dashed black circle shows the simulation inner-boundary which is a sphere of radius 4.5 R_E. The blue dashed circle with a 10 R_E radius encloses the region thought to be too close to the inner boundary to be true. The dotted line is the open-closed magnetic field line boundary of the time-averaged magnetic field.

7.6 Consequences of a realistic magnetic field geometry

Given that in the previous section it was shown that the inner- and outer-mode KH-vortices responded differently to the plasma environment, it is important to continue to take the two modes into consideration with the continued analysis on the realistic magnetic field geometry. For this to be possible, the mean value of λ_{MHD} below the threshold value of $\lambda_{MHD} < -1 \times 10^{-25}\,\mathrm{Pa\,m^{-2}}$, and within 5 R_E of the magnetopause averaged over 25 minutes of simulation time is used. Because the global geomagnetic field changes on a global scale rather than a local one, a further three-dimensional Gaussian filter with a sigma of 0.25 R_E is used to smooth over the data as a visual aid. This filter performs a weighted average of surrounding pixels based on the Gaussian distribution and therefore smooths over sharp discontinuities.

Figure 7.13 shows a three-dimensional rendering of the dusk sector inner- (panel A) and outer-mode (panel B) of the Gaussian filtered time-averaged λ_{MHD} within $5\,R_E$ of the magnetopause using a linear transparency where the transparency is set as fully transparent at $\lambda_{MHD} = -1 \times 10^{-25}\,Pa\,m^{-2}$ and fully opaque at $\lambda_{MHD} = -3 \times 10^{-25}\,Pa\,m^{-2}$. The inner-mode has been selected as being within $5\,R_E$ of the inside of the equilibrium magnetopause boundary and the outer-mode being within $5\,R_E$ of the outside of it. A noon-midnight slice of the magnitude of the time-averaged magnetic field is shown, as is a sphere of radius $5\,R_E$ in white to show the inner-boundary.

There are two distinct regions in both panels – the low latitude region and the cusp/high latitude region. The low-latitude vortices extends much further down tail than the high-latitude vortices. Moiré patterns due to imposing a Cartesian grid onto a curved surface can be seen in both panels; it has been highlighted in the figure and should be ignored. In both panels, there appear to be tendrils of vortex power coming out of the cusps towards the night-side of the magnetosphere. The tendrils do not appear to cross the mid-latitudes or connect to the low-latitude vortices. There are strong λ_{MHD} valued tendrils which reach just off the nose of the cusps which are thought to be related to the existence of cusp-driven KHI seeding taking place as discussed in Section 7.4.

Generally speaking, the inner-mode of the KHI has much stronger λ_{MHD} vortex signatures and a larger latitudinal extent than the outer-mode supporting the claim that the inner-mode is more KH-unstable than the outer-mode (Lee et al. 1981). Both modes appear to decay in latitudinal extent as the vortices propagate and evolve along the magnetopause and the outer-mode appears to decay faster than the inner-mode. This decay has been illustrated on both panels. This is attributed as a consequence of the realistic magnetic field geometry and shall be explained using Figure 7.14.

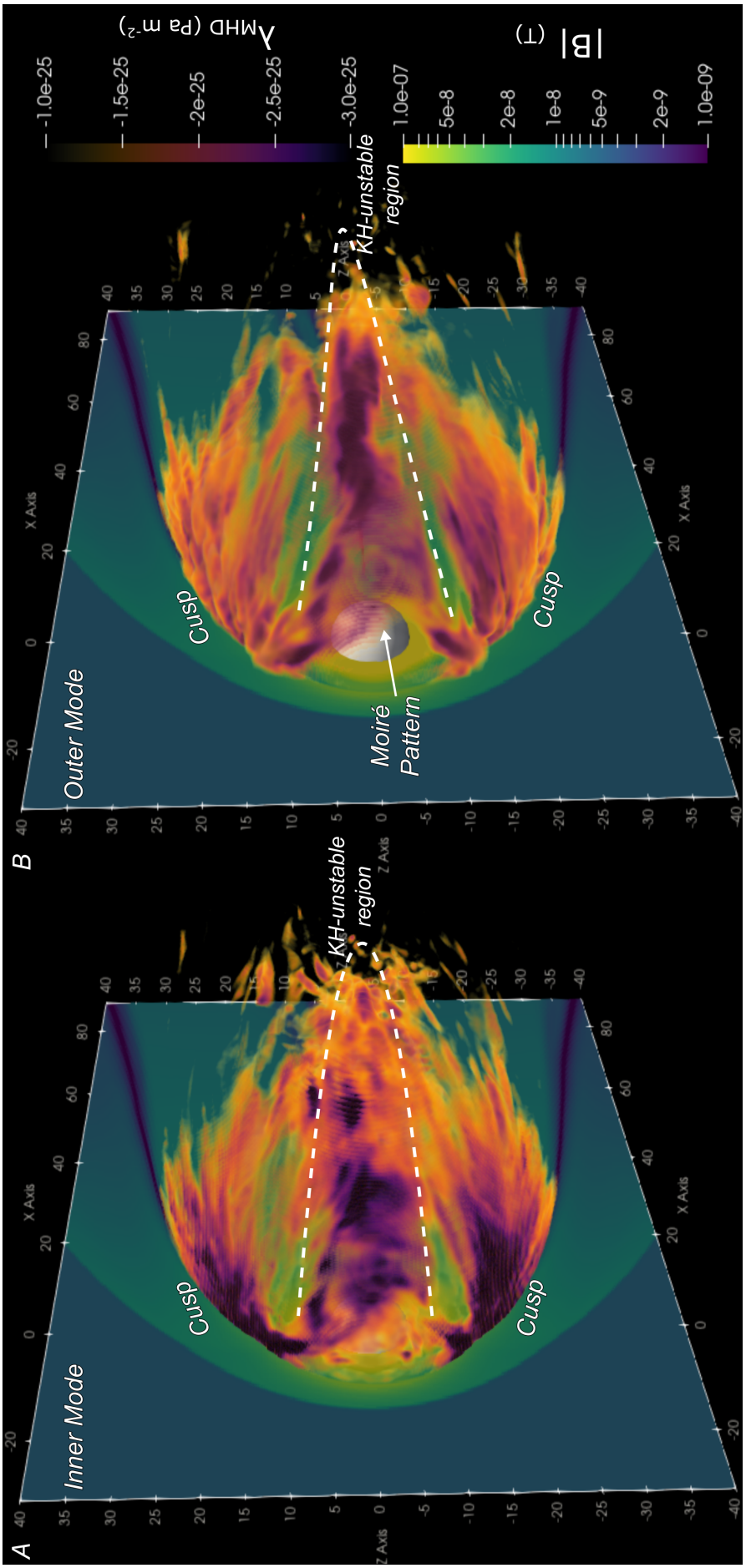


Figure 7.13: A three-dimensional rendering of the inner- (A) and outer-mode (B) mean value of λ_{MHD} shown using a linear transparency colour below the threshold value of $\lambda_{\mathrm{MHD}} < -1 \times 10^{-25}$, and within 5 R_E of the magnetopause in the noon-midnight plane. The noon-midnight plane of the time-averaged magnetic field is shown. The KH-unstable region is highlighted using a white dashed line which differs for the inner- and outer-modes. Moiré patterns are highlighted.

Figure 7.14A shows a three-dimensional view of the noon-midnight slice of the time-averaged magnetic field with field lines connected to the magnetopause boundary drawn in white using a fourth-order Runge-Kutta field line tracer on the time-averaged field which is solved in both directions from the Paraview toolkit (Ahrens et al. 2005). The closed field lines are seeded using a $0.5\,R_E$ sphere point cloud containing 10 points placed at arbitrary distances along the open-closed field line boundary. The panel shows how the dipolar field geometry is strongly perturbed on the night side of the magnetosphere along the magnetopause boundary.

On the dayside of the magnetosphere, the field lines are approximately dipolar and run parallel to the magnetopause surface and thread the equatorial (and shear flow) plane – even in the higher-latitudes. On the night side, however, the field lines extend from the ionosphere and are stretched and bent such that they run parallel to the shear flow as they are stretched into the tail. When they reach the magnetopause, the field lines point perpendicular to the shear flow direction, thread the equatorial plane, and then must run parallel to the shear flow again as they are anchored in the ionosphere. The implications this has on the KHI are explored using concepts from simple linear theory, and the cartoons in Figure 7.14B.

By using Equation 3.6 (Chandrasekhar 1961) and assuming the KHI is being strongly driven beyond the $X = 0$ line and therefore the wave vector direction, $\hat{\mathbf{k}}$, points in the direction of the shear flow driver in the approximate $\hat{X}$-direction (tangential to the magnetopause surface). Now consider only the magnetic field direction as a stabiliser for the KHI. The magnetic tension stabiliser is at a maximum where the magnetic field direction, $\hat{\mathbf{B}}_\mathbf{i}$, is parallel to the wave vector direction, $\hat{\mathbf{k}}$, and can therefore stabilise the boundary to the KHI. Alternatively, where the magnetic field direction, $\hat{\mathbf{B}}_\mathbf{i}$, is orthogonal to the wave vector direction, $\hat{\mathbf{k}}$, the magnetic tension stabiliser is at a minimum and the boundary is unstable to the KHI allowing vortices to grow and evolve. It is worth considering that in reality, the most unstable mode will lie between the optimal direction for the shear flow driver and the optimal direction for the magnetic tension stabiliser, however there is an expected bias towards the magnetic tension stabiliser (Southwood 1968; Walker 1981).

Now applying this to Figure 7.14, where the magnetic field lines in the tail are parallel to the shear flow direction at the magnetopause (and therefore the wave vector), the boundary becomes stable to the KHI and therefore the vortices in these locations decay. Figure 7.14B uses a simple

cartoon to try and explain this effect. With an increasing local time, the magnetic field lines are stretched further into the tail and therefore point more parallel to the KHI wave vector at lower and lower latitudes. This effect is likely causing the latitudinal variation of the vortices in local-time seen in Figure 7.13. As local time increases, the angle between the magnetic field direction and the wave vector reduces, causing the magnetic tension stabiliser term to increase and therefore stabilise the boundary to the KHI. This would cause the vortices to no longer be driven and likely dissipate by either plasma mixing, sending Alfvén waves along the field lines, or sending magnetoacoustic waves into the magnetosphere (Fujimoto et al. 2006; Uberoi 1989; Archer et al. 2024). The wedge where the vortices are seen in Figure 7.13 is the region where the field lines are quasi-perpendicular to the wave vector and this region decreases in latitudinal extent as local time increases.

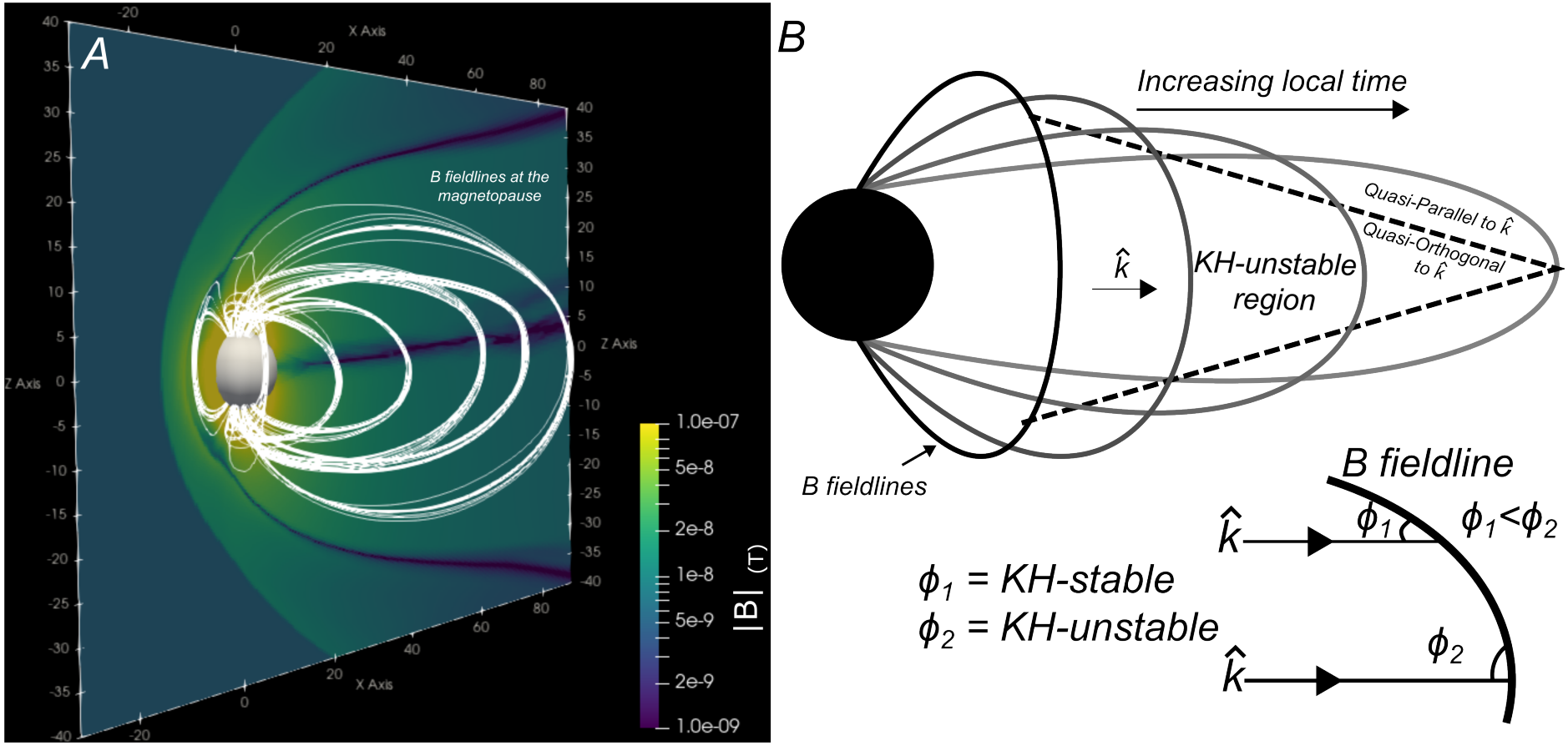


Figure 7.14: A three-dimensional rendering of field lines of the time-averaged magnetic field at the magnetopause is shown alongside the noon-midnight spatial slice in panel A. Panel B is a cartoon illustrating how the different field lines provide varying latitudinal stability to the magnetopause due to their shape and how parallel they are to the wave vector.

The above claim is supported by results from Farrugia et al. (1998) who show that the magnetic shear along the magnetopause is sensitive to the shape of the magnetic dipole field lines which changes along the flank. Furthermore, it has been shown that the KHI is highly sensitive to the magnetic tension stabiliser (Southwood 1968; Walker 1981). Together, these results support the claim here that the shape of the realistic dipolar field is causing the KH-vortices to be limited into the equatorial plane due to magnetic tension stabilisation. This claim is supported by simulations by Michael et al. (2021) who show that changing the IMF clock angle allows for high-latitude KH-waves to form. The implications here suggest that, as the KHI is ubiquitous at the magnetopause (Kavosi and Raeder 2015), the KHI always exists along the magnetopause in a location which is dictated both by the IMF direction, and the dipole field direction. This means by changing the IMF clock angle, the KHI can be shifted along the latitudinal direction of the magnetopause within a spatial limit imposed by the dipole field.

It has now been shown that a realistic plasma environment and magnetic field geometry allows for inner- and outer-mode KH-waves and vortices to exist. As well as this, it also affects how different physical effects affect the evolution of the KHI, it causes a local time dependence on vortex power, and it also causes a latitudinal dependence on the vortex extent. However, it does not explain why the high-latitude vortices exist but it does point towards cusp reconnection being responsible. This leads to the final section of this chapter which explores the coupling between high-latitude vortices and cusp reconnection.

7.7 The connection between high-latitude vortices and cusp reconnection

Throughout this work reference to the presence of cusp reconnection has been made without evidence. This section will give evidence for this and discuss its implications with reference to the vortices identified by λ_{MHD}. Observations have shown that under northward IMF, field lines just tailward of the cusp regions reconnect with draped IMF field lines due to the field lines running almost anti-parallel to each other (e.g. Gosling et al. 1991; Phan et al. 2003). This process does take place in this simulation and is shown in Figure 7.15 which is a three-dimensional visualisation of λ_{MHD} with

equatorial plane and noon-midnight plane slices of the magnitude of the instantaneous magnetic field. Magnetic field lines are traced by using a fourth-order Runge-Kutta method solving in both directions using the Paraview toolkit (Ahrens et al. 2005), the open field lines are plotted in black and the closed field lines are plotted in white. The field lines are seeded using a $5\,R_E$ sphere point cloud centred on the white cross which is placed at the centre of the magnetic island. If a field line is connected at only one inner-boundary hemisphere, then it is categorised as open and is coloured in black. There is a panel showing the magnetic field lines in the noon-midnight plane only which clearly shows the reconnection x-line and a magnetic island in the tailward reconnection outflow.

The main panel of the figure shows the dusk sector of the magnetosphere after 4 hours, 17 minutes, and 15 second of simulation time – the same time as the visualisations in Section 7.4. The figure shows how magnetic reconnection takes place at the cusp as indicated by the x-line shown in the top left panel. The magnetic reconnection event will drive two outflow jets: one sunward and the other tailward (Kulsrud 2001). It is believed that the outflow jet is identified as vortical as it is Alfv'enic, and therefore contains some source of field-aligned vorticity which would be identified in λ_T. The dayside outflow jet is suggested to propagate through the cusp and terminate on the near-nose flank magnetopause, seeding low latitude KHI. The consequences of this are that magnetopause oscillations at the nose of the magnetopause may be driven by pressure variations originating from cusp reconnection. This opens questions regarding the importance of this process for momentum and energy transfer into the magnetosphere and if it drives other phenomena such as magnetopause surface eigenmodes.

The tailward outflow jet contains a secondary magnetic island (Drake et al. 2006) which is on the inside of the magnetopause current sheet and is threaded by a flux rope as seen in the figure. At the magnetic island, where the high-latitude magnetopause perturbation is found, sits a tailward of the cusp vortex. This vortex does not thread the flux rope. It is unclear whether the vortices are twisting the field or vice-versa however, given that the vortex which exists in this region is mostly identified by the rotational component of the magnetic tension term, it is likely that the rotating magnetic field is twisting the plasma due to the frozen-in flux theorem (Alfvén 1942). There is an additional vortex signature within the centre of the flux rope near the mid-latitudes which is also thought to be generated by this process however further work is needed to be sure. It is worth mentioning the flux

rope structure, which are usually assumed to be quasi-force free, either contains unsteady strain or some force that is contributing to its detection. Given that these vortices are not KH-generated, this investigation is left to future work as it is beyond the scope of this thesis. The flux rope does appear to stretch down into the equatorial magnetopause however in this region it is less twisted suggesting that the low-latitude vortices are not causing this twisting either. The flux rope does not appear to connect to the low-latitude vortices identified by λ_{MHD}. However, this may explain why there are low-levels of λ_T in the equatorial plane far down tail – it is because the flux ropes are driving small levels of twisted field which would try to twist the plasma in the equatorial plane. But, as the rotational magnetic tension term does not have a strong contribution in these equatorial regions ($X > 40\,R_E$), there is little evidence to suggest that these magnetic structures influence the equatorial vortices in any significant way but further work into this process may reveal a connection between the two processes.

To be explicit, it is clear that the high-latitude vortices are thought to be a result of the reconnection driving waves (Sonnerup et al. 1981) which rapidly decay as the boundary is stable due to the field geometry. The high-latitude magnetopause perturbations, however, are not at all KH-generated nor is there any evidence to suggest they are a consequence of cusp reconnection driving surface waves. The high-latitude magnetopause perturbations are shown to be a consequence of magnetic islands, generated by cusp reconnection, being advected along the inside of the high-latitude magnetopause. These islands are associated with variations in pressure which push the high-latitude magnetopause away from its equilibrium position. This explains why the high-latitude perturbations are not periodic or uniform as they are driven by outflows from bursty reconnection.

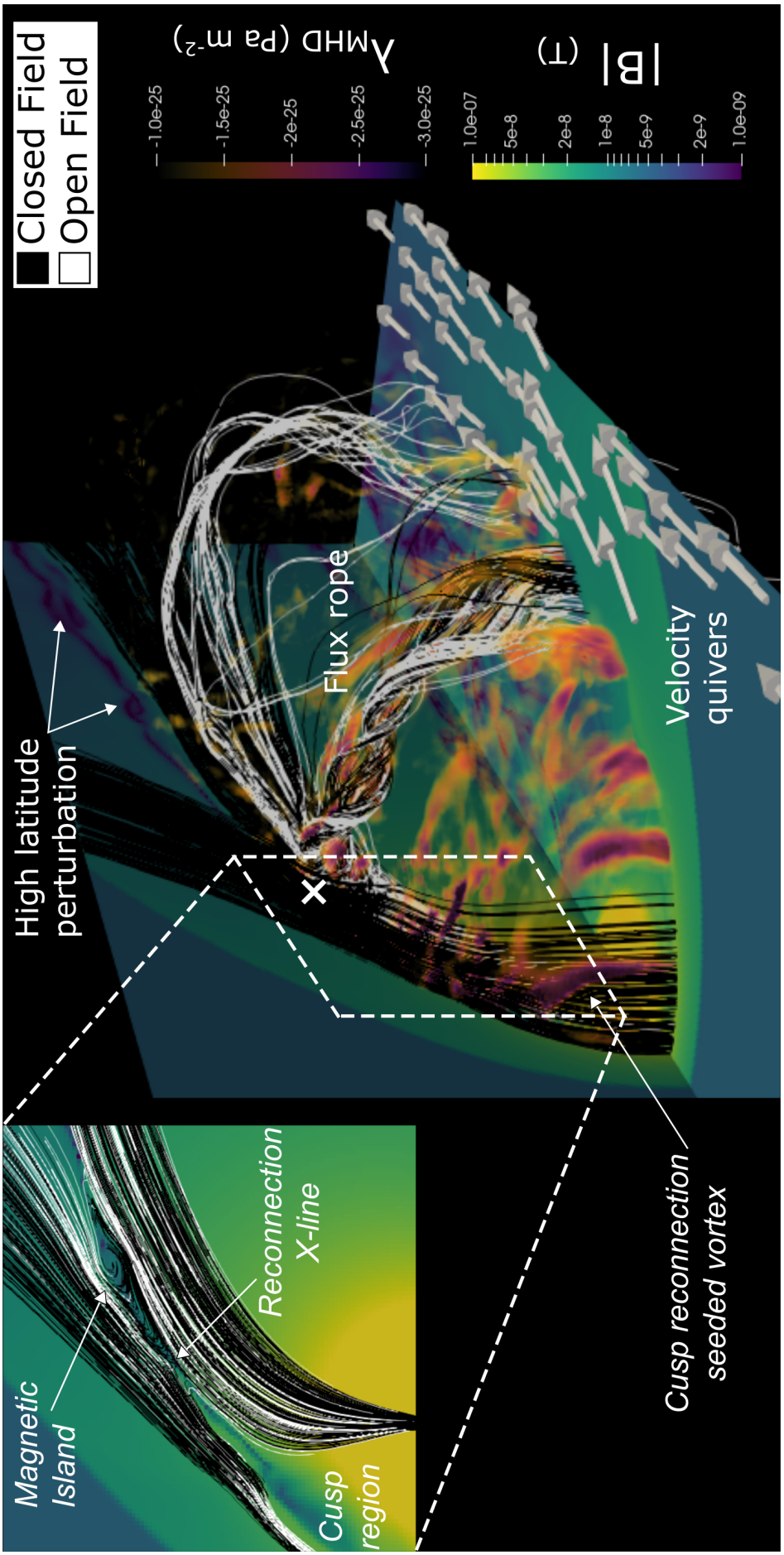


Figure 7.15: A three-dimensional rendering of λ_{MHD} shown using a linear transparency colour below the threshold value of $\lambda_{MHD} < -1 \times 10^{-25}$, and within 5 R_E of the magnetopause in the noon-midnight plane. The equatorial and noon-midnight plane of the magnetic field is shown. As well as this, magnetic field lines a traced from the cusp location to reveal a flux rope composed of open and closed field lines. A two-dimensional slice is taken from the simulation to show the reconnection.

7.8 Summary

To summarise, a vortex identification technique known as λ_{MHD} was used in unison with the Gorgon global MHD simulation to study how the evolution of KH-vortices are affected by the changing magnetic geometry and plasma conditions in a realistic magnetosphere driven with continuous solar wind with perfectly northward IMF. The λ_{MHD} technique allows for a decomposition of the physical contributors to the vortex while also enabling a novel visualisation of the three-dimensional structure of the vortices making a study of this type possible. Vortices were found to exist and propagate along the magnetopause in the low- and high-latitudes. The low-latitude magnetopause was found to be KH-unstable whereas the high-latitude magnetopause was found to be KH-stable with further evidence suggesting that the high-latitude magnetopause perturbations were not KH-driven and were likely a result of magnetic islands from cusp reconnection disturbing the magnetopause boundary. It was found that cusp reconnection is a potential seed mechanism for KH-vortices near the nose of the magnetopause, potentially having implications for energy transfer and magnetopause eigenmodes. Furthermore, vortices were found to exist in the high-latitude cusps which are likely a result of the cusp reconnection process as discussed by Tkachenko et al. (2008).

Both the inner- and outer-modes of the KHI were observed indicating that the inclusion of a realistic plasma and magnetic environment affects the evolution of the KHI as these were not seen in the simplified local-simulation. The low-latitude KH-vortices were found to be seeded $\sim 1\,R_E$ from the magnetopause nose and exist $\sim 1.5\,R_E$ from the boundary at the dayside of the magnetopause but $\sim 5\,R_E$ from the magnetopause on the night side as the waves bifurcated across the thickening boundary layer at the $X = 0$ line. The outer mode's vortices power drops beyond $X = 35\,R_E$ on the dawn and $X = 45\,R_E$ on the dusk flank. The inner mode's vortices power drops beyond $X = 50\,R_E$ on the dawn and $60\,R_E$ on the dusk flank. The inner mode appears to generally survive much further into the tail than the outer mode supporting theoretical findings that it is the more unstable mode (Lee et al. 1981), and the results of simulation work (Michael et al. 2021). The high-latitude vortices are found to be seeded just behind the cusps and are tightly restricted to be within $\sim 1.5\,R_E$ from the magnetopause boundary indicating they are not evolving to large scales like the low-latitude waves. Observations of the KHI at varying distances in the tail can allow for further investigations

into the KHI evolution far down flank (e.g. Feng et al. 2024).

The decomposition of λ_{MHD} into its constituent drivers revealed how vortical momentum, plasma inhomogeneity, fluid compressibility, and rotational magnetic tension affect the inner- and outer-modes of the KHI differently. The analysis showed that a realistic plasma environment and magnetic field geometry alters how these physical effects influence the evolution of the KHI when compared to the results of the study on the simplified local simulation in the previous chapter. The vortical momentum term was found to decay in local time suggesting momentum transfer into the magnetosphere. Vortical momentum also influenced the inner- and outer-modes differently. The momentum term of the inner-mode was seen to decay to lower values more rapidly after the mode bifurcation than the outer mode. This lower-level is found much further into the tail for the inner-mode than the outer-mode which is suggested to be due to mode stability (Lee et al. 1981). The explanation for the outer-mode's strength surviving longer is due to the outer-mode vortices travelling faster and therefore the signatures from the compact non-linear growth vortices survive further into the tail. If these stronger values are attributed to the non-linear stage of the KHI, then this suggests that the evolutionary stages take place at different local times. Furthermore, this variation in evolutionary stages is supported by the density gradient term.

The investigation into plasma inhomogeneity showed that only the outer mode vortices are effected and stabilised by the density variations. Studies by Amerstorfer et al. (2010) suggests this slows the growth rate of the KHI and therefore supports the suggestion that the two modes evolve differently. It was concluded that the plasma homogeneity term is only important in the transition from the quasi-linear into the non-linear stage.

Fluid compressibility was shown to be non-zero which immediately shows that a realistic plasma environment changes the influence of compressibility on the evolution of the KHI. Like the density gradients term, the compressibility term appears to only significantly affect the outer-mode of the KHI when it is in the linear and non-linear stages of evolution. The fast magnetosonic Mach number revealed that this is because the inner-mode plasma was found to be in an incompressible region explaining the small negative values found for the inner-mode. Compressibility contributed to a vortex identification in the linear stages of the outer-mode of the KHI however negated in its non-linear stages. This is explained by previous studies suggesting that compressibility has a destabilising effect

on the boundary and growth rate of the KHI (Fejer 1964; Sen 1965; Southwood 1968). In this highly-nonlinear stage, the KHI is stabilised by compressibility. This can be explained either by the wave growing suitably such that it becomes a leaky oscillatory wave which carries energy away from the boundary and into the magnetosphere and magnetosheath, consequently stabilising the KHI (Pu and Kivelson 1983). Or by the thickness of the boundary in this region nears the scale of the wavelength, stabilising the boundary (Miura 1992).

Rotational component of magnetic tension was shown to effect the inner-mode of the KHI more than the outer-mode. It was suggested that a greater field strength at the inner-mode allowed for the vortex-threading field lines which are anchored in the ionosphere can provide a larger rotational tension force compared to those of the outer mode. This results in the term opposing the vortex on the dayside. Around $X \approx 15\,R_E$, the term begins supporting the existence of a vortex in the vortices turbulent stages. Like in the previous chapter, this shows that the field lines support the growth of small scale vortical structures. The Alfvén Mach number was used to explain the decay in local time found in the term. However, more consequences of a realistic magnetic geometry were found.

It was shown that vortices appear to become more restricted into the equatorial region with increasing local time. This was explained by using linear theory arguments about the stability of the magnetopause boundary. It was shown that the dipole field is draped along the magnetopause boundary in such a way that the field lines are draped parallel to the high-latitude boundary and therefore stabilise it to the KHI due to magnetic tension effects. This stabilisation occurs at lower latitudes with larger local times due to how the field lines are stretched and extended down tail.

Further extensions to this work are needed. A three-dimensional analysis is needed into how vortical momentum, plasma inhomogeneity, fluid compressibility, and the rotational component of the magnetic tension influence the identification of a vortex as a function of latitude. This will hopefully reveal a better understanding into how vortices evolve at different latitudes providing an insight into the different transfer mechanisms which can take place and where they can be observed e.g. how out of plane vortex-induced reconnection can be. It is important to mention that this study was restricted by its simple solar wind and IMF conditions. By introducing variations into the solar wind and IMF will allow a better understanding about when different physical effects become important and also may provide an understanding on how magnetic shear on the nose of the magnetopause

suppresses the KHI.

This chapter has clearly shown that a realistic magnetosphere responds differently to how simplified models predict and thus far this thesis has shown that these vortex trains behave very differently at different local times as well as there existing an inner- and outer-mode. But vortical processes are not the only way the KHI extracts, filters, and redistributes solar wind energy throughout geospace. It is important to now treat these vortex trains as interlinked coherent phenomena and analyse them as surface waves. This chapter has clearly indicated that vortices evolve and advect differently at varying local times and latitudes. And as there is a lack of understanding surrounding how a MSW's frequency and wavelength varies in local time and latitude, this is where the following chapter will begin.

CHAPTER 8

How the Frequency and Wavelength of KH-Generated Surface Waves Vary Along the Magnetopause

8.1 Introduction

So far, this thesis has focussed on the vortices that are generated by the Kelvin-Helmholtz instability. This is because recently there has been a renewed interest into KH-vortices due to evidence of them being responsible for cross-scale energy transfer processes (e.g. Vortex induced reconnection Nykyri and Otto 2001; Nakamura et al. 2017). However, lone vortices are not the sole way that the KHI transfers energy across the magnetopause. The combined behaviour of multiple vortices along the magnetopause form a magnetopause surface wave (MSW) and these MSWs provide both direct and indirect influences throughout magnetospheric regions such as the radiation belts and geostationary orbit, as well as influencing field-aligned currents at the ionosphere (e.g. Hwang and Sibeck 2016; Loto'aniu and Inceoglu 2024). MSWs enable a variety of different pathways for solar wind energy to be rapidly circulated throughout geospace by driving evanescent fast magnetosonic waves into the magnetopsphere (Wang et al. 2017b), they can also couple to body waves (Pu and Kivelson 1983), cavity modes (Plaschke 2016), and Alfvén waves/FLRs (Chen and Hasegawa 1974a; Southwood

1974). When and where this energy is dissipated is heavily dependent on the frequency of the MSWs themselves (Chen and Hasegawa 1974a; Southwood 1974) meaning that understanding the MSW excitation process is imperative to understanding the pathways of ULF wave energy.

Typically, the wavelength of a MSW is measured in-situ (Lin et al. 2014) or in simulation (Li et al. 2012) using crude approximations such as a constant wave speed or assuming a dominant or most unstable frequency. However these are not necessarily true as the understanding of how the frequency and wavelength of an MSW's evolves has competing theories. Simple theory can be used to predict the most unstable MSWs that the KHI is likely to generate for homogeneous conditions tangential to the shear layer (Miura and Pritchett 1982) however, the real magnetopause has highly inhomogeneous plasmas on both sides. Furthermore, the KHI is known to amplify pre-existing disturbances over a wide range of frequencies/wavelengths (e.g. Nykyri et al. 2017). As well as this, the KHI has been suggested to be an advective instability meaning that the unstable modes upstream grow and evolve as they are advected into the downstream (Mills et al. 2000). All these effects together make it unclear whether observed waves have been locally generated by the KHI or have originated from much further upstream and simply been amplified.

The consequence of this is that it becomes unclear what process is dominant: is an observed MSWs frequency and wavelength continuously modulated by the KHI to have the most unstable wave frequency controlled by the local plasma and field conditions like linear theory predicts? Is it a smeared superposition of advected modes from upstream resulting in a complex superposition of frequency along the magnetopause? Or does the dominant KH-wave frequency get fixed at the dayside magnetopause and simply get advected and amplified as it evolves meaning superposition can be ignored due to the inverse cascade?

This chapter brings into question the origin of KH-generated signatures at the magnetopause. When using in-situ measurements the frequency of MSWs is typically extracted through Fourier analysis of the time-series (e.g. Lin et al. 2014), this is then used to estimate the wavelength of the wave by making assumptions about the plasma velocity. Alternatively, when analysing simulations, due to how the data is constructed, it is easier to analyse a single snapshot and measure the wavelength spatially (e.g. Michael et al. 2021), and then infer the frequency from that. As a consequence of this, neither approach is performing spatio-temporal analysis: in situ takes a temporal approach and

simulation takes a spatial approach. And since in situ measurements generally lack simultaneous measurements of the KHI at vastly different local times, they cannot resolve this conundrum meaning a global MHD simulation is required. Furthermore, global spatio-temporal analysis is needed to properly answer the problem. This is simply not computationally feasible using standard wave analysis approaches such as Fourier as they do not reduce the amount of data output. To overcome this issue, and efficiently analyse the data produced by the simulation, a factorisation and dimensionality reduction machine learning technique known as dynamic mode decomposition is used to identify wave-like structures.

8.2 Dynamic Mode Decomposition

Dynamic Mode Decomposition (DMD) is a type of modal decomposition, analogous to a separation of variables, that decomposes a spatiotemporal signal into purely spatial modes, scalar amplitudes, and purely temporal signals (Schmid 2022). DMD makes an assumption that the data contains quasi-stationary temporal variations allowing the technique to identify and extract simple variations, not limited by mode orthogonality. This makes DMD superior to alternative methods such as the commonly used Principal Component Analysis (PCA) (Greenacre et al. 2022; Jolliffe and Cadima 2016). PCA optimises for orthogonal modes and does not make assumptions about the data resulting in it failing to capture simple temporal dynamics. Furthermore, unlike PCA, DMD provides hierarchical and spatial information with the original data being realised from the linear superposition of the decomposition. DMD is unique as it is a data-driven technique that reduces complex dynamic flows into coherent dynamic structures reducing the data into its dominant components. DMD was first developed by Schmid and Sesterhenn (2008) to study hydrodynamical systems and since its development, DMD has been used in a variety of novel ways such as the study of brain waves in neurology (Shiraishi et al. 2020) or studying the oscillatory modes of a duck-shaped membrane (Rot et al. 2022). More pertinently, it has also been used for analysing ionospheric totel electron content (TEC) and plasma density (Landa and Reuveni 2023; Alford-Lago et al. 2023).

DMD is only successful when applied to time varying data from a nonlinear dynamical system such that $d\mathbf{x}/dt = f(\mathbf{x}, t)$. Here $\mathbf{x}$ refers to the data vector of n dimensions meaning that each row

of $\mathbf{x}$ corresponds to a single measurable scalar. Note that if this scalar is distributed in space, the spatial dimension must be flattened and then restored post-processing. The DMD algorithm attempts to approximate the non-linear system $d\mathbf{x}/dt = f(\mathbf{x}, t)$, as a locally linear system $d\mathbf{x}/dt = \underline{\mathbf{M}}\mathbf{x}$. This can be solved for by using the differential equation solution $\mathbf{x} = \mathbf{v}e^{\lambda t}$ resulting in the following eigenvalue problem $\lambda\mathbf{v} = \underline{\mathbf{M}}\mathbf{v}$. Let $\mathbf{v}_i$ be the eigenvector and λ_i be the corresponding eigenvalues. This allows for the linear system to be rewritten in the eigenvector basis such that

$$\mathbf{x} = \sum_{i=0}^{n} b_i \mathbf{v}_i \exp\left(\lambda_i t\right), \tag{8.1}$$

where b_i is the amplitudes corresponding to the coordinates of $\mathbf{x}(t = 0)$ in the eigenvector basis. Equation 8.1 is the fundamental principle of DMD as it has approximated a non-linear system as a linear set of spatial modes (eigenvectors) with associated discrete temporal frequencies (extracted from the eigenvalues), and corresponding hierarchy (amplitudes).

If the determinant of $\underline{\mathbf{M}}$ is zero, then the system is linear and the characteristic equation of the system has one unique solution with a finite number of modes – the systems normal modes. If the determinant of $\underline{\mathbf{M}}$ is non-zero, which it is for all non-linear cases, then the characteristic equation has up to an infinite number of solutions meaning for practicality a different approach is needed. This brings us to the DMD algorithms which can be used to solve the equation.

8.2.1 DMD Algorithm

There are multiple ways to perform DMD. Historically, the original DMD algorithm was formulated through its contextual connection with Krylov subspaces and the Arnoldi algorithm (Schmid 2010). Since then, a more robust algorithm has been developed which uses a singular value decomposition (SVD) approach to better handle noisy data and numerical error while also being more computationally efficient (Tu et al. 2014).

Arnoldi Approach

Begin with a time series of data from a nonlinear dynamical system such that $\mathbf{x}_{k+1} = \mathbf{F}(\mathbf{x}_k)$, where $\mathbf{x}_k$ refers to 'snapshots' of the dynamical system at times t_k, for $k \in \{0, 1, 2, 3, ..., m\}$,

and $\mathbf{F}$ represents the nonlinear governing equations of the system. Start by organising the data into two $n \times (m-1)$ tensors $\underline{\mathbf{X}}_1$ and $\underline{\mathbf{X}}_2$ where the columns of $\underline{\mathbf{X}}_1$ represent the data vectors for snapshots $k = \{0, 1, 2, 3, ..., m-1\}$ and the columns of $\underline{\mathbf{X}}_2$ represent the data vectors for snapshots $k = \{1, 2, 3, 4, ..., m\}$. Recall that each row of the data vectors correspond to a single measurable quantity of which there are n. This results in the two tensors having a time difference of δt in their columns requiring that all the data have a fixed cadence. Recall that the goal of DMD is to solve the equation of $\underline{\mathbf{X}}_2 = \underline{\mathbf{A}}\underline{\mathbf{X}}_1$ where $\mathbf{x}_{k+1} = \mathbf{A}\mathbf{x}_k$ where $\underline{\mathbf{A}}$ is the two dimensional tensor known as the Koopman operator (Koopman 1931; Neumann 1932) which has infinite columns allowing the locally linear operator to be able to exactly describe a non-linear system.

The Koopman operator can be approximately solved for by right multiplying the equation by the pseudo-inverse; a generalisation of the inverse matrix independently described by Moore (1920), Bjerhammar (1951), and Penrose (1955). The pseudo-inverse, denoted with a superscript plus, $\underline{\mathbf{X}}_1^+$, uses a least-square regression algorithm to approximate the inverse of a non-square matrix. This solution minimises the error $||\underline{\mathbf{X}}_2 - \underline{\mathbf{A}}\underline{\mathbf{X}}_1||_F$ where $||\cdot||_F$ is the Frobenius norm given by $||\underline{\mathbf{X}}_1||_F = \sqrt{\sum_{j=1}^{n}\sum_{k=1}^{m} X_{jk}^2}$. This results in the solution of $\underline{\boldsymbol{\mathcal{A}}} = \underline{\mathbf{X}}_2\underline{\mathbf{X}}_1^+$ where $\underline{\boldsymbol{\mathcal{A}}}$ is the data-driven approximation of the Koopman-operator. The eigenvector and eigenvalues of $\underline{\boldsymbol{\mathcal{A}}}$ can then be used to identify the spatio-temporal structures that are seen in the data i.e. to rewrite the data in the eigenvector basis: $\mathbf{x}_k = \sum_{j=0}^{n} b_j v_j \lambda_j^k = \mathbf{b}\mathbf{V}\boldsymbol{\Lambda}^k$ where $\mathbf{x}_0 = \mathbf{v}\mathbf{b}$. This method is known as exact DMD (Tu et al. 2014) and requires constant δt between time steps. A variety of other DMD algorithms now exist (see review by Schmid 2022), one of which is computationally less expensive and is known as singular value decomposition-based DMD, or SVD DMD.

Singular Value Decomposition Approach

In reality when n is large, the matrix $\underline{\boldsymbol{\mathcal{A}}}$ may be too burdensome to efficiently analyse due to the number of modes extracted, many of which will have a negligible amplitude. What this means is a different eigendecomposition approach is needed. Tu et al. (2014) first suggested using a rank-reduced representation of $\underline{\boldsymbol{\mathcal{A}}}$ found through a discrete proper orthogonal decomposition (POD) known as a singular value decomposition (SVD) (Trefethen and Bau 1997) which is also a type of PCA (Chatterjee 2000). The SVD projection of the matrix is denoted as $\underline{\tilde{\boldsymbol{\mathcal{A}}}}$.

The rank of the SVD should generally be half the number of snapshots (Rot et al. 2022). Furthermore, standing waves with a linear dependency between snapshots cause rank deficiency issues (Tu et al. 2014; Kutz et al. 2016), these issues can be overcome by stacking subsequent snapshots into the data tensors. Finally, noisy data and a small number of snapshots can be overcome by time shifting the data (Kutz et al. 2016). The following can be found in Kutz et al. (2016), Algorithm 1.1 and Tu et al. (2014), Algorithm 1. This method has 4 steps:

1. First perform an SVD of the data $\underline{\mathbf{X}}_1 = \underline{\mathbf{U}\boldsymbol{\Sigma}\mathbf{V}}^*$ where $\underline{\mathbf{U}}$ is an $n \times n$ orthonormal matrix, $\underline{\mathbf{V}}$ is an $(m-1) \times (m-1)$ orthonormal matrix with $*$ denoting the conjugate transpose, and $\underline{\boldsymbol{\Sigma}}$ is an $n \times (m-1)$ rectangular diagonal matrix. The elements Σ_{ii} consist of $r = \min(n, m-1)$ non-negative numbers σ_i, which are arranged in decreasing order. The σ's are unique and known as the singular values of $\underline{\boldsymbol{\mathcal{A}}}$ with the number of non-zero singular values of $\underline{\boldsymbol{\mathcal{A}}}$ being its rank. The rank of $\underline{\boldsymbol{\Sigma}}$ can be truncated through user-defined values of r, where the value of σ_i for $i > r$ is 0. This is a rank-reduced representation of the data (Chatterjee 2000).

2. The matrix $\underline{\boldsymbol{\mathcal{A}}}$ can now be calculated from these rank reduced datasets: $\mathcal{A}_{r\times r} = \underline{\mathbf{X}}_2\underline{\mathbf{X}}_1^+ = \underline{\mathbf{X}}_2\underline{\mathbf{U}\boldsymbol{\Sigma}}^{-1}\underline{\mathbf{U}}^*$. In reality, it is more efficient to compute the rank-reduced matrix $\tilde{\underline{\boldsymbol{\mathcal{A}}}}$. This can be done in the following way $\tilde{\underline{\boldsymbol{\mathcal{A}}}} = \underline{\mathbf{U}}^*\underline{\boldsymbol{\mathcal{A}}\mathbf{U}} = \underline{\mathbf{U}}^*\underline{\mathbf{X}}_1'\underline{\mathbf{V}\boldsymbol{\Sigma}}^{-1}$. By defining $\tilde{\underline{\boldsymbol{\mathcal{A}}}}$ in this way, a low-dimensional linear model of the dynamical non-linear system in POD coordinates is described by $\tilde{\mathbf{x}}_{k+1} = \tilde{\boldsymbol{\mathcal{A}}}\tilde{\mathbf{x}}_k$ where the high-dimensional state can be reconstructed using $\mathbf{x}_k = \mathbf{U}\tilde{\mathbf{x}}_k$.

3. Next, compute the eigendecomposition of $\tilde{\underline{\boldsymbol{\mathcal{A}}}}$: $\tilde{\underline{\boldsymbol{\mathcal{A}}}}\underline{\mathbf{W}} = \underline{\mathbf{W}\boldsymbol{\Lambda}}$ where $\underline{\mathbf{W}}$ are eigenvectors and $\underline{\boldsymbol{\Lambda}}$ is a diagonal matrix containing the corresponding eigenvalues λ_k.

4. Finally, the higher-dimensional (not rank-reduced) $\underline{\boldsymbol{\mathcal{A}}}$ eigendecomposition is constructed from $\underline{\mathbf{W}}$ and $\underline{\boldsymbol{\Lambda}}$: $\underline{\boldsymbol{\Phi}} = \underline{\mathbf{X}}_2\underline{\mathbf{V}\boldsymbol{\Sigma}}^{-1}\underline{\mathbf{W}}$. The eigenvalues of $\underline{\boldsymbol{\mathcal{A}}}$ are given by $\underline{\boldsymbol{\Lambda}}$ and the corresponding eigenvectors are given by $\underline{\boldsymbol{\Phi}}$, where the columns of $\underline{\boldsymbol{\Phi}}$ are the eigenvectors or DMD modes. Note that the eigenvalues do not need to be returned to the higher dimensional space.

8.2.2 Interpretation and Outputs

It is important to remember that DMD extracts spatial structures that oscillate and/or exponentially grow/decay temporally. It does this from the eigenvectors and eigenvalues of the data-driven approximation of the Koopman-operator, $\underline{\boldsymbol{\mathcal{A}}}$. It is worth highlighting all the different quantities which can be extracted from DMD and how to calculate them.

Eigenvectors

The eigenvectors of $\underline{\boldsymbol{\mathcal{A}}}$, are complex and known as the DMD modes, and they represent the spatial distributions belonging to the temporally oscillating structures and are unit-less and normalised. If the original data has linear properties such that $d\mathbf{x}/dt = \underline{\mathbf{A}}\mathbf{x}$ is true, then the result will be analogous to the normal modes of the system – that is the temporal dependence is perfectly sinusoidal with fixed frequency and relative phase relation. As the modes are complex, the local phase of the wave can be calculated through the argument of the mode. The time varying mode importance, also called the mode dynamics, B_{ij}, is a complex tensor which corresponds to the projection coefficient of the i-th eigenvector for the j-th data sample, $\underline{\mathbf{X}} = \underline{\boldsymbol{\Phi}}\,\underline{\mathbf{B}}$, where $\underline{\mathbf{B}}$ is defined as

$$\mathbf{B} = \underline{\boldsymbol{\Phi}}^{+}\,\underline{\mathbf{X}} \tag{8.2}$$

where $\underline{\mathbf{X}}$ is the data tensor for all the snapshots. An efficient algorithm for its calculation using the SVD approach is $\underline{\mathbf{B}} = \underline{\mathbf{Z}}^{+}\,\underline{\mathbf{S}}\,\underline{\mathbf{W}}^{+}$ (Tu et al. 2014). It is important to remember that the mode dynamics are complex with the real part and imaginary part being $\pi/2$ out of phase.

The mode dynamics can be reduced into a single value which can be used to inform on the hierarchy of the modes – or perhaps which modes are better represented by the data. This is known as the mode amplitude. The modes are scaled by this amplitude which is retrieved from the decomposition. The amplitude, b_j, is also complex and can be defined in numerous ways, however in this work it is defined such that

$$\mathbf{b} = \underline{\boldsymbol{\Phi}}^{+}\,\mathbf{x}_0 = \mathbf{B}_{k=0}. \tag{8.3}$$

Eigenvalues

Each DMD mode has a corresponding fixed frequency and decay rate – these are extracted from the complex eigenvalues, λ_k, of $\underline{\boldsymbol{\mathcal{A}}}$. To retrieve the real frequency, ν corresponding to a DMD mode, the following equation can be used,

$$\nu_i = \frac{\arg(\lambda_i)}{2\pi\Delta t}, \tag{8.4}$$

where Δt is the time between snapshots and only provides a scaling to the frequency. If a real eigenvalue is found, then the mode corresponds to a DMD frequency of 0 and represents a constant background trend due to a non-zero average. By subtracting the time-averaged mean flow from the data, known as using the perturbation terms denoted with a δ, the background trend can be removed meaning that only complex eigenvalues are found. As well as the frequency, the eigenvalues can provide information about the evolution of the mode amplitude. This is typically called the growth rate, $c_i = |\lambda_i|$. If the $c = 1$ then the mode is perfectly stable and does not grow or decay. If the mode is decaying then $c < 1$, and if it is growing then $c > 1$. This is commonly presented with reference to a unit circle as shown by Figure 8.1.

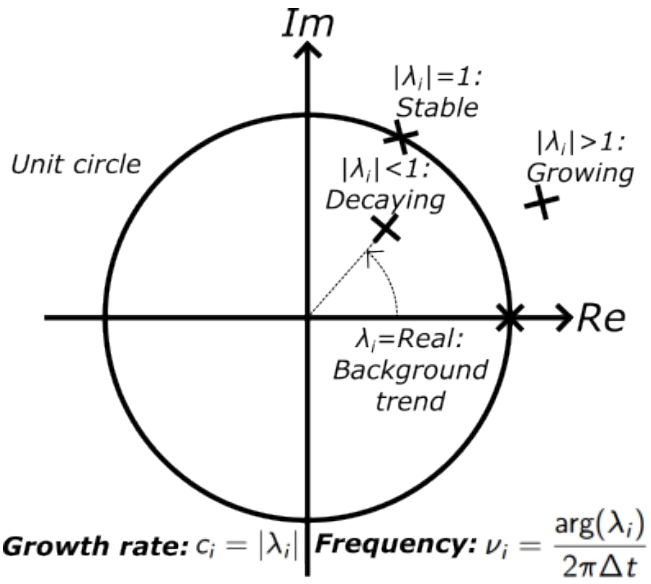


Figure 8.1: A cartoon demonstrating how different parameters can be extracted from the complex eigenvalue outputs of DMD.

Reconstruction and Forecasting

As well as analysis, DMD can be used as a data compression algorithm as it allows for the original data to be reconstructed. The original data is realised by summing the modes with their dynamics such that

$$\mathbf{X}_{DMD} = \underline{\mathbf{\Phi}}\,\underline{\mathbf{B}}. \tag{8.5}$$

This reconstruction can be used to see how well DMD has approximated the original data by calculating a residual, σ, (Bohon et al. 2021)

$$\sigma = \frac{||\underline{\mathbf{X}} - \underline{\mathbf{X}}_{DMD}||_F}{||\underline{\mathbf{X}}||_F}. \tag{8.6}$$

Finally, DMD can also be used to provide future state predictions known as forecasting. This is performed through the equation,

$$\mathbf{x}_{m+1} = \underline{\boldsymbol{\mathcal{A}}}\mathbf{x}_m. \tag{8.7}$$

Forecasting with DMD is included for completeness but will not be used in this work. A visual summary of what DMD can do is shown in Figure 8.2.

Handling real-valued data

A note is needed when passing real data through the DMD algorithm. If the data DMD is applied to is real-valued (not complex or imaginary), then complex conjugate pairs of modes (eigenvectors) are found such that the resulting linear combination is real-valued. If a complex conjugate pair of modes exists, then a complex conjugate pair of eigenvalues are also found. Importantly, one of these will have the negative eigenvalue of the other, and as such corresponds to a negative frequency making it unphysical. But, as they both represent the same oscillating mode, they can therefore be treated as a single mode with twice the amplitude. As the DMD mode just represents the spatial distribution belonging to the temporally oscillating structure, the physically-scaled value needs to be restored by rescaling the mode by its corresponding amplitude or dynamics. That is, if a mode corresponding to a velocity field input is extracted, the mode is unit-less and only tells of the spatial fluctuations; scaling it by the amplitude/dynamics will restore the 'distance per unit-time' units to the mode.

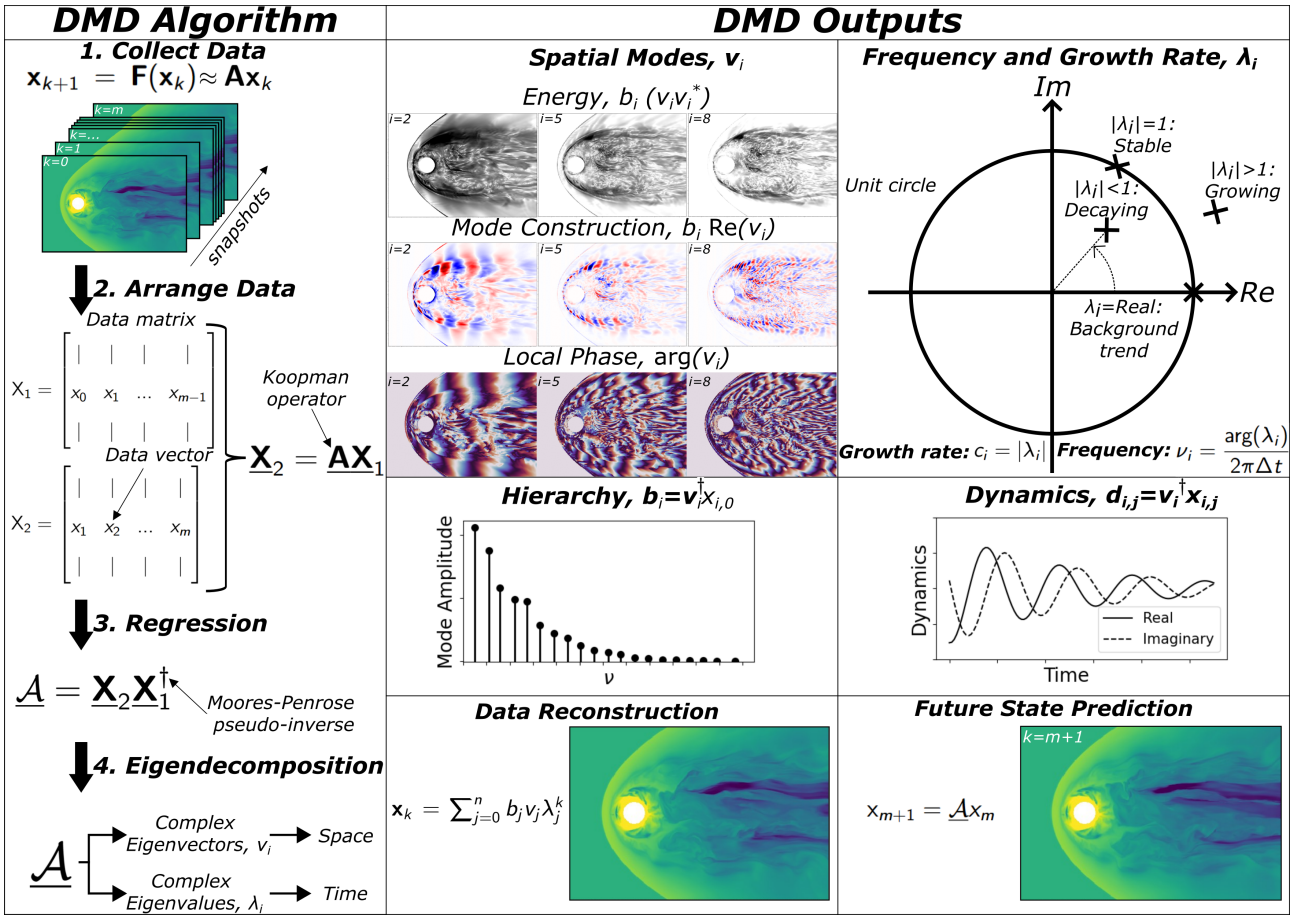


Figure 8.2: An illustrative guide to DMD.

8.3 DMD of a MHD Fluid

DMD was first developed to study the velocity field of hydrodynamic fluids (Schmid and Sesterhenn 2008). This means it needs to be adapted to be applied to MHD. When adapting a hydrodynamic technique for magnetohydrodynamic applications, a level of physical understanding is required to ensure the technique is suitably being applied. In hydrodynamics it is sufficient to describe the entire flow through the velocity field, but in MHD this is not the case. The flow of the plasma is only a component of the fluid, the fields also play a major role meaning that they somehow need to be included in the algorithm. This is why it is important to outline an effective way to apply DMD in MHD as it has never been performed before and it is not as simple as it is for hydrodynamics.

As DMD is data driven, it is important to ensure that all the values in the data vector are comparable so that no single parameter dominates the least-square regression algorithm or the POD step. This is done by rescaling all the parameters such that they have a physically significant

comparability and scaling. As DMD has never before been applied to MHD, this needs to be defined. It is suggested that for ideal MHD, the rescaling used should be found by using the equation for the time-averaged energy density, $\mathcal{E}$, of a harmonic MHD wave: (Walker 2019),

$$\mathcal{E} \equiv \left\{ \frac{1}{4}\rho_0 \boldsymbol{v}\cdot\boldsymbol{v}^* + \frac{p\,p^*}{4\rho_0 V_S^2} + \frac{\boldsymbol{b}\cdot\boldsymbol{b}^*}{4\mu_0} \right\} \equiv \{\mathcal{K}+\mathcal{U}+\mathcal{B}\}\,, \tag{8.8}$$

where $V_S = \sqrt{\gamma P_0/\rho_0}$ is the time-averaged sound speed with $\gamma = 5/3$, ρ_0 is the time-averaged density, p is the pressure, μ_0 is the permeability of free space, $\boldsymbol{v}$ is the velocity, $\boldsymbol{b}$ the magnetic field, and the * represents the complex conjugate. Note that the energy densities are halved from their standard form as they are time-averaged sine-squared waves. Three key components of the equation can be identified: the time-averaged kinetic energy, $\mathcal{K}$, the time-averaged internal energy, $\mathcal{U}$, and the time-averaged magnetic potential energy, $\mathcal{B}$.

By only considering the energies of an MHD wave, this equation stipulates that the parameters need to be input into the data vector are some energy-scaled values of the velocity field, pressure field, and magnetic field. Doing this allows fluctuations in the magnetic field to be compared to fluctuations in the velocity field in a physically meaningful way so that the POD and linear-regression stages of DMD is valid. As stated above, it is useful to remove the background trends (time-averaged value) to ensure that no null frequencies are found. When using these perturbation terms, the terms cannot be squared else directional information is lost preventing the term scaling being reverted out of energy units. Instead, the perturbation terms can be rescaled to the square-root of energy, denoted here with a bar, without losing directional information and therefore allowing for the original parameters to be investigated. In simple terms, the input to the DMD is the following parameters,

$$\delta\overline{v}_i = \sqrt{\delta\mathcal{K}_i} = \frac{1}{2}\sqrt{\rho_0}\delta v_i\,, \tag{8.9a}$$

$$\delta\overline{p} = \sqrt{\delta\mathcal{U}} = \frac{\delta p}{2\sqrt{\rho_0}V_S} = \frac{\delta p}{2\sqrt{\gamma P_0}}\,, \tag{8.9b}$$

$$\delta\overline{b}_i = \sqrt{\delta\mathcal{B}_i} = \frac{\delta b_i}{2\sqrt{\mu_0}}, \tag{8.9c}$$

where $i = x, y, z$, in the following tensor,

$$X_1 = \begin{pmatrix} \delta\overline{v}_{x,0} & \delta\overline{v}_{x,1} & \cdots & \delta\overline{v}_{x,m-1} \\ \delta\overline{b}_{y,0} & \delta\overline{b}_{y,1} & \cdots & \delta\overline{b}_{y,m-1} \\ \delta\overline{b}_{z,0} & \delta\overline{b}_{z,1} & \cdots & \delta\overline{b}_{z,m-1} \\ \delta\overline{b}_{x,0} & \delta\overline{b}_{x,1} & \cdots & \delta\overline{b}_{x,m-1} \\ \delta\overline{b}_{y,0} & \delta\overline{b}_{y,1} & \cdots & \delta\overline{b}_{y,m-1} \\ \delta\overline{b}_{z,0} & \delta\overline{b}_{z,1} & \cdots & \delta\overline{b}_{z,m-1} \\ \delta\overline{p}_{0} & \delta\overline{p}_{1} & \cdots & \delta\overline{p}_{m-1} \end{pmatrix}; \quad X_2 = \begin{pmatrix} \delta\overline{v}_{x,1} & \delta\overline{v}_{x,2} & \cdots & \delta\overline{v}_{x,m} \\ \delta\overline{b}_{y,1} & \delta\overline{b}_{y,2} & \cdots & \delta\overline{b}_{y,m} \\ \delta\overline{b}_{z,1} & \delta\overline{b}_{z,2} & \cdots & \delta\overline{b}_{z,m} \\ \delta\overline{b}_{x,1} & \delta\overline{b}_{x,2} & \cdots & \delta\overline{b}_{x,m} \\ \delta\overline{b}_{y,1} & \delta\overline{b}_{y,2} & \cdots & \delta\overline{b}_{y,m} \\ \delta\overline{b}_{z,1} & \delta\overline{b}_{z,2} & \cdots & \delta\overline{b}_{z,m} \\ \delta\overline{p}_{1} & \delta\overline{p}_{2} & \cdots & \delta\overline{p}_{m} \end{pmatrix}. \tag{8.10}$$

Once performed, it is possible to rescale the DMD outputs back into their original units by rescaling them to energy by using the amplitude or dynamics and then dividing through by their respective constants e.g. $\delta v_i = 2/\sqrt{\rho_0}\,\delta\overline{v}_i$.

8.4 DMD Application

The same simulation used in Chapter 7 is used for this study. Note that this means that cusp reconnection and the anomalous return flow is present in the simulation, however this is inconsequential for this study. SVD-based DMD is applied to 110 evenly distributed time-average subtracted snapshots ($\Delta t = 15\,\mathrm{s}$) from 27 minutes and 45 seconds of simulation time. These variables are calculated at every cell-centred location in the simulation, flattened into a single dimension, and then stacked into the data vector. These data vectors are then collected and constructed into the matrices seen in Equation 8.10. Essentially, this means that every element of the matrices actually correspond to the three-dimensional simulation space flattened into a one-dimensional space.

The data analysis was performed by using the classic DMD function in the Python package PyDMD (Demo et al. 2018; Ichinaga et al. 2024). In this study an SVD of $r = 40$ is used resulting in 20 complex conjugate mode pairs being extracted. This means that only 20 of the modes correspond to real (positive) frequencies meaning that this investigation focuses on 20 of the most dominant modes extracted by DMD. By using this number of modes, a residual of $\sigma = 0.378$ is achieved signifying that $\sim 62.2\%$ of the total harmonic wave energy present in the simulation is being captured

by the 25 modes extracted by DMD.

8.5 Mode Synopsis

Figure 8.3 shows a scatter plot of the eigenvalues of the 20 real frequency modes extracted by DMD in colour on an Argand diagram. The black dashed line is a unit circle centred on the origin which is used to find the stability of the mode as described above. The longest temporal fluctuation which can be captured using Fourier techniques in the simulation data of length 1665 s is 0.6 mHz. However, DMD has extracted the zeroth mode with a frequency at 0.48 mHz meaning that the technique has extracted features which vary on larger timescales than the simulation input. It does this as it is able to capture wave-like motion that has undergone a partial oscillation. Typical KHI frequencies are expected in the ULF Pc3-Pc5 range (Dungey 1955; Atkinson and Watanabe 1966; Walker 1981). Pc5 waves were first defined by Jacobs et al. (1964) as waves with a period between $150 - 600$ s corresponding to frequencies in the range of $1.67 - 6.67$ mHz. The zeroth and first modes have a frequency lower that this range in the Pc6 range – defined as waves with a periodicity > 600 s. The second to tenth modes approximately sit in the Pc5 band - the twelfth to the twentieth mode are in the Pc4 range: a period of $45 - 150$ s corresponding to a frequency of $6.67 - 22.2$ mHz.

All the modes are essentially stable with a mean growth rate of 0.984. What this conveys is that every extracted mode represents stable wave motion which globally is neither growing nor decaying. This is representative of the simulation having reached a quasi-stationary state under the steady driving conditions. It is important to note that the frequencies of the simulation will differ from the frequencies found in reality as a global MHD simulation often has thicker boundary layers than the real magnetopause due to a lack of kinetic scale physics that controls the thickness. This results in longer wavelengths and therefore lower frequencies causing simulations to not match reality. For this study, the lack of a realistic magnetopause thickness is not an issue as the purpose of this study is not to perfectly capture realistic frequencies, it is to understand how a MSW's frequency varies along the magnetopause; that is possible here. But just analysing the mode frequency does not reveal which of the modes are more significant in the simulation, this information is extracted from the mode amplitudes.

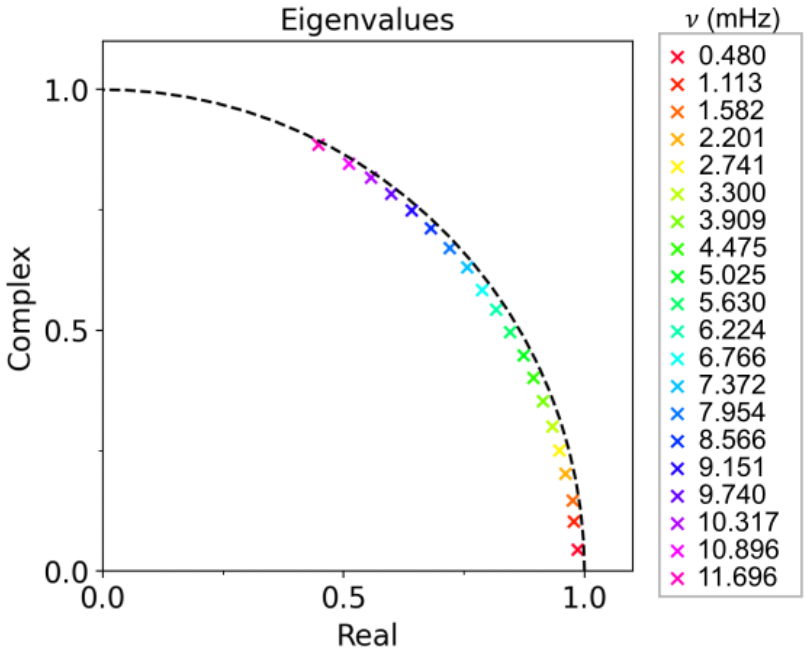


Figure 8.3: A scatter plot of the eigenvalues of the 20 real frequency modes extracted by DMD in colour on an Argand diagram. The black dashed line is a unit circle centred on the origin. The colour of the cross corresponds to a discrete frequency, increasing anti-clockwise from the real positive axis and are listed in the legend on the right rounded to 3 decimal places.

In MHD, the classic DMD amplitude of the modes should be redefined as the total mode energy which is calculated with,

$$E_j = 2\,|b_j|^2\,dV, \tag{8.11}$$

where dV is the volume element which in this case is $(R_E/4)^3$. The factor of 2 coming from discarding the repeated negative frequency complex conjugate modes. The mode hierarchy can now be extracted by comparing the mode energies.

Figure 8.4 shows the mode frequency and mode energy of each of the real frequency modes from DMD. The mode energy is essential in understanding the hierarchy of the modes and from this figure it is clear that the lower the mode frequency, the more energy the mode represents; this relationship is not imposed by DMD. This may be due to the lower frequency modes having larger wavelengths and therefore are more unstable on the boundary (Miura and Pritchett 1982). This is not consistent with a linear or exponential relationship. The majority of the modes identified by DMD do not represent a large portion of the energy fluctuations meaning that analysing all the modes would be an ineffective way to understand the meaningful energy variations within the simulation. A cumulative fraction of

variance is used to understand the effective contribution of each mode to the total reconstruction.

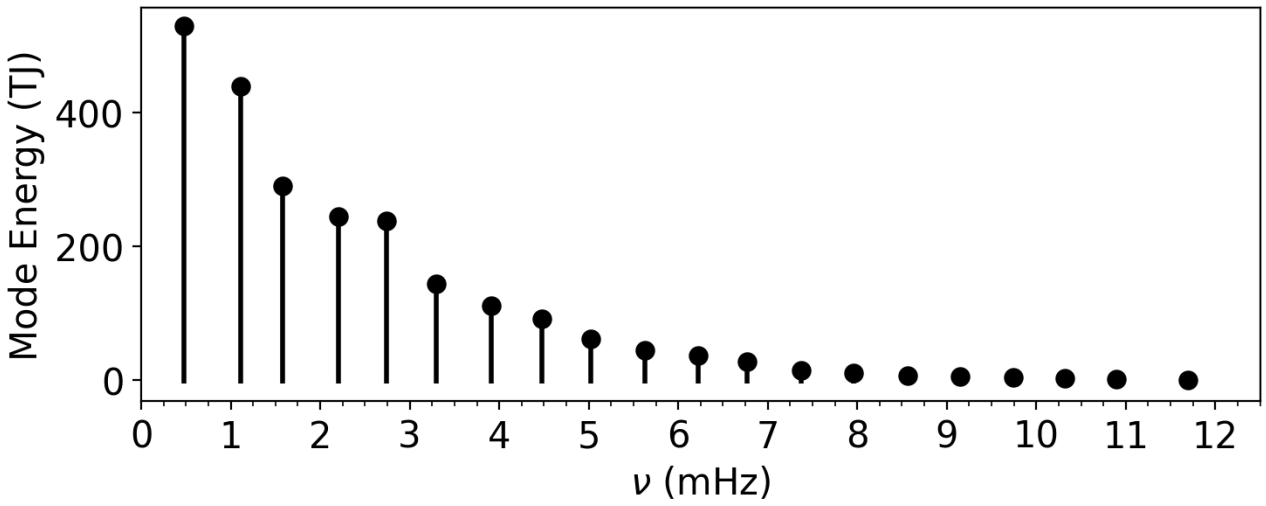


Figure 8.4: A scatter plot of the different mode energies of the 20 real frequency modes extracted by DMD.

Figure 8.5 shows how the cumulative fraction of the total energy fluctuations the modes represent varies with frequency. This clearly shows that $\sim 95\%$ of the energy fluctuations captured by DMD are represented by frequencies below the Pc4 range suggesting that Pc4 waves are insignificant in this simulation. The five lowest frequency DMD modes describe $\sim 75\%$ of the total energy fluctuations captured by DMD corresponding to nearly 47% of the total harmonic wave energy fluctuations in the simulation. Because the five lowest frequency modes capture so much of the fluctuation energy and the addition of more modes does not significantly change the total energy captured, these five modes will be the focus of this study. Truncating the modes like this focuses the study so that only the dominant fluctuation processes are analysed. So far, only the modes amplitude and frequency has been analysed. Moving forward, an understanding as to what the energy division is for each mode and which of those energies are most responsible for the fluctuation amplitudes is needed. To do this, the perturbation energies need to be used.

Figure 8.6 shows how the spatial sum of the kinetic, magnetic potential, and internal perturbation energy of each mode varies with frequency. This figure shows that there is a near energy parity in the simulation between the kinetic and magnetic potential energies with the internal energy fluctuations being $10^4\times$ smaller. This is likely to be due to pure Alfvén and fast magnetosonic waves having an equipartition between kinetic and magnetic energy, and, as MSW's are magnetosonic fast waves and

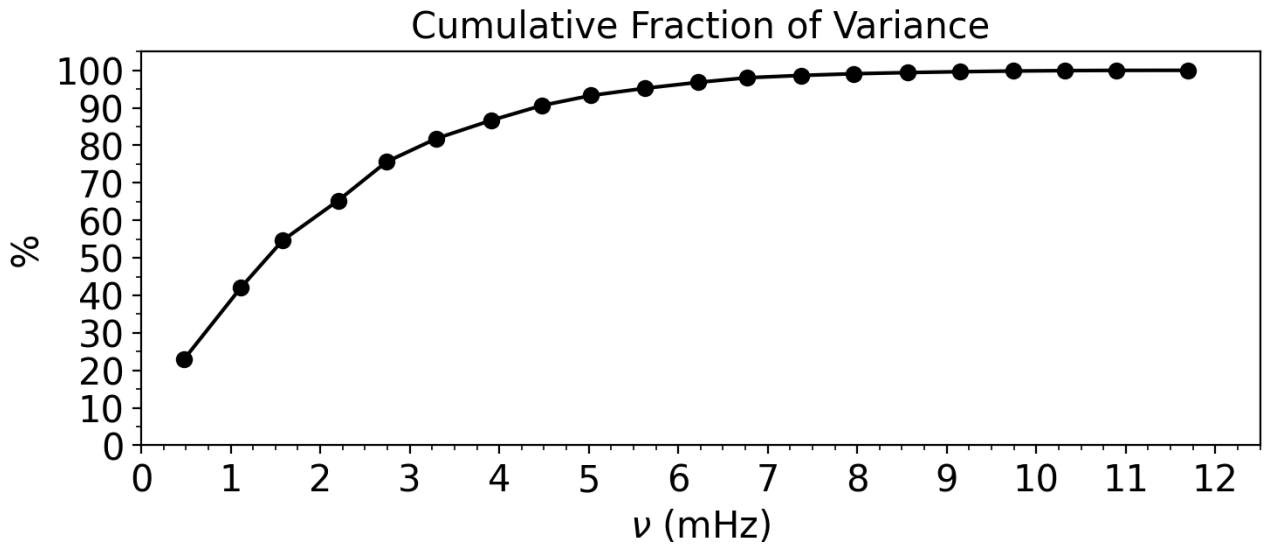


Figure 8.5: A scatter plot of the cumulative fraction of variance from the lowest to highest frequency as a percentage of each of the 20 real frequency modes extracted by DMD.

strongly couple to them (e.g. Southwood 1974), it is likely why this relationship is seen. Especially considering that compressional waves are given Alfvén-like properties in realistic magnetosphere geometries (Southwood and Kivelson 1984; Archer et al. 2022). Interestingly the kinetic energy represents slightly more energy fluctuations than the magnetic potential for mode 0 to 3, and then the magnetic potential energy dominates the rest of the modes.

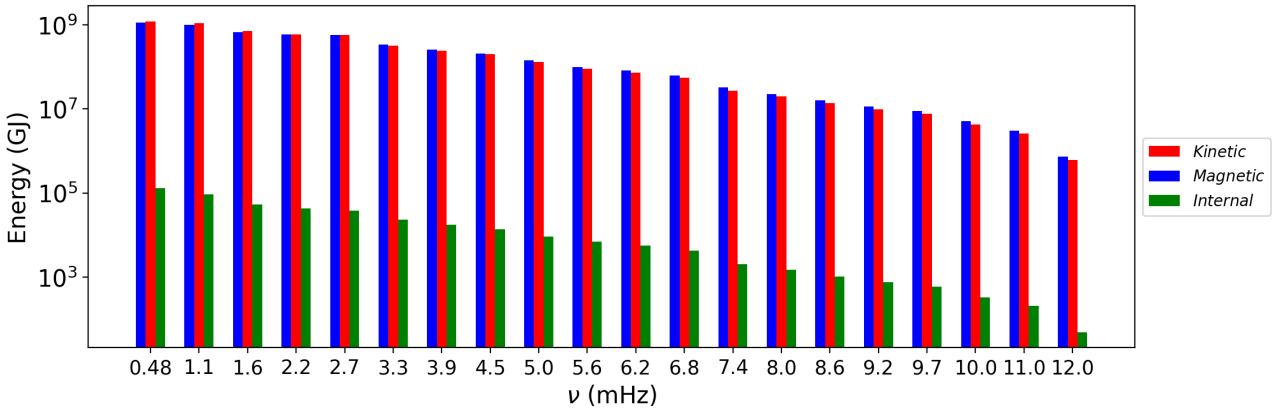


Figure 8.6: A scatter plot of the contribution of the magnetic (blue on left), kinetic (red in centre), and internal (green on right) energies to the total mode energies of the 20 real frequency modes extracted by DMD.

What the analysis has revealed so far is that the 5 lowest frequency modes are responsible for 75% of the total energy fluctuations captured by DMD, and 47% of the total simulation harmonic MHD fluctuation energy. Furthermore, there is an energy parity between the magnetic potential

and kinetic energy components of the modes. So far it is unclear whether these modes are MSW related. Using the spatial distributions will reveal whether or not the modes have wave energy at the magnetopause flanks and confirm if they are MSW-related.

8.6 DMD of the Magnetosphere

One of the powerful uses of DMD as an analysis technique is that it can track the spatial evolution of wave power at a fixed frequency. A mode reconstruction can reveal where in space is oscillating at the same frequency as the magnetopause and therefore identify regions which the MSWs are influencing. To do this, a linear total pressure phasor (neglecting $\delta\mathbf{b}^2$ term) is defined as

$$\delta P_{tot} = \delta p + \frac{\delta\mathbf{b} \cdot \mathbf{B}_0}{\mu_0} \tag{8.12}$$

where δp is the reconstructed thermal pressure modes, $\delta\mathbf{b}$ is the reconstructed magnetic field modes vector, and $\mathbf{B}_0$ is the time-averaged magnetic field vector.

Figure 8.7 shows the total (gas + magnetic) pressure fluctuations of mode 2 in the equatorial plane. The dashed black line shows the inner boundary at a radius of $6\,R_E$ with the dotted black line showing the equilibrium magnetopause. The strongest signatures are along the equilibrium magnetopause where there are strong pressure fluctuations associated with MSWs which have been discussed above. These waves can be seen to be responsible for three notable MSW-driven phenomena: magnetosheath waves, bow shock waves, and plasma sheet waves.

In the same way that magnetopause surface waves drive magnetosonic waves into the magnetosphere, they can also drive magnetosonic waves into the magnetosheath (Kivelson and Chen 1995). However, because the magnetosheath is highly compressible (Plaschke and Glassmeier 2011; Archer and Plaschke 2015) it makes it easier to drive compressible waves, and therefore the magnetosonic mode transitions from being evanescent surface mode into a propagating fast magnetosonic mode in the magnetosheath (Pu and Kivelson 1983). As a result, Figure 8.7 shows that along the flanks, the total pressure fluctuations are shown to cross the magnetosheath and terminate on the bow shock. This causes waves in the magnetosheath which are also advected by the magnetosheath flow. When they terminate, these fluctuations adjust the pressure balance at the bow shock, causing the shock

to move resulting in a driven wave-like behaviour of the bow shock. These waves adjust the shock location by $\sim 0.5\,R_E$ in the shock normal direction and have a wavelength similar to that at the magnetopause at the same local time ($\sim 40\,R_E$). This results in minor deviations of the shock normal. Previously it has been shown this process can take place at the subsolar point due to magnetopause surface eigenmodes (Archer et al. 2021), but this work extends that and suggests that this process happens for larger local times. The implications of this could be explored further in future studies.

Finally, as well as driving waves out of the magnetosphere the inward propagation of waves may potentially drive plasma sheet waves. In Figure 8.7 it can be seen that the MSWs at the flank of the magnetopause, especially between $10\,R_E$ and $60\,R_E$ down tail, pressure waves in the plasma sheet. Previous work using MHD simulations in combination with two-point observations from ARTEMIS (Wang et al. 2017a) suggested that KH-wave driven inward-propagating waves caused an asymmetry in the current sheet resulting in sheet flapping and the kink and sausage modes to occur. Furthermore, questions have been posed surrounding the causality between flank dynamics and central current sheet behaviour (Hwang et al. 2023). This work suggests that the magnetopause flanks may drive pressure fluctuations into the magnetosphere which are then present in the plasma sheet. A further investigation beyond this study is needed for conclusive evidence showing that the magnetopause flanks can drive wave behaviour in the plasma sheet.

8.7 DMD of the Magnetopause

8.7.1 Coordinate frame

It is important to remember that DMD is performed on the entire magnetosphere, not just the magnetopause. This is because it is important to be able to identify where the wave energy is penetrating into the magnetosphere and where resonances may be taking place. A downfall in using this approach is that not all the modes captured may be due to or related to MSWs. Consequently, analysing the global mode is not sufficient for understanding just MSW activity as other periodic processes may be captured. Furthermore, the focus of this study is how the MSWs vary and evolve spatially along the magnetopause meaning that a magnetopause coordinate system is needed. This coordinate system is set such that the origin is at the nose of the magnetopause, the Z- direction is

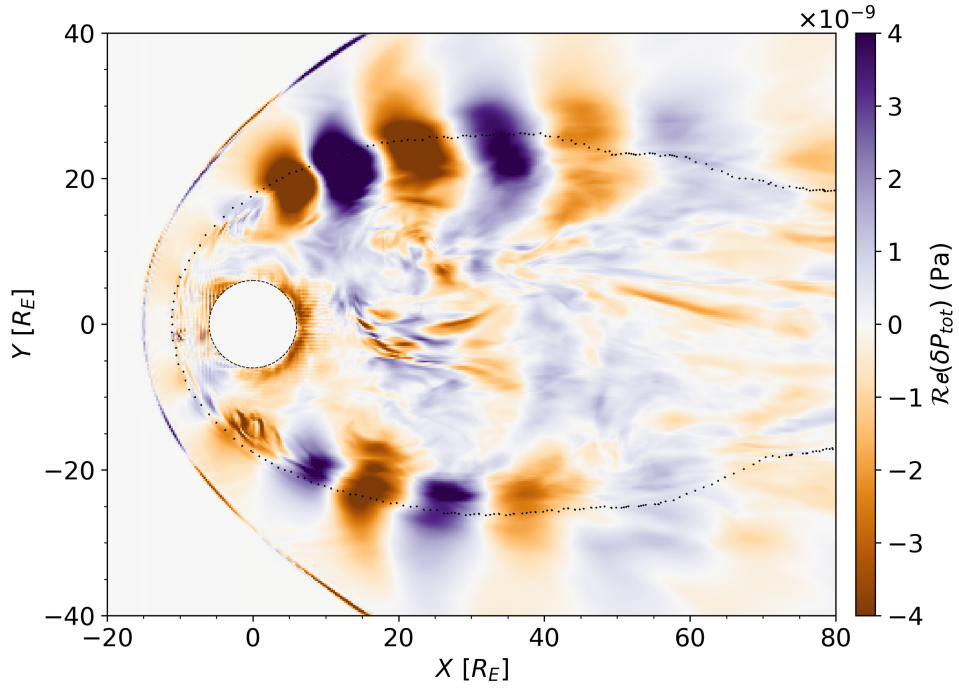


Figure 8.7: Equatorial view of the total pressure fluctuations of mode 2 in colour. The dashed black line shows the redefined inner-boundary which is a sphere of radius 6 R_E. The dotted line is the equilibrium magnetopause.

unchanged, the X- direction is normal to Z and tangential to the magnetopause, and the Y-direction completes the right-handed set and points normal to the magnetopause; this is essentially unwrapping the magnetopause surface into a plane. Note that this is not a universally orthonormal basis, but as analysis does not take place in this coordinate system and it is solely used to present the data, this should be inconsequential. For context, in this frame 50 R_E along the magnetopause from the subsolar point is approximately $X = 0\,R_E$, and 200 R_E along the magnetopause from the subsolar point is approximately $X = 70\,R_E$ down tail and a positive tangent direction corresponds to the dawn sector and a negative value the dusk sector.

Data in this coordinate system is calculated in spherical coordinates by integrating all the values found within 5 R_E of the equilibrium magnetopause into spherical spatial bins such that there are 90 bins in the latitudinal direction ranging from $-90° < \theta < 90°$ and 180 bins in the longitudinal direction ranging from $-175° < \phi < 175°$. The bin count is also recorded allowing for the mean value for each bin to be found. Due to spherical coordinates visually biasing the nose of the magnetopause, the data is then presented in the magnetopause tangent and Z-coordinate system. This is done by calculating the distance along the magnetopause by integrating along the change in the boundary

position vectors in the equatorial plane. Every value that lies within $5\,R_E$ of the magnetopause along the normal direction is also integrated over for each bin at a fixed latitude and longitude. A linear interpolator is then used to transform the longitudinal value of each bin into a distance from the nose along the equilibrium magnetopause. A nearest interpolator is used to locate the equilibrium magnetopause radius from the spherical coordinate bin centres, the latitudinal value of each bin can then be transformed into the Z Cartesian coordinate. A positive tangent direction corresponds to the dawn sector and a negative value the dusk sector. Note that Gouraud shading is applied to smooth over the discrete data as a visual aid.

8.7.2 Frequency Dominance

Figure 8.8 shows the 5 lowest frequency modes of the time-averaged perturbation energy of a harmonic wave within $5\,R_E$ normal to the equilibrium magnetopause (for details on the equilibrium magnetopause please see Section 7.2) in the tangential- and Z- directions; this is essentially unwrapping the magnetopause surface tangentially and then projecting it onto the Z-plane. The bow shock is manually masked out of this data even if it is within $5\,R_E$ of the magnetopause. The dashed line is the equatorial plane.

Mode 0, which has a frequency in the Pc6 range of 0.480 mHz, can be seen in the first panel of Figure 8.8 to have energy peaks far in the tail with low level values in the nose and across the entire magnetopause. The mode appears to be present across most of the magnetopause with the strongest values being restricted to within $\pm 2.5\,R_E$ of the equatorial plane. Interestingly, the stronger values begin $\sim 75\,R_E$ along the magnetopause and tend to grow in energy further down tail which is indicative of the mode being amplified by the KHI beyond this region. This may be due to the mode being more unstable to the KHI in this region (Miura and Pritchett 1982) due to how the LLBL thickens in local time (Hasegawa et al. 2004b) but only frequency is being measured here, not wavelength, making it hard to tell. This suggestion is supported by the mode energy being restricted to the equatorial plane which is where the KHI is most unstable. The mode frequency is quite low compared to observations (Walker 1981), due to the lack of kinetic-scale physics causing the thickness of the magnetopause boundary not representing reality, however other simulations such as SWMF (Tóth et al. 2005) have observed KHI induced variations peaking at 0.5mHz (Ellington

et al. 2016).

As well as this, there are also wave energy lines which span between the cusps within $\pm 50\,R_E$ of the subsolar point which appear to follow where magnetic field lines would be expected to trace. This process may be a result of the cusp reconnection explored in the previous chapter. The reconnection disturbance would flow at Alfvénic speeds towards the dayside disturbing the magnetopause surface, and as this disturbance propagates towards the equatorial plane where it seeds vortices, it is advected by the magnetosheath flow. This causes it to disturb the equatorial plane off of the subsolar point. It can be seen that where these lines cross the equatorial plane, this is where the wave energy begins to extend out across the magnetopause which is synonymous with this being where the cusp-reconnection process seeds the KHI. Furthermore, a high wave energy can be seen to peak along field lines which intersect the subsolar point. This may be an indication of the cusp reconnection outflow jets potentially coupling to magnetopause surface eigenmodes. A further investigation would be needed to confirm this.

Mode 1, which has a frequency in the Pc6 range of 1.113 mHz, can be seen in the second panel of Figure 8.8. The mode has a background value across most of the magnetopause similar to mode 0. This background value may be a signature suggesting that the total magnetopause surface is undulating at this frequency. Like before, this mode shows signs of the KHI: the highest energy values are restricted to within $\pm 2.5\,R_E$ of the equatorial plane and the mode energy is amplified at $\sim 75\,R_E$ along the magnetopause. This may be for the same reasons as discussed for Mode 0. Unlike mode 0, the mode energy decays again after $\sim 125\,R_E$ along the magnetopause which may indicate the wave has transitioned into a propagating mode (Pu and Kivelson 1983). However, it is does suggest that this mode is most KH unstable within a finite region with the mode energy being advected from this most-unstable location down tail by the KHI (Mills et al. 2000). This provides evidence for the KHI both amplifying a disturbance at an unstable frequency but also advecting it into a region where the boundary is more stable to it and thus has become more stable to it.

Mode 2, which has a frequency in the Pc6 range of 1.582 mHz, strongly peaks in energy approximately between $50\,R_E$ to $125\,R_E$ from the subsolar point and is, like mode 0 and 1, limited to the low-latitudes within $\pm 2.5\,R_E$ of the equatorial plane. The mode appears to decay into the higher-latitudes with increasing distance from the nose. Low level wave energy is smeared far from

the nose of the magnetopause. This mode does not contain much wave energy on the dayside of the magnetopause. This mode suggests that the KHI is rapidly growing at this frequency around 50 R_E and then it decays to a lower level beyond 125 R_E from the subsolar point. This pattern may suggest that this mode is the most unstable mode at this point along the magnetopause and the KHI is generating it. Once this mode is no longer the most unstable frequency, the KHI can be seen to advect the wave energy at this frequency into the tail providing evidence for the KHI both generating wave energy at a frequency and then advecting it (Mills et al. 2000).

Finally modes 3 and 4, which have frequencies in the Pc5 range of 2.201 mHz and 2.741 mHz respectively, can be seen to have negligible wave energy at the nose of the magnetopause. These mode appear to gain wave energy beyond 50 R_E which, from the previous mode analysis, is where the KHI appears to be first seeded. The largest mode energy is limited to within $\pm 2.5\,R_E$ of the equatorial plane. These modes are clearly also driven by the KHI however they are not as strongly driven as the lower frequency modes.

The most surprising trend here is that the lower frequency waves are more dominant towards the nose of the magnetopause. It is understood through linear theory (Miura and Pritchett 1982) that the thickness of the LLBL would dictate the wavelength of the most unstable mode which would influence the frequency. Evidence has shown that the LLBL thickness increases with local time (Haerendel et al. 1978), and therefore it would be expected that the lower frequency, larger wavelength waves would exist further from the nose of the magnetopause. This type of relationship has been suggested by (Lin et al. 2014). This further motivates an investigation into the mode dominance as a function of distance from the nose.

By integrating over the Z direction in Figure 8.8 where $-6.5 < Z < 6.5$, Figure 8.9 can be made. This figure shows how the total fluctuation energy of each mode changes as a function of local time when isolated to the low-latitudes. The figure clearly demonstrates that the energy of each mode generally increases from the subsolar point towards the tail. Mode 1 appears to be the most unstable mode as it grows to the highest energy on both flanks. It is possible that mode 0 and mode 1 may be driven modes from the cusp reconnection as they have energy at the subsolar point whereas modes 2-4 have negligibly small energies at the subsolar point. Despite this, approximately 100 R_E along the dusk flank all the modes have a comparable energy meaning that there is a strong

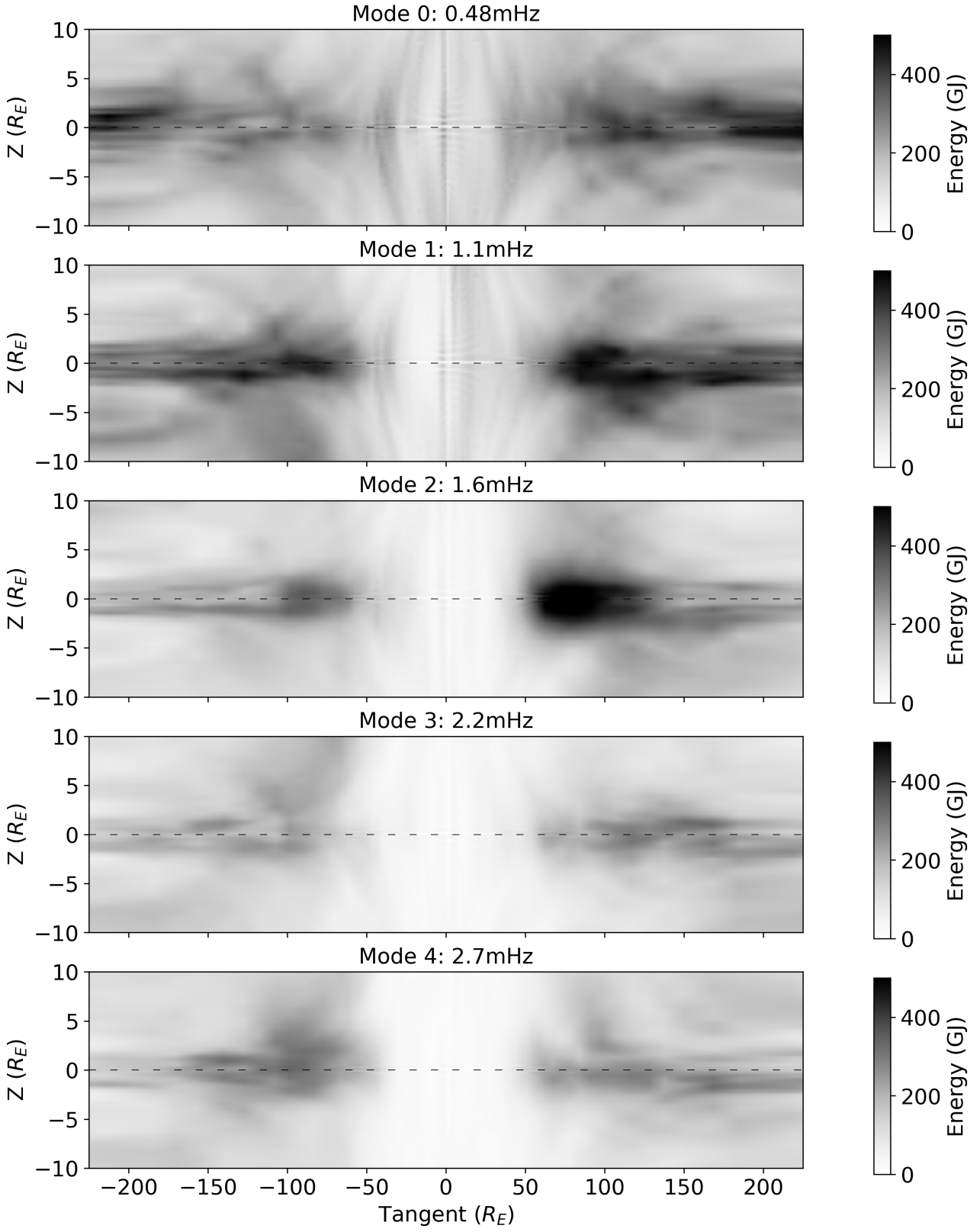


Figure 8.8: A figure showing the spatial distribution of the mean total energy fluctuations of the 5 lowest frequency modes integrated within 5 R_E normal of the equilibrium magnetopause (for details on the equilibrium magnetopause please see Section 7.2) in the tangential- and Z- directions.

superposition of wave modes present here. This is clear evidence that the KHI amplifies pre-existing disturbances (mode 0, 1) while also generating new frequencies but interestingly, it does so in a bias way. The driven modes do not retain their dominance over the intrinsic modes which is what would be expected if they were all driven without bias. This favours the idea that there are more unstable modes as suggested by linear theory (Miura and Pritchett 1982).

Beyond 100 R_E the waves are no longer evolving and appear to be advecting into the downstream (Mills et al. 2000). This advection appears to also result in a decay in the wave energy which is expected as the waves are no longer being driven here. Alternatively, on the dawn flank mode 2 is clearly a more unstable mode than the others due to how it rapidly gains energy from being negligible at the subsolar point, to more than 300 GJ approximately 75 R_E along the dawn flank. Despite this, the other modes also grow implying that, although there may be a most unstable mode frequency, other frequencies are also generated. This dawn-dusk asymmetry in the most unstable mode is likely related to the return flow identified in the previous chapter, however it does also show that the flanks are disconnected and what is the most unstable mode on one is not necessarily the most unstable mode of the other.

This figure clearly demonstrates how the KHI is not just generating frequencies at the magnetopause boundary at the most unstable frequency as typically assumed. Instead, it is generating a broadband of frequency which includes a generative growth of new frequencies, and causes a growth of pre-existing frequencies; this also causes a resonance-like amplification of the most unstable wavelength. Furthermore, there is evidence to suggest that the instability also advects pre-existing frequencies into the downstream. The result of all these different processes together is a complex superposition of different wave frequencies, both higher and lower frequencies to the unstable mode, being present at all local-times. The frequencies which are most unstable at the boundary are amplified by the instability and dominate the wave energy, with the others becoming subdominant.

So far, only the total wave energy has been analysed across the magnetopause surface. This type of analysis focuses only on where the mode contains the most energy and not the type of energy present in each location. This information can be extracted from the total energy by decomposing it into the kinetic, magnetic potential, and internal energy contributors. Figure 8.10 shows the mean kinetic, magnetic potential, and internal energy fluctuations of mode 2 within 5 R_E normal to the

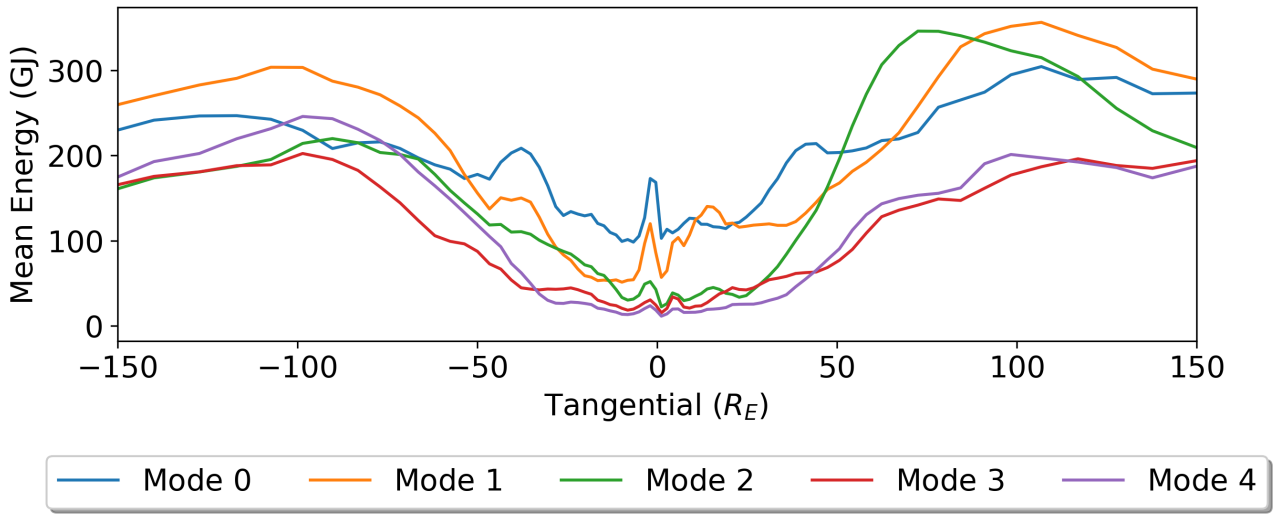


Figure 8.9: A plot showing how the mean energy between $Z = -6.5$ to $Z = 6.5$ of a MSW changes along the magnetopause as a function of frequency showing how there is a superposition of wave frequency at all local times.

equilibrium magnetopause in the tangential- and Z- directions; this is essentially unwrapping the magnetopause surface into a plane. The data is calculated in the same way as Figure 8.8 above.

The different spatial distributions of each wave energy of mode 2 at the magnetopause can be seen in Figure 8.10. The kinetic wave energy peaks where the total wave energy of this mode peaked which was within $\pm 2.5\,R_E$ of the equatorial plane and between $50\,R_E$ to $125\,R_E$ from the subsolar point. The kinetic wave energy can be seen to peak in the equatorial plane and decay in z-extent the further along the magnetopause in the same wedge shape as seen for vortices in the previous chapter implying that the kinetic wave energy is likely describing the vortical component of the wave.

The magnetic potential wave energy describes the magnetic field perturbations and interestingly, these saddle the equatorial plane. This suggests that vortices in the equatorial plane are twisting and perturbing the magnetic field lines out of plane and the undulation of the magnetopause itself is not dominantly generating magnetic potential wave energy. The magnetic potential wave energy is concentrated around $2.5\,R_E$ from the equatorial plane which is where the kinetic wave energy decays suggesting the tips of the vortices are where this energy transfer takes place. This pattern would be expected as the biggest changes in field vectors would be outside of the driving region. This may be expected as a symmetric KH-wave would displace the field lines around equator, but not strongly distort them. But out of the equatorial plane, the field lines would become distorted and twisted (e.g. see Figure 7.10). It is this distortion and twisting that would generate Alfvén waves (Chen and

Hasegawa 1974b; Uberoi 1989; Pilipenko et al. 2005) and an increase in magnetic pressure which, if there is a magnetic shear, could cause VIR (e.g. Faganello et al. 2012). But without a magnetic shear to release this energy, it would result in a saddle of increased magnetic potential energy about the equatorial plane which is what is seen here.

The internal wave energy, which is notably 1000× smaller than the other two energies, peaks in the same region as the kinetic wave energy. This wave energy is a good proxy of understanding where pressure perturbations are being generated. It is clear where the kinetic wave energy peaks, the vortices are strongest, and this generates the largest pressure perturbations. However, it is unclear whether these pressure perturbations actually penetrate the magnetosphere, if any of this wave energy enters the magnetosphere, and whether or not these modes excite the inner- or outer-mode of the KHI.

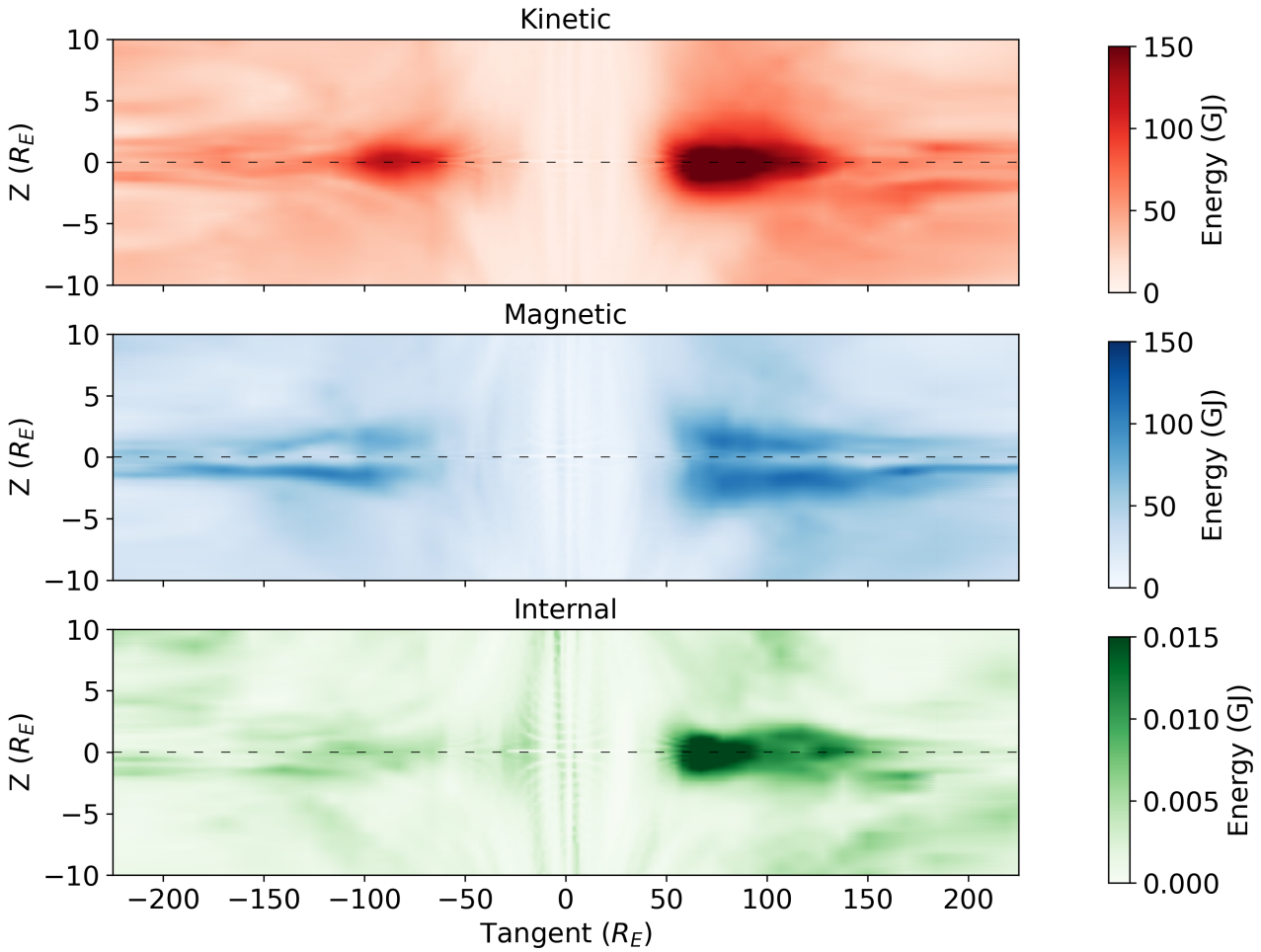


Figure 8.10: Figure showing the mean kinetic, magnetic potential, and internal energy fluctuations of mode 2 within 5 R_E normal to the equilibrium magnetopause in the tangential- and Z- directions. Note the different scale for the internal energy.

To understand whether these waves transfer energy into the magnetosphere, a different spatial cut is needed. Figure 8.8 demonstrated how the KHI is dominantly driving in the equatorial plane. This justifies now restricting the study to the equatorial plane. Figure 8.11 shows the total energy fluctuations in the equatorial plane ($Z = 0\,R_E$) of the 5 lowest frequency modes within $10\,R_E$ normal to the equilibrium magnetopause plotted in the tangential- and normal-directions. The dashed line at the normal $= 0$ line indicates the equilibrium magnetopause boundary. Black dashed lines have been approximately drawn on where the inner- and outer-modes of the KHI are thought to exist, and have no physical derivation. Note that no integration is taking place.

Mode 0 seen in Figure 8.11 contains features useful for orientating the reader. Total energy fluctuations can be seen at the bow shock, these will be explored later in Section 8.6. The inner boundary can be seen and so can large-scale MSW structures. The low frequency mode is clearly highly penetrating into the magnetosphere as the wave power strongly grows within the magnetosphere, a result which coincides with ULF wave observations.

Mode 1 is suggested to be KHI related as there appears to be strong total energy fluctuations localised at the magnetopause region with stronger values close to the subsolar point which then decay towards the tail. This mode demonstrates that the inner- and outer-mode of the KHI do not necessarily contain strong fluctuations at the same frequency. The inner-mode, which has been suggested to be more unstable (Lee et al. 1981), has significantly higher energy at this frequency. Mode 2 is also thought to be KHI-related due to the high energy along the equilibrium magnetopause boundary – especially in the dawn sector. Interestingly, mode 2 doesn't appear to have strong signatures of mode bifurcation and instead the wave energy is strongly located along the equilibrium magnetopause boundary. Mode 3 and 4 are also thought to be KH-related with both modes not having much energy in the boundary but having higher total fluctuation energy along the inner- and outer-LLBL boundary.

Modes 1-4, transfer energy into the magnetosphere as they have energy fluctuations of the same frequency at the boundary which appears to spread into the magnetosphere. This process appears to dominantly take place between approximately $50\,R_E - 100\,R_E$ from the subsolar point. Due to the evanescent nature of a MSW, the power can be seen "leaking" from the boundary as the wave decays away from the magnetopause surface. To better understand how both these processes take

place, the total energy should be decomposed it into the kinetic, magnetic potential, and internal energy contributors.

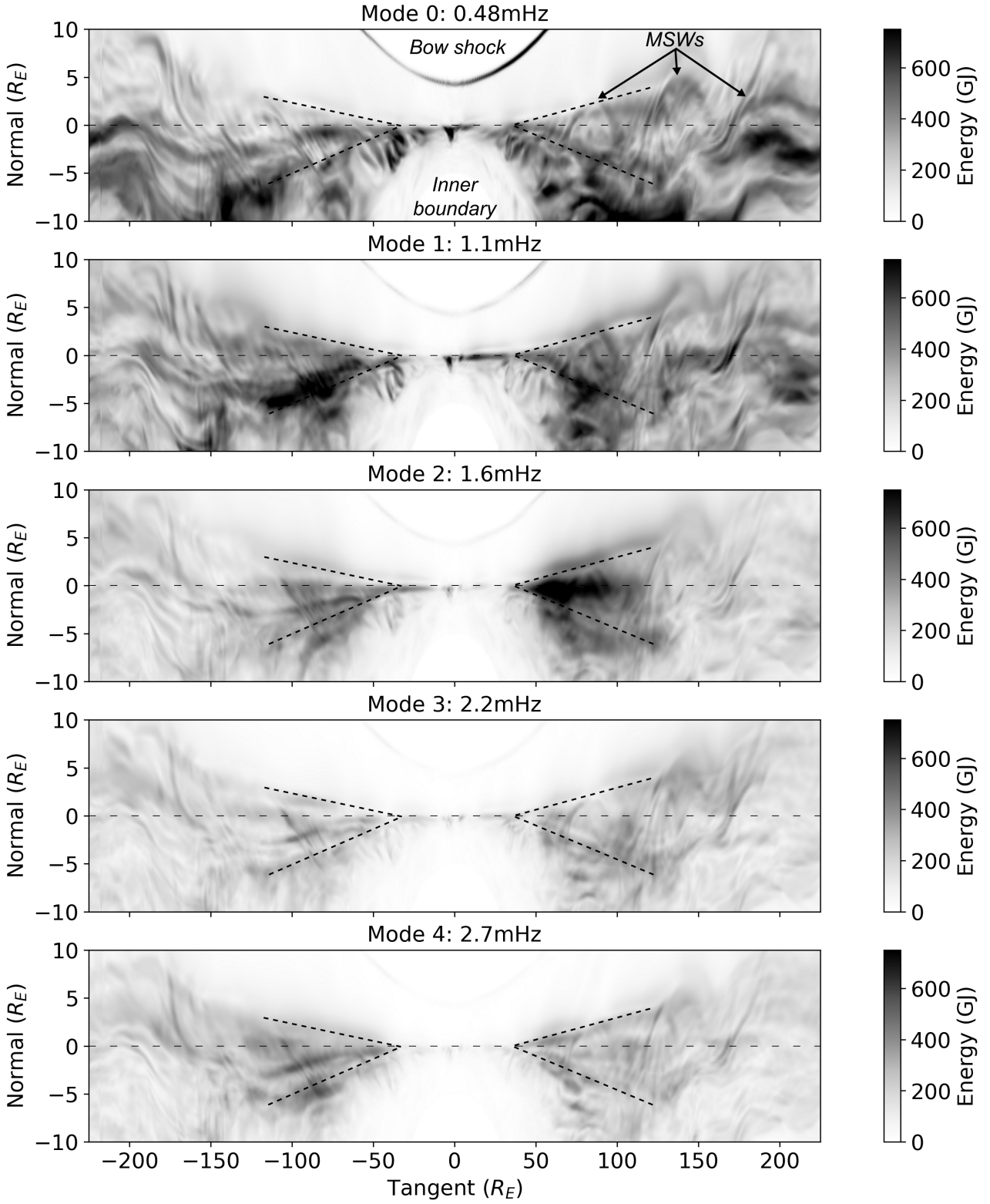


Figure 8.11: A figure showing the spatial distribution of the time-averaged total energy fluctuations of the 5 lowest frequency modes in the tangential- and normal-directions.

The different spatial distributions of each wave energy in the equatorial plane ($Z = 0\,R_E$) of mode 2 and 4 at the magnetopause can be seen in Figure 8.12 in the tangential and normal magnetopause coordinate system. Like indicated in Figure 8.10, the magnetic potential energy is shown to be subdominant to the kinetic energy in the equatorial plane with the internal energy being orders of magnitude smaller. Note the different colourbar scales for each energy.

Each energy type appears to peak in different spatial regions regardless of mode frequency. The kinetic energy in mode 2 peaks approximately $60\,R_E$ dawn-ward along the equilibrium magnetopause boundary. It can also be seen to bifurcate along the inner- and outer-boundaries of the LLBL. As discussed above, fast magnetosonic waves are likely to contain an equipartition of kinetic and magnetic energy. This explains why the kinetic energy evanescently decays away from these boundaries a surface wave is present (Kivelson and Pu 1984). This is supported by the magnetic potential energy strongly corresponding to the kinetic energy. There is a decay in the magnetic potential energy along the magnetopause which is likely due to a reducing field strength further from Earth.

A similar pattern can be seen with the magnetic potential energy in mode 4. The kinetic energy has a maximum approximately $75\,R_E$ dusk-ward of the subsolar point and mode bifurcation can be seen. The magnetic potential energy again only strongly spikes along the inside of the equilibrium magnetopause. Physically, it is expected that the inner-mode would be where the strongest energy values from the magnetic field would be as this is where the field is closed and where it would have a stronger magnitude.

The internal energy is a good proxy for understanding the pressure fluctuations caused by the modes. For both modes, the internal energy peaks where the inner-mode of the KHI can be seen. The internal energy also evanescently penetrates into the magnetosphere. What this means is that the internal wave energy, as well as the magnetic wave energy, caused by the KHI mostly occurs on the inside of the magnetopause. This is explained by MSWs being magnetosonic fast waves which evanescently decay into the magnetosphere and, based on the plasma beta (Archer et al. 2022), either the magnetic or thermal pressure dominates. This is why the two appear to be showing similar behaviour as they are describing the same thing.

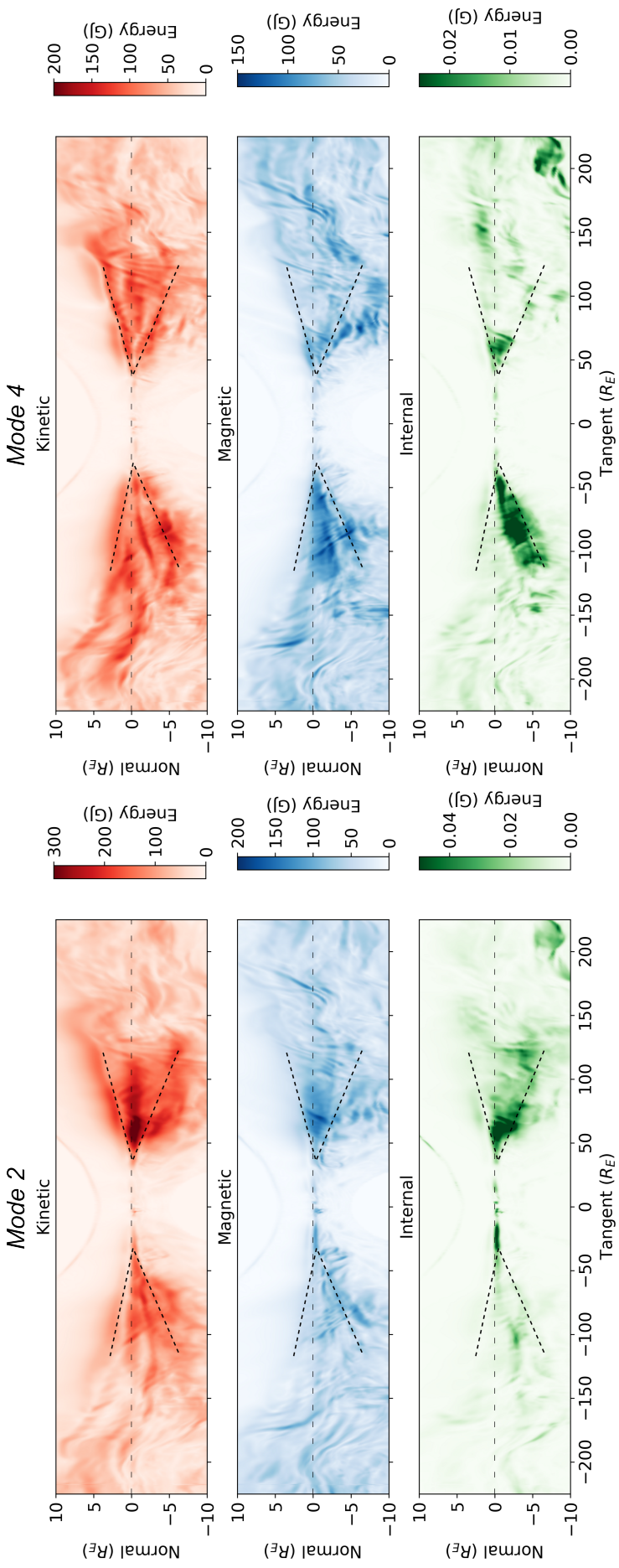


Figure 8.12: The mean kinetic, magnetic potential, and internal energy fluctuations of mode 2 in the tangential- and normal-directions. Note the different scales on all of the energies.

So far, only the different energies of the waves has been investigated which has revealed how the KHI generates, amplifies, and advects both existing and generated frequencies along the magnetopause. However, the frequency does not necessarily vary with wavelength. Having now shown that there is a superposition of frequency present at all local times, it is hard to know whether and how the wavelength is varying along the magnetopause. This motivates the second part of this chapter – an investigation into the wavelength evolution of an isolated MSW frequency.

8.7.3 Wavelength Evolution

So far only the magnitude of the phasors have been used to realise the wave energy fluctuations. But the phasors themselves contain wave phase information which can be used to extract the wavelength of the waves. As well as this, the real part of the phasors is the physical wave. For the work in this section, an isotropic quantity is needed so that a continuous phase can be extracted from the system even if the wave is propagating in an oblique direction. The pressure fluctuations alone, δp, would not completely describe the system due to the varying beta – especially given the internal energy is so insignificant compared to the kinetic and magnetic energies. And the magnitude of the velocity and magnetic field cannot be used as calculating them loses phase information. Knowing that across the boundary the total pressure must be continuous (Kivelson and Chen 1995) means the linear total pressure is the best parameter for this analysis.

Figure 8.13 shows the real part of the total pressure fluctuations. Only the 5 lowest frequency modes are shown integrated within $5\,R_E$ of the equilibrium magnetopause displayed in the tangential- and Z- plane in the same way as Figure 8.8 above. In this figure the scales of the waves described by each frequency becomes more clear. Immediately it can be seen that, as expected, the lowest frequency modes have the largest wavelengths along the magnetopause. For all the modes, the waves are constrained into the lower latitudes and appear to be oscillating tangentially to the magnetopause. The longitudinal wedge-like restriction on the waves z-extent from the local magnetic field line orientation as described in the previous chapter (see Section 7.6) can be seen in all the modes and is drawn on with a green dashed line. Where the total wave energy in Figure 8.8 was high, that is where more coherent wave-like fluctuations can be seen in the total pressure reconstructions in Figure 8.13 – for example in mode 2 along the equatorial plane between $50\,R_E - 150\,R_E$ tangentially

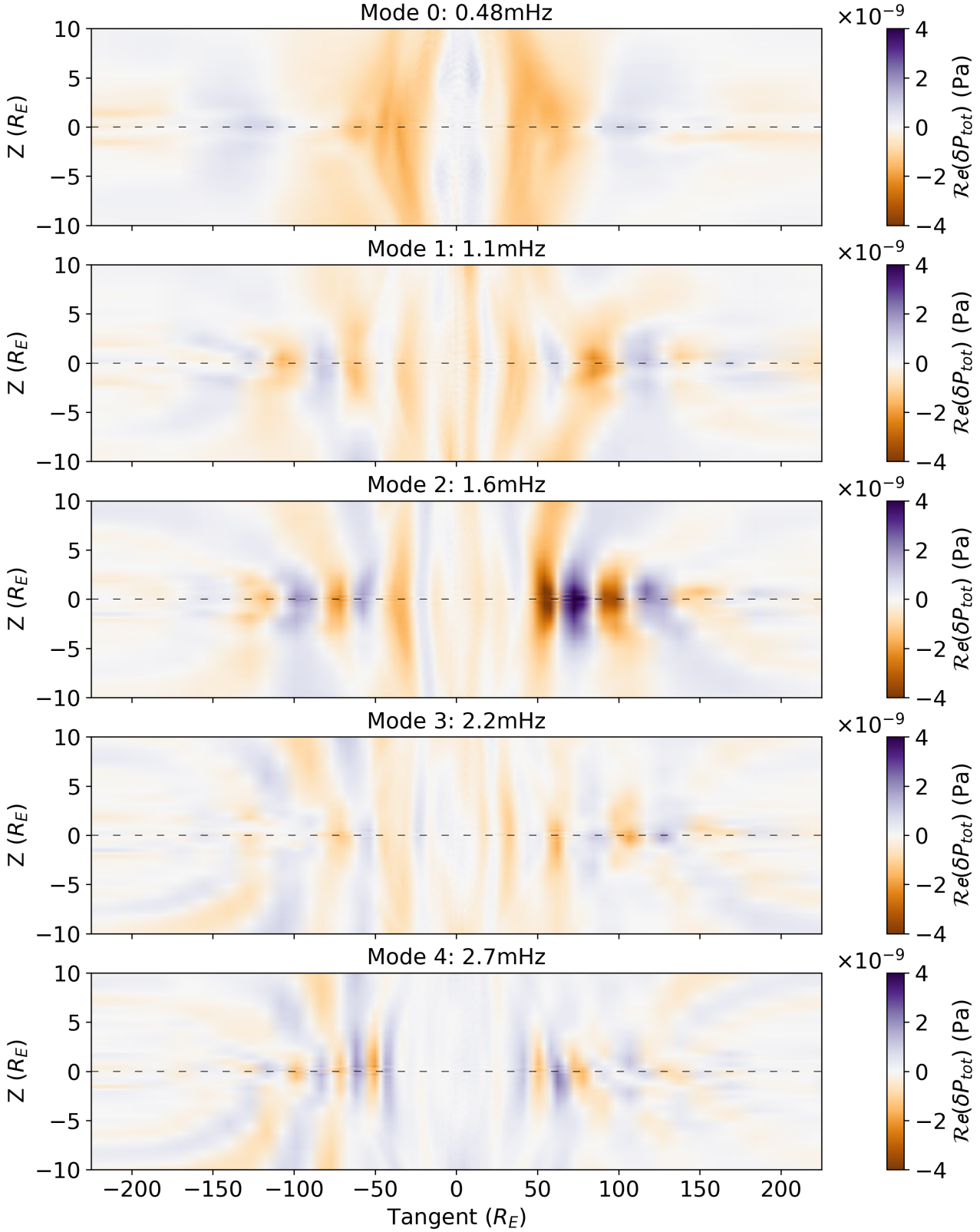


Figure 8.13: The spatial distribution of the real part of the total pressure fluctuations of the 5 lowest frequency modes integrated within 5 R_E normal of the equilibrium magnetopause in the tangential and Z directions.

dawn-ward of the subsolar point. But this type of view is not the best for investigating the evolving phase of the wave. It is worth noting that there is some visible substructure in mode 0 unlike in the other modes which have clean wave-like signatures.

Figure 8.14 shows the real part of the total pressure fluctuations seen in Figure 8.13 but now in the tangential-normal plane at $Z = 0$. This figure shows how the pressure is continuous across the equilibrium magnetopause. It is clear that the pressure fluctuations are evanescent as expected for a MSW. The pressure decays into the magnetosheath as well as the magnetosphere but it does have stronger values within the magnetosphere – this is most clearly seen on the dusk flank of Mode 4. In Mode 2 it is clear that the fluctuations at the magnetopause are also present at the bow shock, this will be explored later. In each panel it is clear how the wavelength of the MSWs is smaller closer to the subsolar point.

In all the modes there are very clear signatures that these waves are present in the magnetosheath and magnetosphere. The magnetosheath waves terminate on the bow shock. The bow shock is also sustaining some type of coherent wave behaviour which is supported by the presence of the wave energy in the bow shock seen in Figure 8.11. In mode 2 there is a clear indication that the bow shock may be being driven by the magnetosheath waves – this will be revisited in a later section.

It is worth recalling now that the total MSW is reconstructed by summing over all the modes. Figure 8.15 shows the sum of the 5 modes seen in Figure 8.14. The sum of the 5 modes is different from each of the decomposed frequencies, however the sum of the modes appears to most resemble mode 2 on the dawn flank; this was previously suggested to be the most unstable mode here. This suggests that the most unstable mode from linear theory may be applicable but it is far from being a complete description of the wave as a whole due to the superposition of many MSW frequencies. The dusk flank, which has previously been shown to have an equal distribution of total energy between the modes, is far messier and does not seem to resemble any of the decomposed modes. As it was previously shown to not have a most unstable mode and be a total superposition this suggests that linear theory is just not applicable here as there does not appear to be a single dominant frequency which describes the MSW. The sum of the 5 modes still captures the wavelength change along the tangential direction implying the phase evolution in the wave is present and, as DMD outputs contain phase information, this should be used to show the trend clearer.

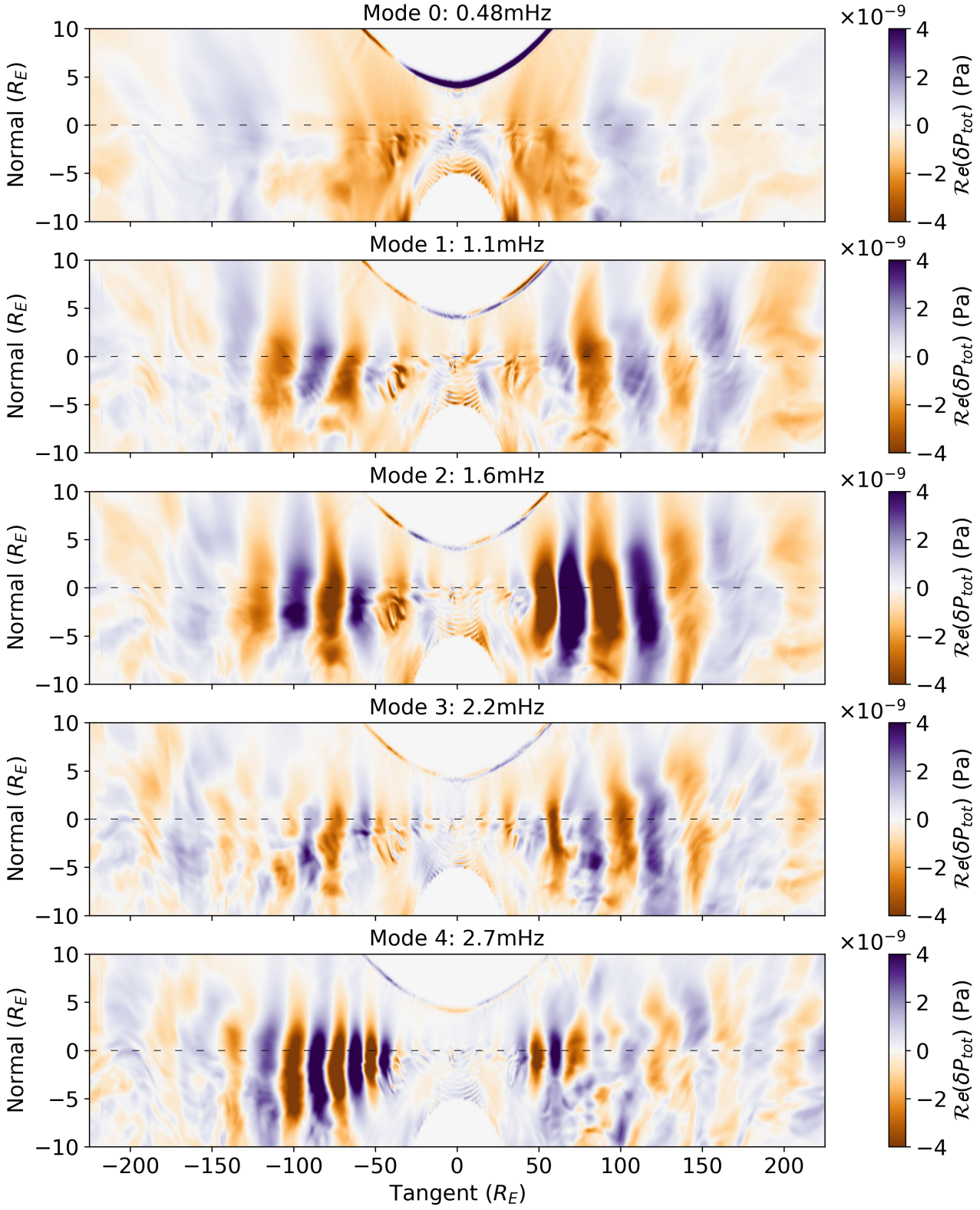


Figure 8.14: The spatial distribution of the real part of the total pressure fluctuations of the 5 lowest frequency modes in the tangential and normal directions.

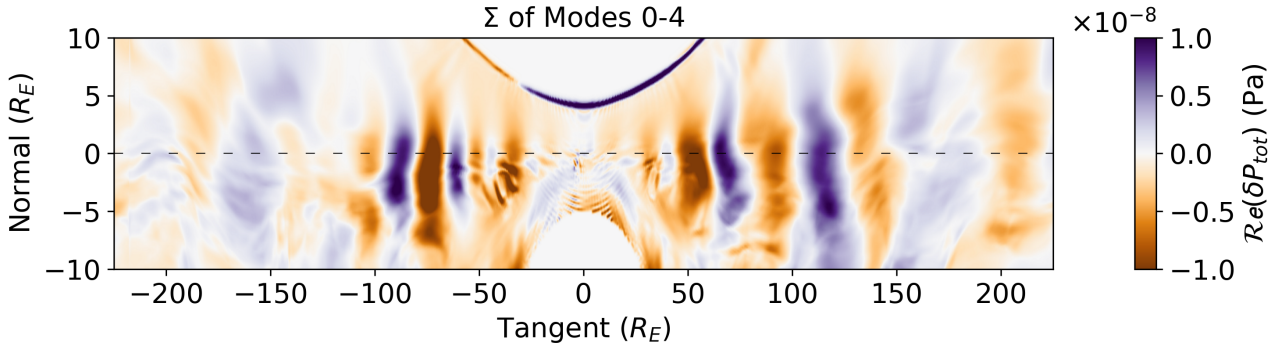


Figure 8.15: The spatial distribution of the real part of the total pressure summed over the 5 lowest frequency modes in the tangential and normal directions.

By taking the argument of the complex total pressure phasor, a spatial map of the local wave phase can be constructed. Figure 8.16 shows the local phase of the 5 lowest-frequency total pressure perturbation modes in the equatorial plane ($Z = 0\,\mathrm{R_E}$) within $10\,\mathrm{R_E}$ normal to the equilibrium magnetopause plotted in the Tangential- and Normal-directions. Fluctuations below 1×10^{-3} nPa are masked out before the phase is taken. A positive tangent direction corresponds to the dawn sector, and a negative value the dusk sector. The dashed line at the normal $= 0$ line indicates the equilibrium magnetopause boundary. There are some Moiré patterns around the subsolar point near the inner boundary which should be ignored.

The wave phase in continuous across the boundary indicating that the magnetopause is generally in pressure balance. It is immediately clear in this plane that as the phase fronts are along the normal direction, the waves are propagating along the tangential direction both inside and outside of the magnetopause. As the phase propagates in the direction of decreasing phase angle, it is clear that the phase propagation is from the nose towards the tail as expected with a MSW.

Across all the modes there is a trend where the phase fronts along the tangential direction are generally getting further away from each other, meaning that the phase gradient is decreasing and therefore the wavelength is increasing. Focussing on mode 2, it can be seen that between $50\,\mathrm{R_E}$ to $100\,\mathrm{R_E}$, a 360° phase change i.e. one wavelength, takes place over $\sim 36\,\mathrm{R_E}$. However this is not consistent. It is clear looking between $150\,\mathrm{R_E}$ to $200\,\mathrm{R_E}$ the wave does not cycle through a whole wavelength meaning that the local wavelength of the wave must be growing with distance from the subsolar point. Fortunately, the local wavelength of the wave can be extracted from the phase and so how the wavelength changes along the magnetopause can be understood.

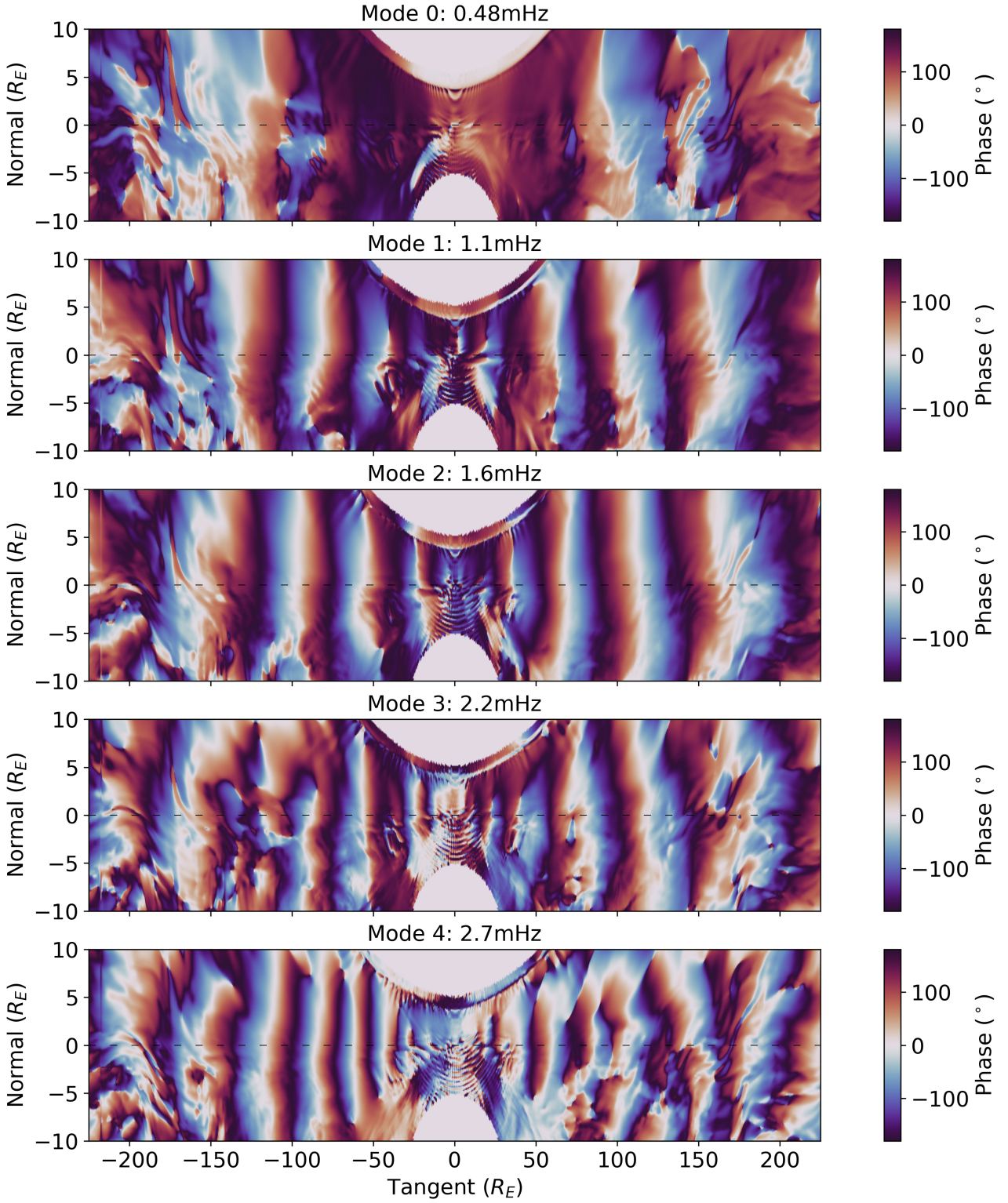


Figure 8.16: A figure showing the spatial distribution of the phase of the total pressure fluctuations of the 5 lowest frequency modes integrated within 5 R_E normal of the equilibrium magnetopause in the tangential- and Z- directions.

A number of steps are needed to extract the wavelength from the phase. The first step is to unwrap the phase separately in the Normal and Tangential directions. Unwrapping the phase means

that whenever the phase discontinuously changes by 360° or more (e.g. goes from −180° to 180°), then it is shifted by 360° until the phase change is less than 360° thus creating a continuous phase. A NumPy package was used to do this (Harris et al. 2020). From the unwrapped phase, the wave vector can be calculated by,

$$k_i = -\partial_i \phi_{\text{unwrapped in i}}, \tag{8.13}$$

where k_i is the wave number in the i-direction and $\phi_{\text{unwrapped in i}}$ is the phase unwrapped in the i-direction. Using this equation and finding the wave number for both the normal and tangential directions allows for the total wave vector to be constructed, $\mathbf{k}$. By using the definition of the wave vector, the wavelength, λ can be calculated by,

$$\lambda = \frac{2\pi}{|\mathbf{k}|}. \tag{8.14}$$

Figure 8.17 shows the mean wavelength of the second mode of the total pressure within $\pm 1\,\mathrm{R_E}$ of the equilibrium magnetopause boundary as a function of distance along the equilibrium magnetopause from the subsolar point in grey. In red is the mean of the time-averaged velocity of the simulation within $\pm 1\,\mathrm{R_E}$ of the equilibrium magnetopause boundary as a function of distance along the equilibrium magnetopause from the subsolar point. In dashed in black is a sixth-order polynomial fitted to the local wavelength using NumPy Polyfit (Harris et al. 2020) which has a root-mean-squared residual of $7.9\,\mathrm{R_E}$. It is plotted to reveal the global trend of the noisy local wavelength and is not used beyond a trend indicator.

The fitted polynomial reveals that the local wavelength of a wave at a specific frequency varies along the magnetopause. The wavelength increases from the subsolar point to approximately $100\,\mathrm{R_E}$ along the tangential direction at which point the wavelength has reached a maximum which is approximately 3× larger than its initial value. In this region, the wavelength grows by $\sim 30\%$ over a single wavelength. This is significant because it means that peak-to-peak simulation wavelength measurements are just not valid in this region which is along the flanks of the magnetopause. After $100\,\mathrm{R_E}$ along the magnetopause from the subsolar point, the wavelength begins to shorten to approximately its original length at $100\,\mathrm{R_E}$ from the subsolar point. From here, the local wavelength rapidly grows again. These changes in wavelength appear sporadic, however taking into account the

local magnetosheath flow speed they are explainable.

There is a clear correlation between the magnitude of the time-averaged velocity at the magnetopause and the local wavelength of mode 2. It would be thought that the local magnetopause velocity would increase moving from the subsolar point toward the tail (e.g. Haaland et al. 2019) however this is not the case, the flow speed both accelerates and decelerates. These changes are likely due to the open-closed boundary being poorly defined in the far tail but also because the magnetopause thickness here will provide variations on the flow speed around the boundary. Furthermore, as the KHI is present, surface roll-ups would reduce the flow speed locally due to the plasma mixing they cause. Regardless of the cause, these changes in the velocity also occur in the wavelength and therefore the velocity must be modulating the wavelength.

Recall that the modes are at distinct fixed frequencies and therefore the frequency is fixed and so by using the wave equation $c = \nu\lambda$ this can be explained. It has been theorised (Axford 1962) and shown in simulation (Li et al. 2012) that the phase speed, c, is dependent on the boundary layer velocities, then for a fixed frequency the wavelength must change proportionally. As the boundary layer speed increases, the wave speed increases and therefore the wavelength is stretched causing it to increase, when the flow speed decreases as does the wave speed causing the wavelength to be compressed. And, as a physical wave in an accelerating flow must maintain the same frequency within a stationary frame, Doppler shift must be changing the wavelength accordingly. This is the reason for the wavelength change.

The wavelengths calculated above agree with a statistical study using 56 KH observations from multiple spacecrafts by Lin et al. (2014) who found the wavelength to be between $\sim 5\,R_E$ near the subsolar point and $\sim 15\,R_E$ when $40\,R_E$ from the sub solar point along the Shue et al. (1998) magnetopause model. Furthermore, this study also shows that the KH-wavelength extends into the tail, as do simulations by Li et al. (2012) who found varying the total solar wind speed (Haaland et al. 2019) did not affect the way the wavelength extended in the tail. However, they did show that the phase speed increased with increasing longitude and found that the wave characteristics were self-consistent with $c = \nu\lambda$. Furthermore, Li et al. (2012) found that the inner-mode had a shorter wavelength compared to the outer-mode which differs to the results here. This may be due to the difference in the methods used. However, the inner- and outer-mode were found to change in the

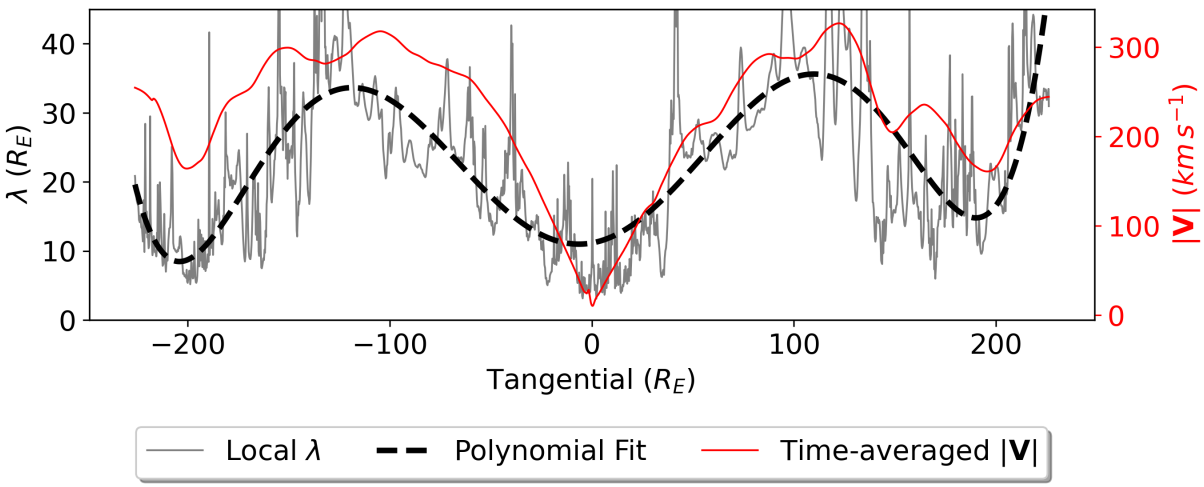


Figure 8.17: A figure showing the mean wavelength of the second mode of the total pressure (grey) and the mean of the time-averaged velocity (red) within $\pm 1\,R_E$ of the equilibrium magnetopause boundary as a function of distance along the equilibrium magnetopause from the subsolar point in grey. The dashed black line is a sixth-order polynomial fitted to the local wavelength. The equation of the fitted polynomial is $2.7 \times 10^{-12}x^6 + 9.4 \times 10^{-11}x^5 + -2.1 \times 10^{-7}x^4 + -4.6 \times 10^{-6}x^3 + 4.0 \times 10^{-3}x^2 + 5.2 \times 10^{-2}x + 11.1 = 0$

same way which agrees with these results.

Generally speaking both simulation and in-situ observations agree with the result of extending wavelength from the subsolar point found here. DMD has allowed for an extension of these works as it isolates a discrete frequency making it possible to show that the wavelength change is not due to the evolution of the most unstable frequency (Miura and Pritchett 1982) due to the thickening of the LLBL (Mitchell et al. 1987; Manuel and Samson 1993) as suggested by Lin et al. (2014) but may instead be due to a stretching of the wavelength supporting the claim that the KHI is an advective instability (Mills et al. 2000). Furthermore, it has allowed for an explanation as to why the wavelength evolution does not vary with different solar wind speeds (Li et al. 2012) as the baseline wave speed would also change. This means that how the solar wind speed changes due to its deflection around the magnetopause obstacle is what is important. Finally, Li et al. (2012) found that the increase in wavelength appears to saturate far in the tail (20.5hr local time). This is not found here but it is suggested that this saturation may be due to the increasing phase speed reaching the threshold for the unstable surface mode to become a stable body mode (Pu and Kivelson 1983).

8.8 Summary and Conclusion

The frequency and wavelength of magnetopause surface waves have been investigated using a factorisation and dimensionality reduction machine learning technique known as Dynamic Mode Decomposition to identify temporally stationary structures in a global MHD simulation. DMD was performed by rescaling the velocity, magnetic, and pressure fields into energy by using the time-averaged energy of a harmonic MHD wave equation. The technique, which before now has never been applied to magnetospheric science, successfully captured $\sim 62.2\%$ of the total energy fluctuations within the simulation with the 5 lowest-frequency modes, which were in the Pc6/Pc5 range, describing $\sim 46.7\%$ of the total energy fluctuations. An energy parity was found showing that the kinetic and magnetic potential energies dominate the total energy fluctuations with the internal energy varying on $\sim 10^4\times$ smaller energy scales. In the equatorial plane it was revealed that both the inner- and outer-modes of the KHI can sustain the same frequencies with the inner-mode having a comparatively larger wave energy due to it being the more unstable mode (Lee et al. 1981).

By transforming and/or integrating the data into a magnetopause reference frame and investigating the total wave energy, it has been found that the Kelvin-Helmholtz instability generates waves at a near-continuum of different ultra-low frequencies at the magnetopause. It was shown how the KHI does not just generate frequencies at or around the most unstable mode as commonly assumed. Instead, the KHI drives a broadband of frequency preferentially at the most unstable mode which results in a generative growth of new frequencies, an amplification of pre-existing frequencies, and a resonance-like amplification of the most unstable frequency. Finally it was shown how the KHI advects freqeuncies from where they are driven into regions where they are not unstable or driven. These three (generate, amplify, advect) processes together resulted in a complex superposition of different frequencies at the magnetopause with a spatially-dependent dominance. This has implications for how liberally used the most unstable mode of linear theory is. As well as this, it clearly shows that any dominant wave frequency at one location of the magnetopause is not necessarily the most dominant elsewhere.

Investigating the different energy contributions to the total energy revealed that the kinetic wave energy was dominant in the equatorial plane, magnetic potential wave energy straddles the equatorial

plane, and internal wave energy appears to align with where the kinetic wave energy peaks. By looking at these energies normal to the magnetopause in the equatorial plane it was found that all the magnetic potential and internal wave energies co-align with the kinetic wave energy. The kinetic wave energy was found to be most dominant having signatures along the inner- and outer-mode, as well as the equilibrium magnetopause. The magnetic potential energy was the second strongest energy in the equatorial plane with its strongest signatures on the inner-mode of the KHI only. Finally, the internal wave energy was shown to predominantly only exist within the magnetopause likely as a result of evanescent fast magnetosonic waves driven by the boundary motion.

By constructing a total pressure fluctuations term (equation 8.12), the wavelength of the different modes was investigated. Looking at the pressure fluctuations tangentially to the magnetopause and in the z-direction unsurprisingly revealed that the wavelength of the waves are dependent on their frequency. By calculating the local wavelength of the second mode of the total pressure it was shown that the wavelength of the discrete frequency mode also varies in local time. This variation is shown to be linearly correlated with the time-averaged local plasma speed indicating that the wave speed is modulated by the local plasma velocity and so for a fixed frequency the wavelength must change proportionally. This is essentially a 'stretching' and 'compressing' of the wavelength as the wave speed varies.

Finally, by inspecting the total pressure variations in the equatorial plane revealed that the MSWs are responsible for three global MSW-driven phenomena: magnetosheath waves, bow shock waves, and plasma sheet waves. The magnetosheath waves are suggested to be fast magnetosonic waves which terminate on the bow shock driving its motion like those seen at the subsolar point from MSEs in Archer et al. (2021). These bow shock waves are thought to negligibly modulate the bow shock normal direction. Finally, there is indications that MSWs may drive wave motion in the plasma sheet however a more conclusive study is needed into this.

This work is a complete study showing that the Kelvin-Helmholtz instability generates a broadband of frequencies of which it amplifies those that are most unstable, and it advects all frequencies along the magnetopause with those with the most energy surviving further into the tail. These findings challenge the simple approaches of measuring the wavelengths of MSWs by taking 'peak-to-peak' measurements (e.g. Li et al. 2012) as the wavelength is ever evolving, 30% over a single wavelength,

meaning that the measurements must be very close together – especially closer to the nose. And even if they are successfully made, they are only locally accurate as the evolution of the phase speed and therefore wavelength is unknown – especially with varying solar wind speeds. Alternatively, the local wavelength can be calculated using $c = \nu\lambda$ as the frequency of the wave can be approximated using Fourier techniques (e.g. Lin et al. 2014). However this approach does require phase speed measurements which already rely on approximations (e.g. Hasegawa et al. 2009) and the need for multi-spacecraft measurements.

Previous studies have suggested that the extension of the wavelength is expected due to the expansion of the LLBL as a function of local time giving a different most unstable mode (Lin et al. 2014; Haerendel et al. 1978; Miura and Pritchett 1982), however it is important to highlight that this is different. DMD has allowed for the extraction of a fixed frequency and shown that this fixed frequency wave is being Doppler shifted. This change in wavelength is not due to the change in dominant mode.

Further extensions to this work are needed. The previous two chapters have shown that plasma conditions (momentum, density gradients, and compressibility) influence the formation of the KHI. Because of this, it is important to understand how these different physical effects influence the different frequencies the KHI can generate, amplify, and advect. As well as this, magnetic field orientation has proven to influence the KHI so introducing different IMF orientations will allow for an understanding on how the IMF can influence how the KHI modulates frequency at the magnetopause. Introducing magnetic shear and studying the effects of magnetopause reconnection / vortex-induced reconnection on the spatial distributions of wave energy and frequency at the magnetopause is imperative to understanding the importance of the KHI under southward IMF. Finally, DMD has proven to be an invaluable tool in this study, and, as it is a data-reduction algorithm, applying it to larger/other data sets would likely be fruitful in understanding the pathways of ULF wave power from the solar wind, through Earth's magnetosphere, and into the ionosphere.

CHAPTER 9

Conclusion

The results of the three previous work chapters are broad with two main branches: science, and techniques. This chapter aims to summarise all the significant contributions made to the field by this thesis.

The literature showed how linear theory suggests that plasma inhomogeneity, compressibility, and magnetic tension all play a role in determining how unstable a boundary is to the KHI. But beyond this, it was unclear how important each effect was and whether each effect played a role in every stage of the instability or just the initial stages. The first chapter answered this question by showing during the linear growth phase, density gradients generally act to oppose vortex formation but become less important in the later stages of vortex evolution. The rotational part of the magnetic tension was shown to become important in small-scale structures and fluid compressibility was found to be insignificant at all stages. This study contributes to the field by providing evidence that suggests that vortices evolve differently based on their plasma environment. This is an important result as it allows for an understanding about the limits of local simulations of the KHI and also when and where they are applicable. As well as this, it provides an insight into which IMF conditions the KHI may become a stronger driver of the viscous-like interaction. But, due to the limits of a local simulation, the study lacked realistic magnetopause plasma and magnetic field conditions which limits its use

across all local times and under more representative magnetic geometries.

This led to the second chapter of work which focussed on the importance of realistic conditions on the formation and evolution of the KHI as the literature showed that the inhomogeneities of a realistic magnetopause cannot be neglected. Building upon the findings of the local simulation, which investigates how the different physical effects influence the evolution of KH-vortices, the next work chapter aimed to investigate how realistic magnetospheric plasma and magnetic field geometry changes how the KHI evolves and how the different drivers/stabilisers effect its evolution. This study showed that a more realistic magnetopause causes important changes to the formation and evolution of the KHI by changing the impacts of the different drivers and stabilisers of the KHI. Furthermore, it revealed how a realistic magnetic field geometry led to different KH-seed processes and also a limitation of the unstable region into the low-latitudes. The implications of this work are important as it highlights that a realistic magnetic geometry is an important factor in the formation of the KHI. As well as this, the magnetopause boundary layer thickness cannot be ignored. This work was limited by its use of idealistic and simplified solar wind and IMF.

The final question answered by this thesis was about testing competing theories on how the KHI manipulates MSW frequency in a realistic magnetosphere. The aim was to understand which frequency mechanism is most dominant in the KHI at the magnetopause: generation, amplification, or advection. This was done by using DMD to analyse multiple fixed frequency waves extracted from a global MHD simulation. The study showed that the KHI causes all three processes to occur at the magnetopause resulting in a complex superposition of wave frequencies at any one local time. As well as this, by analysing the wavelength of a single fixed frequency, it was found that the accelerating magnetosheath flow Doppler-shifted the wavelengths. This study has implications for both in-situ and simulation analysis of MSWs as it shows that any frequency or wavelength measured is only valid locally, and has little global meaning. The study was, again, limited by its simplified solar wind and IMF conditions.

There are many research avenues which are still left to be explored. The relationships between the drivers and stabilisers of the KHI has only been explored with minimal magnetic shear. Introducing magnetic shear is expected to cause significant changes to the results found in this thesis due to the triggering of VIR. KH-waves and vortices have been suggested to be seeded through cusp

reconnection; further investigation is needed into whether this process exists in reality, aiming to understand how often it takes place and its significance. An investigation is needed into how the KH-unstable region along the magnetopause changes as a function of IMF cone angle under realistic magnetic geometries. Within this study an investigation into how the addition of large-scale magnetic reconnection suppresses and changes the evolution of the KHI should be conducted. Finally, an investigation into the frequency and wavelength of driven MSWs at the magnetopause is required to better investigate how the KHI amplifies frequency along the magnetopause.

The novel contributions to the field also include two new analysis techniques. The first is λ_{MHD} which provides a new way to define and analyse MHD-scale vortices. λ_{MHD} remains to be applied to real multi-point spacecraft data potentially resolving the issues with existing methods. It is possible with the future launch of HelioSwarm (Klein et al. 2023) and other muli-point measurement missions that the full λ_{MHD} definition could be calculated in situ. Other hybrid global simulations such as Vlasiator (Alfthan et al. 2014) should also implement this technique to allow for an investigation of the kinetic effects of KH-vortices. The second contribution was the development of how to apply DMD in MHD. Introducing the technique to the field allows for it to be used by other simulation codes for future analysis. As well as this, it provides a basis for how to apply the technique with in situ data. Other examples of where the technique could be applied include the large data structures that are output by ground-based instrumentation such as SuperDARN (Greenwald et al. 1995). Furthermore, DMD is capable of combining multiple different measurement techniques meaning that enormous amounts of data could be analysed in unison, e.g. combining space and ground-based measurements to better understand ULF wave penetration. Finally, imagers could utilise DMD such as the soon-to-launch Solar wind Magnetosphere Ionosphere Link Explorer mission known as SMILE (Branduardi-Raymont and Al. 2018).

Bibliography

Agapitov, O., K.-H. Glassmeier, F. Plaschke, H.-U. Auster, D. Constantinescu, V. Angelopoulos, W. Magnes, R. Nakamura, C. W. Carlson, S. Frey, and J. P. McFadden (2009). "Surface waves and field line resonances: A THEMIS case study". In: *Journal of Geophysical Research: Space Physics* 114.A1, 2008JA013553. ISSN: 0148-0227. DOI: 10.1029/2008JA013553.

Ahrens, J. P., B. Geveci, and C. Law (2005). "ParaView: An end-user tool for large-data visualization". English. In: *Visualization Handbook*. Unknown Publisher, pp. 717–731. DOI: 10.1016/B978-012387582-2/50038-1.

Alford-Lago, D. J., C. W. Curtis, A. T. Ihler, and K. A. Zawdie (2023). "Scale-separated dynamic mode decomposition and ionospheric forecasting". In: *Radio Science* 58.8, pp. 1–24. ISSN: 1944-799X. DOI: 10.1029/2022RS007637.

Alfthan, S. von, D. Pokhotelov, Y. Kempf, S. Hoilijoki, I. Honkonen, A. Sandroos, and M. Palmroth (2014). "Vlasiator: First global hybrid-Vlasov simulations of Earth's foreshock and magnetosheath". In: *Journal of Atmospheric and Solar-Terrestrial Physics* 120, pp. 24–35. ISSN: 1364-6826. DOI: 10.1016/j.jastp.2014.08.012.

Alfvén, H. (1942). "Existence of Electromagnetic-Hydrodynamic Waves". In: *Nature* 150.3805, pp. 405–406. ISSN: 1476-4687. DOI: 10.1038/150405d0.

Alì, G. and J. K. Hunter (2003). "Nonlinear surface waves on a tangential discontinuity in magnetohydrodynamics". In: *Quarterly of Applied Mathematics* 61.3, pp. 451–474. ISSN: 0033-569X, 1552-4485. DOI: 10.1090/qam/1999831.

Amerstorfer, U. V., N. V. Erkaev, U. Taubenschuss, and H. K. Biernat (2010). "Influence of a density increase on the evolution of the Kelvin–Helmholtz instability and vortices". In: *Physics of Plasmas* 17.7, p. 072901. ISSN: 1070-664X. DOI: 10.1063/1.3453705.

Angelopoulos, V. (2008). "The THEMIS Mission". In: *Space Science Reviews* 141.1, pp. 5–34. ISSN: 1572-9672. DOI: 10.1007/s11214-008-9336-1.

Angelopoulos, V., W. Baumjohann, C. F. Kennel, F. V. Coroniti, M. G. Kivelson, R. Pellat, R. J. Walker, H. Lühr, and G. Paschmann (1992). "Bursty bulk flows in the inner central plasma sheet". In: *Journal of Geophysical Research: Space Physics* 97.A4, pp. 4027–4039. ISSN: 2156-2202. DOI: 10.1029/91JA02701.

Arber, T., A. Longbottom, C. Gerrard, and A. Milne (2001). "A Staggered Grid, Lagrangian–Eulerian Remap Code for 3-D MHD Simulations". In: *Journal of Computational Physics* 171.1, pp. 151–181. ISSN: 00219991. DOI: 10.1006/jcph.2001.6780.

Archer, M. O., M. D. Hartinger, F. Plaschke, D. J. Southwood, and L. Rastaetter (2021). "Magnetopause ripples going against the flow form azimuthally stationary surface waves". In: *Nature Communications* 12.1, p. 5697. ISSN: 2041-1723. DOI: 10.1038/s41467-021-25923-7.

Archer, M. O., H. Hietala, M. D. Hartinger, F. Plaschke, and V. Angelopoulos (2019). "Direct observations of a surface eigenmode of the dayside magnetopause". In: *Nature Communications* 10.1, p. 615. ISSN: 2041-1723. DOI: 10.1038/s41467-018-08134-5.

Archer, M. O. and F. Plaschke (2015). "What frequencies of standing surface waves can the subsolar magnetopause support?" In: *Journal of Geophysical Research: Space Physics* 120.5, pp. 3632–3646. ISSN: 2169-9402. DOI: 10.1002/2014JA020545.

Archer, M. O., D. J. Southwood, M. D. Hartinger, L. Rastaetter, and A. N. Wright (2022). "How a Realistic Magnetosphere Alters the Polarizations of Surface, Fast Magnetosonic, and Alfvén Waves". In: *Journal of Geophysical Research: Space Physics* 127.2, e2021JA030032. ISSN: 2169-9402. DOI: 10.1029/2021JA030032.

Archer, M. O., V. A. Pilipenko, B. Li, K. Sorathia, V. M. Nakariakov, T. Elsden, and K. Nykyri (2024). "Magnetopause MHD surface wave theory: progress and challenges". English. In: *Frontiers in Astronomy and Space Sciences* 11. ISSN: 2296-987X. DOI: 10.3389/fspas.2024.1407172.

Arnold, H., K. Sorathia, G. Stephens, M. Sitnov, V. G. Merkin, and J. Birn (2023). "Data Mining Inspired Localized Resistivity in Global MHD Simulations of the Magnetosphere". In: *Journal of Geophysical Research: Space Physics* 128.2, e2022JA030990. ISSN: 2169-9402. DOI: 10.1029/2022JA030990.

Atkinson, G. and T. Watanabe (1966). "Surface waves on the magnetospheric boundary as a possible origin of long period geomagnetic micropulsations". In: *Earth and Planetary Science Letters* 1.2, pp. 89–91. ISSN: 0012-821X. DOI: 10.1016/0012-821X(66)90112-9.

Axford, W. I. (1962). "Note on a problem of magnetohydrodynamic stability". In: *Canadian Journal of Physics* 40.5, pp. 654–656. ISSN: 0008-4204. DOI: 10.1139/p62-064.

Axford, W. I. (1964). "Viscous interaction between the solar wind and the earth's magnetosphere". In: *Planetary and Space Science* 12.1, pp. 45–53. ISSN: 0032-0633. DOI: 10.1016/0032-0633(64)90067-4.

Axford, W. I. and C. O. Hines (1961). "A unifying theory of high-latitude geophysical phenomena and geomagnetic storms". In: *Canadian Journal of Physics* 39.10, pp. 1433–1464. ISSN: 0008-4204. DOI: 10.1139/p61-172.

Baumjohann, W. and R. Treumann (1996). *Basic Space Plasma Physics*. Vol. 15-22. ISBN: 978-1-86094-017-0. DOI: 10.1142/p015.

Belmont, G. and G. Chanteur (1989). "Advances in magnetopause Kelvin-Helmholtz instability studies". In: *Physica Scripta* 40.1, p. 124. ISSN: 1402-4896. DOI: 10.1088/0031-8949/40/1/018.

Belmont, G., F. Reberac, and L. Rezeau (1995). "Resonant amplification of magnetosheath MHD fluctuations at the magnetopause". In: *Geophysical Research Letters* 22.3, pp. 295–298. ISSN: 1944-8007. DOI: 10.1029/94GL03078.

Benson, D. J. (1992). "Computational methods in Lagrangian and Eulerian hydrocodes". In: *Computer Methods in Applied Mechanics and Engineering* 99.2, pp. 235–394. ISSN: 0045-7825. DOI: 10.1016/0045-7825(92)90042-I.

Bjerhammar, A. (1951). "Application of calculus of matrices to method of least squares : with special reference to geodetic calculations". In.

Bohon, M. D., A. Orchini, R. Bluemner, C. O. Paschereit, and E. J. Gutmark (2021). "Dynamic mode decomposition analysis of rotating detonation waves". In: *Shock Waves* 31.7, pp. 637–649. ISSN: 1432-2153. DOI: 10.1007/s00193-020-00975-8.

Brackbill, J. U. and D. A. Knoll (2001). "Transient Magnetic Reconnection and Unstable Shear Layers". In: *Physical Review Letters* 86.11, pp. 2329–2332. DOI: 10.1103/PhysRevLett.86.2329.

Branduardi-Raymont, G. and E. Al. (2018). *SMILE Definition Study Report*. Tech. rep. ESA SCI. DOI: 10.5270/esa.smile.definition_study_report-2018-12.

Burch, J. L., T. E. Moore, R. B. Torbert, and B. L. Giles (2016). "Magnetospheric Multiscale Overview and Science Objectives". In: *Space Science Reviews* 199.1, pp. 5–21. ISSN: 1572-9672. DOI: 10.1007/s11214-015-0164-9.

Buzulukova, N. and B. Tsurutani (2022). "Space Weather: From solar origins to risks and hazards evolving in time". In: *Frontiers in Astronomy and Space Sciences* 9. ISSN: 2296-987X.

Cai, D., B. Lembège, H. Hasegawa, and K.-I. Nishikawa (2018). "Identifying 3-D Vortex Structures At/Around the Magnetopause Using a Tetrahedral Satellite Configuration". In: *Journal of Geophysical Research: Space Physics* 123.12, pp. 10, 158–10, 176. ISSN: 2169-9402. DOI: 10.1029/2018JA025547.

Chakraborty, P., S. Balachandar, and R. J. Adrian (2005). "On the relationships between local vortex identification schemes". In: *Journal of Fluid Mechanics* 535, pp. 189–214. ISSN: 0022-1120, 1469-7645. DOI: 10.1017/S0022112005004726.

Chandrasekhar, S. (1961). *Hydrodynamic and hydromagnetic stability*.

Chapman, S. and V. C. A. Ferraro (1931). "A new theory of magnetic storms". In: *Terrestrial Magnetism and Atmospheric Electricity* 36.3, pp. 171–186. ISSN: 0096-8013. DOI: 10.1029/TE036i003p00171.

Chatterjee, A. (2000). "An introduction to the proper orthogonal decomposition". In: *Current Science* 78.7, pp. 808–817. ISSN: 0011-3891.

Chen, L. and A. Hasegawa (1974a). "A theory of long-period magnetic pulsations: 1. Steady state excitation of field line resonance". In: *Journal of Geophysical Research (1896-1977)* 79.7, pp. 1024–1032. ISSN: 2156-2202. DOI: 10.1029/JA079i007p01024.

Chen, L. and A. Hasegawa (1974b). "A theory of long-period magnetic pulsations: 1. Steady state excitation of field line resonance". In: *Journal of Geophysical Research (1896-1977)* 79.7, pp. 1024–1032. ISSN: 2156-2202. DOI: 10.1029/JA079i007p01024.

Chen, S. .-. and M. G. Kivelson (1993). "On nonsinusoidal waves at the Earths magnetopause". In: *Geophysical Research Letters* 20.23, pp. 2699–2702. ISSN: 1944-8007. DOI: 10.1029/93GL02622.

Chittenden, J. P., S. V. Lebedev, C. A. Jennings, S. N. Bland, and A. Ciardi (2004). "X-ray generation mechanisms in three-dimensional simulations of wire array Z-pinches". In: *Plasma Physics and Controlled Fusion* 46.12B, B457–B476. ISSN: 0741-3335, 1361-6587. DOI: 10.1088/0741-3335/46/12B/039.

Ciardi, A., S. V. Lebedev, A. Frank, E. G. Blackman, J. P. Chittenden, C. J. Jennings, D. J. Ampleford, S. N. Bland, S. C. Bott, J. Rapley, G. N. Hall, F. A. Suzuki-Vidal, A. Marocchino, T. Lery, and C. Stehle (2007). "The evolution of magnetic tower jets in the laboratorya)". In: *Physics of Plasmas* 14.5. ISSN: 1070-664X. DOI: 10.1063/1.2436479.

Collado-Vega, Y. M., V. L. Kalb, D. G. Sibeck, K.-J. Hwang, and L. Rastätter (2018). "Data mining for vortices on the Earth's magnetosphere – algorithm application for detection and analysis". English. In: *Annales Geophysicae* 36.4, pp. 1117–1129. ISSN: 0992-7689. DOI: 10.5194/angeo-36-1117-2018.

Courant, R., K. Friedrichs, and H. Lewy (1928). "ber die partiellen Differenzengleichungen der mathematischen Physik". de. In: *Mathematische Annalen* 100.1, pp. 32–74. ISSN: 0025-5831, 1432-1807. DOI: 10.1007/BF01448839.

Cowee, M. M., D. Winske, and S. P. Gary (2010). "Hybrid simulations of plasma transport by Kelvin-Helmholtz instability at the magnetopause: Density variations and magnetic shear". In: *Journal of Geophysical Research: Space Physics* 115.A6. ISSN: 2156-2202. DOI: 10.1029/2009JA015011.

Coxon, J. C. (2015). "The role of Birkeland currents in the Dungey cycle". thesis. University of Leicester.

Cucitore, R., M. Quadrio, and A. Baron (1999). "On the effectiveness and limitations of local criteria for the identification of a vortex". In: *European Journal of Mechanics - B/Fluids* 18.2, pp. 261–282. ISSN: 0997-7546. DOI: 10.1016/S0997-7546(99)80026-0.

Dang, T., J. Lei, B. Zhang, T. Zhang, Z. Yao, J. Lyon, X. Ma, S. Xiao, M. Yan, O. Brambles, K. Sorathia, and V. Merkin (2022). "Oxygen Ion Escape at Venus Associated With Three-Dimensional Kelvin-Helmholtz Instability". In: *Geophysical Research Letters* 49.6, e2021GL096961. ISSN: 1944-8007. DOI: 10.1029/2021GL096961.

De Keyser, J. (2008). "Least-squares multi-spacecraft gradient calculation with automatic error estimation". English. In: *Annales Geophysicae* 26.11, pp. 3295–3316. ISSN: 0992-7689. DOI: 10.5194/angeo-26-3295-2008.

De Keyser, J., M. Roth, F. Reberac, L. Rezeau, and G. Belmont (1999). "Resonant amplification of MHD waves in realistic subsolar magnetopause configurations". In: *Journal of Geophysical Research: Space Physics* 104.A2, pp. 2399–2409. ISSN: 2156-2202. DOI: 10.1029/1998JA900060.

Demo, N., M. Tezzele, and G. Rozza (2018). "PyDMD: Python Dynamic Mode Decomposition". In: *Journal of Open Source Software* 3.22, p. 530. ISSN: 2475-9066. DOI: 10.21105/joss.00530.

Donaldson, K., A. J. Olsen, C. S. Paty, and J. Caggiano (2024). "Characterizing the Solar Wind-Magnetosphere Viscous Interaction at Uranus and Neptune". In: *Journal of Geophysical Research: Space Physics* 129.8, e2024JA032518. ISSN: 2169-9402. DOI: 10.1029/2024JA032518.

Dong, Y. and W. Tian (2020). "On the thresholds of vortex visualisation methods". In: *International Journal of Computational Fluid Dynamics* 34.4, pp. 267–277. ISSN: 1061-8562. DOI: 10.1080/10618562.2020.1745781.

Drake, J. F., M. Swisdak, K. M. Schoeffler, B. N. Rogers, and S. Kobayashi (2006). "Formation of secondary islands during magnetic reconnection". In: *Geophysical Research Letters* 33.13. ISSN: 1944-8007. DOI: 10.1029/2006GL025957.

Dungey, J. W. (1955). *Electrodynamics of the Outer Atmosphere*.

Dungey, J. W. (1961). "Interplanetary Magnetic Field and the Auroral Zones". In: *Physical Review Letters* 6.2, pp. 47–48. DOI: 10.1103/PhysRevLett.6.47.

Dungey, J. W. and D. J. Southwood (1970). "Ultra low frequency waves in the magnetosphere". In: *Space Science Reviews* 10.5, pp. 672–688. ISSN: 1572-9672. DOI: 10.1007/BF00171551.

Eastman, T. E., E. W. Hones Jr., S. J. Bame, and J. R. Asbridge (1976). "The magnetospheric boundary layer: Site of plasma, momentum and energy transfer from the magnetosheath into the magnetosphere". In: *Geophysical Research Letters* 3.11, pp. 685–688. ISSN: 1944-8007. DOI: 10.1029/GL003i011p00685.

Eastwood, J. P. (2008). "The science of space weather". In: *Philosophical Transactions of the Royal Society A: Mathematical, Physical and Engineering Sciences* 366.1884, pp. 4489–4500. DOI: 10.1098/rsta.2008.0161.

Eggington, J. W. B., J. C. Coxon, R. M. Shore, R. T. Desai, L. Mejnertsen, J. P. Chittenden, and J. P. Eastwood (2022a). "Response timescales of the magnetotail current sheet during a geomagnetic storm: Global MHD simulations". In: *Frontiers in Astronomy and Space Sciences* 9, p. 966164. ISSN: 2296-987X. DOI: 10.3389/fspas.2022.966164.

Eggington, J. W. B., R. T. Desai, L. Mejnertsen, J. P. Chittenden, and J. P. Eastwood (2022b). "Time-Varying Magnetopause Reconnection During Sudden Commencement: Global MHD Simulations". In: *Journal of Geophysical Research: Space Physics* 127.4, e2021JA030006. ISSN: 2169-9380, 2169-9402. DOI: 10.1029/2021JA030006.

Eggington, J. W. B., J. P. Eastwood, L. Mejnertsen, R. T. Desai, and J. P. Chittenden (2020). "Dipole Tilt Effect on Magnetopause Reconnection and the Steady-State Magnetosphere-Ionosphere System: Global MHD Simulations". In: *Journal of Geophysical Research: Space Physics* 125.7, e2019JA027510. ISSN: 2169-9380, 2169-9402. DOI: 10.1029/2019JA027510.

Eggington, J. W. B. (2021). "The drivers and timescales of solar wind-magnetosphere-ionosphere coupling in global MHD simulations". phd. Space and Atmospheric Physics Group, Department of Physics, Imperial College London.

Ellington, S. M., M. B. Moldwin, and M. W. Liemohn (2016). "Local time asymmetries and toroidal field line resonances: Global magnetospheric modeling in SWMF". In: *Journal of Geophysical Research: Space Physics* 121.3, pp. 2033–2045. ISSN: 2169-9402. DOI: 10.1002/2015JA021920.

Elsden, T., A. Wright, and A. Degeling (2022). "A review of the theory of 3-D Alfvén (field line) resonances". English. In: *Frontiers in Astronomy and Space Sciences* 9. ISSN: 2296-987X. DOI: 10.3389/fspas.2022.917817.

Ershkovich, A. I. (1980). "Kelvin-Helmholtz instability in type-1 comet tails and associated phenomena". In: *Space Science Reviews* 25.1, pp. 3–34. ISSN: 1572-9672. DOI: 10.1007/BF00200796.

Escoubet, C. P., M. Fehringer, and M. Goldstein (2001). "*Introduction*
The Cluster mission". English. In: *Annales Geophysicae* 19.10/12, pp. 1197–1200. ISSN: 0992-7689. DOI: 10.5194/angeo-19-1197-2001.

Fadanelli, S., M. Faganello, F. Califano, S. S. Cerri, F. Pegoraro, and B. Lavraud (2018). "North-South Asymmetric Kelvin-Helmholtz Instability and Induced Reconnection at the Earth's Magnetospheric Flanks". In: *Journal of Geophysical Research: Space Physics* 123.11, pp. 9340–9356. ISSN: 2169-9402. DOI: 10.1029/2018JA025626.

Faganello, M., F. Califano, and F. Pegoraro (2008). "Competing Mechanisms of Plasma Transport in Inhomogeneous Configurations with Velocity Shear: The Solar-Wind Interaction with Earth's Magnetosphere". In: *Physical Review Letters* 100.1, p. 015001. DOI: 10.1103/PhysRevLett.100.015001.

Faganello, M., F. Califano, F. Pegoraro, and T. Andreussi (2012). "Double mid-latitude dynamical reconnection at the magnetopause: An efficient mechanism allowing solar wind to enter the Earth's magnetosphere". In: *Europhysics Letters* 100.6, p. 69001. ISSN: 0295-5075. DOI: 10.1209/0295-5075/100/69001.

Faganello, M., F. Califano, F. Pegoraro, and A. Retinò (2014). "Kelvin-Helmholtz vortices and double mid-latitude reconnection at the Earth's magnetopause: Comparison between observations and simulations". In: *Europhysics Letters* 107.1, p. 19001. ISSN: 0295-5075. DOI: 10.1209/0295-5075/107/19001.

Faganello, M. and F. Califano (2017). "Magnetized Kelvin–Helmholtz instability: theory and simulations in the Earth's magnetosphere context". In: *Journal of Plasma Physics* 83.6, p. 535830601. ISSN: 0022-3778, 1469-7807. DOI: 10.1017/S0022377817000770.

Farris, M. H. and C. T. Russell (1994). "Determining the standoff distance of the bow shock: Mach number dependence and use of models". In: *Journal of Geophysical Research: Space Physics* 99.A9, pp. 17681–17689. ISSN: 2156-2202. DOI: 10.1029/94JA01020.

Farrugia, C. J., F. T. Gratton, L. Bender, H. K. Biernat, N. V. Erkaev, J. M. Quinn, R. B. Torbert, and V. Dennisenko (1998). "Charts of joint Kelvin-Helmholtz and Rayleigh-Taylor instabilites at the dayside magnetopause for strongly northward interplanetary magnetic field". In: *Journal of Geophysical Research: Space Physics* 103.A4, pp. 6703–6727. ISSN: 0148-0227. DOI: 10.1029/97JA03248.

Farrugia, C. J., F. T. Gratton, R. B. Torbert, L. Bender, G. Gnavi, K. W. Ogilvie, N. V. Erkaev, R. P. Lepping, and P. Stauning (2003). "On the dependence of dayside Kelvin-Helmholtz activity on IMF orientation". In: *Advances in Space Research* 31.4, pp. 1105–1110. ISSN: 0273-1177. DOI: 10.1016/S0273-1177(02)00889-X.

Fejer, J. A. (1964). "Hydromagnetic Stability at a Fluid Velocity Discontinuity between Compressible Fluids". In: *The Physics of Fluids* 7.4, pp. 499–503. ISSN: 0031-9171. DOI: 10.1063/1.1711229.

Feng, J. Y., Y. Zhou, J. Y. Lu, M. Wang, J. Y. Li, H. X. Zhang, F. Tang, and F. L. Yue (2024). "Occurrence of Kelvin–Helmholtz Instability at Lunar Distance Magnetopause: ARTEMIS Observation". In: *The Astrophysical Journal* 972.1, p. 86. ISSN: 0004-637X. DOI: 10.3847/1538-4357/ad6159.

Foullon, C., C. J. Farrugia, A. N. Fazakerley, C. J. Owen, F. T. Gratton, and R. B. Torbert (2008). "Evolution of Kelvin-Helmholtz activity on the dusk flank magnetopause". In: *Journal of Geophysical Research: Space Physics* 113.A11, 2008JA013175. ISSN: 0148-0227. DOI: 10.1029/2008JA013175.

Fox, N. J., M. C. Velli, S. D. Bale, R. Decker, A. Driesman, R. A. Howard, J. C. Kasper, J. Kinnison, M. Kusterer, D. Lario, M. K. Lockwood, D. J. McComas, N. E. Raouafi, and A. Szabo (2016). "The Solar Probe Plus Mission: Humanity's First Visit to Our Star". In: *Space Science Reviews* 204.1, pp. 7–48. ISSN: 1572-9672. DOI: 10.1007/s11214-015-0211-6.

Franci, L., E. Papini, A. Micera, G. Lapenta, P. Hellinger, D. D. Sarto, D. Burgess, and S. Landi (2022). "Anisotropic electron heating in turbulence-driven magnetic reconnection in the near-Sun solar wind". In: *The Astrophysical Journal* 936.1, p. 27. ISSN: 0004-637X, 1538-4357. DOI: 10.3847/1538-4357/ac7da6.

Fujimoto, M., T. K. M. Nakamura, and H. Hasegawa (2006). "Cross-Scale Coupling Within Rolled-Up MHD-Scale Vortices and Its Effect on Large Scale Plasma Mixing Across the Magnetospheric Boundary". In: *Space Science Reviews* 122.1, pp. 3–18. ISSN: 1572-9672. DOI: 10.1007/s11214-006-7768-z.

Fujita, S., K.-H. Glassmeier, and K. Kamide (1996). "MHD waves generated by the Kelvin-Helmholtz instability in a nonuniform magnetosphere". In: *Journal of Geophysical Research: Space Physics* 101.A12, pp. 27317–27325. ISSN: 2156-2202. DOI: 10.1029/96JA02676.

García, K. S. and W. J. Hughes (2007). "Finding the Lyon-Fedder-Mobarry magnetopause: A statistical perspective". In: *Journal of Geophysical Research: Space Physics* 112.A6. ISSN: 2156-2202. DOI: 10.1029/2006JA012039.

Glassmeier, K. .-. (1995). "Ultralow-frequency pulsations: Earth and Jupiter compared". In: *Advances in Space Research*. Comparative Studies of Magnetospheric Phenomena 16.4, pp. 209–218. ISSN: 0273-1177. DOI: 10.1016/0273-1177(95)00232-4.

Gordeev, E., G. Facskó, V. Sergeev, I. Honkonen, M. Palmroth, P. Janhunen, and S. Milan (2013). "Verification of the GUMICS-4 global MHD code using empirical relationships". In: *Journal of Geophysical Research: Space Physics* 118.6, pp. 3138–3146. ISSN: 2169-9402. DOI: 10.1002/jgra.50359.

Gordeev, E., V. Sergeev, I. Honkonen, M. Kuznetsova, L. Rastätter, M. Palmroth, P. Janhunen, G. Tóth, J. Lyon, and M. Wiltberger (2015). "Assessing the performance of community-available global MHD models using key system parameters and empirical relationships". In: *Space Weather* 13.12, pp. 868–884. ISSN: 1542-7390. DOI: 10.1002/2015SW001307.

Gosling, J. T., M. F. Thomsen, S. J. Bame, R. C. Elphic, and C. T. Russell (1991). "Observations of reconnection of interplanetary and lobe magnetic field lines at the high-latitude magnetopause". In: *Journal of Geophysical Research: Space Physics* 96.A8, pp. 14097–14106. ISSN: 2156-2202. DOI: 10.1029/91JA01139.

Greenacre, M., P. J. F. Groenen, T. Hastie, A. I. D'Enza, A. Markos, and E. Tuzhilina (2022). "Principal component analysis". In: *Nature Reviews Methods Primers* 2.1, pp. 1–21. ISSN: 2662-8449. DOI: 10.1038/s43586-022-00184-w.

Greenwald, R. A., K. B. Baker, J. R. Dudeney, M. Pinnock, T. B. Jones, E. C. Thomas, J. .-. Villain, J. .-. Cerisier, C. Senior, C. Hanuise, R. D. Hunsucker, G. Sofko, J. Koehler, E. Nielsen, R. Pellinen, A. D. M. Walker, N. Sato, and H. Yamagishi (1995). "DARN/SuperDARN". In: *Space Science Reviews* 71.1, pp. 761–796. ISSN: 1572-9672. DOI: 10.1007/BF00751350.

Guo, X. C., C. Wang, and Y. Q. Hu (2010). "Global MHD simulation of the Kelvin-Helmholtz instability at the magnetopause for northward interplanetary magnetic field". In: *Journal of Geophysical Research: Space Physics* 115.A10. ISSN: 2156-2202. DOI: 10.1029/2009JA015193.

Gurnett, D. A. and A. Bhattacharjee (2005). *Introduction to plasma physics: with space and laboratory applications*. eng. Cambridge: Cambridge University Press. ISBN: 978-0-511-80912-5. DOI: 10.1017/CBO9780511809125.

Haaland, S., A. Runov, A. Artemyev, and V. Angelopoulos (2019). "Characteristics of the Flank Magnetopause: THEMIS Observations". In: *Journal of Geophysical Research: Space Physics* 124.5, pp. 3421–3435. ISSN: 2169-9402. DOI: 10.1029/2019JA026459.

Haerendel, G., G. Paschmann, N. Sckopke, H. Rosenbauer, and P. C. Hedgecock (1978). "The frontside boundary layer of the magnetosphere and the problem of reconnection". In: *Journal of Geophysical Research: Space Physics* 83.A7, pp. 3195–3216. ISSN: 2156-2202. DOI: 10.1029/JA083iA07p03195.

Harris, C. R., K. J. Millman, S. J. van der Walt, R. Gommers, P. Virtanen, D. Cournapeau, E. Wieser, J. Taylor, S. Berg, N. J. Smith, R. Kern, M. Picus, S. Hoyer, M. H. van Kerkwijk, M. Brett, A. Haldane, J. F. del Río, M. Wiebe, P. Peterson, P. Gérard-Marchant, K. Sheppard, T. Reddy, W. Weckesser, H. Abbasi, C. Gohlke, and T. E. Oliphant (2020). "Array programming with NumPy". In: *Nature* 585.7825, pp. 357–362. ISSN: 1476-4687. DOI: 10.1038/s41586-020-2649-2.

Hasegawa, A. and L. Chen (1974). "Theory of magnetic pulsations". In: *Space Science Reviews* 16.3, pp. 347–359. ISSN: 1572-9672. DOI: 10.1007/BF00171563.

Hasegawa, H., M. Fujimoto, T.-D. Phan, H. Rème, A. Balogh, M. W. Dunlop, C. Hashimoto, and R. TanDokoro (2004a). "Transport of solar wind into Earth's magnetosphere through rolled-up Kelvin–Helmholtz vortices". In: *Nature* 430.7001, pp. 755–758. ISSN: 1476-4687. DOI: 10.1038/nature02799.

Hasegawa, H., M. Fujimoto, Y. Saito, and T. Mukai (2004b). "Dense and stagnant ions in the low-latitude boundary region under northward interplanetary magnetic field". In: *Geophysical Research Letters* 31.6. ISSN: 1944-8007. DOI: 10.1029/2003GL019120.

Hasegawa, H., A. Retinò, A. Vaivads, Y. Khotyaintsev, M. André, T. K. M. Nakamura, W.-L. Teh, B. U. Ö. Sonnerup, S. J. Schwartz, Y. Seki, M. Fujimoto, Y. Saito, H. Rème, and P. Canu (2009). "Kelvin-Helmholtz waves at the Earth's magnetopause: Multiscale development and associated reconnection". In: *Journal of Geophysical Research: Space Physics* 114.A12. ISSN: 2156-2202. DOI: 10.1029/2009JA014042.

Hasegawa, H. (2012). "Structure and Dynamics of the Magnetopause and Its Boundary Layers". In: *Monographs on Environment, Earth and Planets* 1, pp. 71–119. DOI: 10.5047/meep.2012.00102.0071.

Hashimoto, C. and M. Fujimoto (2006). "Kelvin–Helmholtz instability in an unstable layer of finite-thickness". In: *Advances in Space Research*. Boundary Layers, Waves and Non-Linear Dynamical Processes 37.3, pp. 527–531. ISSN: 0273-1177. DOI: 10.1016/j.asr.2005.06.020.

Heerikhuisen, J., E. J. Zirnstein, and N. V. Pogorelov (2024). "Simulating a Steady-state Heliosphere". In: *The Astrophysical Journal Supplement Series* 276.1, p. 13. ISSN: 0067-0049. DOI: 10.3847/1538-4365/ad927a.

Helmholtz (1868). "XLIII. *On discontinuous movements of fluids*". In: *The London, Edinburgh, and Dublin Philosophical Magazine and Journal of Science* 36.244, pp. 337–346. ISSN: 1941-5982, 1941-5990. DOI: 10.1080/14786446808640073.

Helmholtz, H. (1858). "Über Integrale der hydrodynamischen Gleichungen, welche den Wirbelbewegungen entsprechen." In: *Journal für die reine und angewandte Mathematik (Crelles Journal)* 1858.55, pp. 25–55. ISSN: 0075-4102, 1435-5345. DOI: 10.1515/crll.1858.55.25.

Hockney, R. W. and J. W. Eastwood (2021). *Computer Simulation Using Particles*. Boca Raton: CRC Press. ISBN: 978-0-367-80693-4. DOI: 10.1201/9780367806934.

Hollweg, J. V. (1987). "Incompressible magnetohydrodynamic surface waves - Nonlinear aspects". In: *The Astrophysical Journal* 317, p. 918. ISSN: 0004-637X, 1538-4357. DOI: 10.1086/165341.

Hunt, B. J. (2005). *The Maxwellians*. eng. 1. print. Conrnell history of science series. Ithaca, N.Y: Cornell University Press. ISBN: 978-0-8014-8234-2.

Hunt, J. C. R., A. A. Wray, and P. Moin (1988). "Eddies, streams, and convergence zones in turbulent flows". In.

Hwang, K.-J., K. Dokgo, E. Choi, J. L. Burch, D. G. Sibeck, B. L. Giles, H. Hasegawa, H. S. Fu, Y. Liu, Z. Wang, T. K. M. Nakamura, X. Ma, R. C. Fear, Y. Khotyaintsev, D. B. Graham, Q. Q. Shi, C. P. Escoubet, D. J. Gershman, W. R. Paterson, C. J. Pollock, R. E. Ergun, R. B. Torbert, J. C. Dorelli, L. Avanov, C. T. Russell, and R. J. Strangeway (2020). "Magnetic Reconnection Inside a Flux Rope Induced by Kelvin-Helmholtz Vortices". In: *Journal of Geophysical Research: Space Physics* 125.4, e2019JA027665. ISSN: 2169-9402. DOI: 10.1029/2019JA027665.

Hwang, K.-J., M. M. Kuznetsova, F. Sahraoui, M. L. Goldstein, E. Lee, and G. K. Parks (2011). "Kelvin-Helmholtz waves under southward interplanetary magnetic field". In: *Journal of Geophysical Research: Space Physics* 116.A8. ISSN: 2156-2202. DOI: 10.1029/2011JA016596.

Hwang, K.-J. and D. G. Sibeck (2016). "Role of Low-Frequency Boundary Waves in the Dynamics of the Dayside Magnetopause and the Inner Magnetosphere". In: *Low-Frequency Waves in Space Plasmas*. American Geophysical Union (AGU), pp. 213–239. ISBN: 978-1-119-05500-6. DOI: 10.1002/9781119055006.ch13.

Hwang, K.-J., J. M. Weygand, D. G. Sibeck, J. L. Burch, M. L. Goldstein, C. P. Escoubet, E. Choi, K. Dokgo, B. L. Giles, C. J. Pollock, D. J. Gershman, C. T. Russell, R. J. Strangeway, and R. B. Torbert (2022). "Kelvin-Helmholtz Vortices as an Interplay of Magnetosphere-Ionosphere Coupling". In: *Frontiers in Astronomy and Space Sciences* 9. ISSN: 2296-987X.

Hwang, K.-J., C.-P. Wang, K. Nykyri, H. Hasegawa, M. B. Tapley, J. L. Burch, S. A. Fuselier, J. Goldstein, K. Dokgo, T. Nakamura, M. Sitnov, X. Ma, Y. Lin, and X. Wang (2023). "Kelvin-Helmholtz instability-driven

magnetopause dynamics as turbulent pathway for the solar wind-magnetosphere coupling and the flank-central plasma sheet communication". English. In: *Frontiers in Astronomy and Space Sciences* 10. ISSN: 2296-987X. DOI: 10.3389/fspas.2023.1151869.

Ichinaga, S. M., F. Andreuzzi, N. Demo, M. Tezzele, K. Lapo, G. Rozza, S. L. Brunton, and J. N. Kutz (2024). *PyDMD: A Python package for robust dynamic mode decomposition*.

Jacobs, J. A., Y. Kato, S. Matsushita, and V. A. Troitskaya (1964). "Classification of geomagnetic micropulsations". In: *Journal of Geophysical Research (1896-1977)* 69.1, pp. 180–181. ISSN: 2156-2202. DOI: 10.1029/JZ069i001p00180.

Jennings, C. A. (2006). "Radiation transport effects in wire array Z pinches and magnetohydrodynamic modelling techniques". PhD. Imperial College London.

Jeong, J. and F. Hussain (1995). "On the identification of a vortex". English. In: *Journal of Fluid Mechanics* 285, pp. 69–94. ISSN: 0022-1120. DOI: 10.1017/S0022112095000462.

Jolliffe, I. T. and J. Cadima (2016). "Principal component analysis: a review and recent developments". In: *Philosophical Transactions of the Royal Society A: Mathematical, Physical and Engineering Sciences* 374.2065, p. 20150202. DOI: 10.1098/rsta.2015.0202.

Kavosi, S., J. Raeder, J. R. Johnson, K. Nykyri, and C. J. Farrugia (2023). "Seasonal and diurnal variations of Kelvin-Helmholtz Instability at terrestrial magnetopause". In: *Nature Communications* 14.1, p. 2513. ISSN: 2041-1723. DOI: 10.1038/s41467-023-37485-x.

Kavosi, S. and J. Raeder (2015). "Ubiquity of Kelvin–Helmholtz waves at Earth's magnetopause". In: *Nature Communications* 6.1, p. 7019. ISSN: 2041-1723. DOI: 10.1038/ncomms8019.

Kaweeyanun, N., A. Masters, and X. Jia (2021). "Analytical Assessment of Kelvin-Helmholtz Instability Growth at Ganymede's Upstream Magnetopause". In: *Journal of Geophysical Research: Space Physics* 126.8, e2021JA029338. ISSN: 2169-9402. DOI: 10.1029/2021JA029338.

King, A. C., J. Billingham, and S. R. Otto (2003). *Differential Equations: Linear, Nonlinear, Ordinary, Partial*. Cambridge: Cambridge University Press. ISBN: 978-0-521-81658-8. DOI: 10.1017/CBO9780511755293.

Kivelson, M. G. and D. J. Southwood (1988). "Hydromagnetic waves and the ionosphere". In: *Geophysical Research Letters* 15.11, pp. 1271–1274. ISSN: 1944-8007. DOI: 10.1029/GL015i011p01271.

Kivelson, M. G. and S.-H. Chen (1995). "The Magnetopause: Surface Waves and Instabilities and their Possible Dynamical Consequences". In: *Physics of the Magnetopause*. American Geophysical Union (AGU), pp. 257–268. ISBN: 978-1-118-66397-4. DOI: 10.1029/GM090p0257.

Kivelson, M. G. and Z.-Y. Pu (1984). "The Kelvin-Helmholtz instability on the magnetopause". In: *Planetary and Space Science* 32.11, pp. 1335–1341. ISSN: 0032-0633. DOI: 10.1016/0032-0633(84)90077-1.

Kivelson, M. G. and C. T. Russell (1995). *Introduction to space physics*. eng. Cambridge: Cambridge university press. ISBN: 978-0-521-45104-8.

Klein, K. G., H. Spence, O. Alexandrova, M. Argall, L. Arzamasskiy, J. Bookbinder, T. Broeren, D. Caprioli, A. Case, B. Chandran, L.-J. Chen, I. Dors, J. Eastwood, C. Forsyth, A. Galvin, V. Genot, J. Halekas, M. Hesse, B. Hine, T. Horbury, L. Jian, J. Kasper, M. Kretzschmar, M. Kunz, B. Lavraud, O. Le Contel, A. Mallet, B. Maruca, W. Matthaeus, J. Niehof, H. O'Brien, C. Owen, A. Retinò, C. Reynolds, O. Roberts, A. Schekochihin, R. Skoug, C. Smith, S. Smith, J. Steinberg, M. Stevens, A. Szabo, J. TenBarge, R. Torbert, B. Vasquez, D. Verscharen, P. Whittlesey, B. Wickizer, G. Zank, and E. Zweibel (2023). "HelioSwarm: A Multipoint, Multiscale Mission to Characterize Turbulence". In: *Space Science Reviews* 219.8, p. 74. ISSN: 1572-9672. DOI: 10.1007/s11214-023-01019-0.

Koopman, B. O. (1931). "Hamiltonian Systems and Transformations in Hilbert Space". In: *Proceedings of the National Academy of Sciences of the United States of America* 17.5, pp. 315–318. ISSN: 0027-8424.

Kulsrud, R. M. (2001). "Magnetic reconnection: Sweet-Parker versus Petschek". In: *Earth, Planets and Space* 53.6, pp. 417–422. ISSN: 1880-5981. DOI: 10.1186/BF03353251.

Kutz, J. N., S. L. Brunton, B. W. Brunton, and J. L. Proctor (2016). *Dynamic Mode Decomposition: Data-Driven Modeling of Complex Systems*. Philadelphia, PA: Society for Industrial and Applied Mathematics. ISBN: 978-1-61197-449-2 978-1-61197-450-8. DOI: 10.1137/1.9781611974508.

Laitinen, T. V., P. Janhunen, T. I. Pulkkinen, M. Palmroth, and H. E. J. Koskinen (2006). "On the characterization of magnetic reconnection in global MHD simulations". English. In: *Annales Geophysicae* 24.11, pp. 3059–3069. ISSN: 0992-7689. DOI: 10.5194/angeo-24-3059-2006.

Landa, V. and Y. Reuveni (2023). "Assessment of Dynamic Mode Decomposition (DMD) Model for Ionospheric TEC Map Predictions". In: *Remote Sensing* 15.2, p. 365. ISSN: 2072-4292. DOI: 10.3390/rs15020365.

Le, G. and C. T. Russell (1994). "The thickness and structure of high beta magnetopause current layer". In: *Geophysical Research Letters* 21.23, pp. 2451–2454. ISSN: 1944-8007. DOI: 10.1029/94GL02292.

Le, G., J. A. Slavin, and R. J. Strangeway (2010). "Space Technology 5 observations of the imbalance of regions 1 and 2 field-aligned currents and its implication to the cross-polar cap Pedersen currents". In: *Journal of Geophysical Research: Space Physics* 115.A7, 2009JA014979. ISSN: 0148-0227. DOI: 10.1029/2009JA014979.

Lee, L. C., R. K. Albano, and J. R. Kan (1981). "Kelvin-Helmholtz Instability in the magnetopause-boundary layer region". In: *Journal of Geophysical Research: Space Physics* 86.A1, pp. 54–58. ISSN: 2156-2202. DOI: 10.1029/JA086iA01p00054.

Lerche, I. (1966). "Validity of the hydromagnetic approach in discussing instability of the magnetospheric boundary". In: *Journal of Geophysical Research (1896-1977)* 71.9, pp. 2365–2371. ISSN: 2156-2202. DOI: 10.1029/JZ071i009p02365.

Lewis, Z. M., J. A. Wild, M. Allcock, and M.-T. Walach (2022). "Assessing the Impact of Weak and Moderate Geomagnetic Storms on UK Power Station Transformers". In: *Space Weather* 20.4, e2021SW003021. ISSN: 1542-7390. DOI: 10.1029/2021SW003021.

Li, W. Y., X. C. Guo, and C. Wang (2012). "Spatial distribution of Kelvin-Helmholtz instability at low-latitude boundary layer under different solar wind speed conditions". In: *Journal of Geophysical Research: Space Physics* 117.A8. ISSN: 2156-2202. DOI: 10.1029/2012JA017780.

Li, W., C. Wang, B. Tang, X. Guo, and D. Lin (2013). "Global features of Kelvin-Helmholtz waves at the magnetopause for northward interplanetary magnetic field". In: *Journal of Geophysical Research: Space Physics* 118.8, pp. 5118–5126. ISSN: 2169-9380, 2169-9402. DOI: 10.1002/jgra.50498.

Lin, D., C. Wang, W. Li, B. Tang, X. Guo, and Z. Peng (2014). "Properties of Kelvin-Helmholtz waves at the magnetopause under northward interplanetary magnetic field: Statistical study". In: *Journal of Geophysical Research: Space Physics* 119.9, pp. 7485–7494. ISSN: 2169-9402. DOI: 10.1002/2014JA020379.

Lin, R. L., X. X. Zhang, S. Q. Liu, Y. L. Wang, and J. C. Gong (2010). "A three-dimensional asymmetric magnetopause model". In: *Journal of Geophysical Research: Space Physics* 115.A4. ISSN: 2156-2202. DOI: 10.1029/2009JA014235.

Liu, C., Y.-s. Gao, X.-r. Dong, Y.-q. Wang, J.-m. Liu, Y.-n. Zhang, X.-s. Cai, and N. Gui (2019). "Third generation of vortex identification methods: Omega and Liutex/Rortex based systems". In: *Journal of Hydrodynamics* 31.2, pp. 205–223. ISSN: 1878-0342. DOI: 10.1007/s42241-019-0022-4.

Loto'aniu, P. T. M. and F. Inceoglu (2024). "The Distribution of Pc5 Ultralow-frequency Waves at Geostationary Orbit". In: *The Astrophysical Journal* 969.2, p. 91. ISSN: 0004-637X. DOI: 10.3847/1538-4357/ad41dd.

Lyon, J. G., J. A. Fedder, and C. M. Mobarry (2004). "The Lyon–Fedder–Mobarry (LFM) global MHD magnetospheric simulation code". In: *Journal of Atmospheric and Solar-Terrestrial Physics*. Towards an Integrated Model of the Space Weather System 66.15, pp. 1333–1350. ISSN: 1364-6826. DOI: 10.1016/j.jastp.2004.03.020.

Ma, X., P. Delamere, K. Nykyri, B. Burkholder, S. Eriksson, and Y.-L. Liou (2021). "Ion Dynamics in the Meso-scale 3-D Kelvin-Helmholtz Instability: Perspectives From Test Particle Simulations". In: *Frontiers in Astronomy and Space Sciences* 8, p. 758442. ISSN: 2296-987X. DOI: 10.3389/fspas.2021.758442.

Ma, X., P. Delamere, K. Nykyri, A. Otto, S. Eriksson, L. Chai, B. Burkholder, A. Dimmock, Y.-L. Liou, and S. Kavosi (2024). "Density and Magnetic Field Asymmetric Kelvin-Helmholtz Instability". In: *Journal of Geophysical Research: Space Physics* 129.3, e2023JA032234. ISSN: 2169-9402. DOI: 10.1029/2023JA032234.

Ma, X., P. Delamere, A. Otto, and B. Burkholder (2017). "Plasma transport driven by the three-dimensional Kelvin-Helmholtz instability". In: *Journal of Geophysical Research: Space Physics* 122.10, pp. 10, 382–10, 395. DOI: https://doi.org/10.1002/2017JA024394.

Ma, X., P. A. Delamere, K. Nykyri, B. Burkholder, B. Neupane, and R. C. Rice (2019). "Comparison Between Fluid Simulation With Test Particles and Hybrid Simulation for the Kelvin-Helmholtz Instability". In: *Journal of Geophysical Research: Space Physics* 124.8, pp. 6654–6668. ISSN: 2169-9402. DOI: 10.1029/2019JA026890.

Ma, X., K. Nykyri, A. Dimmock, and C. Chu (2020). "Statistical Study of Solar Wind, Magnetosheath, and Magnetotail Plasma and Field Properties: 12+ Years of THEMIS Observations and MHD Simulations". In: *Journal of Geophysical Research: Space Physics* 125.10, e2020JA028209. ISSN: 2169-9402. DOI: 10.1029/2020JA028209.

Ma, X., A. Otto, and P. A. Delamere (2014a). "Interaction of magnetic reconnection and Kelvin-Helmholtz modes for large magnetic shear: 1. Kelvin-Helmholtz trigger". In: *Journal of Geophysical Research: Space Physics* 119.2, pp. 781–797. ISSN: 2169-9380.

Ma, X., A. Otto, and P. A. Delamere (2014b). "Interaction of magnetic reconnection and kelvin-helmholtz modes for large magnetic shear: 2. Reconnection trigger". In: *Journal of Geophysical Research: Space Physics* 119.2, pp. 808–820. ISSN: 2169-9380.

Mann, I. R., I. Voronkov, M. Dunlop, E. Donovan, T. K. Yeoman, D. K. Milling, J. Wild, K. Kauristie, O. Amm, S. D. Bale, A. Balogh, A. Viljanen, and H. J. Opgenoorth (2002). "Coordinated ground-based and Cluster observations of large amplitude global magnetospheric oscillations during a fast solar wind speed interval". English. In: *Annales Geophysicae* 20.4, pp. 405–426. ISSN: 0992-7689. DOI: 10.5194/angeo-20-405-2002.

Manuel, J. R. and J. C. Samson (1993). "The spatial development of the low-latitude boundary layer". In: *Journal of Geophysical Research: Space Physics* 98.A10, pp. 17367–17385. ISSN: 2156-2202. DOI: 10.1029/93JA01524.

Masters, A. (2018). "A More Viscous-Like Solar Wind Interaction With All the Giant Planets". In: *Geophysical Research Letters* 45.15, pp. 7320–7329. ISSN: 1944-8007. DOI: 10.1029/2018GL078416.

Masters, A., N. Achilleos, J. C. Cutler, A. J. Coates, M. K. Dougherty, and G. H. Jones (2012). "Surface waves on Saturn's magnetopause". In: *Planetary and Space Science* 65.1, pp. 109–121. ISSN: 0032-0633. DOI: 10.1016/j.pss.2012.02.007.

Matsumoto, Y. and M. Hoshino (2004). "Onset of turbulence induced by a Kelvin-Helmholtz vortex". In: *Geophysical Research Letters* 31.2. ISSN: 1944-8007. DOI: 10.1029/2003GL018195.

Maxwell, J. (2010). "On physical lines of force". In: *Philosophical Magazine* 90.sup1, pp. 11–23. ISSN: 1478-6435, 1478-6443. DOI: 10.1080/14786431003659180.

Mejnertsen, L. (2018). "The Dynamics of the Outer Boundaries in Global Simulations of Planetary Magnetospheres". English. phd. London: Imperial College London.

Mejnertsen, L., J. P. Eastwood, J. P. Chittenden, and A. Masters (2016). "Global MHD simulations of Neptune's magnetosphere". In: *Journal of Geophysical Research: Space Physics* 121.8, pp. 7497–7513. ISSN: 2169-9402. DOI: 10.1002/2015JA022272.

Mejnertsen, L., J. P. Eastwood, H. Hietala, S. J. Schwartz, and J. P. Chittenden (2018). "Global MHD Simulations of the Earth's Bow Shock Shape and Motion Under Variable Solar Wind Conditions". In: *Journal of Geophysical Research: Space Physics* 123.1, pp. 259–271. ISSN: 2169-9402. DOI: 10.1002/2017JA024690.

Mejnertsen, L., J. P. Eastwood, and J. P. Chittenden (2021). "Control of Magnetopause Flux Rope Topology by Non-local Reconnection". English. In: *Frontiers in Astronomy and Space Sciences* 8. ISSN: 2296-987X. DOI: 10.3389/fspas.2021.758312.

Merkin, V. G. and J. G. Lyon (2010). "Effects of the low-latitude ionospheric boundary condition on the global magnetosphere". In: *Journal of Geophysical Research: Space Physics* 115.A10. ISSN: 2156-2202. DOI: 10.1029/2010JA015461.

Merkin, V. G., J. G. Lyon, and S. G. Claudepierre (2013). "Kelvin-Helmholtz instability of the magnetospheric boundary in a three-dimensional global MHD simulation during northward IMF conditions". In: *Journal of Geophysical Research: Space Physics* 118.9, pp. 5478–5496. ISSN: 2169-9402. DOI: 10.1002/jgra.50520.

Michael, A. T., K. A. Sorathia, V. G. Merkin, K. Nykyri, B. Burkholder, X. Ma, A. Y. Ukhorskiy, and J. Garretson (2021). "Modeling Kelvin-Helmholtz Instability at the High-Latitude Boundary Layer in a Global Magnetosphere Simulation". In: *Geophysical Research Letters* 48.19, e2021GL094002. ISSN: 1944-8007. DOI: 10.1029/2021GL094002.

Mills, K. J., A. W. Longbottom, A. N. Wright, and M. S. Ruderman (2000). "Kelvin-Helmholtz instability on the magnetospheric flanks: An absolute and convective instability approach". In: *Journal of Geophysical Research: Space Physics* 105.A12, pp. 27685–27699. ISSN: 2156-2202. DOI: 10.1029/1999JA000289.

Mitchell, D. G., F. Kutchko, D. J. Williams, T. E. Eastman, L. A. Frank, and C. T. Russell (1987). "An extended study of the low-latitude boundary layer on the dawn and dusk flanks of the magnetosphere". In: *Journal of Geophysical Research: Space Physics* 92.A7, pp. 7394–7404. ISSN: 2156-2202. DOI: 10.1029/JA092iA07p07394.

Miura, A. (1987). "Simulation of Kelvin-Helmholtz instability at the magnetospheric boundary". In: *Journal of Geophysical Research: Space Physics* 92.A4, pp. 3195–3206. ISSN: 2156-2202. DOI: 10.1029/JA092iA04p03195.

Miura, A. (1990). "Kelvin-Helmholtz instability for supersonic shear flow at the magnetospheric boundary". In: *Geophysical Research Letters* 17.6, pp. 749–752. ISSN: 1944-8007. DOI: 10.1029/GL017i006p00749.

Miura, A. (1992). "Kelvin-Helmholtz instability at the magnetospheric boundary: Dependence on the magnetosheath sonic Mach number". In: *Journal of Geophysical Research: Space Physics* 97.A7, pp. 10655–10675. ISSN: 2156-2202. DOI: 10.1029/92JA00791.

Miura, A. (1999a). "A quantitative test of the self-organization hypothesis of the magnetopause Kelvin-Helmholtz instability as an inverse problem". In: *Geophysical Research Letters* 26.3, pp. 409–412. ISSN: 1944-8007. DOI: 10.1029/1998GL900300.

Miura, A. (1999b). "Self-organization in the two-dimensional magnetohydrodynamic transverse Kelvin-Helmholtz instability". In: *Journal of Geophysical Research: Space Physics* 104.A1, pp. 395–411. ISSN: 2156-2202. DOI: 10.1029/98JA02530.

Miura, A. and J. R. Kan (1992). "Line-tying effects on the Kelvin-Helmholttz instability". In: *Geophysical Research Letters* 19.15, pp. 1611–1614. ISSN: 1944-8007. DOI: 10.1029/92GL01448.

Miura, A. and P. L. Pritchett (1982). "Nonlocal stability analysis of the MHD Kelvin-Helmholtz instability in a compressible plasma". In: *Journal of Geophysical Research: Space Physics* 87.A9, pp. 7431–7444. ISSN: 2156-2202. DOI: 10.1029/JA087iA09p07431.

Montgomery, J., R. W. Ebert, F. Allegrini, F. Bagenal, S. J. Bolton, G. A. DiBraccio, S. A. Fuselier, R. J. Wilson, and A. Masters (2023). "Investigating the Occurrence of Kelvin-Helmholtz Instabilities at Jupiter's Dawn Magnetopause". In: *Geophysical Research Letters* 50.14, e2023GL102921. ISSN: 1944-8007. DOI: 10.1029/2023GL102921.

Moore, E. H. (1920). "The fourteenth western meeting of the American Mathematical Society". In: *Bulletin of the American Mathematical Society* 26.9, pp. 385–396. ISSN: 0002-9904, 1936-881X.

Müller, D., O. C. S. Cyr, I. Zouganelis, H. R. Gilbert, R. Marsden, T. Nieves-Chinchilla, E. Antonucci, F. Auchère, D. Berghmans, T. S. Horbury, R. A. Howard, S. Krucker, M. Maksimovic, C. J. Owen, P. Rochus, J. Rodriguez-Pacheco, M. Romoli, S. K. Solanki, R. Bruno, M. Carlsson, A. Fludra, L. Harra, D. M. Hassler, S. Livi, P. Louarn, H. Peter, U. Schühle, L. Teriaca, J. C. d. T. Iniesta, R. F. Wimmer-Schweingruber, E. Marsch, M. Velli, A. D. Groof, A. Walsh, and D. Williams (2020). "The Solar Orbiter mission - Science overview". In: *Astronomy & Astrophysics* 642, A1. ISSN: 0004-6361, 1432-0746. DOI: 10.1051/0004-6361/202038467.

Nagano, H. (1979). "Effect of finite ion larmor radius on the Kelvin-Helmholtz instability of the magnetopause". In: *Planetary and Space Science* 27.6, pp. 881–884. ISSN: 0032-0633. DOI: 10.1016/0032-0633(79)90013-8.

Nakamura, T. K. M., K. A. Blasl, H. Hasegawa, T. Umeda, Y.-H. Liu, S. A. Peery, F. Plaschke, R. Nakamura, J. C. Holmes, J. E. Stawarz, and W. D. Nystrom (2022). "Multi-scale evolution of Kelvin–Helmholtz waves at the Earth's magnetopause during southward IMF periods". In: *Physics of Plasmas* 29.1, p. 012901. ISSN: 1070-664X. DOI: 10.1063/5.0067391.

Nakamura, T. K. M., W. Daughton, H. Karimabadi, and S. Eriksson (2013). "Three-dimensional dynamics of vortex-induced reconnection and comparison with THEMIS observations". In: *Journal of Geophysical Research: Space Physics* 118.9, pp. 5742–5757. ISSN: 2169-9402. DOI: 10.1002/jgra.50547.

Nakamura, T. K. M., S. Eriksson, H. Hasegawa, S. Zenitani, W. Y. Li, K. J. Genestreti, R. Nakamura, and W. Daughton (2017). "Mass and Energy Transfer Across the Earth's Magnetopause Caused by Vortex-Induced Reconnection". In: *Journal of Geophysical Research: Space Physics* 122.11, pp. 11, 505–11, 522. ISSN: 2169-9402. DOI: 10.1002/2017JA024346.

Nakamura, T. K. M., M. Fujimoto, and A. Otto (2008). "Structure of an MHD-scale Kelvin-Helmholtz vortex: Two-dimensional two-fluid simulations including finite electron inertial effects". In: *Journal of Geophysical Research: Space Physics* 113.A9, 2007JA012803. ISSN: 0148-0227. DOI: 10.1029/2007JA012803.

Nakamura, T. K. M., F. Plaschke, H. Hasegawa, Y.-H. Liu, K.-J. Hwang, K. A. Blasl, and R. Nakamura (2020). "Decay of Kelvin-Helmholtz Vortices at the Earth's Magnetopause Under Pure Southward IMF Conditions". In: *Geophysical Research Letters* 47.13, e2020GL087574. ISSN: 1944-8007. DOI: 10.1029/2020GL087574.

Nakamura, T. K. M. (2021). "The Earth's Low-Latitude Boundary Layer". In: *Magnetospheres in the Solar System*. American Geophysical Union (AGU), pp. 177–191. ISBN: 978-1-119-81562-4. DOI: 10.1002/9781119815624.ch12.

Neumann, J. v. (1932). "Proof of the Quasi-Ergodic Hypothesis". In: *Proceedings of the National Academy of Sciences* 18.1, pp. 70–82. DOI: 10.1073/pnas.18.1.70.

Nykyri, K. and A. Otto (2001). "Plasma transport at the magnetospheric boundary due to reconnection in Kelvin-Helmholtz vortices". In: *Geophysical Research Letters* 28.18, pp. 3565–3568. ISSN: 1944-8007. DOI: 10.1029/2001GL013239.

Nykyri, K. and C. Foullon (2013). "First magnetic seismology of the CME reconnection outflow layer in the low corona with 2.5-D MHD simulations of the Kelvin-Helmholtz instability". In: *Geophysical Research Letters* 40.16, pp. 4154–4159. ISSN: 1944-8007. DOI: 10.1002/grl.50807.

Nykyri, K., X. Ma, A. Dimmock, C. Foullon, A. Otto, and A. Osmane (2017). "Influence of velocity fluctuations on the Kelvin-Helmholtz instability and its associated mass transport". In: *Journal of Geophysical Research: Space Physics* 122.9, pp. 9489–9512. ISSN: 2169-9402. DOI: 10.1002/2017JA024374.

Ong, R. S. B. and N. Roderick (1972). "On the kelvin-Helmholtz instability of the Earth's magnetopause". In: *Planetary and Space Science* 20.1, pp. 1–10. ISSN: 0032-0633. DOI: 10.1016/0032-0633(72)90135-3.

Otto, A. (1990). "3D resistive MHD computations of magnetospheric physics". In: *Computer Physics Communications* 59, pp. 185–195. DOI: 10.1016/0010-4655(90)90168-Z.

Otto, A. and D. H. Fairfield (2000). "Kelvin-Helmholtz instability at the magnetotail boundary: MHD simulation and comparison with Geotail observations". In: *Journal of Geophysical Research: Space Physics* 105.A9, pp. 21175–21190. ISSN: 2156-2202. DOI: 10.1029/1999JA000312.

Palermo, F., M. Faganello, F. Califano, F. Pegoraro, and O. Le Contel (2011). "Compressible Kelvin-Helmholtz instability in supermagnetosonic regimes". In: *Journal of Geophysical Research: Space Physics* 116.A4. ISSN: 2156-2202. DOI: 10.1029/2010JA016400.

Paral, J. and R. Rankin (2013). "Dawn–dusk asymmetry in the Kelvin–Helmholtz instability at Mercury". In: *Nature Communications* 4.1, p. 1645. ISSN: 2041-1723. DOI: 10.1038/ncomms2676.

Parker, E. N. (1958). "Dynamics of the Interplanetary Gas and Magnetic Fields." In: *The Astrophysical Journal* 128, p. 664. ISSN: 0004-637X. DOI: 10.1086/146579.

Paschmann, G. and P. W. Daly (1998). "Analysis Methods for Multi-Spacecraft Data. ISSI Scientific Reports Series SR-001, ESA/ISSI, Vol. 1. ISBN 1608-280X, 1998". In: *ISSI Scientific Reports Series* 1.

Penrose, R. (1955). "A generalized inverse for matrices". In: *Mathematical Proceedings of the Cambridge Philosophical Society* 51.3, pp. 406–413. ISSN: 1469-8064, 0305-0041. DOI: 10.1017/S0305004100030401.

Pérez-Coll Jiménez, J., P. Tenfjord, M. Hesse, C. Norgren, N. Kwagala, H. M. Kolstø, and S. F. Spinnangr (2022). "The Role of Resistivity on the Efficiency of Magnetic Reconnection in MHD". In: *Journal of Geophysical Research: Space Physics* 127.6, e2021JA030134. ISSN: 2169-9402. DOI: 10.1029/2021JA030134.

Phan, T., H. U. Frey, S. Frey, L. Peticolas, S. Fuselier, C. Carlson, H. Rème, J.-M. Bosqued, A. Balogh, M. Dunlop, L. Kistler, C. Mouikis, I. Dandouras, J.-A. Sauvaud, S. Mende, J. McFadden, G. Parks, E. Moebius, B. Klecker, G. Paschmann, M. Fujimoto, S. Petrinec, M. F. Marcucci, A. Korth, and R. Lundin (2003). "Simultaneous Cluster and IMAGE observations of cusp reconnection and auroral proton spot for northward IMF". In: *Geophysical Research Letters* 30.10. ISSN: 1944-8007. DOI: 10.1029/2003GL016885.

Pierce, B., P. Moin, and T. Sayadi (2013). "Application of vortex identification schemes to direct numerical simulation data of a transitional boundary layer". In: *Physics of Fluids* 25.1, p. 015102. ISSN: 1070-6631. DOI: 10.1063/1.4774340.

Pilipenko, V. A., N. G. Mazur, E. N. Fedorov, M. J. Engebretson, and D. L. Murr (2005). "Alfven wave reflection in a curvilinear magnetic field and formation of Alfvenic resonators on open field lines". In: *Journal of Geophysical Research: Space Physics* 110.A10. ISSN: 2156-2202. DOI: 10.1029/2004JA010755.

Pitout, F. and Y. V. Bogdanova (2021). "The Polar Cusp Seen by Cluster". In: *Journal of Geophysical Research: Space Physics* 126.9, e2021JA029582. ISSN: 2169-9402. DOI: 10.1029/2021JA029582.

Plaschke, F. (2016). "ULF Waves at the Magnetopause". In: *Low-Frequency Waves in Space Plasmas*. American Geophysical Union (AGU), pp. 193–212. ISBN: 978-1-119-05500-6. DOI: 10.1002/9781119055006.ch12.

Plaschke, F. and K.-H. Glassmeier (2011). "Properties of standing Kruskal-Schwarzschild-modes at the magnetopause". English. In: *Annales Geophysicae* 29.10, pp. 1793–1807. ISSN: 0992-7689. DOI: 10.5194/angeo-29-1793-2011.

Plaschke, F., N. Kahr, D. Fischer, R. Nakamura, W. Baumjohann, W. Magnes, J. L. Burch, R. B. Torbert, C. T. Russell, B. L. Giles, R. J. Strangeway, H. K. Leinweber, K. R. Bromund, B. J. Anderson, G. Le, M. Chutter, J. A. Slavin, and E. L. Kepko (2016). "Steepening of waves at the duskside magnetopause". In: *Geophysical Research Letters* 43.14, pp. 7373–7380. ISSN: 1944-8007. DOI: 10.1002/2016GL070003.

Plaschke, F., M. G. G. T. Taylor, and R. Nakamura (2014). "Alternative interpretation of results from Kelvin-Helmholtz vortex identification criteria". In: *Geophysical Research Letters* 41.2, pp. 244–250. ISSN: 1944-8007. DOI: 10.1002/2013GL058948.

Pontin, D. I. and E. R. Priest (2022). "Magnetic reconnection: MHD theory and modelling". In: *Living Reviews in Solar Physics* 19.1, p. 1. ISSN: 1614-4961. DOI: 10.1007/s41116-022-00032-9.

Poynting Henry, J. (1884). "XV. On the transfer of energy in the electromagnetic field". In: *Philosophical Transactions of the Royal Society of London* 175, pp. 343–361. ISSN: 0261-0523, 2053-9223. DOI: 10.1098/rstl.1884.0016.

Pu, Z.-Y. and M. G. Kivelson (1980). "The Kelvin-Helmholtz instability at the magnetopause (abstract)". In: *Eos Trans, AGU, 61, 1086*.

Pu, Z.-Y. and M. G. Kivelson (1983). "Kelvin:Helmholtz Instability at the magnetopause: Solution for compressible plasmas". In: *Journal of Geophysical Research: Space Physics* 88.A2, pp. 841–852. ISSN: 2156-2202. DOI: 10.1029/JA088iA02p00841.

Pu, Z.-Y., M. Yei, and Z. X. Liu (1990). "Generation of vortex-induced tearing mode instability at the magnetopause". In: *Journal of Geophysical Research: Space Physics* 95.A7, pp. 10559–10566. ISSN: 2156-2202. DOI: 10.1029/JA095iA07p10559.

Rezeau, L., A. Morane, S. Perraut, A. Roux, and R. Schmidt (1989). "Characterization of Alfvenic fluctuations in the magnetopause boundary layer". In: *Journal of Geophysical Research: Space Physics* 94.A1, pp. 101–110. ISSN: 0148-0227. DOI: 10.1029/JA094iA01p00101.

Rice, R. C., K. A. Blasl, K. Nykyri, S. Kavosi, K. A. Sorathia, and Y.-L. Liou (2024). "Multi-scale processes of the Kelvin-Helmholtz instability at Earth's magnetopause". English. In: *Frontiers in Astronomy and Space Sciences* 11. ISSN: 2296-987X. DOI: 10.3389/fspas.2024.1464010.

Rice, R. C., K. Nykyri, X. Ma, and B. L. Burkholder (2022). "Characteristics of Kelvin–Helmholtz Waves as Observed by the MMS From September 2015 to March 2020". In: *Journal of Geophysical Research: Space Physics* 127.3, e2021JA029685. ISSN: 2169-9402. DOI: 10.1029/2021JA029685.

Rot, M., M. Horvat, and G. Kosec (2022). *Dynamic mode decomposition as an analysis tool for time-dependent partial differential equations*.

Ruhunusiri, S., J. S. Halekas, J. P. McFadden, J. E. P. Connerney, J. R. Espley, Y. Harada, R. Livi, K. Seki, C. Mazelle, D. Brain, T. Hara, G. A. DiBraccio, D. E. Larson, D. L. Mitchell, B. M. Jakosky, and H. Hasegawa (2016). "MAVEN observations of partially developed Kelvin-Helmholtz vortices at Mars". In: *Geophysical Research Letters* 43.10, pp. 4763–4773. ISSN: 1944-8007. DOI: 10.1002/2016GL068926.

Samson, J. C., J. A. Jacobs, and G. Rostoker (1971). "Latitude-dependent characteristics of long-period geomagnetic micropulsations". In: *Journal of Geophysical Research (1896-1977)* 76.16, pp. 3675–3683. ISSN: 2156-2202. DOI: 10.1029/JA076i016p03675.

Schmid, P. and J. Sesterhenn (2008). "Dynamic Mode Decomposition of numerical and experimental data". In: 61, MR.007.

Schmid, P. J. (2010). "Dynamic mode decomposition of numerical and experimental data". In: *Journal of Fluid Mechanics* 656, pp. 5–28. ISSN: 0022-1120, 1469-7645. DOI: 10.1017/S0022112010001217.

Schmid, P. J. (2022). "Dynamic Mode Decomposition and Its Variants". In: *Annual Review of Fluid Mechanics* 54.Volume 54, 2022, pp. 225–254. ISSN: 0066-4189, 1545-4479. DOI: 10.1146/annurev-fluid-030121-015835.

Sen, A. K. (1965). "Stability of the magnetospheric boundary". In: *Planetary and Space Science* 13.2, pp. 131–141. ISSN: 0032-0633. DOI: 10.1016/0032-0633(65)90182-0.

Settino, A., D. Perrone, Y. V. Khotyaintsev, D. B. Graham, and F. Valentini (2021). "Kinetic Features for the Identification of Kelvin–Helmholtz Vortices in In Situ Observations". In: *The Astrophysical Journal* 912.2, p. 154. ISSN: 0004-637X. DOI: 10.3847/1538-4357/abf1f5.

Shiraishi, Y., Y. Kawahara, O. Yamashita, R. Fukuma, S. Yamamoto, Y. Saitoh, H. Kishima, and T. Yanagisawa (2020). "Neural decoding of electrocorticographic signals using dynamic mode decomposition". In: *Journal of Neural Engineering* 17.3, p. 036009. ISSN: 1741-2552. DOI: 10.1088/1741-2552/ab8910.

Shue, J.-H., J. K. Chao, H. C. Fu, C. T. Russell, P. Song, K. K. Khurana, and H. J. Singer (1997). "A new functional form to study the solar wind control of the magnetopause size and shape". In: *Journal of Geophysical Research: Space Physics* 102.A5, pp. 9497–9511. ISSN: 2156-2202. DOI: 10.1029/97JA00196.

Shue, J.-H., P. Song, C. T. Russell, J. T. Steinberg, J. K. Chao, G. Zastenker, O. L. Vaisberg, S. Kokubun, H. J. Singer, T. R. Detman, and H. Kawano (1998). "Magnetopause location under extreme solar wind conditions". In: *Journal of Geophysical Research: Space Physics* 103.A8, pp. 17691–17700. ISSN: 2156-2202. DOI: 10.1029/98JA01103.

Sibeck, D. (1990). "A model for the transient magnetospheric response to sudden solar wind dynamic pressure variations". In: *Journal of Geophysical Research: Space Physics* 95.A4, pp. 3755–3771. ISSN: 2156-2202. DOI: 10.1029/JA095iA04p03755.

Singer, H. J., D. J. Southwood, R. J. Walker, and M. G. Kivelson (1981). "Alfven wave resonances in a realistic magnetospheric magnetic field geometry". In: *Journal of Geophysical Research: Space Physics* 86.A6, pp. 4589–4596. ISSN: 2156-2202. DOI: 10.1029/JA086iA06p04589.

Sisti, M., M. Faganello, F. Califano, and B. Lavraud (2019). "Satellite Data-Based 3-D Simulation of Kelvin-Helmholtz Instability and Induced Magnetic Reconnection at the Earth's Magnetopause". In: *Geophysical Research Letters* 46.21, pp. 11597–11605. ISSN: 1944-8007. DOI: 10.1029/2019GL083282.

Song, P., C. T. Russell, R. J. Fitzenreiter, J. T. Gosling, M. F. Thomsen, D. G. Mitchell, S. A. Fuselier, G. K. Parks, R. R. Anderson, and D. Hubert (1993). "Structure and properties of the subsolar magnetopause for northward interplanetary magnetic field: Multiple-instrument particle observations". In: *Journal of Geophysical Research: Space Physics* 98.A7, pp. 11319–11337. ISSN: 2156-2202. DOI: 10.1029/93JA00606.

Song, P., R. C. Elphic, and C. T. Russell (1988). "ISEE 1 & 2 observations of the oscillating magnetopause". In: *Geophysical Research Letters* 15.8, pp. 744–747. ISSN: 1944-8007. DOI: 10.1029/GL015i008p00744.

Sonnerup, B. U. Ö., G. Paschmann, I. Papamastorakis, N. Sckopke, G. Haerendel, S. J. Bame, J. R. Asbridge, J. T. Gosling, and C. T. Russell (1981). "Evidence for magnetic field reconnection at the Earth's magnetopause". In: *Journal of Geophysical Research: Space Physics* 86.A12, pp. 10049–10067. ISSN: 2156-2202. DOI: 10.1029/JA086iA12p10049.

Southwood, D. J. (1968). "The hydromagnetic stability of the magnetospheric boundary". In: *Planetary and Space Science* 16.5, pp. 587–605. ISSN: 0032-0633. DOI: 10.1016/0032-0633(68)90100-1.

Southwood, D. J. (1974). "Some features of field line resonances in the magnetosphere". In: *Planetary and Space Science* 22.3, pp. 483–491. ISSN: 0032-0633. DOI: 10.1016/0032-0633(74)90078-6.

Southwood, D. J. and M. G. Kivelson (1981). "Charged particle behavior in low-frequency geomagnetic pulsations 1. Transverse waves". In: *Journal of Geophysical Research: Space Physics* 86.A7, pp. 5643–5655. ISSN: 2156-2202. DOI: 10.1029/JA086iA07p05643.

Southwood, D. J. and M. G. Kivelson (1984). "Relations between polarization and the structure of ULF waves in the magnetosphere". In: *Journal of Geophysical Research: Space Physics* 89.A7, pp. 5523–5529. ISSN: 2156-2202. DOI: 10.1029/JA089iA07p05523.

Spreiter, J. R., A. L. Summers, and A. Y. Alksne (1966). "Hydromagnetic flow around the magnetosphere". In: *Planetary and Space Science* 14.3, pp. 223–253. ISSN: 0032-0633. DOI: 10.1016/0032-0633(66)90124-3.

Stawarz, J. E., S. Eriksson, F. D. Wilder, R. E. Ergun, S. J. Schwartz, A. Pouquet, J. L. Burch, B. L. Giles, Y. Khotyaintsev, O. L. Contel, P.-A. Lindqvist, W. Magnes, C. J. Pollock, C. T. Russell, R. J. Strangeway, R. B. Torbert, L. A. Avanov, J. C. Dorelli, J. P. Eastwood, D. J. Gershman, K. A. Goodrich, D. M. Malaspina, G. T. Marklund, L. Mirioni, and A. P. Sturner (2016). "Observations of turbulence in a Kelvin-Helmholtz event on 8 September 2015 by the Magnetospheric Multiscale mission". In: *Journal of Geophysical Research: Space Physics* 121.11, pp. 11, 021–11, 034. ISSN: 2169-9402. DOI: 10.1002/2016JA023458.

"On the Dynamical Theory of Diffraction" (2009a). In: *Mathematical and Physical Papers*. Ed. by G. G. Stokes. Vol. 2. Cambridge Library Collection - Mathematics. Cambridge: Cambridge University Press, pp. 243–328. ISBN: 978-1-108-00263-9. DOI: 10.1017/CBO9780511702259.015.

"On the Theories of the Internal Friction of Fluids in Motion, and of the Equilibrium and Motion of Elastic Solids" (2009b). In: *Mathematical and Physical Papers*. Ed. by G. G. Stokes. Vol. 1. Cambridge Library Collection - Mathematics. Cambridge: Cambridge University Press, pp. 75–129. ISBN: 978-1-108-00262-2. DOI: 10.1017/CBO9780511702242.005.

Sundberg, T., S. A. Boardsen, J. A. Slavin, L. G. Blomberg, and H. Korth (2010). "The Kelvin–Helmholtz instability at Mercury: An assessment". In: *Planetary and Space Science* 58.11, pp. 1434–1441. ISSN: 0032-0633. DOI: 10.1016/j.pss.2010.06.008.

Takagi, K., C. Hashimoto, H. Hasegawa, M. Fujimoto, and R. TanDokoro (2006). "Kelvin-Helmholtz instability in a magnetotail flank-like geometry: Three-dimensional MHD simulations". In: *Journal of Geophysical Research: Space Physics* 111.A8. ISSN: 2156-2202. DOI: 10.1029/2006JA011631.

Takahashi, K. (1998). "ULF waves: 1997 IAGA division 3 reporter review". English. In: *Annales Geophysicae* 16.7, pp. 787–803. ISSN: 0992-7689. DOI: 10.1007/s00585-998-0787-1.

Tanaka, T. (1994). "Finite Volume TVD Scheme on an Unstructured Grid System for Three-Dimensional MHD Simulation of Inhomogeneous Systems Including Strong Background Potential Fields". In: *Journal of Computational Physics* 111.2, pp. 381–389. ISSN: 0021-9991. DOI: 10.1006/jcph.1994.1071.

Terasawa, T., M. Fujimoto, T. Mukai, I. Shinohara, Y. Saito, T. Yamamoto, S. Machida, S. Kokubun, A. J. Lazarus, J. T. Steinberg, and R. P. Lepping (1997). "Solar wind control of density and temperature in the near-Earth plasma sheet: WIND/GEOTAIL collaboration". In: *Geophysical Research Letters* 24.8, pp. 935–938. ISSN: 1944-8007. DOI: 10.1029/96GL04018.

Thomson, W. (1871). "XLVI. *Hydrokinetic solutions and observations*". In: *The London, Edinburgh, and Dublin Philosophical Magazine and Journal of Science* 42.281, pp. 362–377. ISSN: 1941-5982, 1941-5990. DOI: 10.1080/14786447108640585.

Tkachenko, O., J. Šafránková, Z. Němeček, J. Šimůnek, and L. Přech (2008). "Observations of vortex-like structure in the cusp-magnetosheath region during northward IMF orientation". English. In: *Annales Geophysicae* 26.11, pp. 3375–3387. ISSN: 0992-7689. DOI: 10.5194/angeo-26-3375-2008.

Tóth, G., I. V. Sokolov, T. I. Gombosi, D. R. Chesney, C. R. Clauer, D. L. De Zeeuw, K. C. Hansen, K. J. Kane, W. B. Manchester, R. C. Oehmke, K. G. Powell, A. J. Ridley, I. I. Roussev, Q. F. Stout, O. Volberg, R. A. Wolf, S. Sazykin, A. Chan, B. Yu, and J. Kóta (2005). "Space Weather Modeling Framework: A new tool for the space science community". In: *Journal of Geophysical Research: Space Physics* 110.A12. ISSN: 2156-2202. DOI: 10.1029/2005JA011126.

Trefethen, L. N. and D. Bau (1997). *Numerical linear algebra*. Philadelphia: Society for Industrial and Applied Mathematics. ISBN: 978-0-89871-361-9.

Treumann, R. A. and W. Baumjohann (2001). *Advanced space plasma physics*. eng. Reprinted. London: Imperial College Press. ISBN: 978-1-86094-026-2.

Tsurutani, B. T. and R. M. Thorne (1982). "Diffusion processes in the magnetopause boundary layer". In: *Geophysical Research Letters* 9.11, pp. 1247–1250. ISSN: 1944-8007. DOI: 10.1029/GL009i011p01247.

Tu, J. H., C. W. Rowley, D. M. Luchtenburg, S. L. Brunton, and J. N. Kutz (2014). "On dynamic mode decomposition: Theory and applications". In: *Journal of Computational Dynamics* 1.2, pp. 391–421. ISSN: 2158-2491. DOI: 10.3934/jcd.2014.1.391.

Turkakin, H., R. Rankin, and I. R. Mann (2013). "Primary and secondary compressible Kelvin-Helmholtz surface wave instabilities on the Earth's magnetopause". In: *Journal of Geophysical Research: Space Physics* 118.7, pp. 4161–4175. ISSN: 2169-9402. DOI: 10.1002/jgra.50394.

Uberoi, C. (1989). "Resonant absorption of Alfvén compressional surface waves". In: *Journal of Geophysical Research: Space Physics* 94.A6, pp. 6941–6944. ISSN: 0148-0227. DOI: 10.1029/JA094iA06p06941.

Van Leer, B. (1977). "Towards the ultimate conservative difference scheme. IV. A new approach to numerical convection". In: *Journal of Computational Physics* 23.3, pp. 276–299. ISSN: 0021-9991. DOI: 10.1016/0021-9991(77)90095-X.

Vernisse, Y., B. Lavraud, S. Eriksson, D. J. Gershman, J. Dorelli, C. Pollock, B. Giles, N. Aunai, L. Avanov, J. Burch, M. Chandler, V. Coffey, J. Dargent, R. E. Ergun, C. J. Farrugia, V. Génot, D. B. Graham, H. Hasegawa, C. Jacquey, I. Kacem, Y. Khotyaintsev, W. Li, W. Magnes, A. Marchaudon, T. Moore, W. Paterson, E. Penou, T. D. Phan, A. Retino, C. T. Russell, Y. Saito, J.-A. Sauvaud, R. Torbert, F. D. Wilder, and S. Yokota (2016). "Signatures of complex magnetic topologies from multiple reconnection sites induced by Kelvin-Helmholtz instability". In: *Journal of Geophysical Research: Space Physics* 121.10, pp. 9926–9939. ISSN: 2169-9402. DOI: 10.1002/2016JA023051.

Vlasov, A. A. (1968). "THE VIBRATIONAL PROPERTIES OF AN ELECTRON GAS". In: *Soviet Physics Uspekhi* 10.6, pp. 721–733. ISSN: 0038-5670. DOI: 10.1070/PU1968v010n06ABEH003709.

Walker, A. D. M. (1981). "The Kelvin-Helmholtz instability in the low-latitude boundary layer". In: *Planetary and Space Science* 29.10, pp. 1119–1133. ISSN: 0032-0633. DOI: 10.1016/0032-0633(81)90011-8.

Walker, A. D. M. (2019). *Magnetohydrodynamic Waves in Geospace: The Theory of ULF Waves and their Interaction with Energetic Particles in the Solar-Terrestrial Environment*. Boca Raton: CRC Press. ISBN: 978-0-429-09302-9. DOI: 10.1201/9780429093029.

Wang, C.-P., V. G. Merkin, and V. Angelopoulos (2017a). "Mesoscale perturbations in midtail lobe/mantle during steady northward IMF: ARTEMIS observation and MHD simulation". In: *Journal of Geophysical Research: Space Physics* 122.6, pp. 6430–6441. ISSN: 2169-9402. DOI: 10.1002/2017JA024305.

Wang, C.-P., R. Thorne, T. Z. Liu, M. D. Hartinger, T. Nagai, V. Angelopoulos, J. R. Wygant, A. Breneman, C. Kletzing, G. D. Reeves, S. G. Claudepierre, and H. E. Spence (2017b). "A multispacecraft event study of Pc5 ultralow-frequency waves in the magnetosphere and their external drivers". In: *Journal of Geophysical Research: Space Physics* 122.5, pp. 5132–5147. ISSN: 2169-9380, 2169-9402. DOI: 10.1002/2016JA023610.

Wilkins, M. L. (1980). "Use of artificial viscosity in multidimensional fluid dynamic calculations". In: *Journal of Computational Physics* 36.3, pp. 281–303. ISSN: 0021-9991. DOI: 10.1016/0021-9991(80)90161-8.

Winant, C. D. and F. K. Browand (1974). "Vortex pairing : the mechanism of turbulent mixing-layer growth at moderate Reynolds number". In: *Journal of Fluid Mechanics* 63.2, pp. 237–255. ISSN: 1469-7645, 0022-1120. DOI: 10.1017/S0022112074001121.

Wing, S., J. R. Johnson, C. C. Chaston, M. Echim, C. P. Escoubet, B. Lavraud, C. Lemon, K. Nykyri, A. Otto, J. Raeder, and C.-P. Wang (2014). "Review of Solar Wind Entry into and Transport Within the Plasma Sheet". In: *Space Science Reviews* 184.1, pp. 33–86. ISSN: 1572-9672. DOI: 10.1007/s11214-014-0108-9.

Yao, J. and F. Hussain (2018). "Toward vortex identification based on local pressure-minimum criterion in compressible and variable density flows". In: *Journal of Fluid Mechanics* 850, pp. 5–17. ISSN: 0022-1120, 1469-7645. DOI: 10.1017/jfm.2018.465.

Yee, K. (1966). "Numerical solution of initial boundary value problems involving maxwell's equations in isotropic media". In: *IEEE Transactions on Antennas and Propagation* 14.3, pp. 302–307. ISSN: 1558-2221. DOI: 10.1109/TAP.1966.1138693.

Zhang, B., P. A. Delamere, X. Ma, B. Burkholder, M. Wiltberger, J. G. Lyon, V. G. Merkin, and K. A. Sorathia (2018a). "Asymmetric Kelvin-Helmholtz Instability at Jupiter's Magnetopause Boundary: Implications for Corotation-Dominated Systems". In: *Geophysical Research Letters* 45.1, pp. 56–63. ISSN: 1944-8007. DOI: 10.1002/2017GL076315.

Zhang, B., K. A. Sorathia, J. G. Lyon, V. G. Merkin, J. S. Garretson, and M. Wiltberger (2019). "GAMERA: A Three-dimensional Finite-volume MHD Solver for Non-orthogonal Curvilinear Geometries". In: *The Astrophysical Journal Supplement Series* 244.1, p. 20. ISSN: 0067-0049. DOI: 10.3847/1538-4365/ab3a4c.

Zhang, H., Q. Zong, H. Connor, P. Delamere, G. Facskó, D. Han, H. Hasegawa, E. Kallio, Á. Kis, G. Le, B. Lembège, Y. Lin, T. Liu, K. Oksavik, N. Omidi, A. Otto, J. Ren, Q. Shi, D. Sibeck, and S. Yao (2022). "Dayside Transient Phenomena and Their Impact on the Magnetosphere and Ionosphere". In: *Space Science Reviews* 218.5, p. 40. ISSN: 1572-9672. DOI: 10.1007/s11214-021-00865-0.

Zhang, Y., K. Liu, H. Xian, and X. Du (2018b). "A review of methods for vortex identification in hydroturbines". In: *Renewable and Sustainable Energy Reviews* 81, pp. 1269–1285. ISSN: 1364-0321. DOI: 10.1016/j.rser.2017.05.058.

Zhou, Y. and C. Shen (2024). "Estimating gradients of physical fields in space". English. In: *Annales Geophysicae* 42.1, pp. 17–28. ISSN: 0992-7689. DOI: 10.5194/angeo-42-17-2024.

Zou, J., E. Kim, and A. J. Cerfon (2021). "FFT-based free space Poisson solvers: why Vico-Greengard-Ferrando should replace Hockney-Eastwood". In: *arXiv*. DOI: https://doi.org/10.48550/arXiv.2103.08531.

APPENDIX A

Permissions

Figure number	License Number
2.3	5986040568186
2.5	5986050755649
3.2	5972450852106
3.4	Creative Commons Attribution 4.0 International License
3.5a	5973621015215
3.5b	Creative Commons Attribution 4.0 International License
3.6	5976561192485
3.7a	5977080836369
3.7b	5977081366500

Table A.1: A table of all the permissions for figures used in this thesis.